# Force sensing by the vascular protein von Willebrand factor dissected at the single-molecule level

**Jochen Peter Müller**


München 2016

# Force sensing by the vascular protein von Willebrand factor dissected at the single-molecule level

**Jochen Peter Müller**

Dissertation
an der Fakultät für Physik
der Ludwig–Maximilians–Universität
München

vorgelegt von
Jochen Peter Müller
aus Erlangen

München, 20. Mai 2016

Erstgutachter: Prof. Dr. H. Gaub
Zweitgutachter: Prof. Dr. J. Rädler
Tag der mündlichen Prüfung: 12. Juli 2016

# Zusammenfassung

Um übermäßigen Blutverlust im Wundfall zu vermeiden, müssen verletzte Blutgefäße schnell und effektiv wieder verschlossen werden. Ein erster Wundverschluss wird dadurch erreicht, dass sich Blutplättchen an die verletzte Gefäßwand anheften und untereinander zu einem hämostatischen Pfropf verkleben. Bemerkenswerterweise setzen diese Prozesse in Folge lokal veränderter hydrodynamischer Bedingungen im Blut ein, und zwar gekoppelt an die Funktion des Blutproteins von Willebrand Faktor (VWF), welches in Form linearer Multimere im Plasma zirkuliert. Durch seine außerordentliche Länge ist der VWF insbesondere auf erhöhten Elongationsfluss, eine Teilkomponente von hydrodynamischem Scherfluss, sensitiv. Auf lokal erhöhten Elongationsfluss, wie zum Beispiel im Bereich einer Wundstelle, reagiert der VWF mit Konformationsänderungen, die mit einer erhöhten Bindungsaffinität zu Blutplättchen und Kollagen einhergehen. Der VWF vermittelt so die Bildung eines Blutplättchenpfropfs an einer Wundstelle und darüber hinaus das Anheften dieses Pfropfs an die verletzte Gefäßwand, an welcher typischerweise Kollagen aus dem Subendothel freigelegt ist. Ein Mangel an VWF im Blutplasma kann, ebenso wie eine gestörte Funktion des VWF, Ursache des von-Willebrand-Syndroms sein, der häufigsten angeborenen Krankheit mit erhöhter Blutungsneigung. Darüber hinaus gibt es Evidenz, dass der VWF entscheidend zu Thrombose, Arteriosklerose, Herzinfarkt, und anderen weit verbreiteten Krankheiten beiträgt. Der VWF stellt demzufolge nicht nur ein außergewöhnliches biophysikalisches System dar, sondern ist auch medizinisch von höchster Relevanz. Es ist deshalb von großem Interesse, die molekularen Mechanismen zu verstehen, die dem VWF seine Funktion als Sensor hydrodynamischer Kräfte verleihen.
Im Rahmen dieser Dissertation wurde der VWF hinsichtlich solcher molekularer Mechanismen untersucht. Von besonderem Interesse waren dabei große, kraftinduzierte Konformationsänderungen des Proteins, da davon auszugehen ist, dass diese das Verhalten des VWF im Blutfluss entscheidend beeinflussen und somit von herausragender Bedeutung für die Kraftaktivierung des VWF sind. Mittels Rasterkraftmikroskopie (AFM)-basierter Einzelmolekülkraftspektroskopie, welche eine Kraftauflösung von circa 10 pN bietet, wurden einzelne VWF Dimere, die kleinsten sich wiederholenden Untereinheiten von VWF Multimeren, auf ihre Kraftantwort untersucht. Neben dem bereits bekannten Entfaltungssignal der VWF A2 Domäne, zeigten die gemessenen Kraft–Ausdehnungskurven ein zusätzliches Signal, welches auf eine starke intermonomere Interaktion in Dimeren zurückgeführt werden konnte. Die Dissoziation dieser starken Interaktion wurde bei Kräften über 50 pN beobachtet, einhergehend mit einem Längenzuwachs eines einzelnen Dimers von etwa 80 nm. Es wurde gezeigt,

dass die starke intermonomere Interaktion entscheidend von divalenten Ionen abhängt und höchstwahrscheinlich von der VWF D4 Domäne vermittelt wird, da die Interaktion in Dimeren mit einer Deletion der D4 Domäne nicht beobachtet wurde. Darüber hinaus wurde mittels AFM-basierter Bildgebung die Konformation von VWF Dimeren und Multimeren mit einer lateralen Auflösung unter 10 nm visualisiert. Basierend auf Kraft- und Bildgebungsdaten wurde abgeschätzt, dass in VWF Multimeren unter physiologischen Pufferbedingungen etwa die Hälfte aller Dimere durch die starke intermonomere Interaktion geschlossen sind. Dieser Befund impliziert, dass die effektive Länge des VWF, d.h. die Länge, die im Blutfluss entscheidend zum Aufbau hydrodynamischer Kräfte beiträgt, durch fest geschlossene Dimere deutlich verkürzt wird. Es ist deshalb davon auszugehen, dass die Elongation eines Multimers mit fest geschlossenen Dimeren wesentlich höhere Raten von Elongationsfluss erfordert als die Elongation eines Multimers, das nur aus flexiblen Dimeren besteht.
Zudem wurde entdeckt, dass der Anteil fest geschlossener VWF Dimere auf unterschiedliche Weise reguliert werden kann, z.B. über den pH-Wert. So wurde die starke intermonomere Interaktion beispielsweise bei einem physiologischen pH-Wert von 7,4 mit größter Häufigkeit beobachtet, jedoch quasi gar nicht mehr unterhalb eines pH-Wertes von 6,8. Unterhalb dieses Wertes nahm jedoch der Anteil kompakter Dimere mit sinkendem pH-Wert zu, im Einklang mit Ergebnissen einer vorherigen Studie, welche die Konformation des VWF mittels Transmissionselektronenmikroskopie (TEM) untersucht hatte. Die der vorliegenden Dissertation zugrundeliegenden Daten zeigen, dass die Kompaktheit von Dimeren unter pH 6,8 von anderen Interaktionen vermittelt wird, die im Vergleich zur starken intermonomeren Interaktion eine geringe mechanische Stärke aufweisen. Aufgrund eines wesentlich verringerten mechanischen Widerstands des VWF unter leicht sauren Bedingungen darf spekuliert werden, dass lokale Azidose, beispielsweise im Bereich einer Wundstelle, eine Möglichkeit darstellen könnte die hämostatische Aktivität des VWF zu erhöhen.
Da die Kräfte, die im Blutfluss auf den VWF wirken und ihn zur Hämostase aktivieren, entscheidend von der Länge des VWF abhängen, wurde auch die Größenverteilung von VWF Multimeren im Rahmen dieser Arbeit untersucht. Hierzu wurden sowohl AFM-basierte Bildgebungsexperimente als auch Photobleichungsexperimente durchgeführt, wobei letztere auf interner Totalreflexionsfluoreszenzmikroskopie (TIRF-Mikroskopie) basierten. Ergebnisse beider Ansätze untermauern eine exponentielle Größenverteilung des VWF nach seiner Multimerisierung, welche von Kollaborationspartnern im Vorfeld aus Geldaten und Fluoreszenzkorrelationsspektroskopie (FCS)-daten gefolgert worden war.
Zusammenfassend sei festgehalten, dass die Daten dieser Doktorarbeit eine exponentielle Größenverteilung des VWF bestätigen und darüber hinaus wichtige Mechanismen beleuchten, die dem VWF seine Funktion als Sensor hydrodynamischer Kräfte verleihen. Diese Doktorarbeit stellt deshalb einen wichtigen Beitrag dar, die Kraftaktivierung des VWF zur Hämostase und die Rolle des VWF bei Thrombose auf Einzelmolekülebene zu verstehen.

# Abstract

In order to prevent excessive blood loss at sites of vascular injury, damaged vessel walls need to be sealed rapidly and effectively by a hemostatic plug. Remarkably, initiation of hemostasis is triggered by increased elongational blood flow at sites of vascular injury, and for this crucially relies on the multimeric vascular protein von Willebrand factor (VWF). Enabled by its extraordinary length, VWF responds to elongational flow with force-induced conformational changes that increase VWF's binding affinity to platelets and collagen. This ability allows VWF to promote the formation of platelet plugs exactly where needed and to recruit such plugs to injured vessel walls, at which subendothelial collagen is typically exposed. While deficiency or dysfunction of VWF causes the common bleeding disorder von Willebrand disease, an increased activity of VWF has been recognized to contribute to thrombosis, arteriosclerosis, myocardial infarction, and further widespread diseases. Hence, VWF is not only an extraordinary system from a biophysical point of view, but also highly relevant from a medical perspective. It is therefore of outstanding interest to elucidate the molecular mechanisms that are responsible for VWF's unique force-sensing ability.

Within the framework of this thesis, important force-sensing mechanisms of VWF were dissected at the single-molecule level. Of special interest were large-scale conformational changes of VWF induced by force, as such changes can be assumed to decisively influence the interplay between VWF and hydrodynamic flow, which in turn regulates VWF's activation for hemostasis. Using atomic force microscopy (AFM)-based single-molecule force spectroscopy, which provides a force resolution as low as $\sim 10\,\mathrm{pN}$, the force response of individual VWF dimers – the smallest repeating subunits of VWF multimers – was probed. Characteristic force–extension traces revealed, in addition to the well-characterized unfolding of VWF's A2 domain, a strong intermonomer interaction, which was found to crucially involve VWF's D4 domain and to critically depend on divalent ions. Dissociation of this strong interaction occurred at forces above $\sim 50\,\mathrm{pN}$ and provided $\sim 80\,\mathrm{nm}$ of additional length to the elongation of a dimer. Corroborated by the conformation of VWF, which was visualized by AFM imaging with a lateral resolution below 10 nm, it was estimated that, under near-physiological conditions, approximately one-half of the dimers within a VWF multimer are firmly closed via the strong intermonomer interaction. Importantly, hidden length in firmly closed dimers implies a reduced length of VWF contributing to force sensing. Therefore, elongation of a VWF multimer with firmly closed dimers can be expected to require significantly higher rates

of elongational flow than elongation of a fully flexible multimer with the same number of dimers.

Notably, it was found that the ratio of firmly closed dimers in VWF can be tuned in different ways, e.g., by varying the pH. While the strong intermonomer interaction was observed with highest frequency at pH 7.4, it was essentially absent at pH values below 6.8. However, below the latter value, the ratio of compact dimers, as observed by AFM imaging, increased with decreasing pH, in line with a previous transmission electron microscopy (TEM) study. These findings indicate compactness of dimers below pH 6.8 to be promoted by other interactions that possess low mechanical resistance compared to the strong intermonomer interaction. Owing to a markedly decreased mechanical resistance of VWF under acidic pH conditions, it may be speculated that local acidosis, e.g., at sites of vascular injury, represents a means to enhance VWF's hemostatic activity where needed.

As force sensing by VWF critically depends on VWF's multimer size, the size distribution of VWF was also addressed in this thesis. Both AFM imaging and photobleaching experiments employing total internal reflection fluorescence (TIRF) microscopy corroborated an exponentially decaying size distribution of VWF, which had previously been inferred from a quantitative analysis of gel data and fluorescence correlation spectroscopy (FCS) data.

To summarize, in conjunction with underlining an exponential size distribution of VWF, the data presented in this thesis elucidate important force-sensing mechanisms of VWF, which are the key to its function in hemostasis and its role in thrombosis.

# Contents

# 1 Introduction

Nature has developed a complex yet very effective way of sealing damaged blood vessels. The combination of processes that stanch a wound is called hemostasis and is typically subdivided into the steps of vasoconstriction, platelet plug formation (primary hemostasis), and fibrin clot formation (blood coagulation, secondary hemostasis) [1–3]. From a biophysical point of view, primary hemostasis is particularly interesting, as different underlying adhesion mechanisms have evolved in response to the wide spectrum of shear rates in our circulatory system, ranging from 1 to $10^5\,\mathrm{s}^{-1}$ [4–6]. In general, the formation of a platelet plug and its recruitment to an injured vessel wall, at which subendothelial collagen is commonly exposed, provides a first wound closure and prevents excessive blood loss [5, 7]. Although the formation of a platelet plug and the adhesion of platelets to collagen are often considered distinct processes, they are very similar from a mechanistic point of view, as they both involve the adsorption of platelets from the blood stream onto a surface, mediated by adhesive ligand and receptor pairs [7]. It is therefore no surprise that both processes are similarly challenged by high shear rates [7], i.e., shear rates above $\sim 1000\,\mathrm{s}^{-1}$, at which hydrodynamic lift forces increasingly inhibit the formation of large contact areas, thereby making platelet arrestment onto a surface difficult [6].

This problem is overcome with the large plasma glycoprotein von Willebrand factor (VWF), which mediates platelet adhesion to collagen and platelet aggregation only under sufficiently high shear conditions in the bloodstream [6, 8], or more precisely, under sufficiently high rates of elongational flow [9, 10], a component of shear flow [11]. Notably, elongational flow components are markedly increased at sites of vascular injury [10, 12, 13], i.e., exactly where VWF needs to be activated by hydrodynamic forces for primary hemostasis. Adversely, owing to increased elongational flow in stenosed vessels [10, 14], VWF also plays a central role in thrombosis [10, 15], and additionally contributes to arteriosclerosis [16, 17], myocardial infarction [15, 18], and stroke [10, 15]. VWF's sensitivity to elongational flow is a result of VWF's enormous length [10], which arises from VWF's linear multimeric nature [19, 20]. The latter additionally guarantees that a multitude of specific recognition sites are available, thereby enabling strong multivalent binding [8, 13].

VWF's physiological relevance is underlined by mutations in VWF that cause von Willebrand disease (VWD) [20], the most common hereditary bleeding disorder, which is commonly subdivided into 3 types [1]. While in VWD type I plasma concentrations of VWF are significantly

decreased, VWF is almost completely absent in VWD type 3, the most severe form of VWD. In VWD type 2, VWF is qualitatively defective, and the resulting bleeding symptoms can significantly vary. For instance, patients with the subtype 2A exhibit a reduced fraction of large, hemostatically active multimers [10, 21], illustrating the importance of the physiological size distribution of VWF. Commonly, size distributions of VWF and mutants are analyzed by gel electrophoresis [1, 22, 23]. Within a side project of this thesis, the size distribution of wildtype VWF was addressed at the single-molecule level, first in photobleaching experiments based on total internal reflection fluorescence (TIRF) microscopy [24] and afterwards in imaging experiments based on atomic force microscopy (AFM) [25].

From a biophysical point of view, VWF is a force-sensing molecule responding to hydrodynamic forces in the vasculature. In fact, force-sensing molecules are critically involved in a variety of biological processes, such as regulation of muscle gene expression or assembly of the cytoskeleton [26–29]. The molecular mechanisms by which force is converted into a physiological signal are accessible with single-molecule force spectroscopy, which may be performed using different manipulation techniques, e.g., AFM, optical tweezers, or magnetic tweezers [29, 30]. Essentially all previously studied force-sensing molecules rely on well-tuned force-induced conformational changes that lead to the exposure of active recognition sites [29]. Hence, it is an educated guess to assume that critical force-induced conformational changes are also the general mechanisms that regulate VWF's hemostatic potential, e.g., VWF's affinity to platelets [10, 13, 31]. Except for the force-induced down-regulation of VWF, which involves unfolding of the A2 domain and subsequent cleavage of large, hemostatically active multimers into shorter, and less active multimers by the enzyme ADAMTS13 (a disintegrin and metalloprotease with a thrombospondin type 1 motif, member 13) [12, 32], these molecular mechanisms are however not entirely understood. A very special feature of VWF compared to other force-sensing molecules is the fact that VWF's structure itself dictates the forces that VWF is subjected to, as hydrodynamic forces result primarily from an interplay between VWF's length and elongational flow [9, 10, 12, 13]. In other words, force-induced elongation of VWF in elongational flow will lead to increased forces acting on VWF, thereby triggering elongation in a positive feedback. In shear flow, however, VWF's elongation is more complex, as tumbling and relaxation also play a role [11], with characteristic time scales that depend on VWF's length [12, 33]. Undoubtedly, structure, force, and function are so closely connected in the case of VWF that they must be considered together in order to fully comprehend the mechanisms that regulate VWF's hemostatic potential.

In a manner of sense, VWF's function in primary hemostasis is to convert flow into a physiological signal, i.e., to convert flow into an increased affinity to platelets and collagen, as well as into the exposure of the ADAMTS13 cleavage site by A2 unfolding [12, 32]. In this thesis, the conversion of flow into force, and hence into a physiological signal, will be referred to as force sensing by VWF. As indicated above, a force-induced physiological signal may

well result from the exposure of a critical recognition site, or from changes that induce a higher affinity state of a recognition site [31]. Of outstanding interest for the comprehension of VWF's force sensing ability are, however, also those force-induced conformational changes that do not directly involve specific recognition sites, especially if they significantly affect VWF's length. Importantly, such large-scale conformational changes can be assumed to decisively influence the interplay between VWF and hydrodynamic flow, and to thus tune the forces that regulate VWF's hemostatic potential. Within the framework of this thesis, by employing a combination of AFM-based single-molecule force spectroscopy and AFM imaging, large conformational changes of VWF induced by force were dissected at the single-molecule level. Thus, a quantitative understanding of important force sensing mechanisms of VWF was gained. In particular, the combination of force and imaging data proved useful to dissect and locate pH-dependent interactions in VWF and to characterize their mechanical resistance, which crucially underlies force sensing by VWF.

In this thesis, I will first give a short introduction into the general basics of protein structure and review influential research that decisively shaped the current picture of VWF's function from a biophysical perspective. Further, I will give a brief theoretical background on the interplay of linear polymers with hydrodynamic flow, thereby hinting at the complex behavior of VWF in the bloodstream. Important aspects of the current state of research on the one hand and their partially limited understanding on the other hand motivated the experiments that were carried out within the framework of this thesis. The materials and methods that were employed for the performed experiments will be described in the third chapter of this thesis, supplemented here and there with underlying theory and fundamental models. Afterwards, experimental results will be presented and discussed in detail, especially with respect to their implications. Finally, I will summarize the most important insights of this thesis and, picking up on these, give a short outlook towards future experimental and computational research that would link well to the results presented in this work.

# 2 Biophysical background on von Willebrand factor (VWF)

This chapter will give a brief background on the biology and physics of VWF, thereby providing an overview of influential research that motivated the experiments that I performed in the framework of this thesis. After initially presenting VWF's multiple domains and their functions, the critical steps of VWF's biosynthesis will be reviewed. In this context, special emphasis will be placed on the pH dependence of the conformation of dimeric subunits, which is believed to be a prerequisite for orderly multimerization of VWF. As will be further discussed, VWF's linear multimeric nature is the key to its force-sensing ability in the blood, which underlies both VWF's activation for hemostasis and the down-regulation of VWF's thrombotic activity. Owing to the physiological relevance of VWF's shear-induced elongation, insights into the behavior of linear polymers in shear and elongational flow will be given. Finally, to motivate the experiments that were performed within the framework of this thesis, an interim conclusion will be drawn. To facilitate the comprehension for the non-specialist reader, the first section of this chapter will review fundamentals of protein structure and the role of the pH.

## 2.1 Fundamentals of protein structure and the role of the pH

Proteins are one of the basic components of living systems, as these macromolecules serve important functions in essentially all biological processes [34, 35]. For instance, they catalyze reactions as enzymes [35–37], drive immunological responses as antibodies [35, 38], transport and protect other molecules as carrier proteins [39, 40], provide mechanical strength to bones, tendons, ligaments and skin, e.g., as variants of collagen [35, 41], or regulate muscle gene expression or assembly of the cytoskeleton as force sensors [26–29]. The specific function of a protein is directly related to its structure [34], which determines for example the protein's affinity to bind other molecules and which gives rise to certain mechanical properties of the protein. Importantly, changes in the structure of a protein, which can be for instance achieved by applying an external force, can lead to an altered function of the protein, as specific binding interfaces may be affected [29, 42].

From a structural point of view, a protein is a polymer that is built up from a linear sequence of covalently linked amino acids. By convention, such a polymer is commonly called a polypeptide if it consists of less than 100 amino acids [35]. Given that most proteins consist, however, of more than 100 amino acids [34], there are myriad possibilities to construct linear sequences from the 20 canonical amino acids. Such a linear sequence of amino acids is called the primary structure of a protein, and is reported from the amino terminus (N terminus) to the carboxyl terminus (C terminus). Owing to diverse interactions between its constituent amino acids, a protein can fold into a three-dimensional structure [34, 35]. Interactions between amino acids involve non-covalent ones, e.g., hydrogen bonding, van der Waals forces, electrostatic interactions between ions, and hydrophobic interactions, as well as covalent disulfide bonds between cysteine residues [34, 35]. In fact, cysteine is the only amino acid whose characteristic side chain is capable of forming a covalent bond with the side chain of another amino acid, i.e., of another cysteine [34, 35]. Overall, the structure of a protein refers to the three-dimensional arrangement of amino acids, and their constituent atoms.
Commonly, four levels of structure are discriminated – primary, secondary, tertiary, and quaternary [34, 35]. While the primary structure of a protein is the linear sequence of constituent amino acids, the term "secondary structure" refers to regular local substructures such as $\alpha$-helices and $\beta$-sheets, whose formation crucially depends on hydrogen bonding between certain amino acids [34, 35]. Such local substructures can – together with flexible loops – further fold into a compact three-dimensional structure. If folding is independent of other parts of the protein, the corresponding part of the protein is called protein domain, and its three-dimensional structure is called the tertiary structure of the domain. Proteins can consist both of only a single domain or also of a multitude of domains. Multifunctional proteins, such as VWF (see section 2.2), typically possess a modular conformation, consisting of multiple domains, among which distinct domains have different functions [10, 43–45]. For example, while VWF's A1 and A3 domain exhibit specific binding sites to different types of collagen and platelets [10, 46–52], the A2 domain possesses a buried cleavage site for the enzyme ADAMTS13, which is exposed when the A2 domain unfolds (Fig. 2.1) [12, 32]. In fact, unfolding of A2 upon mechanical load is possible, as the domain lacks a long-range disulfide bond, which in case of A1 and A3 protect the respective domain from force-induced unfolding [32, 53]. The term quaternary structure refers to the arrangement of folded protein subunits within a single protein or to complexes of more than one protein, resulting in structures of higher order, such as for instance in the case of VWF. After expression of VWF monomers in the ribosome, monomers are covalently linked at one end to form dimers, which afterwards are covalently linked at their other end to form linear multimers (concatemers, see section 2.3). Here, the formation of concatemers critically depends on the quaternary structure of VWF dimers, e.g., on pairwise associated C-terminal stems, which can be regulated for instance by the pH (see subsection 4.2.2 and Appendix B.1) [54–56].

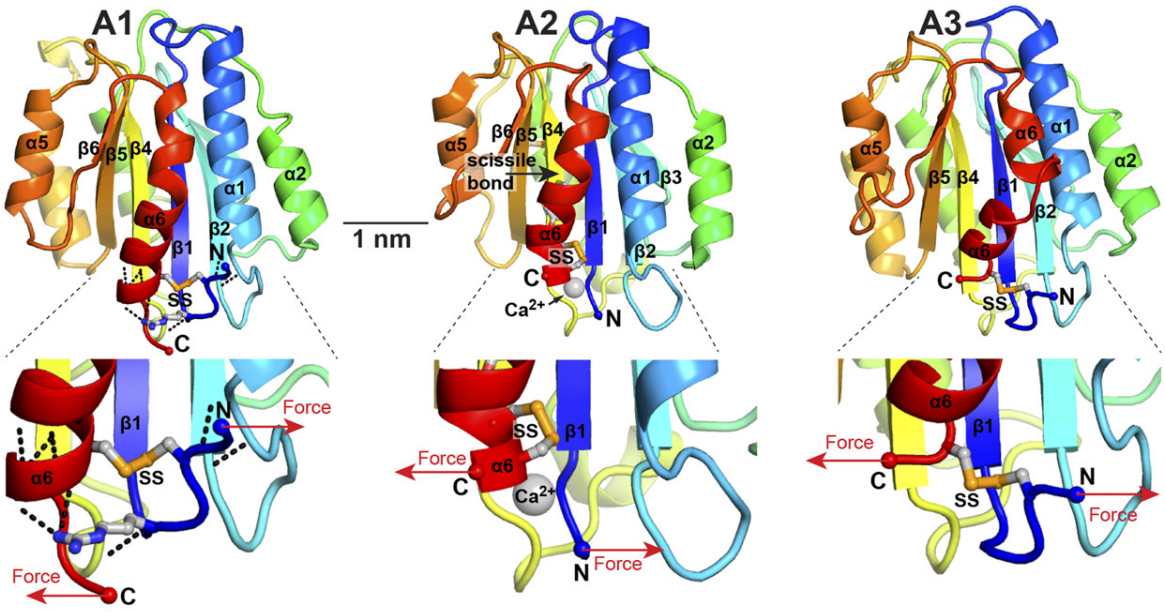


**Figure 2.1:** Crystal structures of VWF's A domains in cartoon representation [10]. Rainbow colors go from N terminus (blue) to C terminus (red). VWF's A domains exhibit a central hydrophobic $\beta$-sheet consisting of 6 $\beta$-strands, surrounded typically by 6 amphipathic $\alpha$-helices. Arrows indicate how domains are loaded with force when present in a VWF concatemer that experiences hydrodynamic force. As A2, in contrast to A1 [46–49] and A3 [50–52], lacks a long-range disulfide bond (orange sticks), it can unfold when subjected to force [12, 32]. In presence of calcium, however, A2 is stabilized, as domain refolding is strongly enhanced when a calcium ion (silver sphere) is bound to a calcium-binding site [57–59]. Adapted with permission from reference [10].

In fact, the structure and function of a protein depend also very generally on its environment. For instance, high concentrations of salt, e.g., sodium chloride, can screen electrostatic interactions in the structure of a protein, and increased temperatures can cause a protein to denature, i.e., to lose its structure and adopt a random coil configuration. As mentioned above, another critical parameter is the pH, which by affecting the protonation state of certain amino acids may change their charge and thereby induce structural changes.

The pH value of an aqueous solution specifies its acidity or alkalinity (basicity). While acids are chemical substances that act as a proton donor, i.e., increase the concentration of $H_3O^+$ (hydronium) ions, bases are substances that act as a proton acceptor, i.e., decrease the concentration of hydronium ions in solution. The pH is defined as the negative decadic logarithm of the activity of hydrogen ions in an aqueous solution. For dilute solutions, it is roughly the negative logarithm to the base 10 of the concentration of hydronium ions divided by the standard molarity $1\,\mathrm{mol\,L^{-1}}$:

$$\mathrm{pH} \approx -\log_{10} \frac{[\mathrm{H_3O^+}]}{1\,\mathrm{mol\,L^{-1}}}\,. \tag{2.1}$$

Due to the autoprotolysis of water, there are also hydronium and hydroxyl ions ($OH^-$) in pure water. At 25°C, the concentration of hydronium and hydroxyl ions is approximately

$1 \cdot 10^{-7}\,\mathrm{mol\,L^{-1}}$, yielding a neutral pH of 7. While pH values below 7 are called acidic, pH values above 7 are called alkaline or basic.
If an acidic substance HA is dissolved in an aqueous solution, it can act as a proton donor and thereby be deprotonated:

$$\mathrm{HA} + \mathrm{H_2O} \rightleftharpoons \mathrm{A^-} + \mathrm{H_3O^+}\,. \tag{2.2}$$

For this reaction, the equilibrium constant $K$, which depends on the change in Gibbs free energy $\Delta G$ of the reaction, is:

$$K = \frac{[\mathrm{A^-}] \cdot [\mathrm{H_3O^+}]}{[\mathrm{HA}] \cdot [\mathrm{H_2O}]} = \exp\left(\frac{-\Delta G}{k_\mathrm{B} T}\right)\,, \tag{2.3}$$

where $k_\mathrm{B}T$ ($\approx 1.38 \cdot 10^{-23}\,\mathrm{J\,K^{-1}}$) is the Boltzmann constant and $T$ the temperature. In case of the solutions typical of biological systems, the concentration of water remains virtually constant, and a new constant $K_\mathrm{a}$ can be defined:

$$K_\mathrm{a} = [\mathrm{H_2O}] \cdot K\,. \tag{2.4}$$

The negative logarithm to the base 10 of $K_\mathrm{a}$ divided by the standard molarity $1\,\mathrm{mol\,L^{-1}}$ is called the $\mathrm{pK_a}$ value:

$$\mathrm{pK_a} = -\log_{10} \frac{K_\mathrm{a}}{1\,\mathrm{mol\,L^{-1}}}\,. \tag{2.5}$$

The latter is, according to Eq. 2.3, proportional to $\Delta G$ and is therefore a measure of the strength of an acidic substance in solution. Small $\mathrm{pK_a}$ values are indicative of strong acids, large $\mathrm{pK_a}$ values are indicative of weak acids. Combining Eq. 2.5 and Eq. 2.1 yields:

$$\mathrm{pH} = \mathrm{pK_a} + \log_{10} \frac{[\mathrm{A^-}]}{[\mathrm{HA}]}\,. \tag{2.6}$$

This formula shows that half-neutralization is reached if the pH is equal to the $\mathrm{pK_a}$ value. In other words, if the difference between the $\mathrm{pK_a}$ value of an acidic substance and the pH is small, the substance can either exist as protonated or deprotonated.
These considerations are of great physiological relevance for proteins in solution, as several amino acids possess functional groups whose protonation state can – depending on their $\mathrm{pK_a}$ value – change with pH (Table 2.1). Strikingly, the imidazole side chain in a histidine residue possesses a $\mathrm{pK_a}$ value of approximately 6.5 [60], which is in a range of pH values that are relevant for many biological systems. Importantly, by changing the charge of amino acid residues in proteins, the pH can evoke structural changes, e.g., change interfaces for specific binding or induce large-scale conformational changes. Here, a very prominent example is hemoglobin's pH-dependent affinity for oxygen binding (Bohr effect), which regulates oxygen uptake and release [39].

| Amino acid | $pK_a$ |
|---|---|
| Aspartic acid / glutamic acid | 4.4 |
| Histidine | 6.5 |
| Cysteine | 8.5 |
| Tyrosine | 10.0 |
| Lysine | 10.0 |
| Arginine | 12.0 |

**Table 2.1:** Titratable amino acids commonly found in proteins. The indicated $pK_a$-values are for free amino acids. In proteins, these values can vary considerably. Values taken from reference [60].

## 2.2 Domain organization

Many of VWF's multiple functions have been related to individual domains in VWF [10, 20], which contain binding sites for certain binding partners and enzymes. As VWF's domains are still a matter of research – and only in parts structurally characterized at high resolution –, different domain annotations are used in the literature. Zhou *et al.* revised a frequently used domain annotation (Fig. 2.2A) and additionally assigned disulfide bonds between Cystein residues (Fig. 2.2B) [61]. Revised assignments by Zhou *et al.* were based on sequence homologies, the outcome of expression experiments of a series of different constructs, visualization of well expressed domains by transmission electron microscopy (TEM), and identification of substructures in larger constructs – such as the C domains in D4-CK dimers.

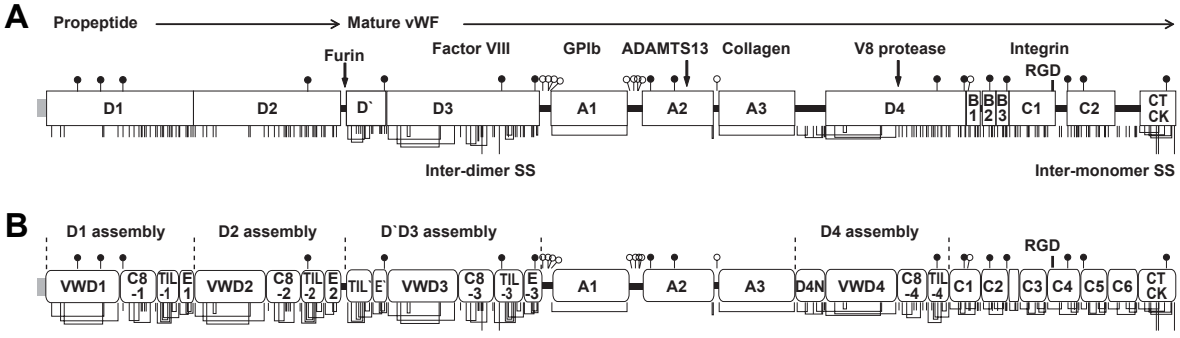


**Figure 2.2:** Domain organization of VWF. Depicted are a domain assignment that is often used in the literature (A) and a revised assignment by Zhou, Springer, and coworkers [61] (B). Binding sites for specific binding partners are shown in (A). Sites of N- and O-linked glycans are indicated by closed and open lollipops, respectively. Cysteines are shown as vertical lines and are connected for chemically defined disulfide bonds in (A) and for additionally predicted ones in (B). Adapted with permission from reference [61].

According to the domain assignment by Zhou *et al.*, which will be used in this thesis, VWF is composed of A domains, C domains, and D domains. The latter are large assemblies of distinct submodules and are largely involved in dimerization and multimerization of VWF (see section 2.3). However, domains D1 and D2 (propeptide, aa 26–763) are not part of

mature VWF (aa 764–2813), as they are cleaved by furin before VWF's secretion into the plasma. Their role for VWF's biosynthesis will be presented within section 2.3, together with the function of D'D3 for N-terminal multimerization. Here, it should however be mentioned that D'D3 harbors a binding site for factor VIII [40]. The latter is an essential clotting factor, which is deficient in hemophilia A [19, 20], the most common form of the hemophilia group of bleeding disorders [62]. Binding to VWF protects factor VIII from rapid degradation in the plasma [19, 20].

VWF's D4 assembly possesses a cleavage site for Staphylococcus aureus V8 protease [63]. Cleavage by V8 was observed in TEM images to obstruct the formation of pH-regulated bouquets in dimers [55], which were still observed for uncleaved D4-CK dimers (see section 2.3). On the one hand, this finding indicated a crucial role of D4 for pH-regulated bouquet formation. On the other hand, however, gel filtration data of V8-cleaved D4-CK dimers exhibited the same pH trends as uncleaved constructs, i.e., were not in line with observations from TEM. While pH-regulated dimeric bouquets in VWF dimers were also observed within the framework of this thesis (see subsection 4.2.2 and Appendix B.1), Achim Löf found in his PhD work that pH-regulated bouquets were not present in dimers with a deletion of D4 (see Appendix B.1), indicating that D4 plays indeed a crucial role for the pH-regulated formation of dimeric bouquets. Moreover, within this thesis, D4 was found to play a crucial role for mediating a strong intermonomer interaction in dimers, which can be assumed to tune force sensing by VWF in the plasma (see section 4.1 and Appendix A.1) [56].

Similarly to the D domains, VWF's C-terminal domains – i.e., C1 to C6 and the C-terminal cystine knot (CK)(CTCK) domain – are mainly stabilized by a large number of intradomain disulfide bonds [10, 61]. While the CK domain, which has been recently characterized at high resolution [64], mediates dimerization of VWF via disulfide bonds [19, 20], both structure and function of the domains C1 to C6 remain less clear. It is tempting to claim that C1 to C6 may give length to VWF, a prerequisite for VWF's force-sensing ability. In fact, the length corresponding to domains C1 to C6 is hidden in dimeric bouquets before secretion into the vasculature (Fig. 2.4), and, as can be expected from results of this thesis, partially also in the vasculature, at least below forces of 50 pN. Uniquely in VWF, the C4 domain possess an RGD motif to which the platelet integrin $\alpha_{\mathrm{IIb}}\beta_3$ can bind. Interestingly, this binding was observed recently in a TEM study under static conditions [61], indicating that it does not require activation of VWF by force.

Notably, VWF's C and D domains are homolgous to N- and C-terminal parts of the gel-forming mucin MUC2, which is evolutionary related to VWF [65, 66]. Both in MUC2 and in VWF, C and D domains appear to be primarily relevant for pH-regulated multimerization and overall structure. In VWF, the specific functions for primary hemostasis can be largely attributed to the A domains. These exhibit a central hydrophobic $\beta$-sheet consisting of 6 $\beta$-strands, typically surrounded by 6 amphipathic $\alpha$-helices (Fig. 2.1). As A1 [46–49] and

A3 [50–52] have a long-range disulfide bond, they are largely protected against unfolding. The A2 domain, however, lacks such a disulfide bond and can therefore unfold when subjected to force, a prerequisite for its cleavage by the enzyme ADAMTS13 [12, 32].
VWF's A1 domain exhibits binding sites for the platelet receptor glycoprotein Ib$\alpha$ (GPIb$\alpha$) and for collagen, although the main collagen binding domain in VWF is A3 [7, 10, 19, 20]. As will be discussed in subsection 2.4.2, specific binding sites for platelets and collagen allow VWF to recruit platelets to an injured vessel wall and to promote the formation of platelet plugs under high shear rates. In this context, it may be mentioned that the flexible linkers adjacent to A1, which are the most prominent linkers in VWF and also the regions of most abundant extent of N- and O-glycosylation, were claimed in a recent review article to regulate the function of A1 and its responsiveness to ristocetin [10]. Finally, A1 can bind to heparin [67] and probably also to extracellular DNA, as suggested by a recent study [68].

## 2.3 From biosynthesis to secretion

The complex biosynthesis of linear VWF multimers (concatemers) in vascular endothelial cells and megakaryocytes involves elaborate posttranslational processing (Fig. 2.3) [19, 20]. Here, several steps crucially depend on pH-regulated conformational changes of VWF's subunits [54, 55]. After expression as pre-pro-proteins – comprising a short signal peptide sequence and pro-peptide domains D1 and D2 in addition to the domains present in mature VWF (D'D3, A1, A2, A3, D4, C1-C6, CK; see Fig. 2.2B) – and subsequent cleavage of the signal peptide, monomers are dimerized in the endoplasmatic reticulum (ER, pH 7.4) in a tail-to-tail fashion via disulfide bonds between their CK domains (Fig. 2.3A) [19]. VWF's dimerization is catalyzed by protein disulfide isomerase (PDI), as was revealed within a project involving work that was performed within the framework of this thesis (see Appendix A.3) [37]. In the ER and the Golgi, dimers are equipped with N- and O-linked glycans [19].
At the lowered pH values of the Golgi and *trans*-Golgi (pH 6.2) (Fig. 2.3B), dimers were observed in TEM images to preferentially adopt a compact conformation, as monomers zip up from the CK domains up to the A2 domains to form so-called dimeric bouquets (Fig. 2.4) [55]. The fact that dimeric bouquets were also observed for truncated dimeric constructs A3-CK and D4-CK indicates that the domains N-terminal of D4 are not crucial for the formation of dimeric bouquets [55]. It was speculated that bouquet formation is mediated by histidine residues in VWF's C-terminal segment D4-CK [55]. Indeed, several of VWF's domains harbor a comparably large number of histidines, in particular VWF's D4 domain, which is an assembly of distinct sub-modules (D4N, D4, C8-4, and TIL4) [61].
Compact dimeric bouquets are thought to favor the formation of closely packed helical tubules built up from dimers in the *trans*-Golgi and Weibel-Palade bodies (Fig. 2.3C) [13, 54, 55]. Latter are secretory granules uniquely found in endothelial cells, possessing a pH of approxi-

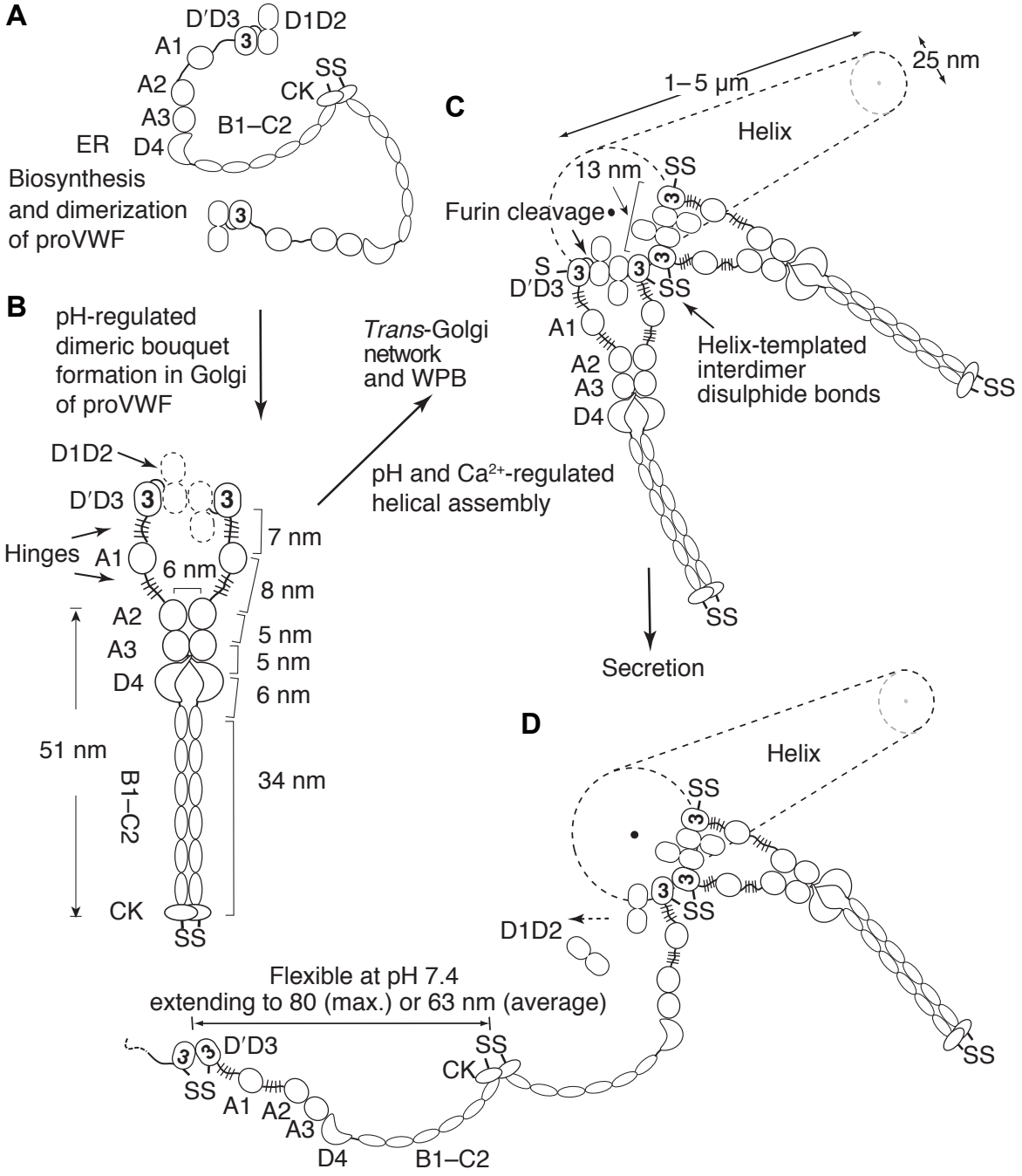


**Figure 2.3:** Biosynthesis of VWF. In the endoplasmatic reticulum (ER, pH $\approx$ 7.4, A), monomers are dimerized in a tail-to-tail fashion via disulfide linkage between their CK domains. At the lowered pH values of the Golgi and *trans*-Golgi (pH $\approx$ 6.2, B), dimers preferentially adopt a compact conformation, as monomers zip up from the CK domains up to the A2 domains to form so-called dimeric bouquets. In the *trans*-Golgi and Weibel-Palade bodies (pH $\approx$ 5.5, C) dimers self-assemble into tightly packed helical tubules and are linked in a head-to-head fashion via formation of disulfide bonds between D'D3 domains. Tubule formation crucially depends on the pH-regulated association of the pro-peptide domains D1-D2 [10, 13, 54], which are cleaved by furin before VWF's secretion into the vasculature. In the plasma (D), VWF encounters a pH of 7.4 and adopts an overall more flexible conformation. However, within the framework of this thesis, it was shown that a strong intermonomer interaction is present in roughly half of VWF's dimeric subunits under near-physiological conditions [56]. All dimensions are averages from class averages (see Fig. 2.4). Adapted with permission from reference [55].

mately 5.4 [69], which is close to VWF's isoelectric point (pI) [70]. The formation of tubules critically depends on pH-regulated association of the pro-peptide domains D1-D2 [19, 54] and goes along with orderly linear multimerization of dimers [54, 55]. Directed by the tubule architecture, linkage of dimers occurs in a head-to-head fashion via formation of disulfide bonds between D'D3 domains [19, 55], resulting in concatemers built up from dimers as smallest repeating subunits. After proteolytic cleavage of the pro-peptide domains D1 and D2 by furin, dimers possess a mass of $\sim 500\,\mathrm{kDa}$.

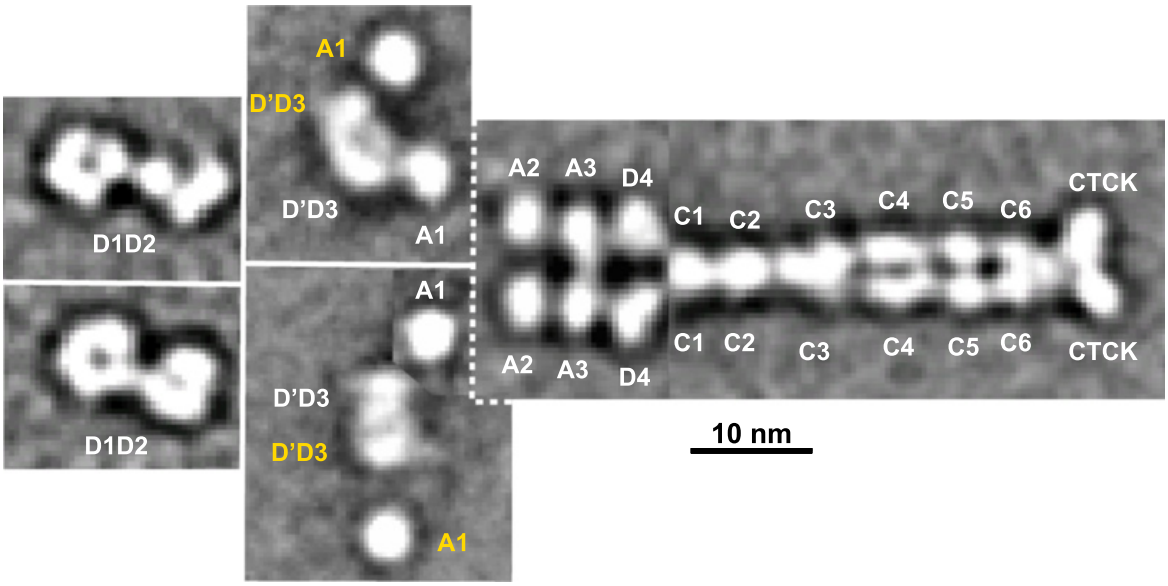


**Figure 2.4:** VWF domains and pH-regulated dimeric bouquet as observed in TEM. Shown are class averages of TEM images of dimeric A1-CK (pH 6.2, [55]), dimeric D'D3-A1 (pH 6.2, [55]), and monomeric D1-D2 constructs (pH 7.4, [61]). Domains that would belong to an individual dimer are labeled in white, and those that would be part of other dimers and be disulfide-linked within concatemers are labeld in yellow. Taken with permission from reference [10].

In the plasma (Fig. 2.3D), VWF encounters a pH of 7.4 and was claimed to adopt a flexible conformation [55]. However, within the framework of this thesis, it was shown that a strong intermonomer interaction is present in roughly half of VWF's dimeric subunits under near-physiological conditions (see section 4.1 and Appendix A.1) [56].

## 2.4 VWF as a sensor of hydrodynamic forces in the vasculature

This section will highlight experimental data that reveal the relevance of force for VWF's function in hemostasis and its role in thrombosis. Moreover, it will be shown that the down-regulation of VWF's thrombotic activity is likewise related to force, although possibly on longer timescales than VWF's activation [12]. Generally, forces on VWF result from a complex interplay between hydrodynamic flow and VWF's extraordinary length [10, 12], which can

exceed 15 µm in the plasma [6]. To establish a basis for comprehending the shown experimental data from a physical point of view, the behavior of linear polymers in shear and elongational flow will be discussed in the beginning of this section.

### 2.4.1 Polymer behavior in shear and elongational flow

In the blood, forces on VWF can be assumed to result primarily from VWF's interplay with hydrodynamic flow [6, 9, 10, 12, 13, 33]. To gain insight into this interplay, an understanding of the behavior of linear polymers in shear and elongational flow is a prerequisite, but, importantly, not the last word on the subject. Already in the case of simple shear flow, the behavior of VWF can be expected to be much more complex than the behavior of an ideal polymer. Most notably, VWF can undergo conformational changes, which on the one hand depend on the interplay between VWF and flow, and which on the other hand dictate how this interplay evolves with time.
Furthermore, it should be taken into account that blood is a complex non-Newtonian fluid [71], as it contains ions, proteins, lipoproteins, cells, etc. For instance, it is well-known that platelets and white blood cells marginate toward the vessel wall, a process that is of great physiological relevance [72, 73]. Moreover, as blood vessels in the human body are multiply branched [74] and strongly differ in size [75], flow conditions show significant variations between different parts of the vasculature [76]. Also, flow conditions vary continuously with time, as blood flow has a pulsatile nature [77]. A quantitative consideration of these effects is, however, beyond the scope of this work.
Here, blood will be assumed to behave like a Newtonian fluid with laminar shear flow and a parabolic velocity profile (Fig. 2.5A), which is actually a good approximation for healthy arteries [76]. Fluid velocity is maximum in the center of the blood vessel and, under the assumption of no-slip boundary conditions, zero close to the vessel wall. The shear rate $\dot{\gamma}$ is defined as the gradient of the velocity $v(r)$ perpendicular to the direction of flow, i.e., in direction of $r$:

$$\dot{\gamma} = \frac{\partial v(r)}{\partial r}\,. \tag{2.7}$$

In contrast to the fluid velocity, the shear rate is maximum at the vessel wall and zero in the center of the vessel. In fact, wall shear rates are commonly used when referring to shear rates in blood vessels [78]. Multiplying the shear rate by the dynamic viscosity $\eta$ of the fluid yields the shear stress $\tau$:

$$\tau = \eta \cdot \frac{\partial v(r)}{\partial r} = \eta \cdot \dot{\gamma}\,. \tag{2.8}$$

When a flexible polymer is subjected to stationary shear flow, it undergoes an end-over-end tumbling motion (Fig. 2.5C), resulting in aperiodic fluctuations of the polymer extension with time [11]. As observed experimentally, e.g., for $\lambda$- DNA [11], but also in simulations [33], the

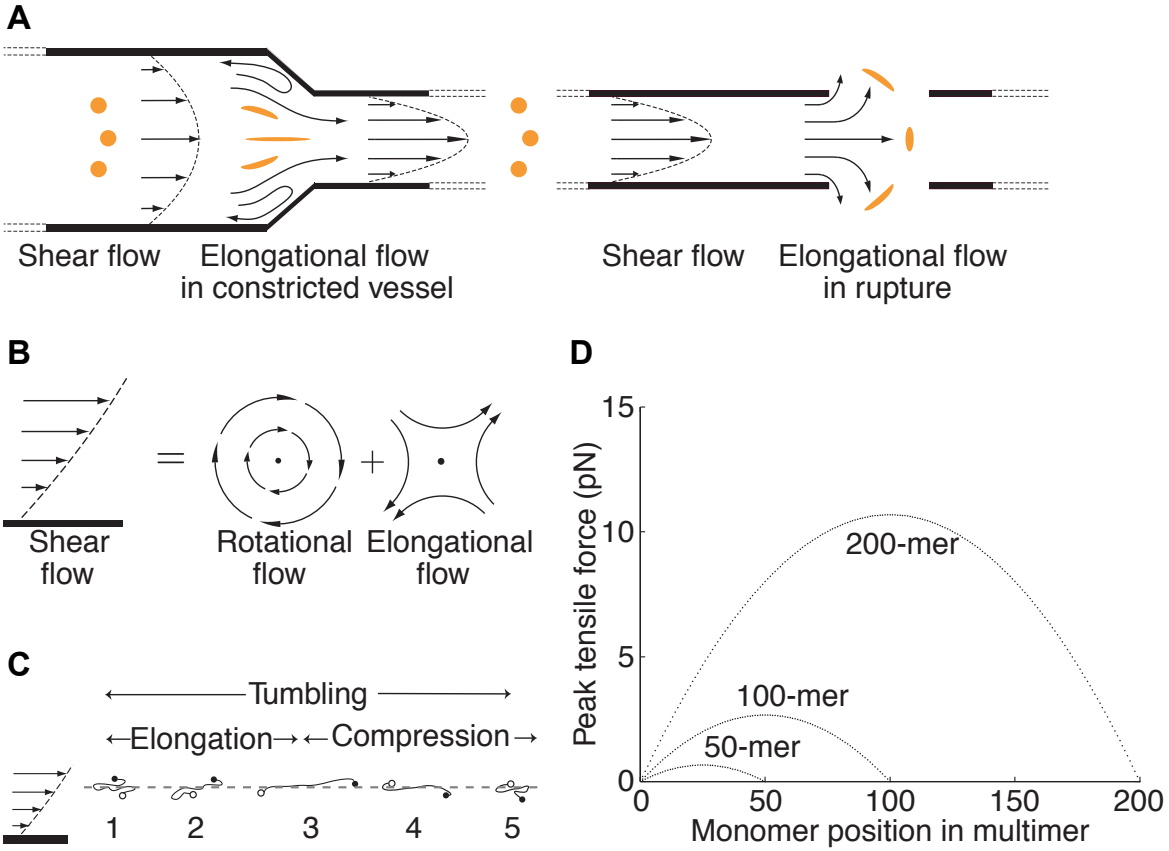


**Figure 2.5:** Behavior of a linear polymer in shear and elongational flow. (A) Schematic of hydrodynamic flow in a blood vessel, showing how shear flow transitions to elongational flow at a site of vasoconstriction or vascular injury. Round orange spheres are a schematic representation of yarn ball-like polymers that are stretched by increased forces. (B) Simple shear flow profile, which can be represented as a superimposition of an elongational and rotational flow component. (C) Schematic illustration of the behavior of a flexible polymer subjected to shear flow. Owing to the velocity gradient perpendicular to the direction of flow, the polymer is subjected to hydrodynamic drag forces. If these forces overcome the entropic forces that give rise to an irregularly coiled conformation, the polymer is stretched. In principle, as soon as the polymer becomes aligned to the direction of flow (dashed line), drag forces decrease and the polymer may relax. Due to Brownian motion, however, the polymer can be kicked out of its aligned state, whereupon it is either stretched again (if the perturbation was against the direction of rotation) or becomes unstable and starts to tumble (if the perturbation was along the direction of rotation). (D) Peak tensile force as a function of monomer position in a VWF concatemer consisting of 50, 100, and 200 monomers at a shear stress of $100\,\mathrm{dyn\,cm^{-2}}$. Forces are based on a simple model for a rigid maximally extended polymer, which remains completely extended during tumbling. In this model, the peak force acting on a monomer was calculated as the sum of the forces on all outer monomers for the situation in which the polymer is almost aligned to the direction of flow ($\theta = 3°$). The latter situation was considered, as simulations suggest that a flexible VWF polymer does not reach its full extension until it is about $\theta = 3°$ from the direction of flow [12]. Adapted with permission from reference [13]. Original version of subfigures B and C in reference [11].

extension fluctuations increase in amplitude and average frequency when increasing the shear rate within a certain regime. To comprehend the tumbling motion of a polymer in shear flow, the latter can be represented as a superimposition of an elongational and a rotational flow component (Fig. 2.5B) [11]. Owing to the rotational flow component, the polymer repeatedly aligns to directions of elongational flow, along which it elongates and contracts (Fig. 2.5C). While increased average frequencies of fluctuations in the polymer extension can be attributed to an increased rotational flow, increased amplitudes, i.e., increased maximum extensions, result from increased elongational flow. In general, Brownian motion leads to aperiodicity in this process. For instance, when the polymer aligns to the direction of flow, hydrodynamic forces decrease, and the polymer may relax. Due to Brownian motion, however, the polymer can be kicked out of its aligned state, thereby causing either further stretching and anew alignment to the flow axis, or instability and tumbling.

A more pronounced and more steady elongation of a linear polymer using hydrodynamic flow can be achieved by pure elongational flow, i.e., by a velocity gradient $\dot{\epsilon}$ along the direction $x$ of flow:

$$\dot{\epsilon} = \frac{\partial v(x)}{\partial x} \,. \tag{2.9}$$

Importantly, elongational flow can be also found in the circulation, for instance at sites of vascular injury, but also at sites of vasoconstriction or stenosis (Fig. 2.5A) [9, 10, 12–14]. At these sites, VWF is prone to becoming activated by force (see subsection 2.4.2), either to mediate hemostasis or, adversely, to provoke thrombosis [9, 10, 12–14].

Zhang *et al.* estimated maximum tensile forces on VWF concatemers in shear flow (Fig. 2.5D). To this end, VWF concatemers were initially assumed to be rigid and fully extended. Forces within rigid VWF concatemers were calculated based on considerations by Shankaran *et al.*, who had modeled a VWF dimer as a dumbbell with two spheres of radius $a = 13\,\mathrm{nm}$ separated by a rigid tether of length $d = 94\,\mathrm{nm}$ [79]. These values were based on the appearance of VWF dimers in TEM images [20, 80], which had revealed massive A and D domains separated by a tether of C domains. To calculate forces, the spheres of the rigid chain were paired off from the ends of the chain, e.g., for a chain with 5 dimers: $5-4-3-2-1-1-2-3-4-5$. The tensile force $F(j)$ on a sphere pair $j$ in a chain with $N$ dimers, i.e., with $N$ pairs, was calculated as the sum of the forces on all the outer dimer pairs, yielding:

$$F(j) \approx \sum_{i=j}^{N} f(i \cdot (d + 2a)) \,, \tag{2.10}$$

where $f(x)$ is the force between two spheres that are a distance $x$ apart. This force is given in reference [79] as $F_\mathrm{n}$, and assumes a maximum value of $\alpha_\mathrm{n}\eta\dot{\gamma}a^2$ when the rigid VWF concatemer forms an angle of $\theta = 45°$ with respect to the direction of flow. Here, $\alpha_\mathrm{n}$ is a dimensionless proportionality factor that depends on the dimensionless separation $\delta = d/a$, as depicted in

Fig. 3A of reference [79]. Considering that $\alpha_n$ is proportional to $\delta$ for the relevant range of $\delta \gg 1$, and given that $\delta$ is proportional to the parameter $i$, the equation for the tensile force can be simplified to:

$$F(j) \approx \frac{(N+j)(N+1-j)}{2} f(d+2a)\,. \tag{2.11}$$

Evidently, the force on a monomer in the center ($j = 1$) of the rigid concatemer scales with $N^2$, whereas the force on a monomer at the end ($j = N$) of the concatemer scales with $N$. For a rigid, extended 200-mer subjected to a high shear stress of $100\,\mathrm{dyn\,cm^{-2}}$, at 45° with respect to the flow direction, Zhang *et al.* reported a maximum value of 100 pN. This value was, however, calculated based on different, and possibly more accurate, values for $a$ (5 nm) and $d$ (110 nm) compared to the ones assumed by Shankaran *et al.* (see above).

An alternative estimation of the tension in a rigid VWF concatemer, yielding however similar results, can be found in the Supporting Material of reference [12]. The latter also includes estimations of tumbling time scales, which are – based on the assumption that the average time period scales with the number of monomers [12]– extrapolated values of the ones reported in references [33, 79]. For instance, for a 200-mer subjected to $100\,\mathrm{dyn\,cm^{-2}}$ [7], a time period of 2 s was found. Furthermore, under the assumption that the force loading time is roughly 20% of the total tumbling time [33, 79], an estimate for the corresponding force loading rate ($25\,\mathrm{pN\,s^{-1}}$) was reported.

The abovementioned force calculations assume a rigid and fully extended VWF concatemer, as in the model by Shankaran *et al.*, which approximates a VWF dimer as a rigid dumbbell. For a rigid concatemer, the maximum forces that are reached in shear flow correspond to the point in tumbling at which the rigid concatemer forms an angle of 45° with respect to the flow direction. However, as strongly suggested by observations from flow experiments and simulations [6, 33], flexible VWF concatemers extend and relax while tumbling in shear flow. In other words, depending on VWF's length and the shear rate, which both determine the tumbling time scale, VWF may not reach its full extension during much of the elongation period. It is therefore difficult to predict at which point in tumbling VWF is subjected to the highest force, which depends on VWF's extension. To obtain an estimate of the maximum forces that act on (flexible) VWF when subjected to $100\,\mathrm{dyn\,cm^{-2}}$, Zhang *et al.* considered the point in tumbling of maximum extension, which they assumed – based on results of simulations [33] – to occur at an angle of $\theta = 3°$ from the direction of flow. For different concatemer lengths, forces at this angle were calculated. To this end, the maximum forces at 45° (100 pN for a 200-mer, see above) were multiplied by $\sin(2\theta)$, yielding for example a peak force at the middle of a flexible 200-mer of slightly above 10 pN, at a shear stress of $100\,\mathrm{dyn\,cm^{-2}}$ (Fig. 2.5D). Overall, the calculated forces by Zhang *et al.* are in agreement with the ones observed in a computational study [9].

### 2.4.2 Activation of VWF for hemostasis and globule–stretch transition

As discussed above, force-induced elongation of VWF can be expected to occur especially at sites where elongational flow components are increased, e.g., at sites of vascular injury or in stenosed vessels [10, 14]. Interestingly, these sites are the ones at which blood clotting and thrombosis are likely to occur. Indeed, Schneider *et al.* showed that binding of VWF to collagen correlates with VWF's elongation (Fig. 2.6) [6]. More precisely, in flow experiments, fluorescently labeled VWF was observed in a collapsed conformation below a critical shear rate $\dot{\gamma}_c$, and in a stretched conformation above that shear rate (Fig. 2.6A). The transition from a collapsed to a stretched conformation was called globule–stretch transition.

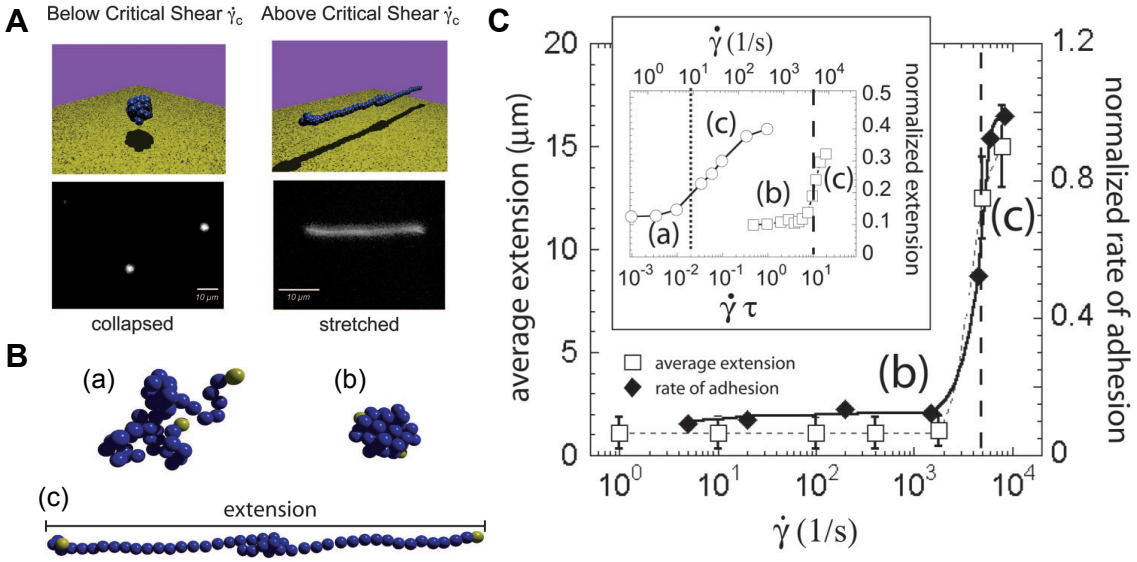


**Figure 2.6:** Globule–stretch transition of VWF. (A) Cartoon and fluorescence images of VWF below and above the critical shear rate $\dot{\gamma}_c$ that is indicated as dashed line in (C). Scale bar is 10 µm. (B) Typical polymer configurations [coiled (a), collapsed (b), and stretched (c)] based on a simple bead model. The coiled and the collapsed polymer were modeled with an attractive contact potential depth of 0.416 and 2.08 $k_BT$. (C) Experimental data showing the average extension (open squares) and the rate of adhesion to collagen (filled diamonds) of VWF concatemers as a function of the shear rate $\dot{\gamma}$. Data was obtained from flow experiments performed with a microfluidic device, whose functionality was achieved by electrically excited surface acoustic waves acting as a localized pump. The inset shows simulated data obtained from stretching the polymers depicted in (B). Subfigures adapted with permission from reference [6] (Copyright (2007) National Academy of Sciences, U.S.A.).

Strikingly, the critical shear rate ($\dot{\gamma}_c = 5000\,s^{-1}$, Fig. 2.6C) found by Schneider *et al.* was two orders of magnitude above the one of purely entropically collapsed DNA molecules ($30\,s^{-1}$) possessing a similar length when stretched [6, 11]. It was hypothesized that this discrepancy in shear rates could be attributed to significant conformational changes that VWF undergoes when stretched [6]. To account for such conformational changes in a simple model, the behavior of VWF in shear flow was simulated based on a polymer bead model in which all repeating subunits are attracted to each other by a Lennard–Jones potential (Fig. 2.6B) [33].

A potential depth of $2.08\,k_{\mathrm{B}}T$ was found to successfully reproduce the critical shear rate observed in the experiments, implying a fully collapsed initial conformation of the modeled bead-polymer. In fact, this simple model did not only match the experimentally observed shear rates, to which the model had actually been adjusted, but, importantly, could also account for the reported reversibility of VWF's elongation [6].

Besides binding of VWF to collagen, shear flow also promotes platelet aggregation in presence of VWF [5]. Activation-independent platelet aggregation, mediated by binding of VWF's A1 domain to the platelet receptor GPIb$\alpha$, was initially observed by Ruggeri *et al.* [8]. A few years later, Chen *et al.* showed, both for platelets and coated glass spheres, that aggregates are highly reversible and controllable, depending mostly on the shear rate and the interaction between the polymer-colloid binding [81]. At a single-domain level, however, the mechansims that activate VWF to bind the platelet receptor GPIb$\alpha$ have remained poorly understood.

One could tentatively assume that the GPIb$\alpha$-binding sites of the A1 domains in a VWF concatemer are preferentially exposed when VWF is subjected to sufficiently high forces. In fact, such a picture is compatible with the observation that both the D'D3 domain and the peptide N-terminal of A1 can shield the recognition of GPIb$\alpha$ by A1 [82, 83]. Similarly, it was reported that upon deletion of the A2 domain – the C-terminal neighboring domain of A1 – critical shear rates for platelet aggregation were lower ($2500\,\mathrm{s}^{-1}$) than in the case of wildtype VWF ($4000\,\mathrm{s}^{-1}$) [84]. Although the observed difference in shear rates is not extreme, this result is of interest, and the difference with respect to forces might be more pronounced than with respect to shear rates. This speculation is based on simple considerations that suggest peak tensile forces, acting on a flexible polymer subjected to shear flow, to scale with the square of polymer length (see subsection 2.4.1) [12]. As the length of soluble VWF in shear flow should be by trend larger in the case of wildtype VWF – in which A2 domains can in principle unfold and significantly increase VWF's length – than in the case of VWF with a deletion of A2, forces at constant shear rate should exhibit similar trends.

The simple picture in which the A1 domains are shielded by adjacent domains is compatible with the observation that, when mediated by isolated dimers of A1 domains (A1 dimers), platelet aggregation did not exhibit a characteristic shear threshold [8]. From another point of view, platelet aggregation mediated by A1 dimers at minute shear rates suggests that isolated A1 domains do not necessarily have to become activated by force, at least not by forces in the pN-regime. Interestingly, however, an elegant single-molecule study could show that binding and unbinding of A1 to GPIb$\alpha$ is altered when forces above $\sim 10\,\mathrm{pN}$ act on both domains [31]. More precisely, above $\sim 10\,\mathrm{pN}$, increased on-rates and decreased off-rates were observed. These findings suggest A1 and/or GPIb$\alpha$ to switch to a second state above $\sim 10\,\mathrm{pN}$. Moreover, force-dependent on- and off-rates were increased and decreased, respectively, by the mutation R1306Q, found in patients with the gain-of-function von Willebrand disease

type 2B. This observation suggests indeed a slight force-induced conformational change in A1 that allows for enhanced platelet binding.
Taken together, it remains unclear if VWF's force activation can at all be tracked back to a single mechanism. In any case, results of aggregation experiments in shear flow are, due to the complex tumbling motion of VWF and the contribution of VWF-bound colloids and aggregates, difficult to break down to an interpretation at a single-domain level. A possible approach to further elucidate the activation of VWF at a single-domain level could be single-molecule flow experiments. For instance, fluorescently labeled VWF could be stretched by an elongational flow – or by shear flow while bound to a surface – and force-induced binding of VWF to soluble GPIb$\alpha$ – which should be certainly labeled with another fluorophore than VWF – could be monitored.

### 2.4.3 Down-regulation of VWF's thrombotic activity

In addition to the activation of VWF for hemostasis, the down-regulation of VWF's thrombotic activity is likewise induced by force. The underlying processes are comparably well understood at the single-molecule level. Cleavage of large, hemostatically active VWF concatemers into shorter ones, which are hemostatically less active, is catalyzed by the enzyme ADAMTS13 [85, 86], which is primarily synthesized in the liver and permanently active in the plasma [87].
Remarkably, the specific cleavage site for ADAMTS13 is buried in the A2 domain and exposed by A2 unfolding (Fig. 2.1) [32, 53]. Zhang *et al.* studied the interplay of force-induced A2 unfolding and enzymatic cleavage by ADAMTS13 in detail at a single-molecule level using optical tweezers (Fig. 2.7A) [12]. In this study, unfolding of an isolated A2 domain was observed at forces of $7 - 14\,\mathrm{pN}$ at loading rates of $0.35 - 350\,\mathrm{pN\,s^{-1}}$ (Fig. 2.7B and D). The force-dependent length increments induced by A2 unfolding were shown to increase from $\sim 38\,\mathrm{nm}$ at $10\,\mathrm{pN}$ to $\sim 45\,\mathrm{nm}$ at $20\,\mathrm{pN}$ (Fig. 2.7C), and were well described by the fit of a Worm-like-chain (WLC) model (for WLC model, see subsection 3.3.1), which yielded a contour length of $57 \pm 5\,\mathrm{nm}$ and a persistence length of $1.1 \pm 0.4\,\mathrm{nm}$. Similar results were obtained in a study by Ying *et al.* [88], in which A2 unfolding was observed in the presence of neighboring A1 and A3 domains. The fact that, in the latter study, A2 unfolding was observed at slightly higher forces of $\sim 20\,\mathrm{pN}$ (at comparable loading rates) might indicate stabilization of A2 through its neighboring domains, but may also be simply attributed to different experimental setups and conditions.
Zhang *et al.* also studied refolding kinetics and found a time scale of $2\,\mathrm{s}$ for an unfolded A2 domain to refold in the absence of force. Furthermore, based on the measured cleavage kinetics of A2, Zhang *et al.* predicted a characteristic time scale of $\sim 200\,\mathrm{s}$ for the cleavage of an unfolded A2 domain at a physiological ADAMTS13 concentration of $6\,\mathrm{nM}$. Therefore,

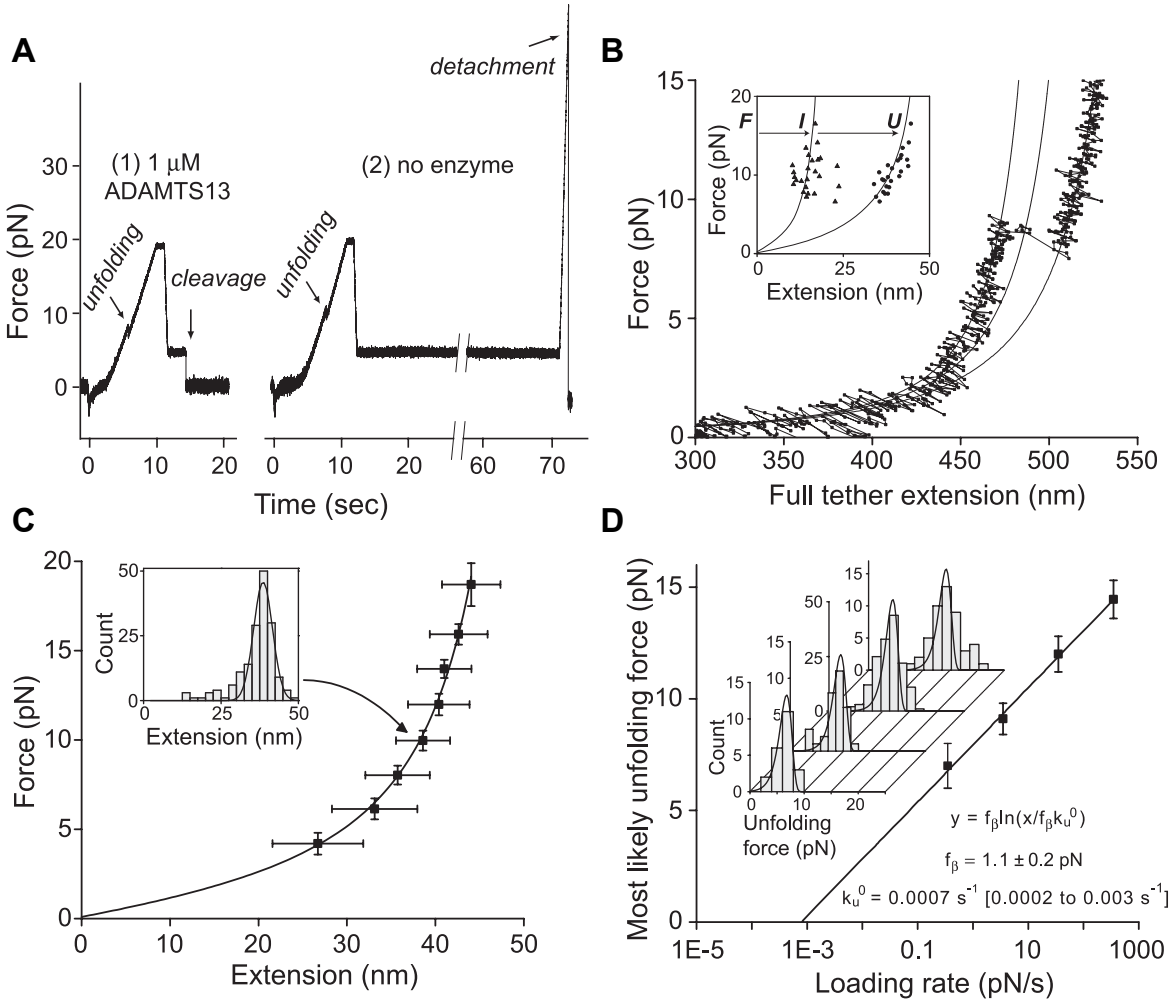


**Figure 2.7:** Unfolding of VWF's A2 domain and cleavage by ADAMTS13 as observed in optical tweezer measurements [12]. (A) Mechanoenzymatic cleavage of the A2 domain by ADAMTS13. Force–time traces showing cleavage of unfolded A2 in the presence of ADAMTS13 and no cleavage in the absence of ADAMTS13. (B) Force–extension trace showing A2 unfolding via a characteristic intermediate state and corresponding WLC curves (for WLC model, see subsection 3.3.1). The high extension values arise from DNA handles that were used to couple A2 domains to beads. (C) Force–extension data of the A2 domain. Mean extension values and errors were obtained by sorting unfolding forces into 2-pN bins and fitting a Gaussian to the extensions for each bin (inset). Force–extension data was fitted with a WLC model yielding a contour length of $57 \pm 5$ nm and a persistence length of $1.1 \pm 0.4$ nm. (D) Force–loading-rate dependence of A2 unfolding and fit of a Bell-Evans model (for Bell-Evans model, see subsection 3.3.1). The inset shows the force distributions for the investigated loading-rates. Subfigures taken with permission from reference [12].

combining refolding kinetics and enzymatic cleavage strongly suggests that for plasma VWF, which continously stretches and relaxes in shear flow, the rate of VWF's cleavage is limited by the physiological concentration of ADAMTS13. In other words, when VWF is subjected to shear flow, the A2 domains are likely to refold before they are cleaved. In fact, later studies could identify calcium to play a crucial role for the quick refolding of A2 [58, 59, 89]. For instance, Xu *et al.* observed refolding kinetics to be enhanced fivefold in the presence of calcium compared to the kinetics of A2 when treated with EDTA. These findings are completely in line with structural considerations that revealed a calcium-binding site in A2 (Fig. 2.1) [57]. Importantly, VWF can be expected to also experience high forces on longer time scales without necessarily relaxing, e.g., when mediating platelet aggregation, or when released as ultralarge VWF (ULVWF) – with lengths of several millimeters [90] – from endothelial cells. In this context, the mechanoenzymatic cleavage of VWF by ADAMTS13 can be assumed to regulate the formation and growing of platelet plugs, which otherwise could lead to thrombotic occlusions [8, 91]. Moreover, force-induced cleavage was shown to down-regulate the thrombotic activity of initially hyperactive ULVWF. Dong *et al.* showed that, in presence of physiological concentrations of ADAMTS13, surface bound ULVWF with attached platelets was cleaved at time scales of seconds to several minutes [90], in agreement with the time scale of 200 s reported by Zhang *et al.* for the cleavage of a permanently unfolded A2 domain.
For plasma VWF, the mechanoenzymatic cleavage of VWF guarantees that larger concatemers, which experience by trend higher forces than shorter ones, are cleaved more readily, thereby ensuring an adequate size distribution of VWF in the blood. Deviations from a healthy size distribution, which can be caused for instance by mutations in VWF's A2 domain or by absence or dysfunction of ADAMTS13, can lead to the bleeding disorder von Willebrand disease type 2A or the life-threatening trombotic thrombocytopenic purpura (TTP) [87, 89].

## 2.5 Interim conclusion and motivation

To motivate the research that was performed within the framework of this thesis, this section will sum up the most important insights of the studies that were mentioned above and discuss limitations of these insights.

Both the activation of VWF for hemostasis and the down-regulation of VWF's thrombotic activity can be induced by force. While the mechanoenzymatic cleavage of VWF's A2 domain has been characterized at the single-molecule level, the molecular mechanisms underlying VWF's force-induced binding to collagen and platelets remain rather unclear. On the one hand, this limited knowledge can be attributed to the fact that the force-induced conformational changes of VWF's A1 domain, together with flanking neighboring linkers and domains D'D3 and A2, are not entirely understood [31, 82, 84]. On the other hand, very little is known

about how force results from the interplay between hydrodynamic flow and VWF's structure, i.e., very little is known about force sensing by VWF. While VWF's structure was shown in a recent TEM study to be strongly pH-dependent, measurements at the physiological pH of 7.4 neglected the critical role of divalent ions [55, 80]. Furthermore, while force-induced unfolding of the A2 domain has been studied in detail, the overall force response of VWF remains unknown. Therefore, even for the simple case of a VWF concatemer subjected to elongational flow, the understanding of VWF's elongation is limited. However, a comprehensive picture of VWF's elongation in elongational flow would be – due to the positive feedback between force and length – of outstanding relevance to estimate forces on VWF and its constituent domains. As described above, the latter may react individually with more or less large conformational changes. For example, unfolding of the A2 domain can be expected to contribute significantly to the elongation of VWF, as the induced length increment of roughly 45 nm (at 20 pN) is almost as large as the end-to-end length of a static monomer [12, 55, 58, 59, 88]. All other domains in VWF were predicted to be stabilized through disulfide bonds [61], but such stabilization lacks experimental evidence. Besides domain unfolding, separation of potential intra- and intermonomer interactions may play a critical role for VWF's elongation. For instance, VWF's force-sensing ability was shown to be tunable by interactions between monomers in various computational studies [6, 33, 92]. Experimentally, self-association of VWF molecules was reported, but could not be attributed to individual domains [93, 94]. One objective of this thesis was to gain a quantitative understanding of how force on VWF results from VWF's interplay with hydrodynamic flow, in particular with elongational flow components, which are believed to be essential for VWF's force activation [9, 10, 12].

While VWF's activation for platelet and collagen binding is believed to be primarily a matter of sufficiently high elongational flow rates at sites of vascular injury [10], a recent review on the physiological and pathophysiological functions of VWF proposed that pH variations may also play a role by affecting critical rates of elongational flow [95]. Certainly, the pH in healthy blood vessels is precisely buffered to maintain a pH of 7.4, and small deviations of 0.1 already represent pathophysiological conditions. However, as suggested by several studies [96–100], the pH may locally vary at sites of injury and inflammation. Indeed, VWF's structure was already shown in abovementioned TEM study to be affected by the pH, as the latter regulates the formation of dimeric bouquets [55]. It has, however, not been clarified to what extent the pH influences VWF's mechanics. Importantly, even in the case that local pH alterations may not occur on timescales that are relevant for primary hemostasis, a comprehensive investigation of the role of the pH is an indispensable step towards a full understanding of the nature of the molecular mechanisms that underlie VWF's force activation. Therefore, another objective of this thesis was to gain a quantitative understanding of how VWF's structure and mechanics are affected by the pH.

As force sensing by VWF critically depends on its multimer size [10, 12], the size distribution of recombinant VWF was also addressed in the framework of this thesis. Particular motivation came from studies by Dr. Svenja Lippok, Prof. Dr. Joachim Rädler, and coworkers, who had found an exponentially decaying size distribution of recombinant VWF in quantitative gel analysis and fluorescence correlation spectroscopy (FCS). In this context, the hypothesis of an exponential size distribution was initially tested, in a joint collaboration with Prof. Dr. Joachim Rädler, by using the method of TIRF microscopy photobleaching (see Appendix A.2) [101]. Imaging experiments employing AFM, as were performed afterwards, revealed diverse advantages, but also limitations compared to high-throughput techniques.

# 3 Materials and methods

In order to gain a quantitative understanding of VWF's force-sensing ability, two complementary approaches were pursued. While AFM-based single-molecule force measurements on VWF dimers were performed to characterize VWF's force-induced conformational changes, AFM imaging on VWF was carried out to shed light on VWF's conformation. Here, I would like to gratefully acknowledge the work of three students that I supervised in their master's studies; while Salomé Mielke performed a variety of control force experiments on VWF constructs [102], Achim Löf and Christof Beer focused on imaging experiments [103, 104].
After listing the employed recombinant VWF constructs and specifying buffer solutions, this chapter will introduce the basic principles of AFM-based single-molecule force measurements and AFM imaging, as well as describe experimental procedures. Special emphasis will be placed on the analysis of force–extension traces of biomolecules and read-out of their information. In this context, a brief introduction into polymer elasticity models will be given, followed by a short description of the physics regarding mechanical stability of specific biomolecular interactions. Finally, this chapter will present basic principles and procedures of TIRF microscopy experiments, which I performed in the beginning of my PhD to estimate the size distribution of recombinant VWF [101].

## 3.1 Recombinant VWF constructs

In the framework of this thesis, a variety of different VWF constructs, involving multimers, dimers, and monomers, were investigated (Table 3.1). These constructs were provided by the group of Prof. Dr. Reinhard Schneppenheim at the University Medical Center of Hamburg-Eppendorf (Department of Pediatric Hematology and Oncology). Engineering of recombinant VWF constructs, involving plasmid construction, transfection of HEK-293 cells [105], and protein expression, was carried out by Tobias Obser and is described in detail in reference [56].
For engineering of dimers and monomers, VWF's multimerization was obstructed by one of two methods: either by deleting the pro-peptide amino acid sequence (aa 26-763) or by deleting VWF's D'D3 domain. While VWF's pro-peptide is responsible for tubule formation, a prerequisite for orderly multimerization, VWF's D'D3 domain contains the cystein residues that are critical for multimerization [10, 19, 54]. To produce monomers, dimerization via

| Notation | Description | Figure(s) |
|---|---|---|
| VWF | wildtype (wt) | 4.13, 4.16, 4.24, and 4.26 |
| delPro-VWF | dimer without tags | 4.11A |
| TwinStrep-delPro-VWF-His + ybbR-delPro-VWF-His | heterodimer composed of two monomers with N-terminal Twin-Strep-tag and ybbR-tag, respectively | 3.5C, 3.5E, 4.1, 4.5, 4.6, 4.7, 4.12A, 4.14, 4.15, and 4.23B |
| Strep-delPro-VWF-His + ybbR-delPro-VWF-His | heterodimer with N-terminal Strep-tag and ybbR-tag | 3.5F and 4.23 |
| Strep-delPro-VWF-His | dimer with N-terminal Strep-tag | 3.5D |
| TwinStrep-delPro-VWF-N1493C/C1670S-His + ybbR-delPro-VWF-N1493C/C1670S-His | heterodimer with disulfide bridged A2 domains and N-terminal Twin-Strep-tag and ybbR-tag | 4.3 |
| TwinStrep-delPro-delA3-VWF-His + ybbR-delPro-delA3-VWF-His | heterodimer lacking the A3 domain (aa 1672–1874), equipped with N-terminal Twin-Strep-tag and ybbR-tag | 4.10A–C |
| TwinStrep-delPro-delD4-VWF-His + ybbR-delPro-delD4-VWF-His | heterodimer lacking the D4 domain (aa 1873–2255), equipped with N-terminal Twin-Strep-tag and ybbR-tag | 4.10D–G, 4.11B, and 4.12B |
| TwinStrep-delD'D3-VWF-His + ybbR-delD'D3-VWF-His | A1-CK heterodimer with N-terminal Twin-Strep-tag and ybbR-tag | 4.7B, 4.7D 4.8A, 4.17, 4.18, 4.19, 4.21, and 4.22 |
| TwinStrep-delD'D3–A1-VWF-His + ybbR-delD'D3–A1-VWF-His | A2-CK heterodimer with N-terminal Twin-Strep-tag and ybbR-tag | 4.2A–C and 4.8B |
| TwinStrep-delD'D3–A2-VWF-His + ybbR-delD'D3–A2-VWF-His | A3-CK heterodimer with N-terminal Twin-Strep-tag and ybbR-tag | 4.2D–F |
| ybbR-delPro-VWF-C2771R-TwinStrep-His | monomer with N-terminal ybbR-tag and C-terminal Twin-Strep-tag | 4.4 and 4.20 |
| Strep-delPro-VWF-C2771R-His | monomer with N-terminal Strep-tag | 4.9 |
| VWF F2561Y | wt with mutation F2561Y | 4.29 |
| TwinStrep-delPro-VWF-F2561Y-His + ybbR-delPro-VWF-His | heterodimer with mutation F2561Y in Twin-Strep-tagged monomer | 4.14 |
| VWF-eGFP | wt with C-terminal eGFP | 4.29 |
| delPro-VWF-eGFP | dimer with C-terminal eGFP | 4.28 and 4.29 |

**Table 3.1:** Recombinant VWF constructs used for the experiments presented in this thesis. The right column specifies the figures in which experimental data of the constructs are shown.

the CK domains was abolished by a single mutation in VWF's CK domain (C2771R), which prevents the formation of C-terminal disulfide bonds [21, 37, 64].
Of outstanding importance for single-molecule force measurements was the construction of VWF heterodimers, composed of two monomers equipped with an N-terminal ybbR-tag as well as either an N-terminal Twin-Strep-tag or a single Strep-tag. Heterodimers were obtained by co-transfection of cells with two plasmids, which also naturally resulted in homodimers, equipped with either two ybbR-tags or two Twin-Strep-tags / single Strep-tags. Besides the importance of tags for force measurements, the Twin-Strep-tag / Strep-tag was also beneficial for protein purification (see subsection 3.3.2), a prerequisite for imaging experiments. Additionally, most of the constructs carried a C-terminal His-tag (6x His), although this tag was actually not used, either in force measurements or in purification procedures for imaging experiments.
To locate the domains that crucially influence both VWF's conformation and its mechanics, several mutated constructs were investigated. Among these constructs were the abovementioned monomers in addition to dimeric constructs with a deletion of distinct domains, as well as full-length dimers with A2 domains protected against unfolding by disulfide bonds, achieved by mutations N1493C and C1670S [53]. Furthermore, heterozygous dimers with a mutation in VWF's C4 domain (F2561Y) were investigated. This polymorphism was of particular interest, as it appears to increase the risk of myocardial infarction and coronary heart disease, especially in young women (personal communication Prof. Dr. Reinhard Schneppenheim, [106]). However, force measurements on these constructs yielded very similar results as measurements on wildtype dimers, i.e., force–extension traces of type I and II that could be tuned by addition of EDTA (Fig. 4.14). It appears plausible that the increased thrombotic activity of this polymorphism is not primarily caused by an overall altered force response of VWF, but rather by a varied – possibly force-dependent – interaction of VWF's C4 domain with the platelet integrin $\alpha_{\mathrm{IIb}}\beta_3$. However, it should be noted that VWF's C4 domain also possesses a static affinity to $\alpha_{\mathrm{IIb}}\beta_3$, as shown in an elegant TEM study [55].
For photobleaching experiments, VWF was genetically engineered with a C-terminal eGFP fluorophore [101, 107], both in multimeric and dimeric form.

## 3.2 Buffers

For AFM single-molecule force measurements and AFM imaging experiments, buffer solutions containing 150 mM NaCl and 20 mM of the following chemicals were used: Na-acetate (pH 5.4), BisTris (pH 6.2, 6.6, and 6.8), Hepes (pH 7.1 and 7.4), or Tris (pH 8.0 and 8.6). The respective pH was adjusted with HCl and NaOH. For measurements in the presence of divalent ions, buffers additionally contained 1 mM $CaCl_2$ and 1 mM $MgCl_2$. Force measurements in the absence of divalent ions were performed after initially incubating surface immobilzed

proteins for at least 8 h with 10 mM EDTA. After this incubation period, measurements were performed either in buffer solution containing solely NaCl and buffering agent, or additionally 10 mM EDTA. As long as samples were initially treated with EDTA as described above, the presence of EDTA in the measurement buffer did not affect the measured force–extension traces. For imaging experiments in the absence of divalent ions, protein samples were incubated with 10 mM EDTA for at least 8 h and then buffer exchanged to the measurement buffer. Force measurements in the presence of free Imidazole were performed at pH 7.4 in the presence of NaCl, divalent ions and 200 mM free Imidazole (Imidazole buffer). Prior to measurements in the presence of Imidazole, surface immobilized proteins were initially incubated with Imidazole buffer for at least 8 h. Similarly, for imaging experiments, protein samples were buffer exchanged to Imidazole buffer and incubated for at least 8 h prior to adsorption. TIRF measurements were conducted in the presence of 1 x phosphate buffered saline (PBS).

## 3.3 Atomic force microscopy (AFM)

Since its invention by Binnig, Quate, and Gerber in 1986 [25], the atomic force microscope has evolved into an instrument of utmost importance for many nanoscientific disciplines. For instance, solid state physics and semiconductor science, as well as molecular and cell biology benefit from this versatile tool. In fact, the atomic force microscope is not only of great value for imaging non-conductive samples, but also beneficial for manipulation purposes, e.g., for nanoscale arrangement of biomolecules on a surface [108], or for direct force measurements, e.g., to estimate the stability of receptor-ligand systems and the strength of chemical bonds [109–111]. Moreover, the possibility to measure forces enables local quantification of the elastic and viscoelastic properties of microscopic samples by nanoindentation [112–115] and investigation of the influence of force on the conformation and function of individual biomolecules [27, 29, 116, 117].

The force sensor of an atomic force microscope is a small cantilever (Figs. 3.1A and 3.4), which for most applications bears a small tip at its end. Commonly, the distance between sample and surface can be varied by actuating a $z$ piezo. Forces acting on the cantilever, for instance when the cantilever tip indents a sample in an approach cycle or when tip-adhered molecules are stretched in a retract cycle, cause the cantilever to bend. Using the spring constant $k$ of the cantilever, which can be obtained by analyzing the thermal noise spectrum of the cantilever and applying the equipartition theorem [118], the force $F$ that acts on the cantilever can be calculated from the bending $\Delta d$ of the latter (Fig. 3.1B):

$$F = k \cdot \Delta d \,. \tag{3.1}$$

A means to assess the bending of the cantilever is to measure the deflection of a laser beam, which is reflected off the backside of the cantilever onto a segmented photodiode. The bending of the cantilever is then obtained by multiplying the change in the deflection signal $\Delta U_{\mathrm{D}}$ by the inverse optical laser intensity (InvOLS, Fig. 3.1B), which can be determined from a force trace on a hard substrate:

$$\Delta d = \Delta U_{\mathrm{D}} \cdot \mathrm{InvOLS}\,. \tag{3.2}$$

In general, the geometry and the size of both cantilever and cantilever tip vary and have to be chosen according to the application. While the cantilever is frequently of rectangular geometry with lengths ranging from tens to a few hundred micrometers, the tip often needs to be very sharp, e.g., to yield high lateral resolution in imaging applications or to favor single-molecule events in force measurements. A lot of cantilevers possess tips of roughly pyramidal geometry (half opening angles between approximately 10 and 40°) with curvature radii of the tip apex on the order of 10 nm.
Finally, many atomic force microscopes are equipped with an $x$–$y$ stage, which allows for scanning a sample line-by-line in imaging applications or for recording force traces at different sample spots in force measurements.

### 3.3.1 AFM-based single-molecule force measurements

Single-molecule force measurements represent a powerful means to investigate the force-dependent dynamics of individual biomolecules. Besides AFM, the most common single-molecule techniques are certainly optical tweezers and magnetic tweezers [30], although other techniques, such as single-molecule centrifugation [119], have also been introduced. From a conceptual point of view, AFM is often considered to be the simplest method [30]. Further advantages of AFM probably involve the potential to automate force measurements, the possibility to perform imaging in addition to force measurements, and a comparably small contact area. A key limitation of the atomic force microscope is certainly its restricted force resolution, which is – due to the identity $k \cdot \langle \Delta x^2 \rangle = k_{\mathrm{B}}T$ – fundamentally linked to the spring constant of the AFM cantilever:

$$\delta F = \sqrt{\langle \Delta F^2 \rangle} = \sqrt{k^2 \langle \Delta x^2 \rangle} = \sqrt{k \cdot k_{\mathrm{B}}T}\,. \tag{3.3}$$

For a relatively low spring constant of $20\,\mathrm{pN\,nm^{-1}}$, this limit implies a fundamental force resolution of approximately 9 pN, two orders of magnitude above the force resolution of optical tweezers (approximately 0.1 pN) [30], and at least three orders of magnitude above the force resolution of magnetic tweezers (below 0.01 pN) [30]. From a more technical point of view, it must be further considered that measurements are always taken within a certain bandwidth $B$, which improves the obtained force resolution. According to reference [120], the force resolution

within a limited bandwidth is approximately given by:

$$\delta F = \sqrt{4 k_\mathrm{B} T R B}\,, \tag{3.4}$$

where $R$ denotes the viscous drag on the cantilever. Therefore, to achieve a satisfying resolution of forces in AFM-based single-molecule force measurements, cantilevers should not only be soft, but also small to minimize the viscous drag.

### Principle of AFM-based single-molecule force measurements

A prerequisite for specifically stretching biomolecules in single-molecule force measurements are specific handles (tags) that need to be located at well-defined attachment points of the molecules of interest. These tags must be chosen such that on the one hand they allow proteins to be immobilized on a functionalized substrate and on the other hand to specifically adhere to a – preferentially differently – functionalized cantilever tip. In general, small tags are favorable, e.g., tags composed of only a few amino acids, as genetic engineering procedures are less elaborate and less time-consuming. Moreover, folding of protein constructs can be assumed to be generally less influenced in the case of small tags. However, a side project of this thesis demonstrated that in principle, both engineering and force measurements also work with larger tags. More precisely, those force measurements were performed on Cnidoin, an elastic protein recently found in *Hydra* nematocysts (see Appendix A.4) [121]. For specific pulling, Cnidoin constructs were equipped with a C-terminal type I Dockerin domain (64 residues), thereby allowing for pulling Cnidoin specifically via a type I Cohesin functionalized cantilever [122]. For the sake of completeness, it may be mentioned that attachment of Cnidoin to the surface was achieved by a small N-terminal ybbR-tag, which can bind covalently to Coenzyme A functionalized slides.
As the basic idea of single-molecule force measurements is to measure characteristic force–extension traces of the biomolecules of interest, the AFM cantilever tip must undergo repetetive approach and retract cycles, i.e., move repeatedly towards and away from the sample surface. In the case of the custom-built setups (Fig. 3.1A), which were used for the measurements in the framework of this thesis, the cantilever can be moved perpendicular to the sample via a $z$ piezo, which moves one of the supporting holders. How a voltage signal on the $z$ piezo translates into displacement of the cantilever base ($z$ sensor sensitivity, Fig. 3.1B) can be measured by simple laser interferometry, as described in reference [123]. To calculate the extension of the stretched biomolecule, the displacement $\Delta z$ of the cantilever base needs to be corrected for the bending of the cantilever (Fig. 3.1B):

$$x = \Delta z - \Delta d\,. \tag{3.5}$$

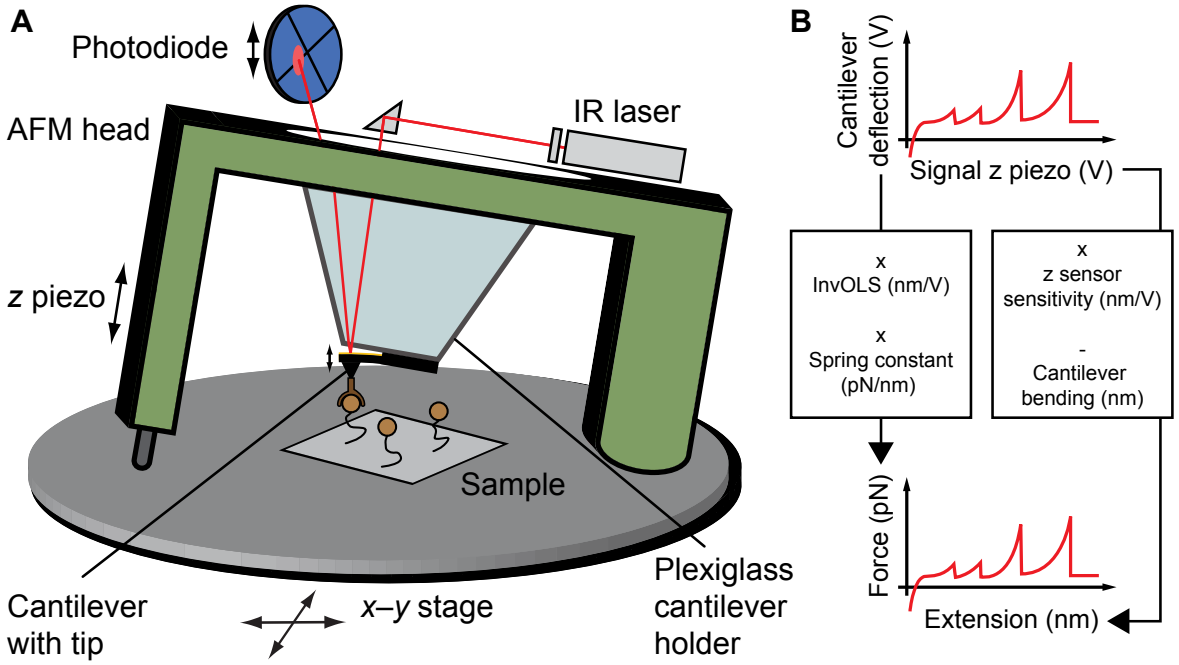


**Figure 3.1:** Basic principle of AFM-based single-molecule force measurements. (A) Schematic of experimental setup (not drawn to scale). The key element of an atomic force microscope is a cantilever with a sharp tip (tip radius of used cantilevers approximately 10 nm), which is positioned on a plexiglass cantilever holder in the case of the custom-built setups. A $z$ piezo allows for moving the cantilever perpendicular to the sample surface. For single-molecule force measurements, cantilevers can be functionalized with biochemical handles that, when approaching the cantilever tip to the surface, specifically bind to the biomolecules that are immobilized on the surface. If one or more biomolecules bind to the cantilever tip, the cantilever is bent upon retraction. The bending of the cantilever, which is proportional to the applied force, can be measured via the deflection of a reflected IR laser beam on a photodiode. An $x$–$y$ stage allows for moving the sample after each pulling cycle and to thereby probe different biomolecules. (B) Data processing. After offsetting traces by the mean value of the almost constant deflection value at the end of the trace (baseline), the deflection signal is multiplied by the inverse optical laser intensity (InvOLS), yielding the deflection (bending) of the cantilever. In order to obtain force values, the cantilever deflection is further multiplied by the spring constant of the cantilever. Multiplying the $z$ piezo signal by the $z$ sensor sensitivity yields values characterizing the distance that the cantilever base was moved into $z$ direction. To obtain values for the extension of the probed biomolecules, i.e., values of the distance between the cantilever tip and the sample surface, the cantilever bending needs to be subtracted from the abovementioned distance values (the ones of the cantilever base). The zero extension is typically defined as the extension value corresponding to the intersection of the cantilever deflection signal and a line fit with zero slope to the baseline. Depending on the questions that an experimenter wants to answer, only force–extension traces corresponding to pulling events of a single molecule may be relevant for further analysis. In this context, both the use of characteristic fingerprint domains, present in the biomolecules of interest, and an analysis of characteristic peak forces in traces – which in the simplest case are statistically hierarchical – are of great importance.

In this context, the zero extension is often defined as the intersection of the cantilever deflection signal and a line fit with zero slope to the baseline. The latter denotes the part of constant deflection at the end of a trace, corresponding to the situation in which the cantilever is no longer subjected to forces resulting from stretched biomolecules, e.g., after rupture of the molecules from the AFM tip.
In the case of the custom-built setups that were used (Fig. 3.1A), an $x$–$y$ stage allows for moving the sample after each pulling cycle and to thereby probe different biomolecules. It should, however, be emphasized that in force experiments, not all recorded traces correspond to specific pulling events of a single molecule. For instance, many traces may display no interaction at all with a molecule, or they correspond to pulling events of multiple molecules in parallel. Moreover, the use of specific tags and cantilever functionalization does not guarantee that all molecules are always stretched in the desired geometry, as unspecific binding of molecules to the tip may still occur. For many investigations, however, only force–extension traces corresponding to specific pulling events of a single molecule may be relevant for further analysis. Therefore, both the use of characteristic fingerprint domains, present in the biomolecules of interest, as well as an analysis of characteristic peak forces in traces – which in the simplest case are statistically hierarchical – are of utmost importance.

### Polymer elasticity

A prerequisite for a thorough interpretation of force–extension traces of single biomolecules is a basic knowledge of the entropic force response of a simple polymer, which relates nonlinearly to the extension of the polymer. As simple polymer models typically assume a polymer without any secondary structure, they appear at first glance to be especially well-suited to describe the entropic force response of overall rather unstructured molecules, such as single-stranded DNA or mostly unfolded proteins. A priori, it appears unclear to what extent purely entropic polymer models describe the force–extension behavior of large folded proteins. For instance, forces may give rise to small conformational changes in overall stable protein domains, without actually unfolding them. In other words, the overall force response of largely folded proteins may also include enthalpic contributions and, depending on the impact of these contributions, may no longer be sufficiently described by a simple entropic model.
A simple entropic model that was tested within this thesis (see subsection 4.1.1) regarding its applicability to the force response of VWF dimers – in a force range from 20 to 120 pN – is the Worm-like-chain (WLC) model [124, 125]. The WLC model assumes a continuously flexible isotropic rod that is subjected to thermal fluctuations. While the length of this rod is parameterized by the contour length $L_C$, its elasticity is quantified by the persistence length $P$. More precisely, the latter quantity measures the length along which tangent vectors

to the chain lose their correlation with respect to direction. An approximation for the force response of a WLC-like polymer is:

$$F = \frac{k_\mathrm{B}T}{P}\left[\frac{1}{4}\left(1-\frac{x}{L_\mathrm{C}}\right)^{-2} - \frac{1}{4} + \frac{x}{L_\mathrm{C}}\right], \tag{3.6}$$

where $F$ denotes the force and $x$ the extension (end-to-end distance) of the polymer. In fact, the WLC model can be extended to also account for enthalpic contributions. For instance, the extensible WLC model [126], which will also be used within subsection 4.1.1, contains an additional stretch modulus $S$. For high forces, e.g., above 20 pN, the extensible WLC model can be approximated as:

$$x = L_\mathrm{C}\left[1 - \frac{1}{2}\left(\frac{k_\mathrm{B}T}{FP}\right)^{1/2} + \frac{F}{S}\right]. \tag{3.7}$$

Further – purely entropic – polymer models that can be found in the literature are the freely-jointed chain model [127, 128] and the freely-rotating chain model [129].

In principle, fitting an entropic polymer model to a measured force–extension trace yields information about the entropic elasticity of the pulled biomolecule, e.g., quantification by the persistence length within the context of the WLC model. However, polymer models are often not used in practice to assess elasticity parameters, but rather because their application to force–extension traces provides a means to quantify discrete contour length values that a biomolecule of interest adopts during unfolding (Fig. 3.2). Distances between such contour lengths are of particular interest, as they represent a characteristic fingerprint of the pulled biomolecule. In fact, a known characteristic contour length pattern of distinct fingerprint domains is often used to identify specific single-molecule events in force–extension traces [27, 122, 130, 131]. Contour length values can be obtained by fitting Eq. 3.6, or by contour length transformation assuming a fixed value for the persistence length (Fig. 3.2) [132]. More precisely, contour length values are obtained by solving Eq. 3.6 for each data point $(x/F)$ of the force–extenion trace and inserting $P$. It should be mentioned that the method of contour length transformation is not restricted to the WLC model, as contour length values can in principle be also inferred in the context of other polymer models.

However, a limit of contour length transformation arises when transforming force–extension data at low forces, e.g., data below 20 pN. In this case, as a result of thermal noise, inferred contour length peaks are relatively broad and classification criteria based on contour length differences become virtually useless. In the framework of this thesis, low-force data of VWF constructs, i.e., unfolding peaks of VWF's A2 domains at approximately 20 pN, were analyzed to identify specific pulling events. A suitable approach was to directly analyze increments in extension space as a function of force and to compare these increments to the ones reported for A2 unfolding (Fig. 2A in reference [12]). Reproducibility of obtained force–extension traces could be confirmed by characteristic overlays. Naturally, for a well-chosen persistence length,

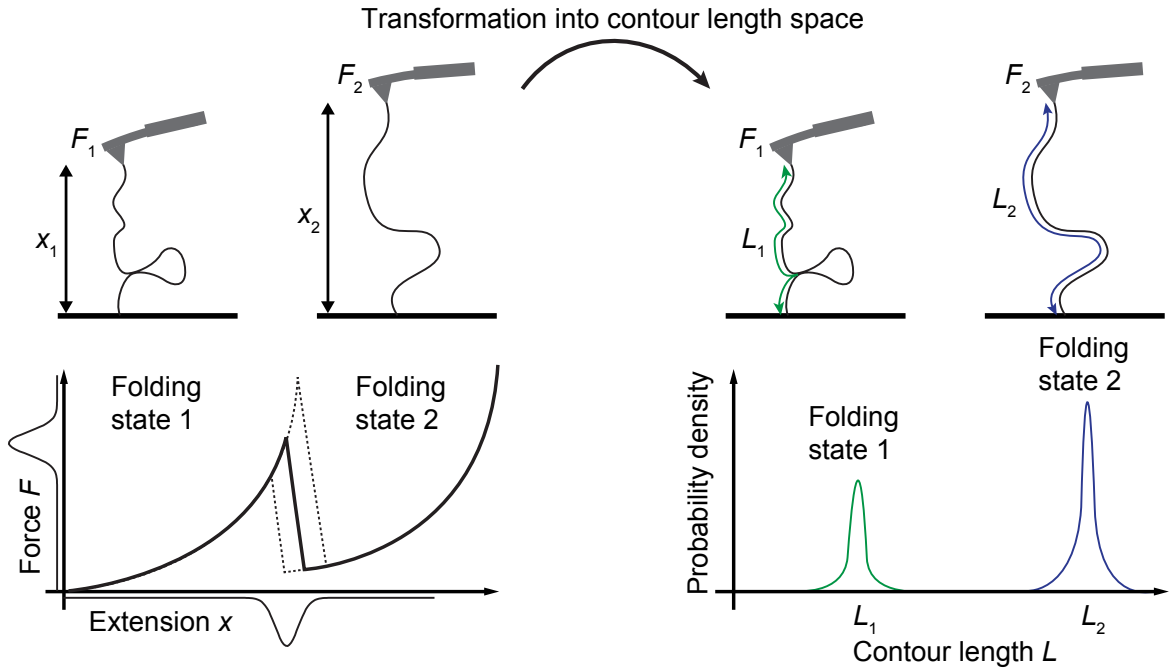


**Figure 3.2:** Transformation of force–extension data into contour length space [132]. Under the assumption of a certain polymer model, force–extension data (left) can be transformed into contour length space (right). For instance, assuming a WLC behavior and a value for the persistence length, for each data point of the force–extension trace a value of the contour length can be calculated. The contour length values obtained for all data points of the force–extension trace can be represented in the form of a histogram or a kernel density estimate [133]. Absolute values of unfolding positions and contour length values typically vary due to fluctuations in linker lengths and a slightly varied pulling geometry. However, distances between peaks in contour length space, which represent the folding states of the investigated biomolecule, are virtually unaffected. Graphical representation inspired by Fig. 1 of reference [132].

transforming such overlays into contour length space yields sharper peaks than transforming individual force–extension traces. However, in the case of the analyzed VWF constructs, the additional information that could be extracted from a contour length pattern inferred from an overlay was limited. Firstly, A2 unfolding peaks as such had already been identified for individual traces in the extension space, and secondly, the increments obtained from opening firmly closed dimers (Fig. 4.7) were only moderately described by a simple WLC fit.

### Mechanical stability of biomolecular interactions and protein domains

Single-molecule force spectroscopy is a powerful method to probe the kinetic and thermodynamic properties of single biomolecules. To outline how these properties are affected by force, a two-state model system (Fig. 3.3) will be considered in the following. Such a system may for instance describe binding and unbinding of a receptor-ligand pair or folding and unfolding of a protein domain. Naturally, the described concepts can be extended to more complex

scenarios, such as a three-state model system when describing the unfolding and refolding of a protein domain with an intermediate state [59, 89].

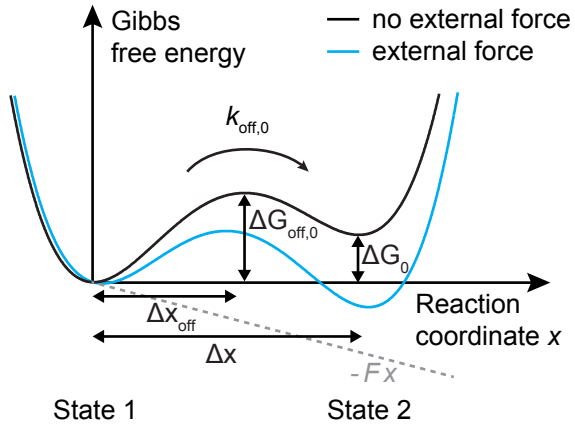


**Figure 3.3:** Influence of an external force on the free energy landscape of a two-state system. Depicted is the energy landscape of a two-state model system in the absence (black line) and presence of an external force (blue line). In the presence of an external force, the energy landscape is tilted due to an additional energy term $F \cdot x$. As a result, the thermodynamic equilibrium between the two states, initially described by the Gibbs free energy difference $\Delta G$, is shifted towards the second state. Moreover, an external force lowers the Gibbs free energy difference to the transition state $\Delta G_{\text{off}}$, thereby increasing the critical off-rate $k_{\text{off}}$.

In one dimension, a two-state model system is defined by a Gibbs free energy landscape that bears two local minima along a reaction coordinate $x$. In thermodynamic equilibrium and absence of an external force, these states are populated with a ratio of $\exp(\Delta G_0/k_{\text{B}}T)$, where $\Delta G_0$ denotes the energy difference of the two states – which is the energy difference of the two local minima. Of course, the state with the lower free energy will have a higher probability of occupation than the higher state. When applying an external force $F$ along the reaction coordinate, the energy landscape is tilted due to an additional energy term $F \cdot x$, thereby shifting the thermodynamic equilibrium between the two states. The influence of the external force depends on the distance $\Delta x$ between the two states. Assuming that this distance is not significantly altered by the external force, the probability of occupation of the two states is given by $\exp((\Delta G_0 - F \cdot \Delta x)/k_{\text{B}}T)$.

Besides altering the overall probability of occupation between two states, an external force also affects the dynamics of a system. To point out the basic ideas for the exemplary two-state system, a transition from state 1 to state 2 will be considered, and the underlying rate will be denoted as off-rate $k_{\text{off}}$. Fundamentally, in the absence of an external force, the lifetime of state 1 depends exponentially on the Gibbs free energy difference $\Delta G_{\text{off, 0}}$ between state 1 and the transition barrier, which corresponds to the local maximum of the energy landscape between the two local minima. In the presence of an external force, this energy difference is decreased. The extent of this decrease depends on the critical distance $\Delta x_{\text{off}}$ between state 1 and the transition state and is equal to $F \cdot \Delta x_{\text{off}}$, under the assumption of an unvaried $\Delta x_{\text{off}}$ value.

The above considerations are the essence of the Bell model [134]. In terms of force-dependent off-rates $k_{\text{off}}(F)$, which are the inverse lifetimes, the Bell model can be written as:

$$k_{\text{off}}(F) = \nu_0 \cdot e^{-\frac{\Delta G_{\text{off}}(F)}{k_{\text{B}}T}} = \nu_0 \cdot e^{-\frac{\Delta G_{\text{off},0} - F \cdot \Delta x_{\text{off}}}{k_{\text{B}}T}} = k_{\text{off},0} \cdot e^{\frac{F \cdot \Delta x_{\text{off}}}{k_{\text{B}}T}} . \tag{3.8}$$

Here, $\nu_0$ is an attempt frequency, which is on the order of the oscillation frequency of atoms in solids [134]. Importantly, the Bell model sets the theoretical basis to assess, by single-molecule force spectroscopy, the kinetic parameters $\Delta x_{\mathrm{off}}$ and $k_{\mathrm{off},0}$. For instance, in force-clamp applications, different constant forces are applied to the system of interest and critical off-rates $k_{\mathrm{off}}$ are determined. These off-rates are inverse to the force-dependent lifetimes $\tau(F)$, which can be inferred from considering the survival probability as a function of time. Fitting the Bell model to the measured off-rates as a function of force yields values for $k_{\mathrm{off}}$ and $\Delta x_{\mathrm{off}}$. In other applications, the applied force is not fixed, but rather increases with time, e.g., when a retracting AFM cantilever stretches tip-adhered molecules. In these cases, unbinding / unfolding forces can be analyzed by using for instance the Bell–Evans model [135–138]. This model, which assumes a constant force-loading rate $\dot{F} = dF/dt$ and the validity of Eq. 3.8 for infinitesimal periods of time, predicts the most probable unbinding / unfolding force as a function of the applied force-loading rate:

$$F^*(\dot{F}) = \frac{k_{\mathrm{B}}T}{\Delta x}\left[\ln\left(\frac{\Delta x \cdot \dot{F}}{k_{\mathrm{off},0} \cdot k_{\mathrm{B}}T}\right)\right] . \tag{3.9}$$

Based on the Bell–Evans model, the parameters $\Delta x$ and $k_{\mathrm{off},0}$ can be obtained by varying the applied force-loading rate – which in the case of AFM can be achieved by varying the retraction velocity of the cantilever – and representing the observed most probable unbinding / unfolding forces as a function of the applied loading-rates. In this context, it should be noted that, due to the typical force–extension profiles of biomolecules, the time dependence of the force is generally non-linear. Importantly, however, in proximity to the relevant unbinding / unfolding forces, the force–time dependence can be approximated by a line [122, 130].
Another approach to assess the parameters $\Delta x$ and $k_{\mathrm{off},0}$ is based on the Dudko–Hummer–Szabo equation [139], which allows inference of estimates for bond lifetimes at constant force from the distribution of unbinding / unfolding forces obtained for a given loading rate [59, 140].

### Experimental procedures of force measurements

VWF constructs, bearing a Twin-Strep-tag II (WSHPQFEKGGGSGGGSGGGSWSHPQFEK) / single Strep-tag II (WSHPQFEK) and a ybbR-tag (DSLEFIASKLA), were covalently attached to Coenzyme A functionalized glass slides. For functionalization, slides were silanized with (3-aminopropyl)-dimethyl-ethoxysilane (APDMES) [141], and then incubated with Na-Borate buffer (pH 8.5). Afterwards, slides were coated with 25 mM of a 5 kDa N-Hydroxy-Succinimide (NHS)-PEG-Maleimide linker in Na-Borate buffer, and finally treated with 25 mM CoA. Functionalized slides were incubated overnight and at 4 °C with 1 mg mL$^{-1}$ of VWF constructs in OPTIPRO-SFM medium (Life Technologies, Darmstadt, Germany) supplemented

with Sfp-transferase and $MgCl_2$ [142]. After incubation with proteins, slides were carefully rinsed with the measurement buffer (see section 3.2), ensuring removal of non-immobilized proteins. Prior to measurements with EDTA, immobilized proteins were incubated for 8 h with EDTA buffer (see section 3.2).
AFM cantilevers with a silicon tip (BL-AC40TS-C2, Olympus, Japan) were silanized with APDMES, then incubated with Na-Borate buffer, and afterwards coated with 25 mM of the 5 kDa NHS-PEG-Maleimide linker in Na-Borate buffer. Maleimide chemistry allowed for covalent attachment of a Strep-Tactin construct bearing a single Cysteine residue (Strep-Tactin-Cys).[1] To this end, Strep-Tactin-Cys stored in 1 x PBS was initially reduced in the presence of TCEP beads and then separated from TCEP beads by filtering. After incubation of cantilevers with the NHS-PEG-Maleimide linker, cantilevers were incubated with 10 µM of reduced Strep-Tactin-Cys. Finally, cantilevers were washed with the measurement buffer (see section 3.2).
Single-molecule force measurements were performed using custom-built instruments [143], each driven by an MFP-3D AFM controller (Asylum Research, Santa Barbara, CA). Spring constants of the cantilevers were determined individually using the thermal noise method [118]. Force–extension traces were recorded in closed-loop mode at 6 different pulling speeds ranging from 200 nm s$^{-1}$ to 6400 nm s$^{-1}$. In order to probe different VWF molecules, an $x$–$y$ stage was moved by 100 nm after each trace.

### Analysis of force–extension traces

For analysis, force–extension traces were subjected to total variation denoising (TVD) [144, 145]. In the case of dimeric VWF constructs, only traces with two A2 unfolding peaks were evaluated. To estimate the ratio of type I and type II traces for different pH values (see section 4.2), bimodal distributions of the position of the first A2 unfolding peak were fitted with a double Gaussian function. More precisely, five free parameters were fitted, involving peak amplitudes and positions for both peaks individually and a single value for the width of either peak, accounting for experimental uncertainties that were virtually the same for type I and type II traces. Overlays of force–extension traces were generated by offsetting undenoised characteristic traces in the direction of the extension axis. The offsets, which were chosen to align traces with respect to the stretch prior to the rupture peak, were within $\sim$20 nm. Heatmaps of overlays were generated based on a binsize of 2 pN x 2 nm.

[1] Strep-Tactin-Cys was kindly provided by Dr. Diana Pippig. Preparation of this construct is described in detail in the *SI Materials and Methods* section of [56].

### 3.3.2 AFM imaging

The atomic force microscope is a powerful instrument to image biological samples with lateral resolutions that can be as low as a few nanometers [146–148]. A key advantage of imaging samples with the atomic force microscope compared to using other methods that yield a similar resolution, e.g., transmission electron microscopy (TEM), lies in the fact that information about the sample height is also obtained. For instance, when imaging biomolecules, information on sample height can be beneficial for unambiguously identifying distinct parts of the molecule of interest. In addition, binding of small molecules to larger biomolecules can also be detected based on sample height, as shown within a side project for binding of protein disulfide isomerase (PDI) to VWF's CK domain (see Appendix A.3) [37].
In fact, there are several AFM imaging modes, all of which bear different advantages and disadvantages and hence have to be chosen according to the application. In brief, AFM imaging modes can be divided into contact and non-contact modes. While in the former the cantilever tip is in direct contact with the sample surface, in the latter the cantilever oscillates at a fixed frequency close to the sample surface, typically within a distance of 1 to 100 nm. Imaging in non-contact mode naturally prevents sample damage and cantilever tip contamination, but usually requires lower scan speeds and yields lower resolution. To keep sample damage low while still providing a satisfying lateral resolution, biological samples are frequently imaged in intermittent contact mode, also known as AFM tapping mode.

#### Basics of AFM tapping mode

In AFM tapping mode (Fig. 3.4), the AFM cantilever is excited externally with a fixed frequency close to the cantilever's free resonance frequency. The oscillation frequency typically lies within a range of approximately 1 to 500 kHz. The oscillation of the cantilever is usually achieved with a small piezo element located in the cantilever holder, although it can also be accomplished by other methods, such as heating with a modulated laser beam [149]. While scanning the sample in a line-by-line pattern, the cantilever tip is kept close to the surface and taps the sample during the oscillation cycle. Importantly, as forces between the cantilever tip and the sample critically shift the resonance frequency of the cantilever, they result in a change of the oscillating amplitude and the phase between oscillation and excitation. The oscillating amplitude, which commonly ranges from approximately 1 to 100 nm, can be used as a signal for regulation. More precisely, while scanning the sample with an $x$–$y$ piezo, a feedback loop usually maintains a constant oscillating amplitude by varying the distance between the AFM tip and the sample. Variation of this distance is commonly achieved by a $z$ piezo. AFM tapping mode is widely used for imaging soft biological samples, as it largely benefits from lateral forces acting on the sample that are low compared to the ones that are

present in contact mode. Samples can be imaged in air, but also in a solution, and hence at conditions that approximate their native environment.

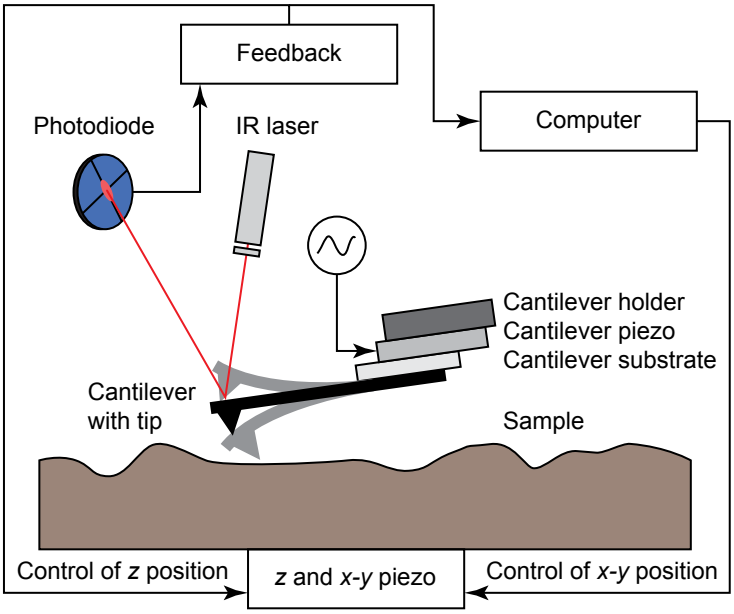


**Figure 3.4:** Basic principle of AFM tapping mode (not drawn to scale). A piezo element excites the AFM cantilever to oscillate at a fixed frequency, typically very close to its free resonance frequency. During the oscillation cycle, the cantilever tip touches the sample intermittently. Importantly, forces between the cantilever tip and the sample shift the resonance frequency of the cantilever, thereby changing its oscillating amplitude. A feedback loop maintains a constant amplitude by varying the $z$ position of the sample through a piezo element. Graphical representation inspired by Fig. 22.10 of reference [150].

### Experimental procedures of AFM imaging

All AFM imaging data presented in this thesis were collected by Achim Löf and Christof Beer. More precisely, while AFM imaging of VWF dimers and monomers was performed by Achim Löf, imaging of multimer samples, which naturally include a large fraction of dimers [101], was performed by Christof Beer. Details on imaging, both in terms of experimental procedures and results, can be found in Achim Löf's and Christof Beer's master's theses [103, 104].
Crucial for AFM imaging applications is a pure sample and a very flat surface on which the molecules can adsorb. To achieve clean samples, VWF constructs carrying either a Twin-Strep-tag or a single Strep-tag were purfied via a HiTrap StrepTrap (GE Healthcare Europe GmbH, Freiburg, Germany) and afterwards buffer exchanged to the measurement buffer (see section 3.2). Here, it should be noted that AFM imaging revealed contamination in the form of tentacle-like polymer chains protruding from the N termini of Twin-Strep-tagged dimers (Fig. 3.5A and C, for comprehension of dimer conformations, please refer to subsection 4.1.2.). The fact that such tentacles were not observed for constructs equipped with a single Strep-tag (Fig. 3.5B and D) strongly suggested that the tentacles originated from the $(GGGS)_3$ linker within the Twin-Strep-tag. Given that heavy O-glycosylation of GGGS linker repeats had been observed before for proteins produced in HEK cells [151–154], the observed tentacles were hypothesized to be large O-linked sugar chains [56]. Interestingly, the extent of glycosylation was markedly higher for the full-length constructs than for the truncated constructs,

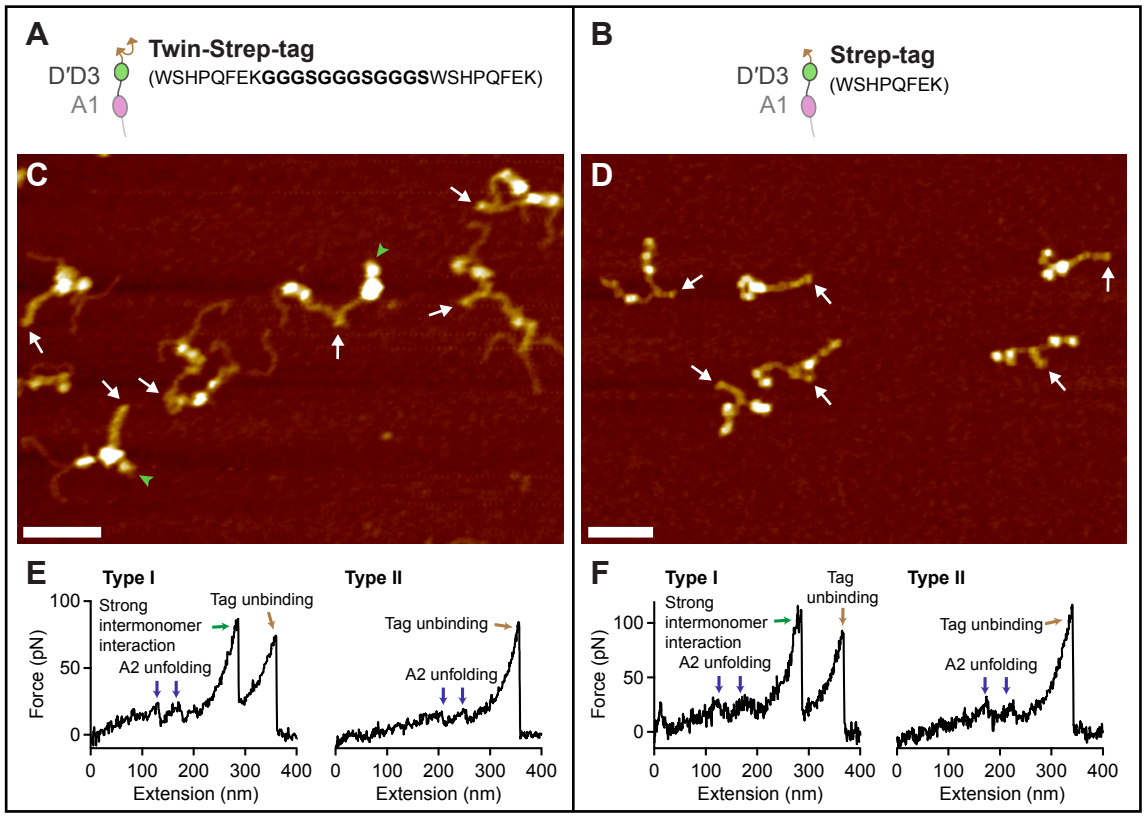


**Figure 3.5:** O-Glycosylation of GGGS linker repeats in Twin-Strep-tagged VWF [151–154]. (A–B) Schematics of N-terminally linked Twin-Strep-tag (A) and single Strep-tag (B), and corresponding peptide sequences. (C) Representative AFM image of Twin-Strep-tagged VWF dimers purified via a Strep-Tactin column. Most constituent monomers exhibited tentacle-like polymer chains protruding from their N termini. Such tentacles were only observed in dimers carrying a Twin-Strep-tag and never observed as isolated ones on the surface. As a result of the purification, at least one of the two constituent monomers of a dimer carried an N-terminal Twin-Strep-tag and hence exhibited tentacles. Green arrowheads mark N termini free of tentacles, very likely corresponding to ybbR-tagged monomers in heterodimers. White arrows indicate positions of CK domains. (Scale bar, 50 nm; range of color scale, 2.4 nm.) (D) Representative AFM image of VWF homodimers carrying single N-terminal Strep-tags without GGGS linker repeats. Tentacle-like polymer chains were not observed. Scale bar and range of color scale are as in C. (E–F) Representative force–extension traces of VWF dimers, obtained from force measurements on heterodimers carrying either a Twin-Strep-tag (E) or a single Strep-tag (F). Evidently, the two characteristic types of force–extension traces, which are discussed in detail within sections 4.1 and 4.2, were not affected by the heavy glycosylation of the Twin-Strep-tag. Please also refer to subsections 4.1.2 and 4.1.1.

such as A1-CK [103]. Importantly, the conformation of tagged constructs was unaffected by the heavy glycosylation, as verified by comparison with constructs lacking peptide tags. In particular, tagged dimers – both full-length and truncated ones – exhibited a very similar degree of compactness as untagged constructs. In line with a uniform conformation of VWF constructs, force-extension traces of dimers were unaffected by abovementioned glycosylation, as checked by pulling heterodimers with a single Strep-tag, which lacked the $(GGGS)_3$ linker (Fig. 3.5E and F, for comprehension of force–extension traces of VWF dimers, please refer to subsection 4.1.1.).

Dimers lacking peptide tags (Fig. 4.11A) were purified by centrifuge filtration using Amicon Ultra-15 MWCO 100 kDa (Merck Chemicals, Schwalbach, Germany). Dimers shown in Fig. 4.15A and delD4 dimers shown in Fig. 4.11B were selected from samples that were purified by centrifuge filtration only, and very likely correspond to ybbR-tagged homodimers, present as byproduct in samples of heterodimers. Multimeric samples were purified by centrifuge filtration using Amicon Ultra-15 MWCO 100 kDa and buffer exchanged to near physiological buffer. In principle, untagged VWF can also be purified in more specific ways, for instance via an antiVWF affinity column or via special gel filtration columns, as described more in detail in Christof Beer's thesis [104]. However, while gel filtration via a HiPrep Sephacryl S-500 HR column (GE Healthcare Life Sciences, UK) could not succesfully separate VWF from cell material present in the samples, purification via an antiVWF affinity column [CaptureSelect-VWF-affinity resin (Life Technologies, USA)], involving harsh elution with 3 M Thiocyanate, was found to induce prominent aggregation within VWF's N-terminal headgroups (Fig. 3.6, for a general comprehension of VWF conformations, please refer to subsection 4.1.2.).

For substrate preparation, a method similar to the one reported by Vanderlinden and coworkers [155] was employed. Freshly cleaved mica sheets (grade I, SPI Supplies, West Chester, PA), which under near-neutral pH conditions are negatively charged, were incubated with 20 µL of a positively charged poly-L-lysine (PLL) solution (MW 500-2000; 0.01 % w/v; Sigma-Aldrich; in ultrapure water) for 30 s. Subsequently, sheets were rinsed with 25 mL of ultrapure water and dried in a stream of nitrogen. 20 µL of buffer solution containing approximately 5 µg $mL^{-1}$ of VWF constructs were deposited on the functionalized mica substrates and incubated for 30 s. As VWF constructs at near-neutral pH conditions are overall negatively charged [70], they can adsorb well on the positively charged PLL. Afterwards, the substrates were rinsed with 20 mL of ultrapure water and dried in a stream of nitrogen.

AFM images were recorded in tapping mode in air using an MFP-3D AFM (Asylum Research) and silicon tips with resonance frequencies of approximately 300 kHz and a nominal spring constant of 26 N $m^{-1}$ (AC160TS-R3, Olympus). In the majority of the cases, the image size was 1 µ$m^2$ and the resolution given by 1024 x 1024 pixels.

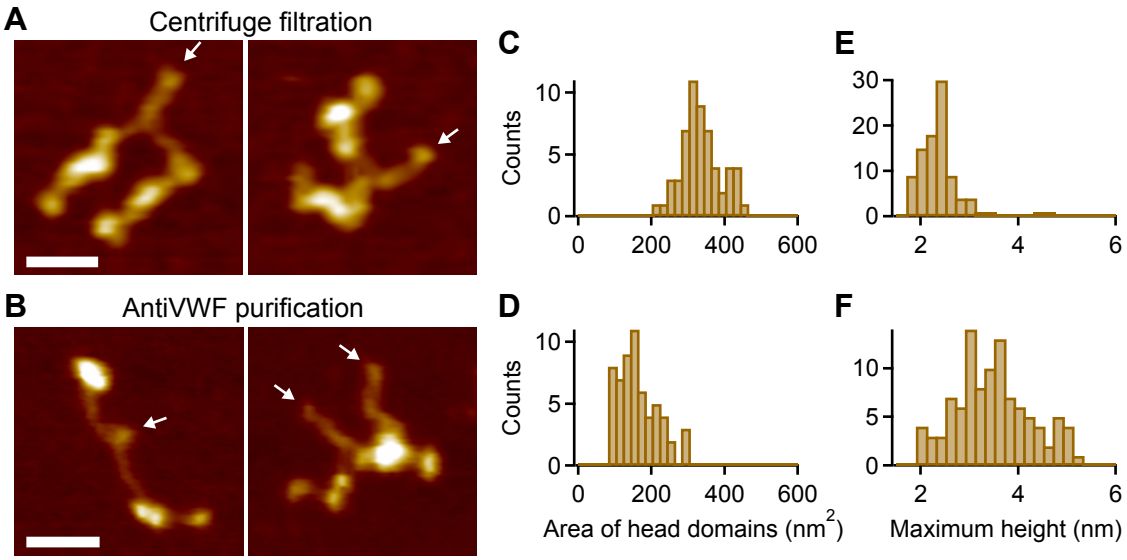


**Figure 3.6:** Conformational changes in VWF's N-terminal domains induced by antiVWF purification, which involves harsh elution with Thiocyanate. (A–B) AFM images of VWF molecules purified by centrifuge filtration (A) and via an antiVWF affinity column (B). Strikingly, antiVWF purification induced aggregation of N-terminal portions of dimers. White arrows indicate positions of CK domains. [Scale bars, 30 nm; ranges of color scale, 2.6 nm (A) and 3.1 nm (B)]. (C–D) Area of head domains quantified for VWF dimers purified via a StrepTrap (C) and via an antiVWF affinity column (D). Clumpy head groups, induced by antiVWF purification, are characterized by a significantly decreased area in the $x$–$y$ plane. (E–F) Maximum height of N-terminal portions for VWF dimers purified via a StrepTrap (E) and via an antiVWF affinity column (F). As a result of aggregated head groups in antiVWF purified dimers, maximum height values are markedly increased compared to the ones purified via a StrepTrap. Please also refer to subsection 4.1.2.

### Image processing and analysis

All AFM imaging data presented in this thesis were processed and analyzed by Achim Löf and Christof Beer [103, 104], using SPIP software (v6.3.4 – v6.5; Image Metrology, Denmark). Image processing included plane correction (third order polynomial plane-fitting and flattening according to the histogram alignment routine) and Gaussian filtering. Dimers were individually traced along their contour by following local maxima in height, and different characteristic lengths were extracted from the resulting height profiles. To quantify the compactness of a dimer, its stem length was determined, i.e., the distance from the CK domains to the position at which the two constituent monomers separate from each other. Further, the distance between the CK domains and the beginning of higher N-terminal domains was determined for the two constituent monomers of a dimer, and the mean of these distances was used to normalize the stem length.

## 3.4 Total internal reflection fluorescence (TIRF) microscopy

Fluorescence microscopy is an essential tool to image biological samples with contrasts that are much higher than in the case of other optical microscopy techniques. For fluorescence microscopy, biological samples are labeled with fluorophores, i.e., chemical agents that exhibit the phenomenon of fluorescence. Fluorophores are excited by absorbing light of a specific wavelength, and they emit light of longer wavelengths when relaxing into lower energy levels. In fluorescence microscopy, samples with attached fluorophores are visualized by irradiating with light of appropriate wavelength and by separating the emitted fluorescent light from the excitation light. Specifically, the excitation wavelengths are filtered out from the light path to the detector.
Critical for achieving single-molecule resolution in fluorescence microscopy is the signal-to-noise ratio of the individual fluorophores. While for a high signal, fluorophores with high exctinction coefficients and quantum yields have to be chosen, relatively low noise can be achieved by restricting the excitation volume. This approach is pursued for example in confocal microscopy [156] and in TIRF microscopy [24].

### Basic principles of TIRF microscopy

In TIRF microscopy, restriction of the excitation volume is achieved by using an evanescent field, which is generated by the total internal reflection of an incident laser beam at the interface of a substrate and the sample liquid [24]. In the case of an objective-based system (Fig. 3.7), the evanescent field is generated directly above the substrate, and the half-space above the sample remains free, which bears the potential for parallel applications, such as AFM [108, 143].

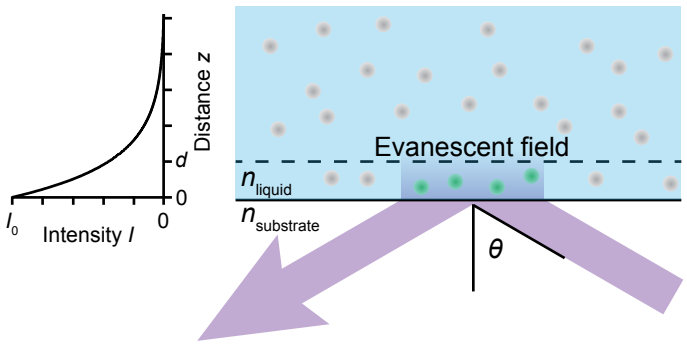


**Figure 3.7:** Basic principle of TIRF microscopy, illustrated for an objective-based system. To excite fluorophores only within a restricted region of the sample, TIRF microscopy uses an evanescent field, whose intensity decays within a distance $d$ of roughly 100 to 200 nm above the substrate. Such an evanescent field is generated by total internal reflection of an incident laser beam at the substrate–liquid interface.

Total internal reflection occurs when the angle of incidence $\theta$ is larger than the critical value $\theta_c = \arcsin(n_{liquid}/n_{substrate})$. In the latter expression, $n_{liquid}$ denotes the refractive index of the liquid and $n_{substrate}$ the refractive index of the substrate. The intensity $I$ of the evanescent

field in a distance $z$ above the substrate is given by

$$I(z) = I_0 \cdot e^{-z/d}, \tag{3.10}$$

where $I_0$ is the intensity at zero distance and $d$ the characteristic decay length. The latter is given by

$$d = \frac{\lambda}{4\pi n_{\text{liquid}}} \left( \frac{\sin^2 \theta}{\sin^2 \theta_c} \right)^{-0.5}, \tag{3.11}$$

where $\lambda$ is the wavelength of the incident beam in vacuum. Typical values of $d$ are on the order of 100 to 200 nm.

### Subunit counting in multimeric proteins by photobleaching

When subjected to continous excitation of appropriate wavelength, fluorophores undergo a series of absorption-emission cycles. In fact, for a given fluorophore, each of these cycles bears an equal probability to cause a phenomenon called photobleaching, after which the fluorophore is not able to fluoresce anymore. In other words, depending on the excitation intensity, fluorophores have a characteristic lifetime within which they are able to fluoresce. It should, however, be mentioned that some fluorophores can also switch back and forth between a fluorescent and a dark state. Importantly, such blinking behavior may also lead to a state from which the fluorophore will be photobleached irreversibly. Generally, photobleaching is believed to result from photochemical reactions, i.e., light-induced reactions with other molecules that damage the fluorophore.
In TIRF microscopy, photobleaching of fluorescent molecules can be used to count fluorophore-labeled subunits of individual biomolecules [157–159]. Here, the number of subunits is assessed by counting discrete steps of photobleaching of single fluorophores. In this context, the use of genetically engineered fluorophores ensures that every tagged subunit carries exactly one fluorophore and avoids non-specific labeling that may occur when using dyes that require an additional labeling reaction.

### Experimental procedures and data analysis of TIRF measurements

VWF constructs bearing a C-terminal eGFP molecule on each monomer [101] were immobilized on an epoxysilane (3-glycidyloxypropyltrimethoxysilane) coated glass slides and imaged using the setup presented in reference [143]. For excitation in the total internal reflection mode, a 473 nm laser (iBeam smart, TOPTICA, Gräfelfing, Germany) was used at a power of 0.4 mW. The corresponding filter set consisted of a Chroma z 470/10, a Chroma z 470 RDC, and a Chroma HQ525/50 (Chroma Technology GmbH, Olching, Germany). The emitted

light signal was detected by a back-illuminated EMCCD camera (DU-860D, Andor, Belfast, Ireland). The EMCCD chip was operated at a temperature of $-90°C$ and the electron multiplication gain was set to 300-fold. Per image sequence, 3000 frames of $21 \times 21\,\mu m^2$ were taken at a recording rate of 10 frames/s. To minimize bleaching of eGFP fluorophores before the actual measurements, all adjustment procedures were carried out at a comparably low laser power of 0.1 mW.

For data analysis, an average image of the first 100 frames was calculated and regions of interest that showed a pronounced fluorescence signal were selected. Bleaching steps in intensity-time traces of these regions were identified by using the step detection algorithm described in reference [160]. As the routine cannot distinguish between on- and off-steps and fails in detecting steps that occur within a very short time slot, the obtained step number was corrected by eye for blinking and missed steps.

# 4 Results and discussion

This chapter will present results of the experiments that were performed in the framework of this thesis. Special emphasis will be placed on the discovery of a strong intermonomer interaction in VWF's dimeric subunits and its implications for VWF's force-sensing ability. In particular, it will be discussed that the latter can be regulated by the pH, as the strong intermonomer interaction was found to be heavily pH-dependent. As force sensing by VWF critically depends on its multimer size, the size distribution of recombinant VWF was also addressed in the framework of this thesis. At the end of this chapter, results from two single-molecule approaches regarding this issue, namely AFM imaging and TIRF microscopy photobleaching experiments, will be presented and discussed.

## 4.1 A strong intermonomer interaction in VWF's dimeric subunits

To dissect the remarkable force-sensing ability of VWF, the force response of VWF dimers – and of a variety of other VWF constructs – was probed in AFM-based single-molecule force measurements. As will be shown in the following, under near physiological buffer conditions, these measurements revealed a strong intermonomer interaction in VWF's dimeric subunits that involves the D4 domain and critically depends on divalent ions. The existence of this interaction was confirmed using AFM imaging, both for isolated dimers and for dimers as constituents of higher-order concatemers. The combination of force and imaging data allows for a quantitative understanding of the mechanisms that underlie VWF's force-sensing ability.

### 4.1.1 Dissecting the force response of VWF dimers under near physiological buffer conditions

For AFM-based single-molecule force measurements, genetically engineered VWF heterodimers were employed (Fig. 4.1A). These heterodimers were composed of two monomers with different N-terminal peptide tags. While a ybbR-tag at the end of one of the monomers enabled covalent anchoring to a Coenzyme A (CoA) functionalized glass surface [142, 161], a Twin-Strep-tag at the end of the other monomer allowed for specific pulling via a Strep-Tactin functionalized AFM cantilever [162]. The Twin-Strep-tag was preferred over a single

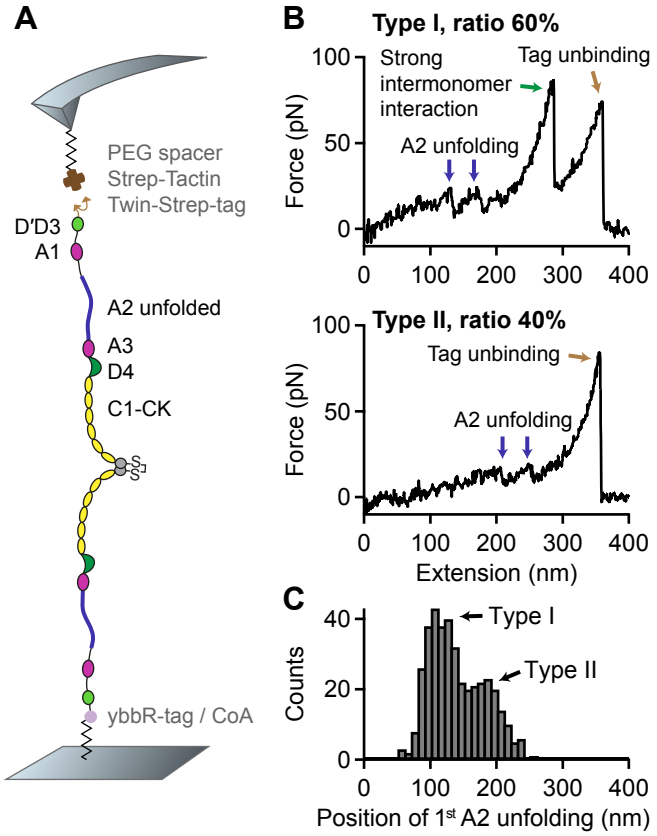


**Figure 4.1:** Single-molecule force measurements on VWF dimers. (A) Schematic representation of pulling genetically engineered VWF heterodimers (not drawn to scale). A ybbR-tag at the N terminus of one of the monomers allowed for covalent anchoring to a CoA coated substrate, and a Twin-Strep-tag at the N terminus of the other monomer enabled specific pulling via a Strep-Tactin functionalized AFM cantilever. (B) Denoised force–extension traces of dimers showing A2 unfolding peaks (blue arrows) at low (type I traces) or at high extension values (type II traces). Type I traces repeatedly exhibited a peak (strong intermonomer interaction, green arrow) at higher force. The final peak (brown arrow) corresponds to the unbinding of the Twin-Strep-tag from Strep-Tactin. (C) Bimodal distribution of the position of the first A2 unfolding event.

Strep-tag to achieve more stable binding and reduced off-rates [162] as well as a high tag accessibility. Polyethylene glycol (PEG) spacers were used both at glass surface and cantilever to minimize protein–surface interaction (for details see chapter 3).

Force–extension traces of specific pulling events were identified by using the characteristic unfolding signal of the A2 domain as a positive fingerprint (Fig. 4.1B). In other words, due to the existence of two A2 domains in dimers, only traces with two A2 unfolding peaks were considered. The observed peak forces of $\sim$ 10–20 pN, followed by length increments of 45 nm, are in very good agreement with reported values for A2 unfolding [12, 58, 59, 88]. Importantly, the origin of the A2 fingerprint was directly verified in different control experiments. First, force–extension traces of truncated A2-CK dimers were compared with traces of A3-CK dimers that lacked the A2 domain (Fig. 4.2); as expected, traces of A3-CK dimers did not exhibit any peaks similar to the A2 fingerprint peaks. Secondly, force–extension traces of heterodimers with A2 domains protected against unfolding by disulfide bonds did not exhibit A2 unfolding peaks either (Fig. 4.3). Thirdly, force–extension traces of monomers only exhibited one A2 unfolding peak (Fig. 4.4). The fact that forces of the last peak (rupture peak) in force–extension traces are further in line with those reported for dissociating the Strep-tag/Strep-Tactin interaction [163, 164] underlines the specific nature of the analyzed pulling events (Fig. 4.5).

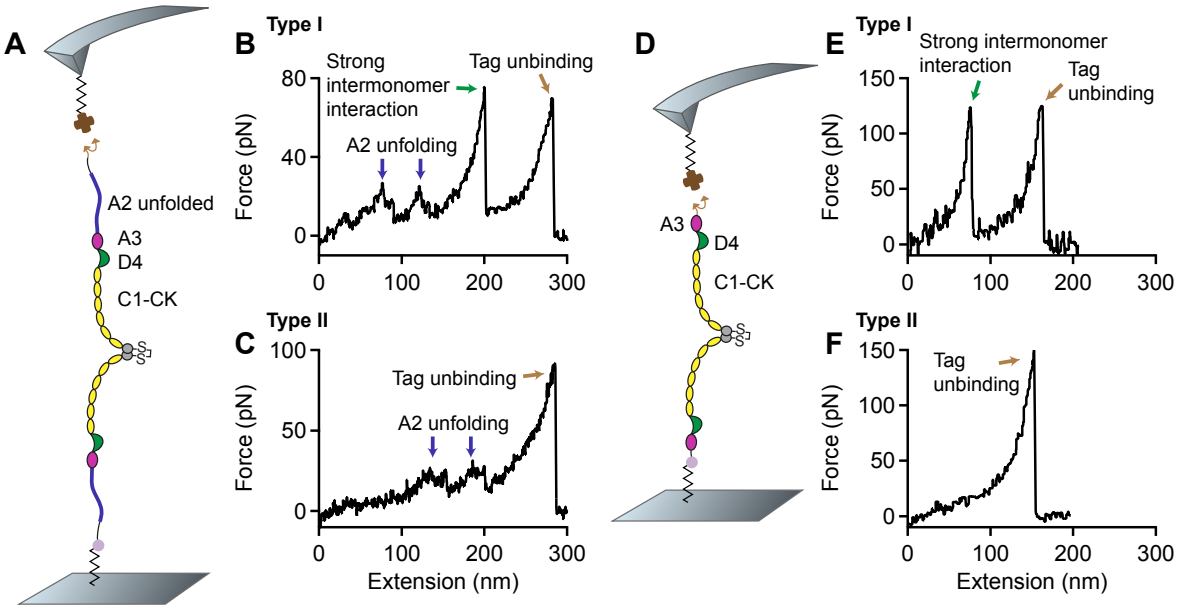


**Figure 4.2:** Single-molecule force measurements on truncated dimeric constructs A2-CK and A3-CK. (A) and (D) Schematic representations of the respective pulling configuration (not drawn to scale). (B–C) Denoised force–extension traces of A2-CK dimers (type I with the characteristic high-force peak and type II without). (E–F) Denoised force–extension traces (type I and type II) of A3-CK dimers. As expected, due to the lack of A2 domains in A3-CK dimers, force–extension traces did not exhibit A2 unfolding peaks.

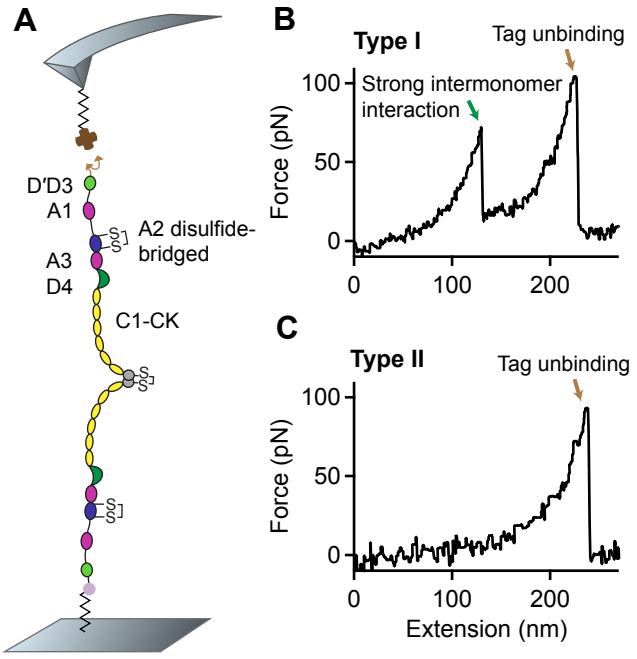


**Figure 4.3:** Single-molecule force measurements on VWF dimers with mutations N1493C and C1670S, which induce a disulfide bridge that protects the A2 domain against unfolding [53]. (A) Schematic representation of the pulling configuration (not drawn to scale). (B–C) Denoised force–extension traces (type I with the characteristic high-force peak and type II without) lacking the characteristic A2 unfolding peaks.

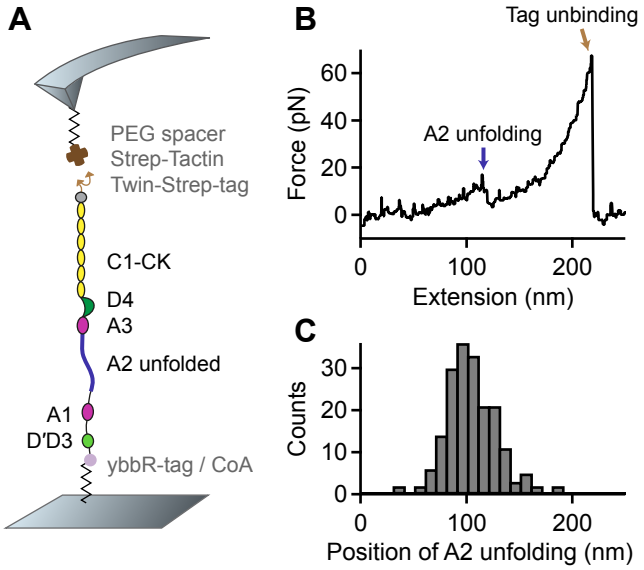


**Figure 4.4:** Single-molecule force measurements on VWF monomers. (A) Schematic representation of the pulling configuration (not drawn to scale). A ybbR-tag at the N terminus and a Twin-Strep-tag at the C terminus enabled specific pulling via a Strep-Tactin functionalized cantilever. (B) Denoised force–extension trace showing a single A2 unfolding peak and lacking the high-force peak characteristic for the opening of firmly closed C-terminal rods in dimers. (C) Unimodal distribution of the position of A2 unfolding.

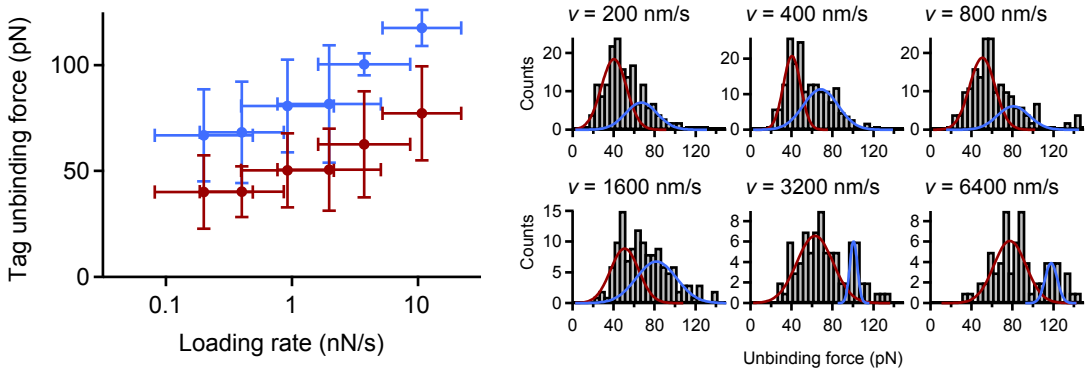


**Figure 4.5:** Tag unbinding forces as a function of the applied loading rate. Tag unbinding represents the dissociation of the Twin-Strep-tag from tetravalent Strep-Tactin. Mean forces were obtained by fitting a bimodal Gaussian function to the distribution of unbinding forces for each pulling speed. Loading rates were obtained by fitting a line to force–extension traces before the last peak. Mean values of loading rates were obtained by fitting a Gaussian to the loading-rate distributions for each pulling speed. Error bars are 1 SD. Force–loading-rate dependency and bimodality of the individual force distributions are in line with previous investigations of the specific Strep-tag/Strep-Tactin interaction [163].

Under near-physiological buffer conditions, VWF dimers yielded two types of force–extension traces (Fig. 4.1B), showing A2 unfolding peaks at low (type I) and at high extension values (type II). Type II traces revealed the first A2 unfolding peak at extension values of $179 \pm 29$ nm and the second A2 unfolding peak at $226 \pm 37$ nm. Given a static end-to-end length of 130 nm for a VWF dimer and an overall linker length of 60 nm, these traces are in line with expectations for loading a flexible (open) dimer [55]. Traces of type I showed A2 unfolding

peaks at considerably lower extension values of 110 ± 22 nm (first A2) and 161 ± 22 nm (second A2). Classification of traces into two types is backed up by a bimodal distribution of the position of both first (Fig. 4.1C) and second A2 unfolding. From a double-Gaussian fit to the distribution of the first A2 unfolding position, the ratio of type I traces was estimated to be 60% and the one of type II traces to be 40%.

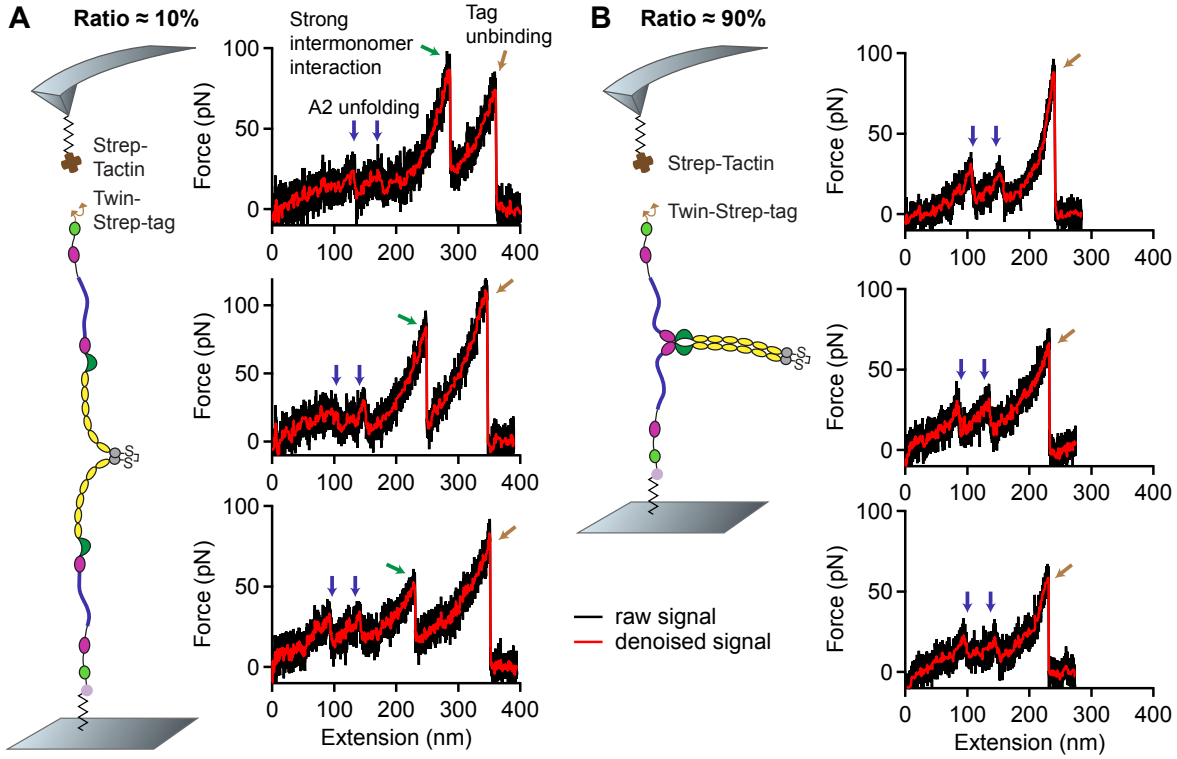


**Figure 4.6:** Temporal order of opening firmly closed dimers and tag unbinding. (A) Three representative force–extension traces of type I showing the characteristic high-force peak (green arrow), which corresponds to the dissociation of a strong intermonomer interaction in VWF dimers. After dissociation of the strong intermonomer interaction, the entire dimer is loaded with force and stretched (not drawn to scale). Finally, the construct detaches from the cantilever (brown arrow) as the Twin-Strep-tag dissociates from Strep-Tactin. (B) Three representative force–extension traces of type I exhibiting the peak of tag unbinding at an early stage of elongation. Positions of A2 unfolding events (blue arrows) are very similar to the ones seen in the traces in A, strongly indicating that these traces likewise originate from pulling firmly closed dimers. However, as tag unbinding occurs too early, the strong intermonomer interaction is not dissociated and dimers remain only semistretched until tag unbinding.

Force–extension traces of type I repeatedly exhibited an additional high-force peak (green arrow in Fig. 4.1B) before the rupture peak. In these cases, the position of rupture closely matched the one observed in type II traces. However, as a result of the relatively weak Twin-Strep-tag/Strep-Tactin interaction, this additional peak only showed up in 10% of type I traces (Fig. 4.6A). In the remaining 90% of type I traces, rupture of the construct from the cantilever occurred before observing a high-force peak, and at considerably lower extension values (Fig. 4.6B).

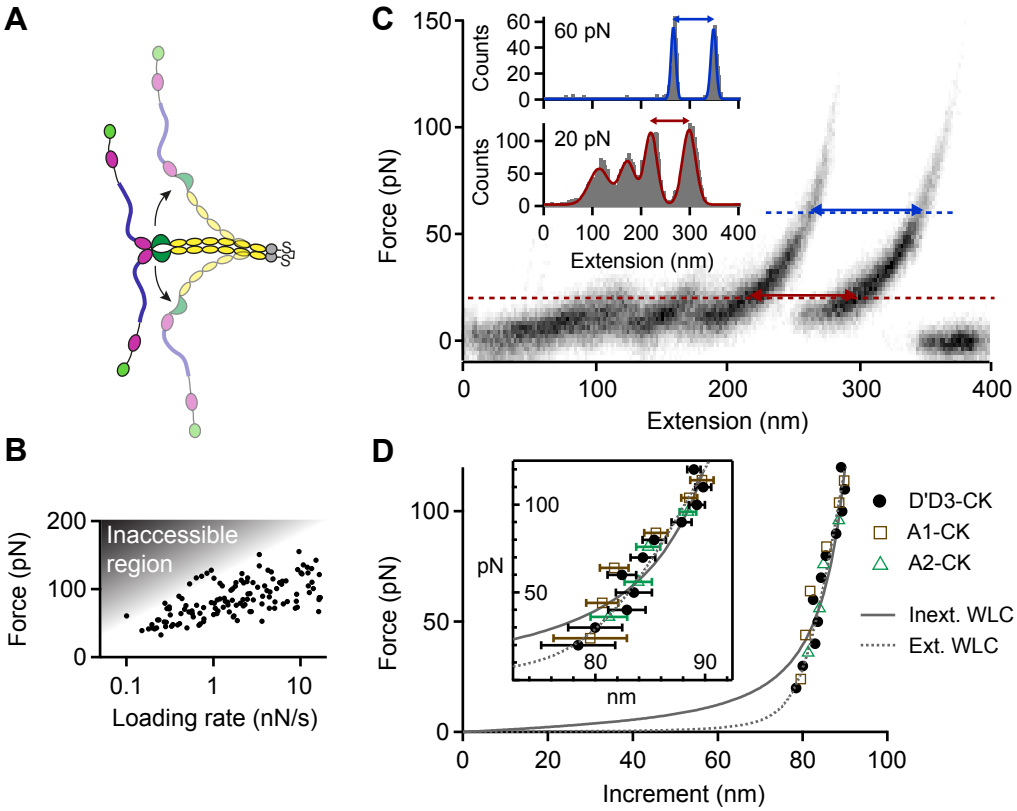


**Figure 4.7:** Analysis of the high-force peak in type I force–extension traces of VWF dimers, resulting from the dissociation of a strong intermonomer interaction in dimers. (A) Illustration of the corresponding force-induced conformational changes of VWF dimers (not drawn to scale). Unfolding of the mechanically less stable A2 domain (blue) precedes the opening of the dimer. (B) Force–loading-rate dependency of the dissociation of the strong intermonomer interaction. Due to the relatively weak Strep-tag/Strep-Tactin interaction, most events may be missed due to an inaccessible region in the force–loading-rate space. (C) Overlay of 30 force–extension traces of type I. Cross-section profiles at constant force, as shown for 20 and 60 pN, were fitted to a multipeak Gaussian distribution, and the distance between the two last peaks yielded a characteristic length increment. The overlay was created based on the raw signal of the underlying traces. (D) Length increments, gained from the dissociation of the strong intermonomer interaction, as a function of force. Solid and dashed lines are fits of the inextensible and extensible WLC model, respectively. Error bars were calculated by propagation of the uncertainties of the mean positions of the last two Gaussian peaks (1 SD). Dimeric constructs A1-CK (brown squares) and A2-CK (green triangles) exhibited very similar increments (Fig. 4.8).

The high-force peak was observed at forces ranging from roughly 50 to 120 pN, depending on the applied loading rate (Fig. 4.7B). Importantly, the high-force peak was never observed twice in a trace and, moreover, was never observed in monomer traces (Fig. 4.4). Consequently, domain unfolding could be excluded as the origin of this high-force peak, in agreement with the prediction of disulfide bonds stabilizing all domains in VWF against unfolding except the A2 domain [61]. Hence, the high-force peak was hypothesized to result from the dissociation of a strong intermonomer interaction, which may be conceptualized as the opening of a firmly closed C-terminal rod of dimers (Fig. 4.7A).

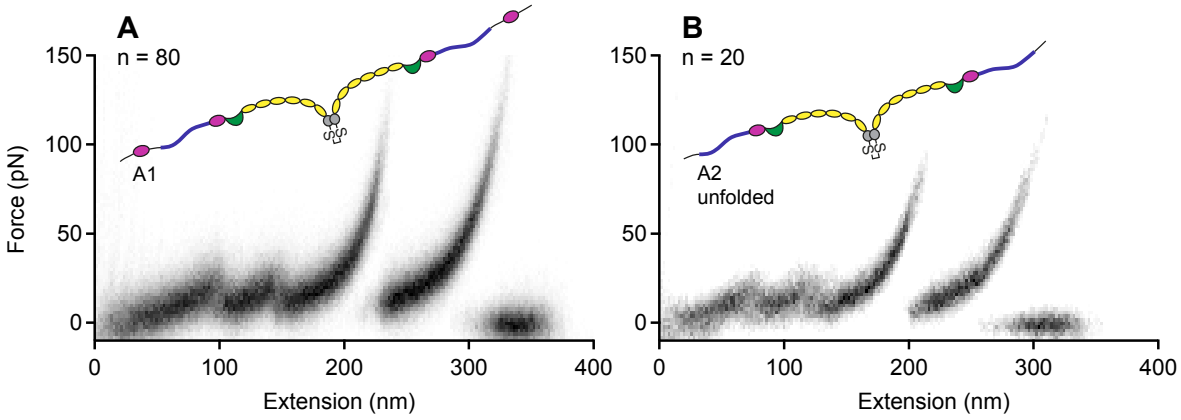


**Figure 4.8:** Overlays of multiple type I force–extension traces for truncated dimeric constructs A1-CK (A) and A2-CK (B). The overlays were created based on the raw signal of the underlying traces. The schematic representations of the pulled dimeric constructs are not drawn to scale.

In order to estimate the incremental length obtained from such opening events, type I force–extension traces were overlaid and cross-sections at constant force (Fig. 4.7C), ranging from 20 to 100 pN, were analyzed. This method was preferred over the method of contour length transformation [122, 130, 132, 166], which relies on a model describing the elasticity of a uniform polymer. Characteristic length increments above 80 nm that increased with force were obtained (Fig. 4.7D). Additional measurements on truncated dimeric constructs lacking either only the N-terminal D'D3 domains (A1-CK; squares in Fig. 4.7D) or both D'D3 and adjacent A1 domains (A2-CK; triangles) yielded the same results (Fig. 4.8). For the full-length constructs, the length increase with force was approximately described by the (inextensible) Worm-like-chain (WLC) model ($\chi^2_{\mathrm{red}} = 1.9$; Fig. 4.7D, solid line, [124]), yielding a contour length of $L_C = 102$ nm and a persistence length of $P = 0.6$ nm. Including an (enthalpic) stretch modulus $S$ in the WLC model (extensible WLC model, [126]) yielded a better fit ($\chi^2_{\mathrm{red}} = 1.3$; Fig. 4.7D, dashed line), with fitting parameters $L_C = 84$ nm, $S = 1120$ pN and $P = 6.4$ nm. Latter is in excellent agreement with the value of $P = 6.4$ nm inferred from AFM imaging (Fig. 4.9).

A comparison of the length increments with distances reported for static dimers suggested the observed interaction to be mediated by the D4 or A3 domain of VWF [55]. To locate the

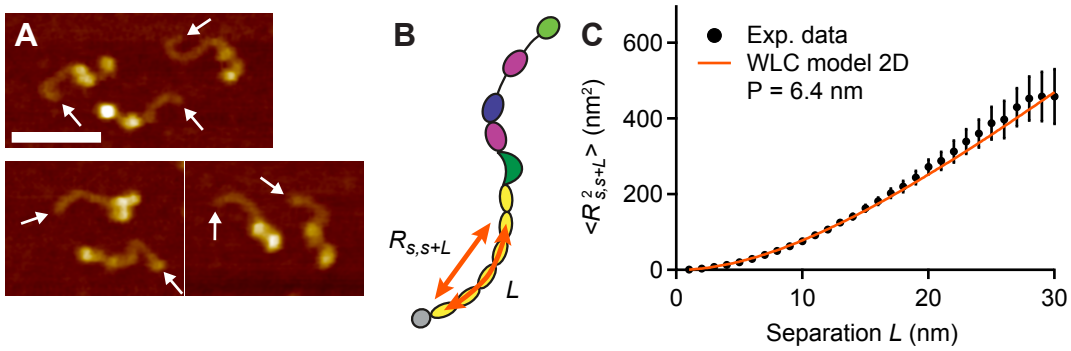


**Figure 4.9:** Estimation of the persistence length of VWF's C-terminal region from AFM imaging. (A) AFM images of VWF monomers. (Scale bar, 50 nm; range of color scale, 2.4 nm.) (B) Schematic representation of a VWF monomer and illustration of the parameters $\langle R^2_{s,s+L} \rangle$ (mean-squared-distance between two points on the C-terminal rod of a monomer, which are parameterized by the coordinate $s$) and $L$ (separation of the two points along the contour of the C-terminal rod) analyzed in (C). (C) Mean value of the mean-squared-distance $\langle R^2_{s,s+L} \rangle$ as a function of the separation $L$ along the contour of C-terminal rods in VWF monomers ($N = 10$). The experimental data were fitted using the following expression for 2D equilibrated polymer chains [165]: $\langle R^2_{s,s+L} \rangle = 4P \cdot \left(L + 2P\left(e^{-L/2P} - 1\right)\right)$. The fitting parameter $P$ denotes the bending persistence length in the context of the WLC model. The value of 6.4 nm (reduced $\chi^2_{\text{red}} = 0.76$) obtained for $P$ is close to the size of individual C domains [61]. Fitting a different model that assumes kinetic trapping on adsorption yielded a clearly nonsensical value of $P = 3.5\,\mu\text{m}$ ($\chi^2_{\text{red}} = 6.85$), supporting the assumption of full equilibration. It should be noted that minor deviations from full equilibrium would imply that the obtained value slightly underestimates the persistence length. Errors bars represent the standard deviation of the mean values.

responsible domain, force measurements on VWF dimers with a deletion of either domain were performed (Fig. 4.10). The characteristic high-force peak was still observed upon deletion of the A3 domain (Fig. 4.10A–C). In contrast, deletion of the D4 domain (D4N-TIL4, Fig. 4.10D) resulted in a loss of the characteristic high-force peak and yielded only a single type (type II) of force–extension traces (D4N-TIL4, Fig. 4.10E and G) and a unimodal distribution of the position of both first (Fig. 4.10F) and second A2 unfolding.

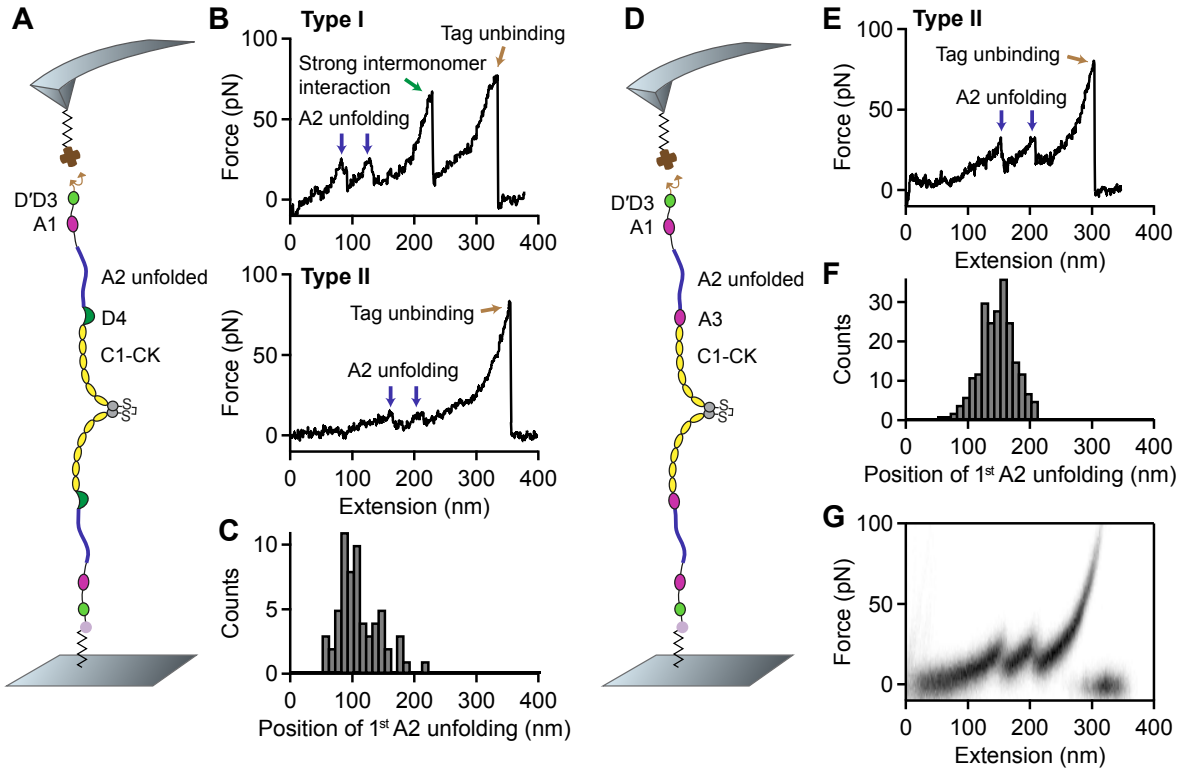


**Figure 4.10:** Single-molecule force measurements on VWF dimers lacking either the A3 or the D4 domain. (A) Schematic representation of pulling VWF dimers lacking the A3 domain (not drawn to scale). (B) Denoised force–extension traces of dimers lacking the A3 domain. Traces were essentially unaffected by deletion of A3, in particular the characteristic high-force peak. (C) Distribution of the position of the first A2 unfolding event for all traces of dimeric VWF lacking the A3 domain. (D) Schematic representation of pulling VWF dimers lacking the D4 domain (not drawn to scale). (E) Denoised force–extension trace of a VWF dimer lacking the D4 domain. The high-force peak characteristic for opening firmly closed dimers was never observed. (F) Unimodal distribution of the position of the first A2 unfolding peak obtained for dimers lacking the D4 domain. (G) Overlay of 76 force–extension traces of dimeric VWF lacking the D4 domain. The overlay was created based on the raw signal of the underlying traces.

### 4.1.2 Conformation of VWF under near physiological buffer conditions

Employing AFM imaging, the conformation of VWF, adsorbed from near physiological buffer onto a poly-L-lysine coated mica surface, was visualized. Dimers exhibited conformations ranging from fully flexible to fully closed (Fig. 4.11A). In order to quantify the compactness of a dimer, its stem length was analyzed. This length was defined as the distance from the CK domains to the position where the two constituent monomers separate from each other. Additionally, the distance between the CK domains and the beginning of higher N-terminal domains was measured for the two constituent monomers (Fig. 4.11). The mean of these distances was used to normalize the stem length. For wildtype dimers, the distribution of the normalized stem length (Fig. 4.12A) yielded one peak decaying from zero stem length (flexible

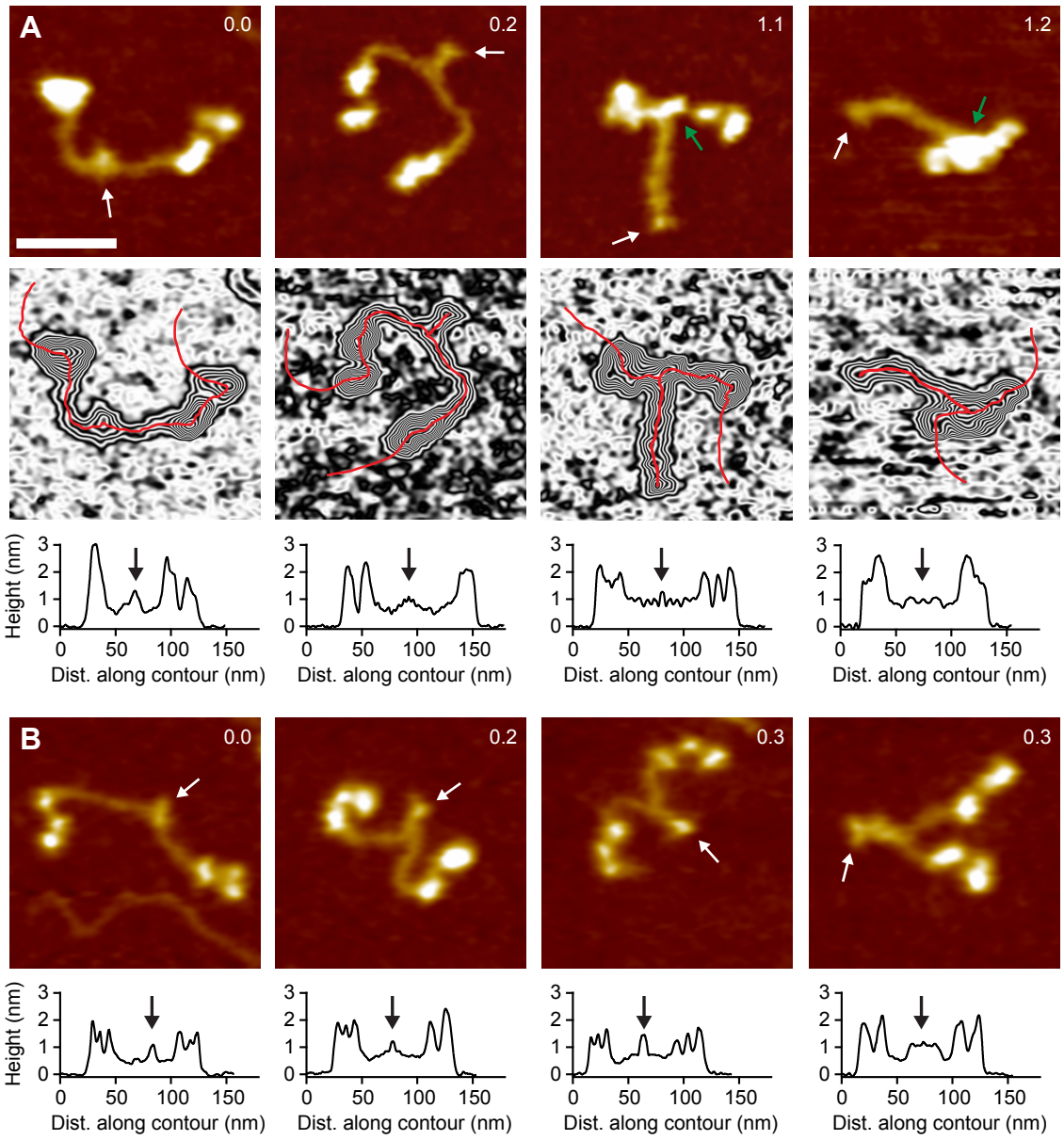


**Figure 4.11:** Conformation of dimeric VWF constructs under near physiological buffer conditions. Characteristic lengths were determined from height profiles of individual dimers, obtained by tracing each dimer in AFM images individually along its contour, following local maxima in height. White and black arrows indicate positions of CK domains, which were identified with the last C-terminal local maximum in height. The beginning of the higher N-terminal domains was defined as the position where the first large increase in height N-terminal of the CK domains reached its half-maximum value. Green arrows mark positions corresponding to potential strong intermonomer interactions. Numbers in images indicate values of the normalized stem length. (Scale bar, 30 nm; range of color scale, 2.4 nm.) (A) Images and analysis of wild-type dimers. (B) Images and analysis of dimers lacking the D4 domain.

dimers, $\sim 65\,\%$), and another peak centered slightly above 1 (closed dimers, $\sim 35\,\%$). Dimers lacking the D4 domain (delD4 dimers, Fig. 4.11B) exhibited only the population of normalized stem lengths decaying from zero (Fig. 4.12B). As the observed stem length distribution of delD4 dimers reflects the frequency of $n$ pairs of C domains to interact ($n = 0, 1, ..., 6$), it can be used to estimate the Gibbs free energy corresponding to intermonomer C-domain-interactions, yielding a value of $\sim 0.5\, k_{\mathrm{B}}T$ [56]. The fact that no peaks were observed in force measurements that would correspond to the dissociation of pairwise interacting C domains indicates that in this particular case chemical and mechanical affinity go rather hand in hand.

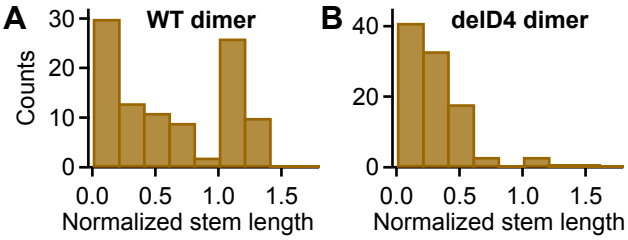


**Figure 4.12:** Distributions of the normalized stem length for wildtype (WT) dimers (A) and dimers lacking the D4 domain (B). While the distribution for WT dimers shows a peak decaying from zero stem length and a peak centered slightly above 1, the one for dimers lacking the D4 domain only shows the peak decaying from zero stem length.

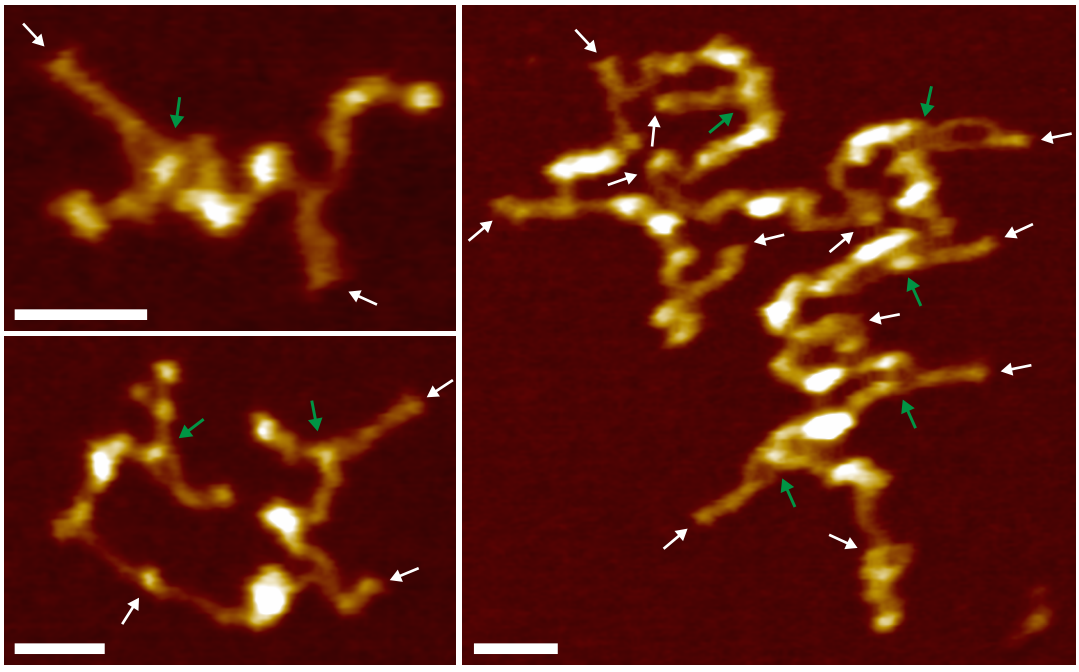

**Figure 4.13:** Conformation of VWF concatemers under near physiological buffer conditions. Shown are AFM images of VWF concatemers with different numbers of dimeric subunits. Evidently, dimers as constituents of concatemers exhibited similar conformations and a similar degree of compactness as isolated ones. White arrows indicate positions of CK domains, green arrows mark positions corresponding to potential strong intermonomer interactions. (Scale bars, 30 nm; ranges of color scales, 2.5 nm in upper left image, 2.6 nm in lower left image, and 2.5 nm in right image.)

AFM imaging further revealed that dimers as constituents of concatemers (Fig. 4.13) exhibit similar conformations and a similar degree of compactness as isolated ones. Especially in multimeric samples, dimers repeatedly exhibited colocalization of N-terminal portions of the constituent monomers, despite not possessing a fully closed stem (e.g., upper left dimer in Fig. 4.13). This colocalization may well result from the strong intermonomer interaction. Importantly, no clear colocalization between distinct dimers within a concatemer – except the intrinsic multimerization through D'D3 – was observed.

### 4.1.3 Flexibility of VWF at pH 7.4 in the absence of divalent ions

To test for the influence of divalent ions, force measurements on VWF dimers were also performed after addition of EDTA. Strikingly, the high-force peak in force–extension traces disappeared and only traces of type II were observed (Fig. 4.14A and C), backed up by unimodal distributions of the position of both first and second A2 unfolding peak (Fig. 4.14B). In line with the results from force measurements, dimers adsorbed onto a mica substrate from buffer containing EDTA and adjusted to pH 7.4 exhibited a flexible conformation, i.e., only partially or fully open stems (Fig. 4.15A). Consequently, the distribution of the normalized stem lengths only showed a population decaying from zero (Fig. 4.15B). Of course, dimers as constituent of concatemers were similarly affected by addition of EDTA (Fig. 4.16).

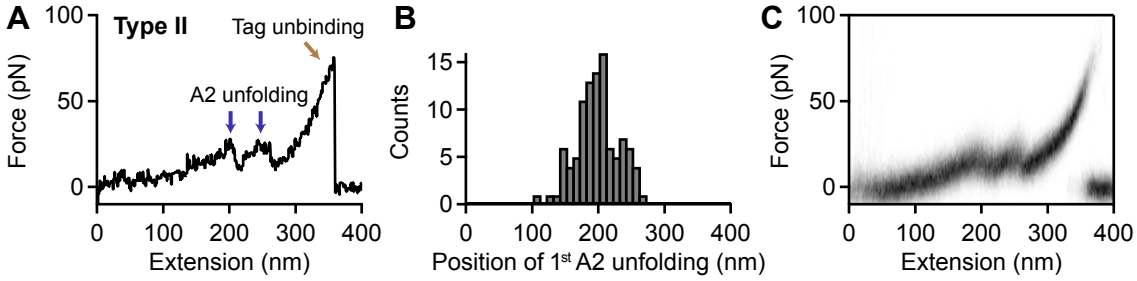


**Figure 4.14:** Obstruction of the strong intermonomer interaction by addition of EDTA. (A) Representative denoised force–extension trace of EDTA-treated dimers showing A2 unfolding peaks only at high extension values (type II). The characteristic high-force peak, which was observed for dimers under near-physiological conditions, was never observed. (B) Unimodal distribution of the position of the first A2 unfolding event. (C) Overlay of 50 force–extension traces of EDTA-treated dimers. The overlay was created based on the raw signal of the underlying traces. The shown data were in parts also taken from heterozygous dimers with the mutation F2561Y, which did not affect the force response of dimers (see section 3.1).

Clearly, the fact that the high-force peak was lost both upon deletion of the D4 domain (see subsection 4.1.1) and upon addition of EDTA strongly indicates a highly specific interaction involving the D4 domain and divalent ions. Here, it should be mentioned that it could not be clarified which divalent ions are responsible for the observed effect. Measurements performed

in the presence of either magnesium or calcium, after prior incubation with EDTA, did not indicate reformation of the strong intermonomer interaction [102].

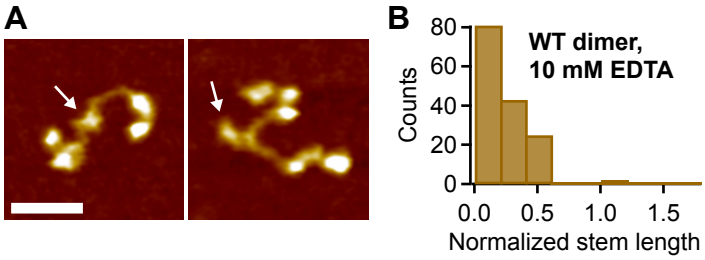


**Figure 4.15:** Conformation of VWF dimers at pH 7.4 after treatment with EDTA. (A) Representative AFM images of individual VWF dimers adsorbed from EDTA buffer at pH 7.4. Arrows mark the positions of the CK domains. (Scale bar, 30 nm; range of color scale, 2.4 nm.) (B) Distribution of the normalized stem length of dimers adsorbed from EDTA buffer at pH 7.4, showing a single peak decaying from zero stem length.

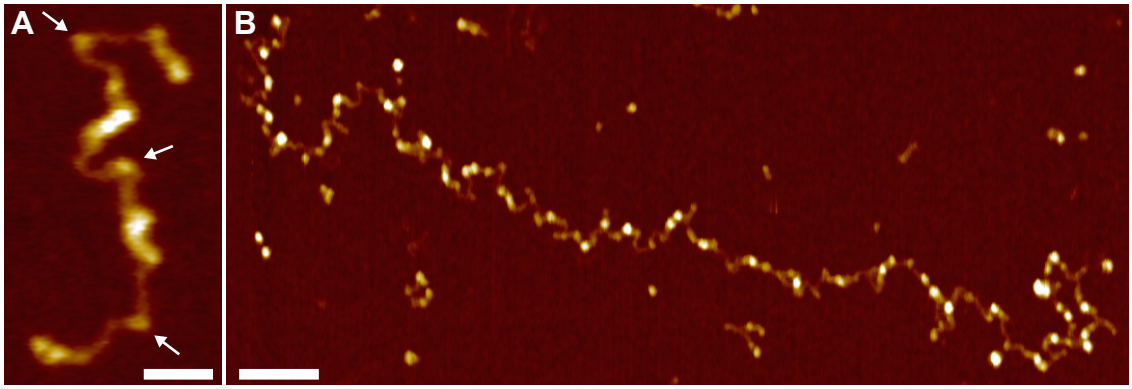


**Figure 4.16:** Conformation of VWF concatemers at pH 7.4 after treatment with EDTA. (A) AFM image of a VWF concatemer consisting of three dimeric subunits, adsorbed from EDTA buffer at pH 7.4. Arrows mark the positions of the CK domains. (Scale bar, 30 nm; range of color scale, 2.4 nm.) (B) AFM image of a stretched VWF concatemer consisting of more than 20 dimers, adsorbed from EDTA buffer at pH 7.4 after fast pipetting of the sample solution onto the mica substrate. (Scale bar, 100 nm; range of color scale, 2.7 nm.)

### 4.1.4 Implications of the strong intermonomer interaction for VWF's force-sensing ability

This section focused on the force response of VWF dimers at pH 7.4 and under near physiological ionic conditions. In AFM single-molecule force experiments a strong intermonomer interaction in dimers was identified. This interaction withstood forces of 50–120 pN at loading rates ranging from 0.1 to 10 nN s$^{-1}$. For each loading rate, the measured forces presumably represent only the lower part of a distribution of forces required for dissociating the strong

intermonomer interaction. This bias is a result of the relatively weak Twin-Strep-tag/Strep-Tactin interaction, which was used for pulling VWF and dissociates at forces that are in a similar range as those of the strong intermonomer interaction. It is therefore likely that the force–loading-rate dependency of the dissociation of the strong intermonomer interaction is characterized by higher mean forces than the ones measured in the presented force experiments.

The strong intermonomer interaction appears to be highly specific, judging from a reproducible length increase after dissociation. Additionally, the strong intermonomer interaction appears to involve divalent ions, as the interaction disappeared upon addition of EDTA. These results are corroborated by observations from AFM imaging, which revealed both compact and flexible conformations of VWF dimers at pH 7.4 in the presence of divalent ions, but only flexible conformations upon addition of EDTA. This finding is in line with a TEM study on VWF at pH 7.4 in the absence of divalent ions, in which some samples were treated with EDTA before TEM imaging [80]. Further evidence for a specific intermonomer interaction comes from experiments on deletion constructs. While deletion of the A3 domain did not significantly change the force response of VWF dimers, the strong intermonomer interaction disappeared upon deletion of the D4 domain. This finding is again supported by AFM imaging, which showed that deletion of D4 promotes a flexible conformation of dimers. A recent TEM study showed that a D4–D4 complex forms at pH 6.2 and promotes stem formation [55]. Based on the presented force and imaging data, it can be expected that a D4–D4 complex can also form under physiological conditions, although direct evidence for such a complex still needs to be obtained.

Force–extension traces of firmly closed dimers are characterized by A2 unfolding peaks at low extension values. Flexible dimers, such as those induced by addition of EDTA, show A2 unfolding peaks at considerably higher extension values. Under near physiological buffer conditions, two populations in the positions of first and second A2 unfolding events were found. A rough estimation based on a double Gaussian fit yielded a ratio of 60 % firmly closed and 40 % flexible dimers. The existence of firmly closed and flexible dimers is corroborated by AFM imaging results, although quantified with roughly inverted ratios (35 % closed, 65 % flexible). The difference in ratios may well originate both from uncertainties of the double Gaussian fit and from the strict criterion of a fully formed stem for assigning dimers as compact. Of additional significance could be the fact that in force experiments the AFM tip – when approaching the sample surface – increases the effective concentration of the two binding partners responsible for the strong intermonomer interaction, resulting in a higher probability to probe a firmly closed dimer. Remarkably, the observed ratios were close to one half firmly closed and one half flexible dimers, both in force and imaging experiments, indicating a difference in Gibbs free energy close to zero between the firmly closed and the open state. Given the fact that the dimer bond is mechanically strong, this implies that the

exchange kinetics between the two states are exceptionally slow, at least along the reaction coordinate probed in the force measurements. For elucidating the underlying structural mechanisms, high-resolution structures of the D4 domain and of the C domains are of outstanding interest. AFM imaging further revealed that dimers within VWF concatemers have a very similar conformation to isolated ones. In particular, flexible and closed dimers were found with very similar ratios. As no clear colocalization of domains between distinct dimers was observed, it was assumed that the force response of VWF can be largely tracked back to its individual dimers.

In blood vessels, forces on VWF concatemers result from their interplay with hydrodynamic flow, in particular with an elongational flow component [9, 10], characterized by a velocity gradient along the direction of flow. It can be expected that VWF subjected to pure elongational flow will align to the stretching axis already at moderate rates. Partially formed stems of dimers not shielded by the strong intermonomer interaction are expected to unzip. At rates that induce peak forces in VWF of 10 to 20 pN, A2 domains of VWF will start to unfold. Indeed, simulations strongly suggest that such forces will be reached for a 5 µm long polymer when subjected to a physiologically relevant elongational flow rate of $1000\,\mathrm{s}^{-1}$ [9]. A2 unfolding is likely to set in at the middle of concatemers, where tensile forces are highest [12], but may propagate rapidly through VWF, favored by the positive feedback between force and concatemer length in hydrodynamic flow. The overall increase of VWF's effective length – i.e., its length contributing to the sensing of hydrodynamic forces – due to unfolding of the A2 domain can be estimated based on the presented force data of dimers. While in the case of a flexible dimer unfolding of the A2 domain almost doubles the distance between the N-termini, the distance is roughly tripled in the case of a firmly closed dimer. This means that the effective length of a concatemer may be increased by a factor of 2 to 3 due to A2 unfolding. Since hydrodynamic peak forces scale with the square of effective length [10, 12], it can be assumed that, after A2 unfolding, VWF will be subjected to peak forces that are up to 9 times higher than the ones that induced initial A2 unfolding. At such high forces, the strong intermonomer interaction in firmly closed dimers can dissociate, whereupon VWF can fully elongate. The additional length increase due to this last elongation step can be estimated to be approximately 20 %, assuming that half of the constituent dimers were initially firmly closed. In general, lower forces than specified above will also trigger the described conformational changes of VWF, yet on longer timescales.

The above considerations suggest that unfolding of A2 domains may trigger the full elongation of VWF. This cooperative behavior may explain the abrupt elongation behavior of VWF under high shear conditions [6]. However, it should be noted that in shear flow, which can be conceptualized as a superposition of an elongational and rotational flow component [11], VWF undergoes a tumbling motion, whereupon individual subunits may relax and refold. While the refolding of the A2 domain has already been studied in detail [12, 58, 59], it will be

of great value to study the dynamics of stem formation in dimers and the reversibility of the strong intermonomer interaction, e.g., with the help of a markedly stronger tag. Interestingly, a recent study has identified two distinct regimes of VWF bundle relaxation [167]. One could speculate that the regime of fast relaxation may be a result of A2 refolding and that the regime of slow relaxation may be associated with the formation of partially or fully formed stems.

Hidden length in firmly closed dimers implies a significantly reduced length of VWF contributing to force sensing. Thus, a higher ratio of firmly closed dimers in a concatemer leads to a decreased initial force response to elongational flow. For example, the force-sensing length of a concatemer comprised half of firmly closed dimers is decreased by approximately 30 % compared to a completely flexible concatemer with the same number of dimers. Subjected to elongational flow, the concatemer with firmly closed dimers will therefore experience only roughly half of the force compared to the fully flexible concatemer. Consequently, elongation of a VWF concatemer with firmly closed dimers will require significantly higher rates of elongational flow than elongation of a fully flexible concatemer with an identical number of dimers. Importantly, small changes of the local environment, mutations, and possibly drugs may drastically affect the ratio of firmly closed dimers, thereby shifting critical rates of elongational flow to activate VWF for hemostasis and thrombosis.

## 4.2 Influence of the pH on VWF's force-induced conformational changes

This section will focus on the influence of the pH on VWF's force-sensing ability. It will be shown that VWF's conformational changes are precisely regulated by the pH, as the strong intermonomer interaction was found in force and imaging experiments to be strongly pH-dependent. Interestingly, the observed pH dependence was found to be opposite to the pH-regulated formation of dimeric bouquets [55], which is believed to favor multimerization and storage of VWF in the *trans*-Golgi and Weibel-Palade bodies. At the end of this section, results from force and imaging experiments will be combined to discuss how force-sensing by VWF can be tuned by the pH.

### 4.2.1 Force response of dimeric VWF under varied pH conditions

For single-molecule force measurements under varied pH conditions, dimeric A1-CK constructs were preferred over full-length constructs (Fig. 4.17A), as they resulted in significantly higher yields of specific pulling events. Increased yields may be a result of improved accessibility of peptide tags when located at the native linker N-terminal of A1 compared to being located directly at the N terminus of D'D3. Measurements were performed under different pH conditions, ranging from pH 6.2 to pH 8.6, yet under equal ionic conditions (150 mM NaCl, 1 mM $CaCl_2$, 1 mM $MgCl_2$, and possibly trace amounts of other ions). Force–extension traces corresponding to specific pulling events were identified as described in subsection 4.1.1, i.e., by making use of two A2 unfolding-peaks as a positive fingerprint. For all probed pH values, traces corresponding to specific pulling events did not exhibit any further characteristic peaks except those of A2 unfolding and – in traces of type I – the high-force peak corresponding to the dissociation of the strong intermonomer interaction in initially firmly closed dimers. Traces of type I exhibited A2 unfolding peaks at low extension values, traces of type II at high extension values (first A2 unfolding peak at roughly 80 and 150 nm, respectively).
While traces of type I were only observed at pH values of 6.8 and above (Fig. 4.17B), traces of type II were observed for all examined pH values (Fig. 4.17C). In other words, at a pH of 6.2 and 6.6 only type II traces were observed (Fig. 4.18), whereas at pH values of 6.8 and above both type I and type II traces were obtained (Fig. 4.19), yet with markedly varied ratios. Accordingly, quantifying the position of the first A2 unfolding peak in force–extension traces yielded unimodal distributions for pH 6.2 and 6.6 (Fig. 4.17D and E), and characteristic bimodal distributions for pH values of 6.8 and above (Fig. 4.17F–J). These distributions revealed that the mean values of the positions of first A2 unfolding were, both for type I and type II traces, conserved throughout the probed pH range within a standard deviation of 5 nm. This observation gives evidence that no domains were significantly destabilized by

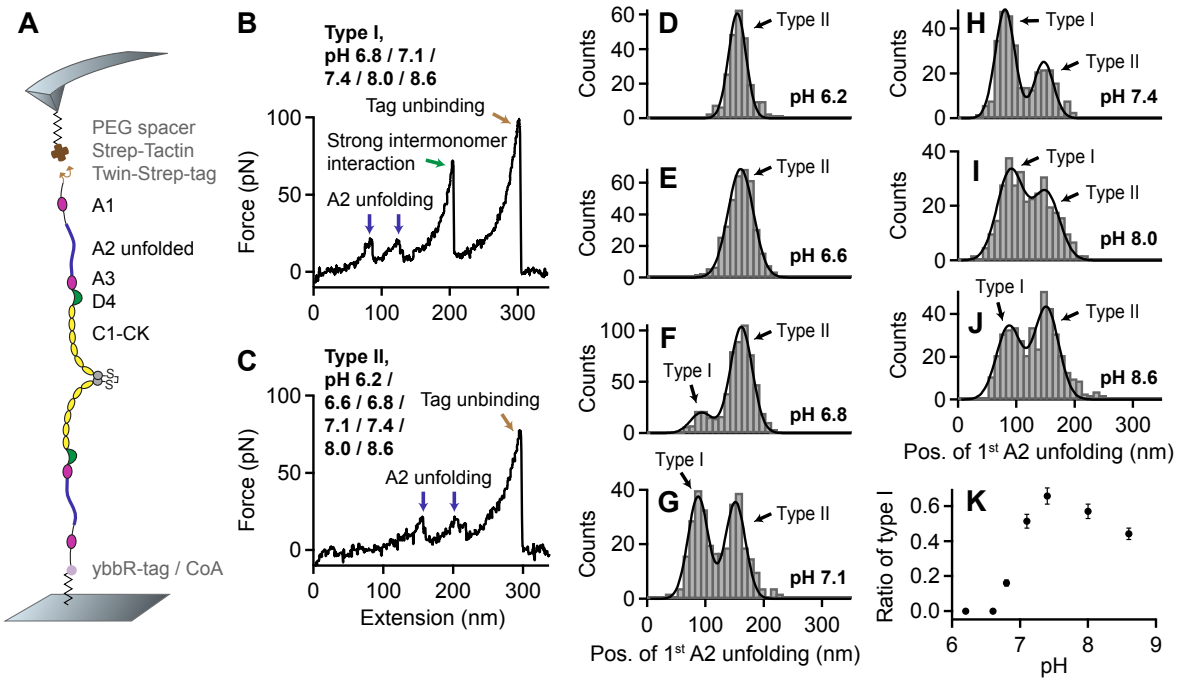


**Figure 4.17:** Single-molecule force measurements on dimeric VWF A1-CK constructs under varied pH conditions. (A) Schematic of pulling dimeric A1-CK constructs (not drawn to scale). Recombinantly expressed heterodimeric constructs carried a ybbR-tag at the N terminus of one of the two constituent monomers, and a Twin-Strep-tag at the N terminus of the other monomer. While the first enabled covalent attachment to a CoA functionalized glass surface, the second allowed for specific pulling via a Strep-Tactin functionalized AFM cantilever. (B–C) Denoised force–extension traces of type I and type II, characterized by A2 unfolding peaks (blue arrows) at low (type I) and at high extension values (type II), respectively. While type II traces were observed throughout the probed pH range, type I traces, showing the force response of dimers that were initially firmly closed via the strong intermonomer interaction, were essentially only obtained at pH values of 6.8 and above. Importantly, at all pH values at which type I traces were observed, dissociation of the strong intermonomer interaction (green arrow) yielded unvaried characteristic length increments. The final peak (brown arrow) corresponds to tag unbinding, i.e., to the dissociation of the specific Twin-Strep-tag/Strep-Tactin interaction and rupture of the probed molecule from the AFM tip [163]. (D–E) Unimodal distributions of the position of the first A2 unfolding peak, obtained for pH 6.2 (D) and 6.6 (E). The distributions are well described by fits of Gaussian functions (solid lines). (F–J) Bimodal distributions of the position of the first A2 unfolding peak, obtained for pH values of 6.8 (F), 7.1 (G), 7.4 (H), 8.0 (I), and 8.6 (J). To estimate the ratio of type I and type II traces, the distributions were fitted with double Gaussian functions (solid lines). (K) Ratio of type I traces as a function of the pH. Error bars represent Poisson noise (1 SD).

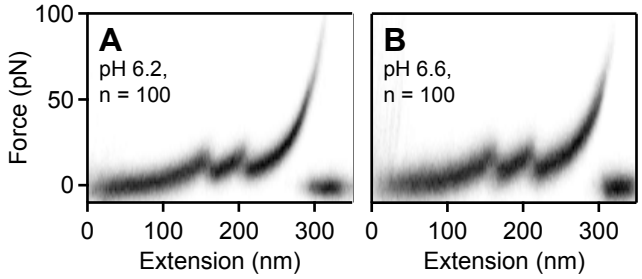


**Figure 4.18:** Overlays of 100 force–extension traces of A1-CK dimers, measured at pH 6.2 (A) and pH 6.6 (B), respectively. The overlays were created based on the raw signal of the underlying traces.

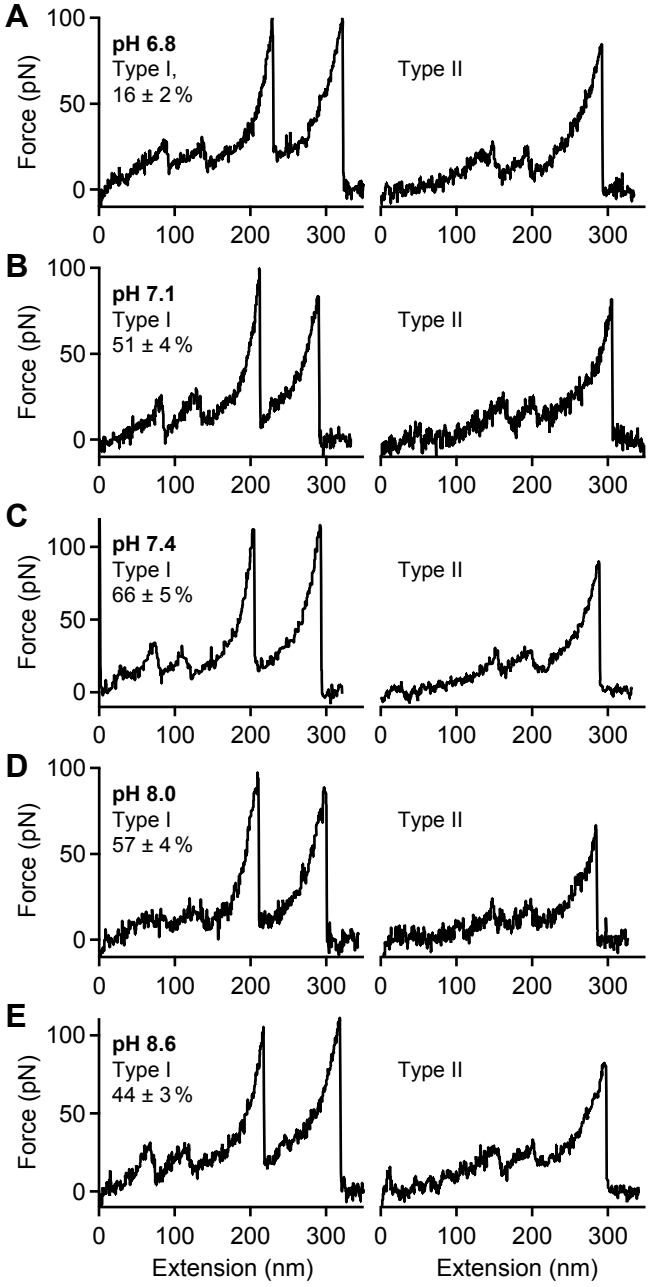


**Figure 4.19:** Denoised force–extension traces of type I and II showing the force response of A1-CK dimers at pH 6.8 (A), 7.1 (B), 7.4 (C), 8.0 (D), and 8.6 (E). While the functional shape of type I and type II traces was conserved within the specified range of the pH, the frequency of both types of traces was significantly affected by the pH (see Fig. 4.17K).

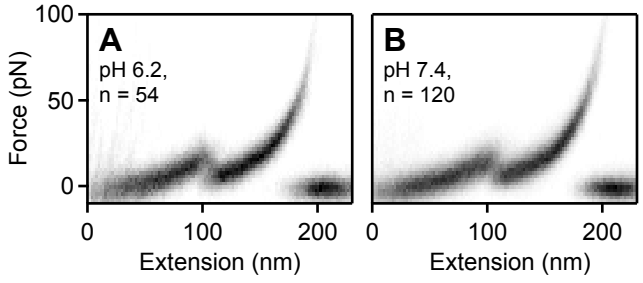


**Figure 4.20:** Overlays of force–extension traces of VWF monomers (D'D3-CK), measured at pH 6.2 (A, $n = 54$) and at pH 7.4 (B, $n = 120$). The overlays were created based on the raw signal of the underlying traces. Importantly, monomer traces were essentially unaffected by the pH.

acidic pH, e.g., due to destabilized disulfide bonds. In line with this, force–extension traces of VWF monomers (D'D3-CK) at pH 6.2 were essentially identical to the ones obtained at pH 7.4 (Fig. 4.20). To estimate the ratios of type I and type II traces for pH 6.8 and above, double Gaussian functions were fitted to the distributions of the first A2 unfolding position. The ratio of type I traces as a function of the pH exhibited an abrupt increase at approximately pH 7.0 and a maximum value of $66 \pm 5\%$ at pH 7.4 (Fig. 4.17K), closely matching the ratio observed for full-length dimers (see subsection 4.1.1). Upon further alkalization, the ratio of type I traces slightly decreased, resulting in a value of $44 \pm 3\%$ at pH 8.6. It should be noted that both at pH 8.0 and 8.6 the yield of specific pulling events, i.e., force–extension traces exhibiting two clear A2 unfolding peaks, was lower than at pH 7.4 and below. Overall, these data show that the formation of the strong intermonomer interaction in VWF's dimeric subunits is critically regulated by the pH.

In order to test for reversibility of the underlying molecular mechanisms, after measurements at pH 6.6 (histogram of first A2 unfolding position shown in Fig. 4.17E and Fig. 4.21A) the buffer of immobilized proteins was exchanged to buffer solution adjusted to pH 7.4. Importantly, force–extension traces of type I were recovered, indicating that the molecular mechanisms underlying the formation of firmly closed dimers are largely reversible. However, the ratio of type I traces was lower ($35 \pm 3\%$) compared to experiments without prior incubation at acidic pH, as inferred from the bimodal distribution of the position of first A2 unfolding (Fig. 4.21B).

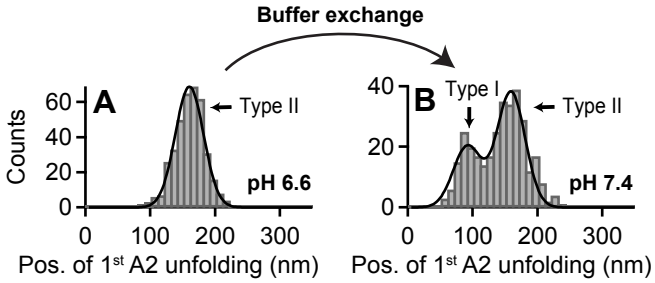


**Figure 4.21:** Reversibility of the molecular mechanisms underlying the pH-dependent formation of the strong intermonomer interaction in VWF's dimeric subunits. (A) Unimodal distribution of the position of the first A2 unfolding peak in force–extension traces of A1-CK dimers measured at pH 6.6 (same histogram as shown in Fig. 4.17, indicating that only type II traces were observed. (B) Histogram of the position of the first A2 unfolding peak, obtained after buffer exchanging immobilized proteins to buffer solution of pH 7.4 and with the same cantilever that was used at pH 6.6. Bimodality of the distribution indicates that a significant number of type I traces was observed, proving that the molecular mechanisms underlying the pH-dependent formation of the strong intermonomer interaction are largely reversible. Fitting a double Gaussian (solid line) yielded a ratio of $35 \pm 3\%$ type I traces.

To gain further insights into the underlying molecular mechanisms, in particular to shed light on the role of histidine residues, force measurements were additionally conducted in the presence of free Imidazole, which naturally competes against the Imidazole side chains of histidines. These measurements were conducted at pH 7.4, where the strong intermonomer

interaction had been observed with highest frequency, and in the presence of 200 mM free Imidazole. Strikingly, essentially only force–extension traces of type II were obtained (Fig. 4.22A and C), backed up by a unimodal distribution of the position of the first A2 unfolding event (Fig. 4.22B). This finding shows that free Imidazole obstructs the formation of the strong intermonomer interaction in dimers, and is in line with flexible dimers observed at pH 7.4 in a recent TEM study, in which free Imidazole had been used for sample purification [55].[1]

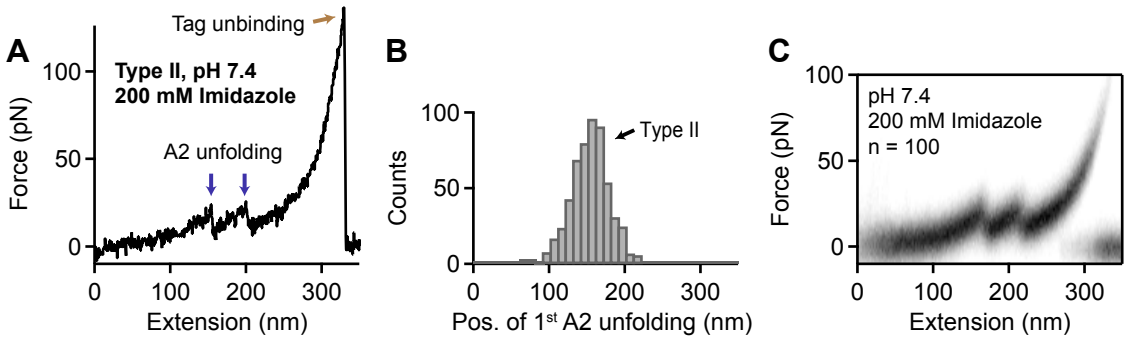


**Figure 4.22:** Obstruction of the strong intermonomer interaction by Imidazole. (A) Denoised force–extension trace of Imidazole-treated A1-CK dimers showing A2 unfolding peaks only at high extension values (type II). The high-force peak characteristic for the dissociation of the strong intermonomer interaction was never observed. (B) Unimodal distribution of the position of the first A2 unfolding peak. (C) Overlay of 100 force–extension traces of Imidazole-treated A1-CK dimers. The overlay was created based on the raw signal of the underlying traces.

### 4.2.2 Conformation of VWF under varied pH conditions

Employing AFM imaging, the conformation of VWF dimers under varied pH conditions was assessed, both in the presence and absence of divalent ions (Fig. 4.23A). It should be noted that for dimers adsorbed from alkaline buffer, a non-negligible fraction of molecules – up to approximately 40% at pH 8.6 – was discarded from analysis, as self-aggregation repeatedly impeded unequivocal tracing. Self-aggregation of dimers at alkaline pH values had also been observed in the framework of a recent TEM study [55].

In the presence of divalent ions (Fig. 4.23B, blue circles), compactness of dimers was in general favored by low pH. However, this general trend, which was also observed for dimers as constituents of concatemers (Fig. 4.24), did not hold true throughout the whole pH range. More precisely, upon increasing the pH from 6.8 to 7.4, compactness of dimers slightly increased. Further alkalization resulted in a gradual decrease of compact dimers, yielding a local maximum of compactness at a pH of 7.4. These observations strongly suggest that at least two different pH-dependent mechanisms regulated the compactness of dimers.

[1] Obstruction of the strong intermonomer interaction by free Imidazole was corroborated by AFM imaging experiments on full-length dimers, performed by Achim Löf in the framework of his PhD work (see Appendix B.1).

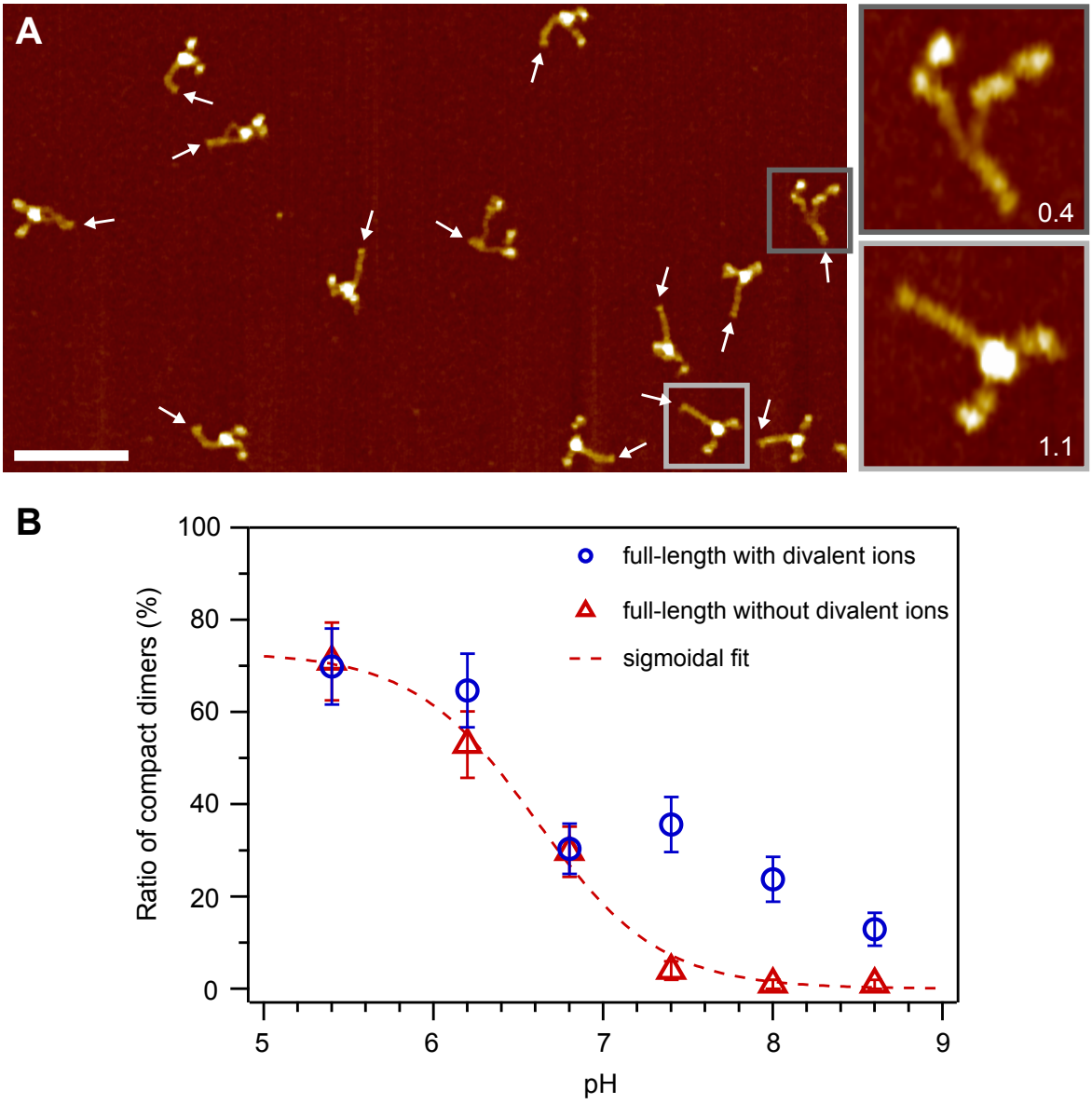


**Figure 4.23:** Compactness of dimeric VWF under varied pH and ionic conditions, assessed by AFM imaging. (A) Representative AFM image of full-length VWF dimers (D'D3-CK), adsorbed onto a functionalized mica surface from buffer solution without divalent ions and adjusted to pH 6.2. Arrows mark positions of CK domains. A large fraction ($> 50\%$) of dimers exhibited a compact conformation with fully formed C-terminal stems. Insets show exemplary cases of a flexible dimer possessing a partially formed stem and a compact dimer with a fully formed stem, respectively. Numbers indicate values of the normalized stem length. (Scale bar, 100 nm; range of color scale, 2.4 nm.) (B) pH titration curves quantifying the compactness of dimeric VWF. Only dimers with a normalized stem length above 1 were assigned as compact. Shown are data of full-length dimers in the presence of divalent ions (blue circles) and in the absence of divalent ions (red triangles), i.e., under conditions that obstruct the formation of the strong intermonomer interaction. The dashed red line is a sigmoidal fit (half-maximum value at pH 6.6) to the data obtained in the absence of divalent ions. Error bars represent Poisson noise (1 SD). For each data point, $n \geq 100$ dimers were analyzed.

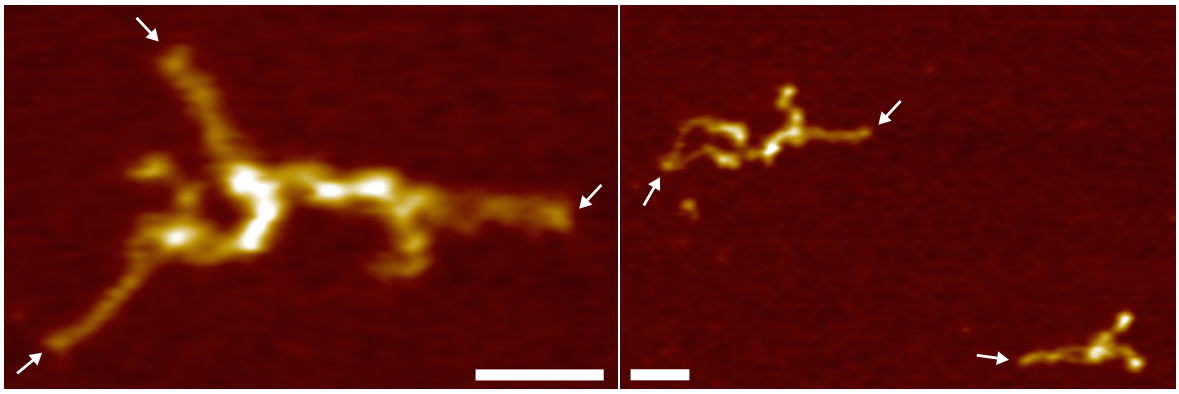

**Figure 4.24:** Conformation of dimers as constituents of concatemers at pH 6.2. Very similarly to isolated dimers, most dimers within concatemers exhibited a compact conformation at pH 6.2. The upper left dimer in the right image shows as an exception an open stem. Arrows mark the positions of the CK domains. (Scale bars, 30 nm; ranges of color scales, 2.4 nm in left image and 2.3 nm in right image.)

In order to dissect the mechanisms that govern the compactness of dimers, a pH titration curve was also measured for dimers after prior treatment with EDTA (Fig. 4.23B, red triangles), thereby obstructing the formation of the strong intermonomer interaction. At pH values of 6.8 and below, the ratios of compact dimers were virtually identical to those obtained for dimers not treated with EDTA (Fig. 4.23A). However, above pH 6.8, dimers were significantly less compact than the ones that had not been treated with EDTA. Importantly, the increase of compactness with decreasing pH exhibited a monotonic behavior in the absence of divalent ions. This behavior was very well described by the fit of a sigmoidal function (dashed line) reaching its half-maximum at a pH of approximately 6.6. The simple sigmoidal behavior suggests compactness to be mainly driven by a single mechanism in the absence of divalent ions.

### 4.2.3 Influence of the pH on VWF's force-sensing ability

In this section, it was shown that the pH regulates the mechanical resistance of VWF's dimeric subunits, as quantified by the ratio of type I force–extension traces, i.e., traces corresponding to the force response of dimers that were initially firmly closed via the strong intermonomer interaction. Interestingly, at low pH values of 6.2 and 6.6, virtually no dimers exhibited the strong intermonomer interaction. At first glance, this finding may appear contradictory to imaging data, which revealed that, almost throughout the whole examined pH range, low pH favors a compact conformation of dimers, thereby confirming a previous TEM study [55]. In fact, combining the results from force and imaging experiments leads to the conclusion that compact dimers below pH 6.8 have a low mechanical resistance (Fig. 4.25, top), and accordingly, that the strong intermonomer interaction in VWF dimers is absent at these low pH

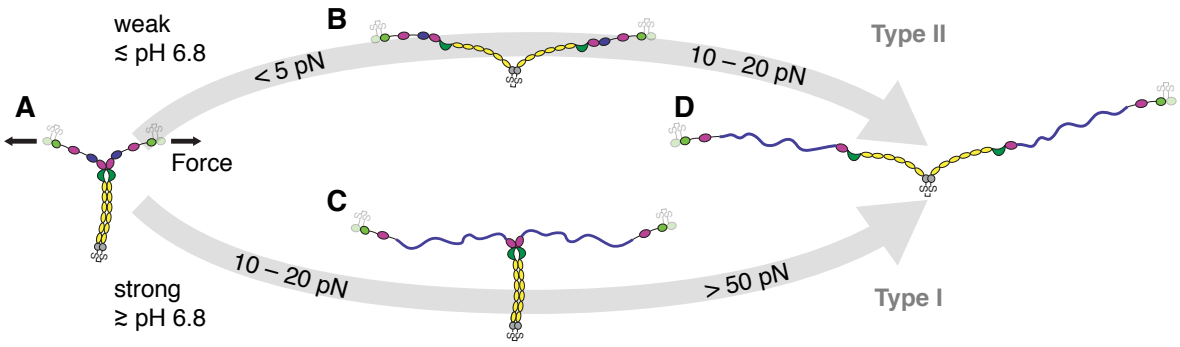


**Figure 4.25:** Strong and weak C-terminal rods in VWF's dimeric subunits. Schematically depicted are force-induced conformational changes (indicated forces correspond to loading rates probed in single-molecule force experiments) of VWF dimers that initially possess a fully formed C-terminal stem (C-terminal rod, A). At pH values below approximately 6.8, C-terminal rods are by trend weak and can dissociate at forces clearly below the detection limit of AFM force experiments, i.e., dissociation occurs very likely well below 5 pN (B). At forces of roughly 10 to 20 pN, VWF's A2 domains unfold and add a contour length of approximately 60 – 70 nm (lengths in schematic are drawn roughly to scale) each to the elongation of dimers [12, 58, 59, 88] (D). At pH values above approximately 6.8 however, C-terminal rods are by trend firmly closed via the strong intermonomer interaction. In this case, unfolding of the A2 domains at 10 to 20 pN is the first critical step of elongation (C). At forces above 50 pN, the strong intermonomer interaction can dissociate and add approximately 80 nm to the elongation of dimers (D). Importantly, forces on VWF result from a positive feedback between elongational flow and length. For a VWF concatemer subjected to elongational flow under acidic pH conditions, forces of for instance 10 to 20 pN – as required for A2 unfolding – will be reached more readily, compared to near physiological conditions, due to rapid initial opening of weak rods.

values. In other words, compactness of dimers under acidic pH conditions is not accomplished by the strong intermonomer interaction, suggesting a second pH-regulated process to promote compactness under acidic pH conditions [55]. Indeed, the pH titration curve quantifying the compactness of dimers in the presence of divalent ions strongly suggests at least two pH-dependent mechanisms promoting compactness. While at pH values below 6.8 compactness decreased with increasing pH, it slightly increased again with pH in a range from 6.8 to 7.4. Clearly, the mechanism that promotes compactness above pH 6.8 is the formation of the strong intermonomer interaction (Fig. 4.25, bottom), as proved by two observations: first, the critical pH of 6.8, above which additional compactness sets in, equals the critical pH of the strong intermonomer interaction observed in force experiments; and secondly, compactness above pH 6.8 can be abolished by taking out divalent ions from solution, in line with a loss of the strong intermonomer interaction observed in force experiments after treating samples with EDTA.

The sigmoidal titration curve of the compactness of dimers in the absence of divalent ions suggests unidirectional pH-dependent interactions promoting an increase of compactness with decreasing pH that do not rely on divalent ions. In fact, AFM imaging data of dimers with a deletion of the D4 domain, measured by Achim Löf in the framework of his PhD work (see Appendix B.1), have revealed a crucial role of the D4 domain for promoting compactness of

dimers under acidic pH conditions, strongly suggesting the existence of a second intermonomer interaction mediated by D4. In contrast to the strong intermonomer interaction, the latter is mechanically less stable. The existence of a second D4-mediated intermonomer interaction in dimers is completely in line with the reported flexibility of dimers at pH 6.2 after cleaving their D4 domains with V8 protease [55, 63]. Overall, it appears plausible that the mechanically weak intermonomer interaction mediated by D4 under acidic conditions possesses an intrinsic pH dependence. Remarkably, the latter is opposite to the pH dependence of the strong intermonomer interaction mediated by the same domain. Both the pH dependence of the weak D4-mediated interaction and of the stem formation may play a pivotal role for orderly multimerization and packing of VWF in the *trans*-Golgi and WPB [55].

A key result of this section is undoubtedly the pH dependence of the strong intermonomer interaction in VWF's dimeric subunits. Strikingly, decreasing the pH from 7.4 by less than one unit switches off the strong intermonomer interaction, thereby drastically decreasing the mechanical resistance of dimers. While the strong intermonomer interaction was virtually not observed at pH 6.6, it could form again after buffer exchange to buffer solution adjusted to pH 7.4. This finding indicates that the molecular mechanisms that underlie the pH dependence of the strong intermonomer interaction are largely reversible. Importantly, the key domain D4 possesses a high density of histidine residues, whose imidazole sidechains can be protonated, resulting in a change of their net charge, around a pH of approximately 6.5 ($pK_a$-value of free histidines [60]). This value is very close to the pH range over which the strong intermonomer interaction was abruptly switched off. A crucial role of histidines was indeed indicated by measurements in the presence of free imidazole – as a competitor against imidazole side chains of histidines – which revealed obstruction of the strong intermonomer interaction. It may be noted that this effect should be taken into account when using Imidazole in protein purification procedures. Given that the strong intermonomer interaction crucially depends on divalent ions, one could speculate that coordination of metal ions by histidine residues may play a fundamental role for the formation of the strong intermonomer interaction. Importantly, full obstruction of the strong intermonomer interaction was not achieved by a simple buffer exchange to buffer without divalent ions, but required addition of EDTA (see section 3.2). This implies that ion species not added to the buffer solutions, for instance ions of transition metals such as Zinc, could also be involved in the formation of the strong intermonomer interaction.

Histidine residues might also play a role for mediating the increase in compactness of dimers under acidic conditions, as suggested by the sigmoidal titration curve obtained in the absence of divalent ions, which reached its half-maximum value at a pH of approximately 6.6, close to the $pK_a$-value of histidines. High-resolution structures, especially of the D4 domain and its constituent modules, will be of great value to elucidate pH dependencies within VWF.

In the vasculature, activation of VWF for hemostasis crucially depends on its ability to sense hydrodynamic forces [6, 8, 10], originating from an interplay of concatemer length and elongational flow components [9–12, 168]. Importantly, force sensing by VWF is tuned by the strong intermonomer interaction in its dimeric subunits, as it markedly shortens the effective length of a concatemer contributing to force sensing. For the pH values probed in the presented experiments, the fraction of firmly closed dimers reached a maximum at a pH of 7.4, indicating that VWF's mechanical resistance is maximized with respect to the physiological pH of 7.4 in the blood. Accordingly, critical rates of elongational flow needed to activate VWF for hemostasis, i.e., to initiate collagen binding and platelet aggregation, will be highest at physiological pH. Certainly, this prediction assumes that the interaction of VWF with collagen and platelets as such remains unvaried by pH.

It is tempting to speculate on the role of this pH-regulation, considering that in the blood the pH may be disturbed locally at sites of vascular injury. Indeed, it is widely accepted that local pH variations, especially acidification, occur in connection with injury and inflammation [96–100], although it remains unclear to what extent and on which timescales the blood pH might be affected. Clearly, the presented data suggest that deviations from physiological pH will lower critical rates of elongational flow to activate VWF for hemostasis. In particular, acidification is expected to very effectively reduce such critical elongational flow rates. Indeed, data obtained from flow experiments and published within the framework of a PhD thesis (Dr. Daniel Steppich, University of Augsburg, Germany) suggest that critical shear rates for VWF's elongation are lowered both upon acidification and alkalization [169]. In principle, the relative impact of pH on critical elongational flow rates can be estimated based on the ratio of firmly closed dimers in VWF observed at a given pH. For instance, at a pH of 6.6, where virtually no dimers exhibit the strong intermonomer interaction, the critical elongational flow may only be roughly half compared to the one at pH 7.4. In the latter case VWF's effective force-sensing length is expected to be decreased by approximately 30%, assuming approximately half of VWF's dimeric subunits to be firmly closed via the strong intermonomer interaction. It should be noted that under acidic conditions, VWF's force-sensing length will initially be lower than under physiological conditions, due to compact yet mechanically relatively unstable dimers. However, as strongly suggested by the presented force data, most compact dimers below pH 6.8 will open up at comparably very low elongational flow rates and consequently increase VWF's effective force-sensing length very rapidly, thereby triggering further elongation, due to the positive feedback between hydrodynamic force and length. Succinctly put, one could speculate that VWF's pH-dependent elongation behavior represents a smart mechanism to enhance VWF's hemostatic activity where needed.

## 4.3 VWF multimer analysis

As discussed within section 4.1, activation of VWF for hemostasis crucially depends on VWF's multimer size, as hydrodynamic forces scale with the square of VWF's effective force-sensing length. The importance of concatemer length is underlined by mutations that impair VWF's multimerization, as in patients with von Willebrand disease (VWD) type 2A [10, 21, 101]. In the framework of this thesis, the size distribution of recombinant VWF was assessed by AFM imaging and TIRF microscopy. This section will present results obtained from both approaches and discuss both approaches with respect to limitations and benefits.

### 4.3.1 VWF multimer analysis by AFM imaging

From AFM images of surface-adsorbed VWF, the multimer size of a VWF molecule can be determined by directly counting dimeric subunits (Fig. 4.26A), facilitated by characteristic heights both of N-terminal head groups and C-terminal CK domains [37], and characteristic distances between the latter [56].

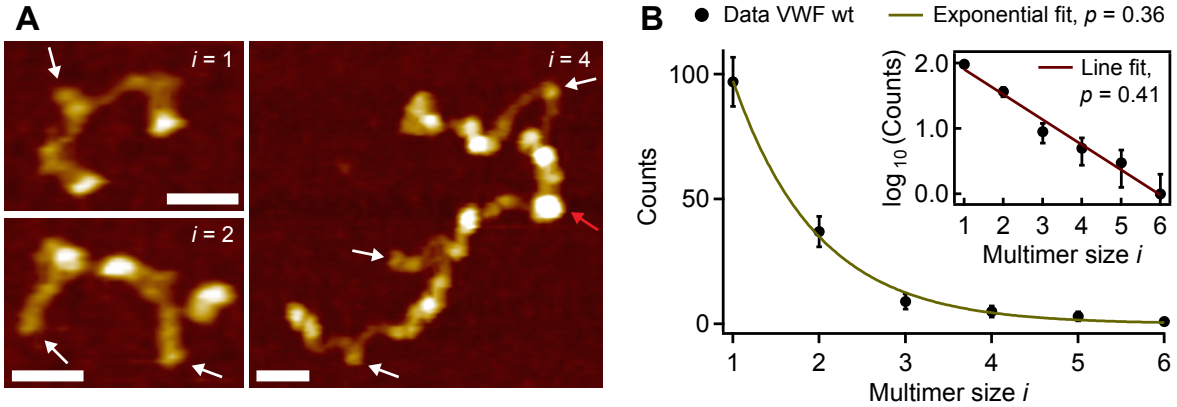


**Figure 4.26:** VWF multimer analysis by AFM imaging. (A) AFM images of individual VWF molecules of multimer sizes $i = 1$, $i = 2$, and presumably $i = 4$. While the molecule with four dimeric subunits was chosen from a wildtype sample treated with EDTA, the molecules with one and two dimeric subunits, respectively, were chosen from a sample of mutated VWF (2561Y). The latter exhibited – similar to VWF wildtype – fully closed and flexible dimers. White arrows indicate positions of CK domains. The red arrow in the image on the right indicates the presumed position of a CK domain that might be covered by either portions of N-terminal head groups or dirt. (Scale bars, 30 nm; range of color scale, 2.6 nm in images on the left and 3.0 nm in image on the right.) (B) Size distribution of VWF wildtype (wt), inferred from AFM images of $2 \times 2\,\mu m^2$. Fitting the exponential distribution given in Eq. 4.1 yielded an extent of polymerization of $p = 0.36$. The inset shows the logarithmic values of the individual counts. From the slope of a line fit, the extent of polymerization was estimated to be $p = 0.41$. Error bars are Poisson noise and were not included in fitting procedures.

Following the approach of direct counting, a distribution of the multimer size was obtained for a sample of recombinant VWF wildtype (Fig. 4.26B). The size distribution was well-described

by an exponential function of the form

$$N_i = N \cdot (1-p) \cdot p^{i-1}\,, \tag{4.1}$$

which was used in reference [101] to initially estimate the extent of polymerization $p$ for diverse VWF samples. In Eq. 4.1, $N_i$ denotes the number of counts for a given multimer size $i$ and $N$ the total number of counts. In this context, the multimer size is defined with respect to dimeric subunits, such that $i = 1$ refers to dimers, $i = 2$ to tetramers, and so on. Applying Eq. 4.1 to the measured data yielded $p = 0.36$ when fitted to the number of counts in linear representation (Fig. 4.26B) and $p = 0.41$ when fitted as a line to the logarithm of the number of counts (Fig. 4.26B, inset). The minor mismatch between the obtained $p$ values is a result of the least-square method used for fitting, which naturally places more weight on the large number of counts for small multimer sizes when represented linearly. The obtained values of $p = 0.36$ and $p = 0.41$ are smaller than the value of $p = 0.70$ inferred from quantitative gel analysis [101]. Importantly, in the latter study, the $p$ value was inferred from fitting Eq. 4.1 for multimer sizes ranging from zero to 14 (Fig. 2E in reference [101]) and not only from zero to 6, as done for AFM imaging data. In fact, fitting the gel data (Fig. 2E in reference [101]) within a range from zero to $i = 6$ would yield smaller p values, as data points in that range slightly deviated from an ideal exponential decay towards a higher number of counts.

Clearly, a drawback of using AFM imaging instead of quantitative gel analysis for analyzing VWF's multimer size is its limitation to rather small multimer sizes, which is a matter of two different aspects. The first is of rather practical nature and arises from the exponentially decaying size distribution of VWF wildtype, which limits the throughput at high multimer sizes. For instance, in a $2\,\mathrm{x}\,2\,\mu\mathrm{m}^2$ AFM image, typically $\sim 20$ VWF molecules were found. Therefore, the number of VWF molecules assessed in a total of ten AFM images was limited to roughly 200. Within this statistical framework, due to the exponential decay of VWF's size distribution, molecules above $i = 5$ were only rarely observed (Fig. 4.26B).
The second aspect arises from the fact that identification of dimeric subunits becomes increasingly complicated for an increasing multimer size (Fig. 4.27). In principle, the size distribution of surface-adsorbed molecules could also be estimated based on a – potentially automated – volume analysis, which would ideally correct for the geometry and size of the used AFM tip [104]. However, importantly, in some cases it remains even unclear how many distinct molecules are observed (Fig. 4.27).
Identification of dimeric subunits and assessment of the number of molecules observed is further limited by impurities in the sample (Fig. 4.26A), which cannot be lost by centrifuge filtration only. As discussed within subsection 3.3.2, a more specific purification of VWF via an antiVWF antibody, involving harsh elution with Thiocyanate, was found to induce aggregation of VWF's N-terminal domains. As aggregation may also occur within different

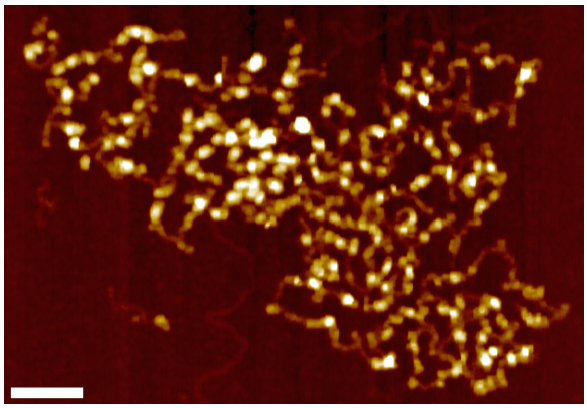

**Figure 4.27:** Limitations of multimer analysis by AFM imaging in the case of large VWF. AFM image of one or several large VWF molecules. While several dimeric subunits can be clearly identified, other dimeric subunits appear to overlap and cannot be identified. Although it is impossible to directly count the total number of dimeric subunits in the image, the latter could in principle be estimated based on a volume analysis. However, it remains overall also unclear how many distinct molecules are observed. (Scale bar, 50 nm; range of color scale, 3.2 nm.)

molecules, such purification is not suited for multimer analysis of VWF by AFM imaging.
Another drawback of – low-speed – AFM imaging in air is that it cannot measure real-time kinetics changing the size distribution of VWF over time. The latter can be assessed for instance based on fluorescence correlation spectroscopy [101], which, in combination with a microfluidic shear cell, can monitor shear-induced degradation of VWF by ADAMTS13 [170].
An important key advantage of AFM imaging for multimer analysis of VWF, however, lies in the possibility to visualize individual VWF molecules. More precisely, not only dimeric subunits of VWF, but also monomers and their arrangement within concatemers can be resolved. This capability is irreplaceable for screening VWF samples whose size distribution is affected by an impaired dimerization of monomers, as induced for instance by mutations C2771R, C2773R, or C2811A [21, 37]. For such mutations, the concept of a single $p$ parameter measuring the extent of VWF's polymerization can be potentially extended to a second parameter that quantifies the degree of dimerization. In fact, for the abovementioned mutations, AFM imaging can provide information that – when performing gel analysis – remains hidden in gel bands of dimers ($i = 1$), tetramers ($i = 2$), and so on. For example, dimers may consist of either N-terminally linked or C-terminally linked monomers, and tetramers may consist of either two N-terminally linked native dimers or of a central native dimer with two flanking N-terminally linked monomers. In other words, it can for instance be analyzed, if – for the abovementioned mutants – N-terminal linkage of a monomer to a native dimer is equally probable as N-terminal linkage of a native dimer to a native dimer. Therefore, AFM imaging not only sheds light on the size distribution of disease-related mutants, but can potentially also provide unique information on VWF's biosynthesis.
Finally, AFM imaging can be performed after adsorbing VWF molecules from buffer solution adjusted to pH 6.2 and high calcium concentrations [54], thus mimicking pH and ionic conditions in the *trans*-Golgi network and Weibel-Palade bodies. For instance, hypothetical mutations may affect VWF's pH-dependent conformational changes and thereby VWF's multimerization and the resulting size-distribution. Using AFM imaging, the impact of such mutations on VWF's size distribution can in principle be comprehended.

### 4.3.2 VWF multimer analysis by TIRF microscopy-based photobleaching

Another single-molecule approach that was used within the framework of this thesis to estimate the size distribution of VWF was based on TIRF microscopy photobleaching. To this end, VWF was genetically engineered with an eGFP molecule attached to the C terminus of each monomer (VWF-eGFP, Fig. 4.28) [101].

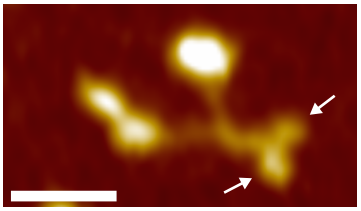

**Figure 4.28:** AFM image of an eGFP-tagged VWF dimer. As these constructs were genetically engineered, every constituent monomer carried exactly one C-terminal eGFP molecule. Arrows indicate positions of eGFP molecules. (Scale bar, 30 nm; range of color scale, 2.4 nm.)

Under continuous excitation, the fluorescence signal of VWF-eGFP was observed to decrease in discrete steps over time (Fig. 4.29A and B). As described in references [157–159], the number of bleaching steps can be taken as a measure to assess the number of eGFP-tagged monomers in a VWF molecule. Counting bleaching steps therefore provides a means to estimate the size distribution of VWF. The frequency for detecting a certain number of photobleaching steps was plotted versus the number of steps (Fig. 4.29C). While for VWF dimers, traces exhibited either 1 or 2 steps, up to 9 steps were observed for VWF multimers. As the multimer size is counted in the number of dimers $i$, while bleaching steps scale with the number of monomers, two bleaching steps add up to an increase of one in the multimer size. Odd numbers of bleaching steps were rounded up to the next even number to estimate the multimer size $i$. The number of counts obtained for a multimer size was plotted versus the multimer size $i$ (Fig. 4.29D). Fitting the exponential function of Eq. 4.1 yielded an extent of polymerization of $p = 0.29$. A very similar value of $p = 0.30$ was obtained when fitting a line to the logarithmic values of the counted numbers (Fig. 4.29D, inset). These values are in good agreement with the ones inferred from AFM imaging ($p = 0.36$ and $p = 0.41$, respectively; see subsection 4.3.1).

Evidently, multimer analysis by TIRF microscopy-based photobleaching is severely limited to small multimer sizes (e.g. $i < 5$), as an unambiguous detection of discrete steps becomes increasingly challenging for an increasing number of subunits [157]. In the case of eGFP-tagged VWF, identification of steps became very complicated for step numbers above $\sim 4$, corresponding to a multimer size of $i > 2$. In fact, more than 8 steps ($i > 4$) were practically not observed, which may – from another point of view – of course also result from VWF's exponential size distribution and the statistical framework of this single-molecule approach. In principle, for large multimer sizes, estimates for the number of dimeric subunits can be made based on the total starting fluorescence and the average size of a single bleaching step [157]. However, it should be noted that in the case of the presented experiments, eGFP-tagged

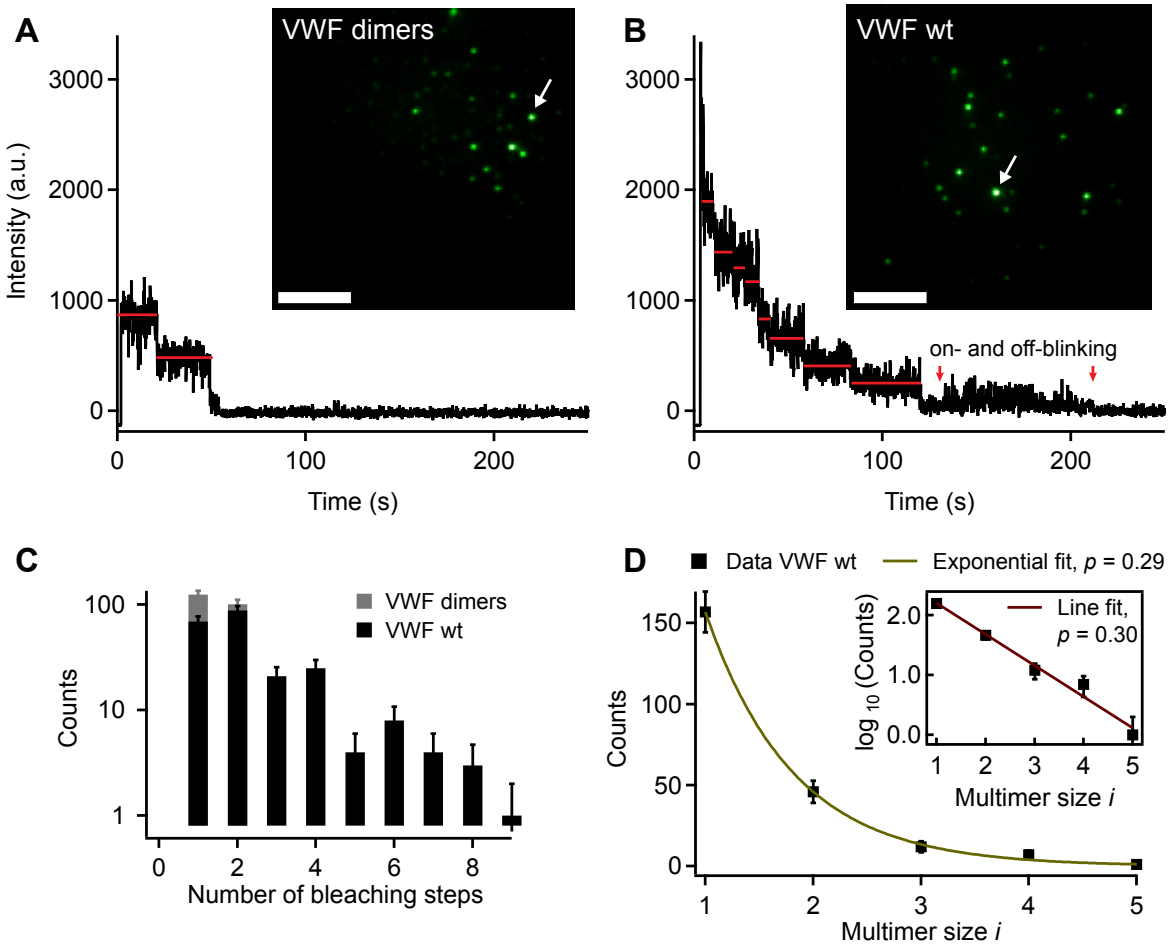


**Figure 4.29:** VWF multimer analysis by TIRF microscopy-based photobleaching. (A–B) Intensity–time traces of an eGFP-tagged VWF dimer and multimer, respectively. The red lines mark the intensity–time segments that were assigned as constant. Insets show TIRF microscopy images (average of the first 100 frames) of surface immobilized eGFP-tagged VWF dimers and multimers, respectively. Arrows point to the locations from which the shown intensity–time traces were taken. (Scale bars, 5 µm; equal ranges of color scales) (C) Frequency for detecting a certain number of steps in intensity–time traces of dimers (grey sticks) and multimers (black sticks). (D) Size distribution of VWF wildtype (wt) inferred from the number of bleaching steps. Fitting the exponential distribution given in Eq. 4.1 yielded an extent of polymerization of $p = 0.29$. The inset shows the logarithmic values of the individual counts. From the slope of a line fit, the extent of polymerization was estimated to be $p = 0.30$. Error bars are Poisson noise and were not included in fitting procedures.

VWF was immobilized via free amino groups on an epoxysilane coated glass slide. Binding of eGFP molecules to the surface can be expected to restrict the rotational degrees of freedom of eGFP, which influences the effective excitation and thus the intensity of the light emitted by the fluorophore [171]. Therefore, steps in the shown intensity traces may exhibit heights with significant variations (Fig. 4.29A and B), which complicate a quantitative analysis of large VWF multimers based on an initial starting intensity.

To avoid the problems described above, i.e., a strong restriction of the rotational degrees of freedom of eGFP molecules, specific attachment chemistry could help. For instance, VWF could be engineered with an N-terminal ybbR tag in addition to C-terminal eGFP, thereby enabling covalent and site-specific attachment. It appears plausible that, when attaching such ybbR-labeled VWF via the N termini of consituent monomers to a CoA coated surface, C-terminal eGFP molecules would remain more flexible. Owing to the length of a VWF monomer, C-terminal eGFP molecules would be still within $\sim 60\,\mathrm{nm}$ above the surface, and hence well within the evanescent field.

Another complication that arises when using eGFP as a fluorophore is blinking [159], i.e., on-off transitions in fluorescence (Fig. 4.29B). Therefore, when using an automated step detection algorithm, the total number of counted steps has to be corrected for blinking events [101, 160].

An advantage of using genetically engineered VWF-eGFP, however, is that this approach ensures that every tagged subunit carries exactly one fluorophore. Non-specific labeling that may occur when using dyes that require an additional labeling reaction is therefore not an issue. Inconventiently, however, it is well-known that not not 100% of all eGFP molecules are fluorescent. A prior study reported a value of $\sim 20\%$ non-fluorescent eGFP molecules in distinct fusion proteins [157], which of course contribute to odd numbers in detected bleaching steps. Indeed, a value of 80% fluorescent eGFP molecules is in agreement with the observation that the frequencies for 1 or 2 bleaching steps, respectively, were roughly equal in dimer samples.

Doubtlessly, multimer analysis of VWF by TIRF microscopy photobleaching is limited by several important aspects, especially with respect to the analysis of multimer sizes above $\sim 5$. Still, this method allows for distinguising samples of dimers and multimers, and presumably also samples of monomers, although only with respect to entire samples and not to individual molecules. For instance, bleaching steps may be missed or eGFP molecules may not fluoresce at all. Importantly, TIRF microscopy-based photobleaching proved useful to confirm the high amount of dimers in multimer samples, a result of VWF's exponential size distribution.

# 5 Conclusion and outlook

In this thesis, VWF's conformation and force response were investigated at the single-molecule level to quantitatively understand important force-sensing mechanisms of VWF in the bloodstream. Of special interest were large-scale force-induced conformational changes of VWF, as they can be assumed to decisively influence the interplay between VWF and hydrodynamic flow. This interplay crucially determines how critical domains in VWF are loaded with force, and hence regulates VWF's activation for hemostasis and its down-regulation by the enzyme ADAMTS13.

The key finding of this thesis is probably the existence of a strong intermonomer interaction in VWF's dimeric subunits. This interaction crucially involves the D4 domain of the protein, and its occurrence critically depends both on divalent ions and the pH. Under near-physiological buffer conditions, the strong intermonomer interaction was estimated to be present in approximately half of VWF's dimeric subunits. Its dissociation occurred at forces above $\sim 50\,\mathrm{pN}$, i.e., after unfolding of the less stable A2 domain [12, 58, 59, 88, 89], and provided $\sim 80\,\mathrm{nm}$ flexible length to VWF, corresponding to previously hidden length in C-terminal stems. Importantly, hidden length in firmly closed dimers implies a reduced length of VWF contributing to force sensing. Therefore, elongation of a VWF concatemer with firmly closed dimers can be expected to require higher rates of elongational flow than elongation of a fully flexible concatemer with the same number of dimers.
In principle, the impact of firmly closed dimers on VWF's behavior in hydrodynamic flow could be underlined by computer simulations [6, 33, 92, 172], in which dimers as constituents of larger concatemers could be modeled by four linearly connected beads. While A2 unfolding could be taken into account by interactions between the first and the second as well as the third and the fourth bead, firmly closed dimers could be incorporated by adjusting the interaction between the second and the third bead. Importantly, simulations could provide insights into the behavior of VWF in shear flow. However, as shear flow can be expected to cause tumbling of VWF, and thus relaxation of individual subunits, information on the (force-dependent) formation of the strong intermonomer interaction would be of outstanding interest. To experimentally study the formation of C-terminal stems and the formation of the strong intermonomer interaction, both the use of a stronger tag and of a technique capable of resolving lower forces than AFM – e.g., magnetic tweezers – would be advantageous [30].

Experimentally, the impact of firmly closed dimers on VWF's force-sensing ability could be confirmed in flow experiments with fluorescently labeled VWF [6]. For instance, the critical elongational flow rates, and presumably also the critical shear rates, needed to elongate and activate VWF can be assumed to be significantly lowered upon addition of EDTA, which was observed to obstruct the formation of the strong intermonomer interaction. A similar effect can be expected when lowering the pH, as the strong intermonomer interaction was observed with highest frequency at the physiological pH of 7.4, whereas it was essentially absent at pH values below 6.8. Evidently, this finding suggests highest mechanical resistance of VWF at physiological pH and a lowered mechanical resistance in the case of acidification. It is tempting to speculate that this effect may enhance VWF's hemostatic activity at sites where the pH locally deviates from the physiological value. In fact, it is widely accepted that the pH may vary locally in the cases of inflammation, ischemia, and other pathological conditions. However, it is unclear if such local pH changes generally occur in the wake of injuries. In particular, it remains to be investigated to what extent and on which timescales such pH variations in the blood can locally take place.

Besides possible physiological implications, the presented results represent an indispensable step towards a full understanding of the mechanisms that crucially underlie VWF's mechanics and structure. For instance, insights were gained into the nature of fully formed C-terminal stems in dimers under acidic pH conditions, i.e., at pH values below 6.8, as they had previously been observed in a TEM study [55]. Strikingly, the mechanical resistance of such stems under acidic pH conditions is low compared to stems that are closed via the strong intermonomer interaction at near-physiological pH. Moreover, the formation of fully formed stems under acidic pH conditions does not rely on divalent ions, in contrast to their formation via the strong intermonomer interaction at near-physiological pH. To gain structural insights into the underlying mechanisms, a high-resolution structure of the D4 domain – or maybe already of one or more of its constituent submodules [61] – would be of great value. While it remains unclear what submodules of D4 are responsible for the strong intermonomer interaction, it appears plausible that histidine residues, which change their net charge at a pH around 6.5 [60] and are abundant in all submodules of the D4 domain, are involved. Given that the strong intermonomer interaction critically depends on divalent ions, it may be speculated that coordination of transition metal ions involving histidine residues plays a fundamental role for the formation of the strong intermonomer interaction. Indeed, the strong intermonomer interaction was obstructed by treatment with Imidazole, which has virtually no affinity towards magnesium and calcium ions, but is capable of strong coordination bond formation with metal ions [110]. In any case, due to its effect on VWF's structure and mechanics, Imidazole should be used carefully in purification of VWF, and especially of VWF's D4 domain.

Further studies of this thesis helped reveal an exponentially decaying size distribution of recombinant VWF, as had been previously inferred by Dr. Svenja Lippok and Prof. Dr. Joachim Rädler from a quantitative analysis of gel data and FCS data [101]. TIRF microscopy photobleaching experiments, which were performed in a joint collaboration with Prof. Dr. Joachim Rädler, particularly confirmed the high fraction of dimers in multimer samples. An exponential size distribution of VWF was further corroborated by results from AFM imaging experiments, which were carried out some time later. Compared to the method of TIRF microscopy photobleaching, AFM imaging bears diverse advantages for VWF multimer analysis, among which the most important one probably lies in the possibility to visualize individual VWF molecules and resolve constituent dimers and monomers.
The benefits of AFM imaging should be used in the future to analyze mutations that impair dimerization of VWF. For instance, for the mutations C2771R and C2773R, the extent of dimerization abolishment could be quantified, respectively, thereby complementing a previous study, which involved both experimental and computational approaches [21]. Morevoer, from the distribution of molecules, it could be inferred if during multimerization in the Golgi a monomeric building block is equally probable to be linked N-terminally to an existing VWF molecule as a dimeric building block, thus elucidating the essential process of multimerization. In fact, such a quantitative analysis is not possible based on gel data, as different types of molecules may be hidden in the same band of a gel. For instance, a tetramer may consist of either two N-terminally linked native dimers or of a central native dimer with two flanking N-terminally linked monomers.
Furthermore, AFM imaging could potentially elucidate the role of the cystein residue 2811, which was hypothesized to act as a protective cover in addition to the structurally essential disulfide bonds between residues 2771 and 2773 [37]. For example, the mutation C2811A was shown to also yield monomers, trimers, etc., which were predicted to result from partial reopening of the disulfide bonds between C2771 and C2773 [37]. If reopening occurs after multimerization, the distribution of molecules should be markedly different from the one that would be obtained in the case reopening occurred prior to multimerization. Importantly, from AFM imaging data, also the probability of reopening could be quantified, thereby verifying the structural mechanisms that were predicted to underlie VWF's dimerization [21, 37, 64].

Taken together, VWF was comprehensively characterized with respect to its conformation and its force response. Besides information on VWF's size distribution, a quantitative understanding of important force-sensing mechanisms of VWF was gained. Special emphasis was placed on the role of a strong intermonomer interaction in VWF's dimeric subunits, which was found to be strongly pH-dependent. Based on the presented data, it can be expected that VWF's force-induced elongation – and therefore possibly also its activation – requires lower rates of elongational flow at sites where the pH locally deviates from the physiological value of 7.4. These considerations may be stimulating not to take for granted a purely force-induced

initiation of hemostatic plug formation, but also to take into account possible influences of environmental parameters, such as the pH. Hopefully, this work will motivate researchers, both experimental and computational, to take further steps, e.g., by elucidating underlying structural mechanisms, and to thereby contribute to a more complete understanding of VWF's function in hemostasis and its dysfunction in clotting disorders and thrombosis.

# A Publications

## A.1 Publication 1: Force sensing by the vascular protein von Willebrand factor is tuned by a strong intermonomer interaction

# Force sensing by the vascular protein von Willebrand factor is tuned by a strong intermonomer interaction

by

Jochen P. Müller, Salomé Mielke, Achim Löf, Tobias Obser, Christof Beer, Linda K. Bruetzel, Diana A. Pippig, Willem Vanderlinden, Jan Lipfert, Reinhard Schneppenheim, and Martin Benoit

published in

Proceedings of the National Academy of Sciences of the United States of America (PNAS), Vol. 113, No. 5, 1208–1213, 2016

PNAS

# Force sensing by the vascular protein von Willebrand factor is tuned by a strong intermonomer interaction

Jochen P. Müller[a,1], Salomé Mielke[a], Achim Löf[a], Tobias Obser[b], Christof Beer[a], Linda K. Bruetzel[a], Diana A. Pippig[a], Willem Vanderlinden[a,c], Jan Lipfert[a], Reinhard Schneppenheim[b], and Martin Benoit[a]

[a]Department of Physics and Center for Nanoscience, Ludwig Maximilian University of Munich, 80799 Munich, Germany; [b]Department of Pediatric Hematology and Oncology, University Medical Center Hamburg-Eppendorf, 20246 Hamburg, Germany; and [c]Department of Chemistry, Division of Molecular Imaging and Photonics, KU Leuven–University of Leuven, 3001 Leuven, Belgium

Edited by James A. Spudich, Stanford University School of Medicine, Stanford, CA, and approved December 2, 2015 (received for review August 14, 2015)

**The large plasma glycoprotein von Willebrand factor (VWF) senses hydrodynamic forces in the bloodstream and responds to elevated forces with abrupt elongation, thereby increasing its adhesiveness to platelets and collagen. Remarkably, forces on VWF are elevated at sites of vascular injury, where VWF's hemostatic potential is important to mediate platelet aggregation and to recruit platelets to the subendothelial layer. Adversely, elevated forces in stenosed vessels lead to an increased risk of VWF-mediated thrombosis. To dissect the remarkable force-sensing ability of VWF, we have performed atomic force microscopy (AFM)-based single-molecule force measurements on dimers, the smallest repeating subunits of VWF multimers. We have identified a strong intermonomer interaction that involves the D4 domain and critically depends on the presence of divalent ions, consistent with results from small-angle X-ray scattering (SAXS). Dissociation of this strong interaction occurred at forces above ∼50 pN and provided ∼80 nm of additional length to the elongation of dimers. Corroborated by the static conformation of VWF, visualized by AFM imaging, we estimate that in VWF multimers approximately one-half of the constituent dimers are firmly closed via the strong intermonomer interaction. As firmly closed dimers markedly shorten VWF's effective length contributing to force sensing, they can be expected to tune VWF's sensitivity to hydrodynamic flow in the blood and to thereby significantly affect VWF's function in hemostasis and thrombosis.**

hemostasis | molecular force sensors | protein mechanics | single-molecule force spectroscopy | atomic force microscopy

Force-sensing molecules are critically involved in a variety of biological processes, such as regulation of muscle gene expression or assembly of the cytoskeleton (1–4). In the vasculature, activation of the plasma glycoprotein von Willebrand factor (VWF) for hemostasis crucially depends on its distinct ability to sense hydrodynamic forces (5–7). These forces result from the interplay between hydrodynamic flow and VWF's extraordinary length (8–10), which can exceed 15 μm in the plasma (6). VWF's length arises from its linear multimeric nature. Linear multimers (concatamers) are composed of a variable number of dimers, which are linked N-terminally via disulfide bonds. Dimers, the smallest repeating subunits of VWF with a molecular mass of ∼500 kDa, consist of two monomers that are linked via C-terminal disulfide bonds (11, 12).

Under static conditions, VWF was reported to adopt a collapsed conformation (6). When subjected to sufficiently high forces, as for instance at sites of vascular injury, vasoconstriction, or stenosis, VWF undergoes an abrupt transition from the collapsed to a stretched conformation (Fig. 1*A*) (6). This transition was shown to correlate with an increased adhesiveness to collagen and platelets (6, 13), enabling stretched VWF to recruit platelets to an injured vessel wall and to promote the formation of a platelet plug. VWF's physiological importance is underlined by mutations that can cause von Willebrand disease (14), the most common hereditary bleeding disorder.

Down-regulation of VWF's hemostatic potential is achieved by the cleavage of long concatamers into shorter ones by the enzyme ADAMTS13 (a disintegrin and metalloprotease with a thrombospondin type 1 motif, member 13) (15). Notably, the specific cleavage site is buried in the A2 domain and exposed by A2 unfolding (8, 16). The interplay of force-induced A2 unfolding and enzymatic cleavage has been investigated in detail at single-molecule level (8). In this context, unfolding of an isolated A2 domain was shown to occur at forces of ∼ 7–14 pN at loading rates ranging from 0.35 to 350 pN·s$^{-1}$. In the presence of neighboring A1 and A3 domains, A2 unfolding was observed at slightly higher forces of ∼ 20 pN and comparable loading rates (17).

VWF's activation for hemostasis correlates with its elongation above a critical force threshold (6, 7). However, the current understanding of the underlying molecular mechanisms is limited. Clearly, A2 unfolding is likely to contribute significantly to the elongation of VWF, as the induced length increment of roughly 45 nm (at 20 pN) is almost as large as the end-to-end length of a static monomer (8, 17–19). Stabilization of all other domains in VWF through disulfide bonds was predicted (20), but lacks experimental evidence.

Besides domain unfolding, separation of potential intramonomer and intermonomer interactions may play a crucial role for VWF's elongation. For example, interactions between monomers may tune VWF's force-sensing ability by promoting compactness, as suggested by various computational studies (6, 21, 22). Experimentally, self-association of VWF molecules was reported, but has not been assigned to individual domains (23, 24).

## Significance

**Excessive blood loss at a site of vascular injury is prevented by recruitment of platelets to the injured vessel wall and the formation of a platelet plug. Under elevated shear flow conditions, these processes are critically mediated by the large plasma glycoprotein von Willebrand factor (VWF). Remarkably, VWF's activation for hemostasis correlates with its abrupt elongation at sufficiently high shear rates. In this study, we have discovered a strong intermonomer interaction in VWF that is expected to tune VWF's ability to sense hydrodynamic forces in the bloodstream. Our data will help to comprehend the force-induced activation of VWF and provide clues for understanding clotting disorders, such as von Willebrand disease and thrombosis, at the single-molecule level.**

Author contributions: J.P.M., R.S., and M.B. designed research; J.P.M., S.M., A.L., C.B., and L.K.B. performed research; T.O. and D.A.P. engineered recombinant proteins; J.P.M., S.M., A.L., C.B., L.K.B., W.V., and J.L. analyzed data; and J.P.M. wrote the paper with input from coauthors.

The authors declare no conflict of interest.

This article is a PNAS Direct Submission.

Freely available online through the PNAS open access option.

[1]To whom correspondence should be addressed. Email: jochen.mueller@physik.uni-muenchen.de.

This article contains supporting information online at www.pnas.org/lookup/suppl/doi:10.1073/pnas.1516214113/-/DCSupplemental.

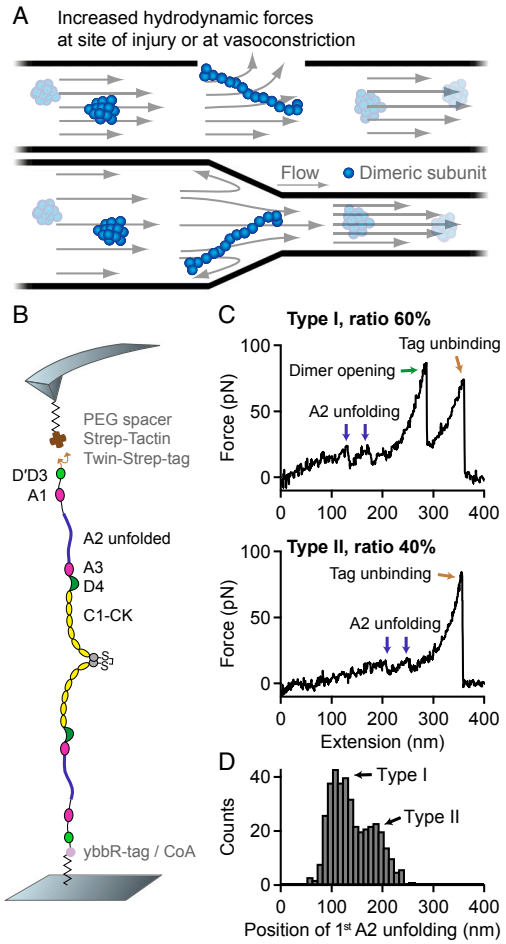


**Fig. 1.** Single-molecule force measurements on VWF dimers. (*A*) Illustration of VWF's ability to sense hydrodynamic forces in blood vessels. When subjected to sufficiently high forces, for instance at sites of vascular injury, vasoconstriction, or stenosis, VWF undergoes an abrupt transition from a collapsed to a stretched conformation and promotes hemostasis. (*B*) Schematic representation of pulling recombinant VWF dimers. A ybbR-tag at the N terminus of one of the monomers allowed for covalent anchoring, and a Twin-Strep-tag at the N terminus of the other monomer enabled specific pulling via a Strep-Tactin functionalized AFM cantilever. (*C*) Denoised force–extension traces of dimers showing A2 unfolding peaks (blue arrows) at low (type I traces) or at high extension values (type II traces). Type I traces repeatedly exhibited a peak (dimer opening, green arrow) at higher force. The final peak (brown arrow) corresponds to the unbinding of the Twin-Strep-tag from Strep-Tactin. (*D*) Bimodal distribution of the position of the first A2 unfolding event.

In this study, we report on force-induced conformational changes of VWF and present a strong intermonomer interaction that is expected to tune VWF's force-sensing ability in the bloodstream. Evidence for this interaction comes from force–extension traces of dimers, which were probed in atomic force microscopy (AFM)-based single-molecule force measurements. Complementarily, we characterized the static conformation of VWF by AFM imaging and small-angle X-ray scattering (SAXS). From the combination of force and imaging data, we gain a quantitative understanding of the mechanisms underlying the force-sensing ability of VWF.

## Results

**Force Response of VWF Dimers.** For AFM-based single-molecule force experiments, we genetically engineered VWF heterodimers, composed of two monomers with different peptide tags (Fig. 1*B*). These tags were located at the N termini of constituent monomers, thus allowing for pulling VWF in its native force-sensing direction. A ybbR-tag at the end of one of the monomers enabled covalent anchoring to a Coenzyme A (CoA) functionalized glass surface (25), and a Twin-Strep-tag at the end of the other monomer allowed for specific pulling via a Strep-Tactin functionalized AFM cantilever (26). The Twin-Strep-tag was preferred over a single Strep-tag to achieve more stable binding and reduced off-rates. To minimize protein–surface interaction, polyethylene glycol (PEG) spacers were used both at glass surface and cantilever (*Materials and Methods*).

Force–extension traces of specific pulling events were identified by using the characteristic unfolding pattern of the A2 domain as a positive fingerprint (Fig. 1*C*). Due to the existence of two A2 domains in dimers, only traces with two A2 unfolding peaks were considered. We verified that this fingerprint corresponds to A2 unfolding by pulling heterodimers with disulfide bridged A2 domains (Fig. S1) and by pulling bifunctional monomers (Fig. S2). Characteristic peak forces on the order of 20 pN and subsequent length increments of ∼ 45 nm are in agreement with reported values for A2 unfolding (8, 17–19). Moreover, forces of the last peak (rupture peak) in force–extension traces are in line with those reported for dissociating the Strep-tag/Strep-Tactin interaction (27), underlining the specific nature of the analyzed pulling events (Fig. S3).

We obtained two types of force–extension traces of VWF dimers under near-physiological buffer conditions (Fig. 1*C* and Fig. S4), showing A2 unfolding peaks at low (type I) and at high extension values (type II). Type II traces revealed the first A2 unfolding peak at extension values of $179 \pm 29$ nm and the second A2 unfolding peak at $226 \pm 37$ nm. Given a static end-to-end length of ∼130 nm for a VWF dimer and an overall linker length of 60 nm, these traces are in line with expectations for loading a flexible (open) dimer (28). Traces of type I showed A2 unfolding peaks at considerably lower extension values of $110 \pm 22$ nm (first A2) and $161 \pm 22$ nm (second A2). Classification of traces into two types is backed up by a bimodal distribution of the position of both first (Fig. 1*D*) and second A2 unfolding. From a double-Gaussian fit to the distribution of the first A2 unfolding position, we estimated the ratio of type I traces as 60% and type II traces as 40%.

In traces of type I, we repeatedly observed an additional high-force peak (green arrow in Fig. 1*C*) before the rupture peak. In these cases, the position of rupture closely matched the one observed in type II traces. However, as a result of the relatively weak Twin-Strep-tag/Strep-Tactin interaction, this additional peak only showed up in ∼10% of type I traces. In the remaining 90% of type I traces, rupture of the construct from the cantilever occurred before observing a high-force peak, and at considerably lower extension values (Fig. S5).

The high-force peak was observed at forces ranging from roughly 50–120 pN, depending on the applied loading rate (Fig. 2*B*). Importantly, the high-force peak was never observed twice in a trace and, moreover, was never observed in monomer traces (Fig. S2). Consequently, we excluded domain unfolding as the origin of this high-force peak, in agreement with the prediction of disulfide bonds stabilizing all domains in VWF except the A2 domain (20). Hence, we hypothesized this peak to result from the dissociation of a strong intermonomer interaction, which may be conceptualized as the opening of a firmly closed dimer (Fig. 2*A*).

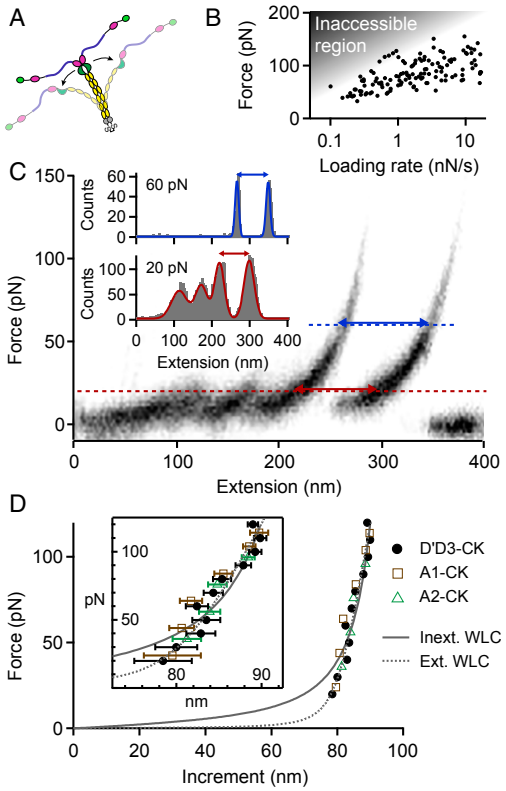


**Fig. 2.** Analysis of the high-force peak in type I force–extension traces of VWF dimers, resulting from the opening of firmly closed dimers. (*A*) Illustration of the corresponding conformational changes of VWF dimers. Due to a strong intermonomer interaction, unfolding of the mechanically less stable A2 domain (blue) precedes the opening of the dimer. (*B*) Force–loading-rate dependency of the dissociation of the strong intermonomer interaction. Due to the relatively weak Strep-tag/Strep-Tactin interaction, most events may be missed due to an inaccessible region in the force–loading-rate space. (*C*) Overlay of 30 force–extension traces of type I. Cross-section profiles at constant force, as shown for 20 and 60 pN, were fitted to a multipeak Gaussian distribution, and the distance between the two last peaks yielded a characteristic length increment. (*D*) Length increments of dimer opening events as a function of force. Solid and dashed lines are fits of the inextensible and extensible WLC model, respectively. Error bars were calculated by propagation of the uncertainties of the mean positions of the last two Gaussian peaks (1 SD). Dimeric constructs A1-CK (brown squares) and A2-CK (green triangles) exhibited very similar increments.

To estimate the incremental length obtained from such opening events, we overlaid 30 type I traces and analyzed cross-sections at constant force (Fig. 2*C*), ranging from 20 to 100 pN. This method was preferred over the method of contour length transformation (29, 30), which relies on a model describing the elasticity of a uniform polymer. We obtained characteristic length increments above 80 nm that increased with force (Fig. 2*D*). Additional measurements on truncated dimeric constructs lacking either only the N-terminal D′D3 domains (A1-CK; squares in Fig. 2*D*) or both D′D3 and adjacent A1 domains (A2-CK; triangles) yielded the same results (Fig. S6). For the full-length constructs, the length increase with force was approximately described by the (inextensible) Worm-like chain (WLC) model [$\chi^2_{red}$ = 1.9; Fig. 2*D*, solid line (31)], yielding a contour length of $L_C$ = 102 nm and a persistence length of $P$ = 0.6 nm. Including an enthalpic stretch modulus $S$ in the WLC model [extensible WLC model (32)] yielded a better fit ($\chi^2_{red}$ = 1.3; Fig. 2*D*, dashed line), with fitting parameters $L_C$ = 84 nm, $S$ = 1,120 pN, and $P$ = 6.4 nm. Latter is in excellent agreement with the value of $P$ = 6.4 nm inferred from AFM imaging (Fig. S7).

A comparison of the length increments with distances reported for static dimers suggested the observed interaction to be mediated by the D4 or A3 domain of VWF (28). To locate the responsible domain, we performed force measurements on VWF dimers with a deletion of either domain. We still observed the characteristic high-force peak upon deletion of the A3 domain (Fig. S8). In contrast, deletion of the D4 domain (D4N-TIL4, Fig. 3*A*) resulted in a loss of the characteristic high-force peak and yielded only a single type (type II) of force–extension traces (Fig. 3*B*) and a unimodal distribution of the position of both first (Fig. 3*C*) and second A2 unfolding. Additionally, we found that upon addition of EDTA the high-force peak disappeared, resulting solely in traces of type II (Fig. S9). These findings strongly indicate a highly specific interaction involving the D4 domain and divalent ions.

**Static Conformation of VWF.** By AFM imaging, we visualized the static conformation of dimeric VWF constructs (Fig. 4 and Figs. S10–S12), adsorbed from near-physiological buffer onto a poly-L-lysine–coated mica surface. We found dimers with conformations ranging from fully flexible to fully closed (Fig. 4*A*). To quantify the compactness of a dimer, we measured its stem length, i.e., the distance from the CK domain to the position at which the two constituent monomers separate from each other. Additionally, we determined the distance between the CK domain and the beginning of higher N-terminal domains for the two constituent monomers and used the mean of these distances to normalize the stem length (Fig. S10). For wild-type dimers, the distribution of the normalized stem length (Fig. 4*B*) yielded one peak decaying from zero stem length (flexible dimers, ~65%), and another peak centered slightly above 1 (closed dimers, ~35%). Dimers lacking the D4 domain (Fig. 4*C*) and full-length dimers adsorbed from buffer containing EDTA (Fig. S9) exhibited only the population of normalized stem

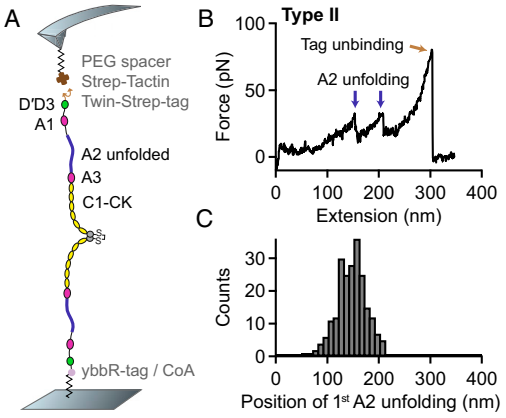


**Fig. 3.** Single-molecule force measurements on VWF dimers lacking the D4 domain. (*A*) Schematic representation of the pulling configuration. (*B*) Denoised force–extension trace lacking the high-force peak characteristic for opening firmly closed dimers. (*C*) Unimodal distribution of the position of the first A2 unfolding event.

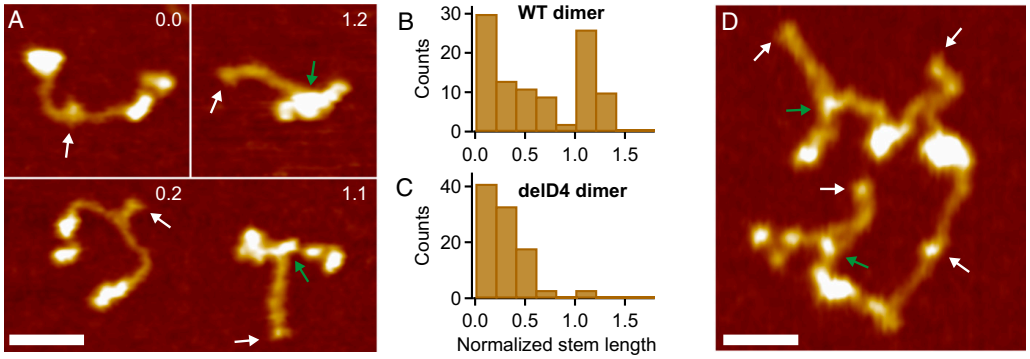


**Fig. 4.** Static conformation of VWF probed by AFM imaging. (*A*) Images of individual VWF dimers. Conformations of dimers range from fully flexible (normalized stem length of 0) to fully closed (normalized stem length above 1). Numbers in images are values of the normalized stem length. White arrows mark the CK domains, and green arrows mark positions corresponding to potential strong intermonomer interactions. (Scale bar, 30 nm; range of color scale, 2.4 nm.) (*B*) Distribution of the normalized stem length of wildtype (WT) dimers, showing a peak decaying from zero stem length and a peak centered slightly above 1. (*C*) Distribution of the normalized stem length of dimers lacking the D4 domain, showing only the peak decaying from zero stem length. (*D*) Image of a VWF concatamer consisting of four dimeric subunits. Arrows and scales are as in *A*.

lengths decaying from zero (Fig. 4*C* and Fig. S9). The observed stem length distributions are consistent with a simple model assuming C domains to zip up pairwise from the CK domains with a constant domain–domain interaction free energy (Fig. S11). This model suggests that forces in the low piconewton range—below the force resolution of AFM force measurements—are sufficient to break C-domain interactions.

Additionally, we probed the conformation of dimeric VWF constructs (A1-CK) in solution using SAXS (*Supporting Information*). The SAXS data indicate a change in the conformational ensemble from relatively rigid conformations under near-physiological buffer conditions to more flexible and as a result more globular conformations in the presence of EDTA (Fig. S9), fully consistent with the AFM results.

AFM imaging further revealed that dimers as constituents of concatamers (Fig. 4*D*) exhibit similar static conformations and a similar degree of compactness as isolated ones. Especially in multimeric samples, we also observed dimers exhibiting colocalization of N-terminal portions of the constituent monomers, likely resulting from the strong intermonomer interaction, despite not possessing a fully closed stem (lower left dimer in Fig. 4*D*). Importantly, we did not observe any clear colocalization between distinct dimers within a concatamer except the intrinsic multimerization through D′D3.

## Discussion

In this study, we used AFM-based single-molecule force measurements to probe the force response of VWF dimers. We identified a strong intermonomer interaction that withstood forces of 50–120 pN at loading rates ranging from 0.1 to 10 nN·s$^{-1}$. For each loading rate, the measured forces presumably represent only the lower part of a distribution of forces required for dissociating the strong intermonomer interaction. This bias is a result of the relatively weak Twin-Strep-tag/Strep-Tactin interaction, which was used for pulling VWF and dissociates at forces that are in a similar range as those of the strong intermonomer interaction. It is therefore likely that the force–loading-rate dependency of the dissociation of the strong intermonomer interaction is characterized by higher mean forces than measured in our experiments.

The strong intermonomer interaction appears to be highly specific, judging from a reproducible length increase after dissociation. Additionally, the interaction was only observed in the presence of divalent ions. These results are corroborated by observations from AFM imaging, which revealed both compact and flexible conformations of VWF dimers at pH 7.4 in the presence of divalent ions, but only flexible conformations upon addition of EDTA. This finding is in line with previous transmission electron microscopy (TEM) studies on VWF at pH 7.4 in absence of divalent ions (28, 33). Further evidence for a specific intermonomer interaction comes from experiments on deletion constructs. While deletion of the A3 domain did not significantly change the force response of VWF dimers, the strong intermonomer interaction disappeared upon deletion of the D4 domain. This finding is again supported by AFM imaging, which showed that deletion of D4 promotes a flexible conformation of dimers. Recent TEM studies showed that a D4–D4 complex forms at pH 6.2 in the presence of calcium and promotes stem formation (28). We hypothesize that a D4–D4 complex also forms under physiological conditions, explaining our force and imaging data.

Force–extension traces of firmly closed dimers are characterized by A2 unfolding peaks at low extension values. Flexible dimers, such as induced by addition of EDTA, show A2 unfolding peaks at considerably higher extension values. Under near-physiological buffer conditions, we found two populations in the positions of first and second A2 unfolding events. A rough estimation based on a double-Gaussian fit yielded a ratio of 60% firmly closed and 40% flexible dimers. The existence of firmly closed and flexible dimers is corroborated by AFM imaging results, although quantified with roughly inverted ratios (35% closed, 65% flexible). The difference in ratios may well originate both from uncertainties of the double-Gaussian fit and from the strict criterion of a fully formed stem for assigning dimers as compact. Remarkably, the observed ratio of approximately one-half firmly closed and one-half flexible dimers indicates a difference in Gibbs free energy close to zero between the firmly closed and the open state. Given the fact that the dimer bond is mechanically strong, this implies that the exchange kinetics between the two states are exceptionally slow, at least along the reaction coordinate probed in our force measurements. For elucidating the underlying structural mechanisms, high-resolution structures of the D4 domain and of the C domains are of outstanding interest. AFM imaging further revealed that dimers within VWF concatamers have a similar conformation as isolated ones. In particular, we found flexible and closed dimers with very similar ratios. As we did not observe any clear colocalization

of domains between distinct dimers, we assume that the force response of VWF can be largely tracked back to its individual dimers.

In blood vessels, forces on VWF concatamers result from their interplay with hydrodynamic flow, in particular with an elongational flow component (7, 34), characterized by a velocity gradient along the direction of flow. We expect that VWF subjected to pure elongational flow will align to the stretching axis already at moderate rates. Partially formed stems of dimers not shielded by the strong intermonomer interaction are expected to unzip. At rates that induce peak forces in VWF of 10–20 pN, A2 domains of VWF will start to unfold. Indeed, simulations strongly suggest that such forces can be reached for a 5-μm-long polymer when subjected to a physiologically relevant elongational flow rate of 1,000 $s^{-1}$ (34). A2 unfolding is likely to set in at the middle of concatamers, where tensile forces are highest (8), but may propagate rapidly through VWF, favored by the positive feedback between force and concatamer length in hydrodynamic flow. The overall increase of VWF's effective length—i.e., its length contributing to the sensing of hydrodynamic forces—due to unfolding of the A2 domain can be estimated based on our force data of dimers. Although in the case of a flexible dimer unfolding of the A2 domain almost doubles the distance between the N termini, the distance is roughly tripled in the case of a firmly closed dimer. This means that the effective length of a concatamer may be increased due to A2 unfolding by a factor of 2–3. Because hydrodynamic peak forces scale with the square of effective length (7, 8), we assume that after A2 unfolding VWF will be subjected to peak forces that are up to nine times higher than the ones that induced initial A2 unfolding. At such high forces, the strong intermonomer interaction in firmly closed dimers can dissociate, whereupon VWF can fully elongate. The additional length increase due to this last elongation step can be estimated to be ~ 20%, assuming that one-half of the constituent dimers were initially firmly closed. In general, lower forces than specified above will also trigger the described conformational changes of VWF, yet on longer timescales.

The above considerations suggest that unfolding of A2 domains may trigger the full elongation of VWF. This cooperative behavior may explain the abrupt elongation behavior of VWF under high shear conditions (6). However, we note that in shear flow, which can be conceptualized as a superposition of an elongational and rotational flow component (10), VWF undergoes a tumbling motion, whereupon individual subunits may relax and refold. Although the refolding of the A2 domain has already been studied in detail (8, 18, 19), it will be of great value to study the dynamics of stem formation in dimers and the reversibility of the strong intermonomer interaction, e.g., with the help of a markedly stronger tag. Interestingly, a recent study has identified two distinct regimes of VWF bundle relaxation (35). We speculate that the regime of fast relaxation might be a result of A2 refolding and that the regime of slow relaxation might be associated with the formation of partially or fully formed stems.

Hidden length in firmly closed dimers implies a significantly reduced length of VWF contributing to force sensing. Thus, a higher ratio of firmly closed dimers in a concatamer leads to a decreased initial force response to elongational flow. For example, the force-sensing length of a concatamer comprised one-half of firmly closed dimers is decreased by ~ 30% compared with a completely flexible concatamer with the same number of dimers. Subjected to elongational flow, the concatamer with firmly closed dimers will therefore experience only roughly one-half of the force compared with the fully flexible concatamer. Consequently, elongation of a VWF concatamer with firmly closed dimers will require significantly higher rates of elongational flow than elongation of a fully flexible concatamer with an identical number of dimers. Importantly, small changes of the local environment, mutations, and possibly drugs may drastically affect the ratio of firmly closed dimers, thereby shifting critical rates of elongational flow to activate VWF for hemostasis and thrombosis.

## Conclusion

In AFM-based single-molecule force measurements, we have identified a strong intermonomer interaction in VWF dimers that involves the D4 domain and critically depends on divalent ions. At high forces above ~ 50 pN, the strong interaction could dissociate and thereby provide ~80-nm flexible length to VWF, corresponding to the previously hidden stem length. We estimate that in VWF concatamers roughly one-half of the constituent dimers are firmly closed. While flexible dimers may serve to finely sense hydrodynamic forces at an early stage of elongation, the ratio of firmly closed dimers clearly affects the effective length of VWF and will thus tune its force-sensing ability in the bloodstream. Overall, our data elucidate force-sensing mechanisms of VWF, which are the key to its function in hemostasis and its role in thrombosis.

## Materials and Methods

**Experimental Procedures, Data Analysis, and Engineering of Recombinant Proteins.** Please refer to *Supporting Information*.

**Buffers.** To mimic physiological conditions, we used 20 mM Hepes, 150 mM NaCl, 1 mM $CaCl_2$, 1 mM $MgCl_2$, pH 7.4. For measurements with EDTA, we used 20 mM Hepes, 150 mM NaCl, 10 mM EDTA, pH 7.4.

**ACKNOWLEDGMENTS.** We are very grateful to Prof. Dr. Hermann E. Gaub and Prof. Dr. Erich Sackmann for helpful discussions. Gesa König is acknowledged for technical assistance in preparation of recombinant VWF. We further thank Thomas Nicolaus for technical assistance in protein purification, as well as Lukas Milles for sharing a data-processing and denoising algorithm. Moreover, we acknowledge Dr. Adam Round and Dr. Cy M. Jeffries for support at the SAXS beamlines BM29 and P12, respectively. This study was supported by research funding from the German Research Foundation to the Research Group FOR1543: "Shear Flow Regulation of Hemostasis—Bridging the Gap Between Nanomechanics and Clinical Presentation." We thank the Nanosystems Initiative Munich and the Center for Nanoscience for support. W.V. acknowledges the Research Foundation Flanders for a postdoctoral fellowship and a travel grant.

1. Vogel V (2006) Mechanotransduction involving multimodular proteins: Converting force into biochemical signals. *Annu Rev Biophys Biomol Struct* 35:459–488.
2. Puchner EM, et al. (2008) Mechanoenzymatics of titin kinase. *Proc Natl Acad Sci USA* 105(36):13385–13390.
3. del Rio A, et al. (2009) Stretching single talin rod molecules activates vinculin binding. *Science* 323(5914):638–641.
4. Puchner EM, Gaub HE (2012) Single-molecule mechanoenzymatics. *Annu Rev Biophys* 41:497–518.
5. Ruggeri ZM (1997) von Willebrand factor. *J Clin Invest* 99(4):559–564.
6. Schneider SW, et al. (2007) Shear-induced unfolding triggers adhesion of von Willebrand factor fibers. *Proc Natl Acad Sci USA* 104(19):7899–7903.
7. Springer TA (2014) von Willebrand factor, Jedi knight of the bloodstream. *Blood* 124(9):1412–1425.
8. Zhang X, Halvorsen K, Zhang C-Z, Wong WP, Springer TA (2009) Mechanoenzymatic cleavage of the ultralarge vascular protein von Willebrand factor. *Science* 324(5932): 1330–1334.
9. Perkins TT, Smith DE, Chu S (1997) Single polymer dynamics in an elongational flow. *Science* 276(5321):2016–2021.
10. Smith DE, Babcock HP, Chu S (1999) Single-polymer dynamics in steady shear flow. *Science* 283(5408):1724–1727.
11. Wagner DD (1990) Cell biology of von Willebrand factor. *Annu Rev Cell Biol* 6:217–246.
12. Huang R-H, et al. (2008) Assembly of Weibel-Palade body-like tubules from N-terminal domains of von Willebrand factor. *Proc Natl Acad Sci USA* 105(2):482–487.
13. Ruggeri ZM, Orje JN, Habermann R, Federici AB, Reininger AJ (2006) Activation-independent platelet adhesion and aggregation under elevated shear stress. *Blood* 108(6):1903–1910.
14. Sadler JE (1998) Biochemistry and genetics of von Willebrand factor. *Annu Rev Biochem* 67:395–424.
15. Tsai HM (1996) Physiologic cleavage of von Willebrand factor by a plasma protease is dependent on its conformation and requires calcium ion. *Blood* 87(10):4235–4244.
16. Baldauf C, et al. (2009) Shear-induced unfolding activates von Willebrand factor A2 domain for proteolysis. *J Thromb Haemost* 7(12):2096–2105.
17. Ying J, Ling Y, Westfield LA, Sadler JE, Shao J-Y (2010) Unfolding the A2 domain of von Willebrand factor with the optical trap. *Biophys J* 98(8):1685–1693.

18. Jakobi AJ, Mashaghi A, Tans SJ, Huizinga EG (2011) Calcium modulates force sensing by the von Willebrand factor A2 domain. *Nat Commun* 2:385.
19. Xu AJ, Springer TA (2012) Calcium stabilizes the von Willebrand factor A2 domain by promoting refolding. *Proc Natl Acad Sci USA* 109(10):3742–3747.
20. Zhou Y-F, et al. (2012) Sequence and structure relationships within von Willebrand factor. *Blood* 120(2):449–458.
21. Alexander-Katz A, Schneider MF, Schneider SW, Wixforth A, Netz RR (2006) Shear-flow-induced unfolding of polymeric globules. *Phys Rev Lett* 97(13):138101.
22. Alexander-Katz A (2014) Toward novel polymer-based materials inspired in blood clotting. *Macromolecules* 47(5):1503–1513.
23. Savage B, Sixma JJ, Ruggeri ZM (2002) Functional self-association of von Willebrand factor during platelet adhesion under flow. *Proc Natl Acad Sci USA* 99(1):425–430.
24. Ulrichts H, et al. (2005) The von Willebrand factor self-association is modulated by a multiple domain interaction. *J Thromb Haemost* 3(3):552–561.
25. Yin J, et al. (2005) Genetically encoded short peptide tag for versatile protein labeling by Sfp phosphopantetheinyl transferase. *Proc Natl Acad Sci USA* 102(44):15815–15820.
26. Schmidt TGM, et al. (2013) Development of the Twin-Strep-tag® and its application for purification of recombinant proteins from cell culture supernatants. *Protein Expr Purif* 92(1):54–61.
27. Kim M, Wang CC, Benedetti F, Marszalek PE (2012) A nanoscale force probe for gauging intermolecular interactions. *Angew Chem Int Ed Engl* 51(8):1903–1906.
28. Zhou Y-F, et al. (2011) A pH-regulated dimeric bouquet in the structure of von Willebrand factor. *EMBO J* 30(19):4098–4111.
29. Puchner EM, Franzen G, Gautel M, Gaub HE (2008) Comparing proteins by their unfolding pattern. *Biophys J* 95(1):426–434.
30. Stahl SW, et al. (2012) Single-molecule dissection of the high-affinity cohesin–dockerin complex. *Proc Natl Acad Sci USA* 109(50):20431–20436.
31. Bustamante C, Marko JF, Siggia ED, Smith S (1994) Entropic elasticity of lambda-phage DNA. *Science* 265(5178):1599–1600.
32. Odijk T (1995) Stiff chains and filaments under tension. *Macromolecules* 28:7016–7018.
33. Fowler WE, Fretto LJ, Hamilton KK, Erickson HP, McKee PA (1985) Substructure of human von Willebrand factor. *J Clin Invest* 76(4):1491–1500.
34. Sing CE, Alexander-Katz A (2010) Elongational flow induces the unfolding of von Willebrand factor at physiological flow rates. *Biophys J* 98(9):L35–L37.
35. Steppich DM, et al. (2008) Relaxation of ultralarge VWF bundles in a microfluidic-AFM hybrid reactor. *Biochem Biophys Res Commun* 369(2):507–512.
36. Lipfert J, Doniach S (2007) Small-angle X-ray scattering from RNA, proteins, and protein complexes. *Annu Rev Biophys Biomol Struct* 36:307–327.
37. Putnam CD, Hammel M, Hura GL, Tainer JA (2007) X-ray solution scattering (SAXS) combined with crystallography and computation: Defining accurate macromolecular structures, conformations and assemblies in solution. *Q Rev Biophys* 40(3):191–285.
38. Svergun DI, Koch MHJ (2003) Small-angle scattering studies of biological macromolecules in solution. *Rep Prog Phys* 66:1735–1782.
39. Doniach S (2001) Changes in biomolecular conformation seen by small angle X-ray scattering. *Chem Rev* 101(6):1763–1778.
40. Zimmermann JL, Nicolaus T, Neuert G, Blank K (2010) Thiol-based, site-specific and covalent immobilization of biomolecules for single-molecule experiments. *Nat Protoc* 5(6):975–985.
41. Gumpp H, Stahl SW, Strackharn M, Puchner EM, Gaub HE (2009) Ultrastable combined atomic force and total internal reflection fluorescence microscope. *Rev Sci Instrum* 80(6):063704.
42. Hutter JL, Bechhoefer J (1993) Calibration of atomic-force microscope tips. *Rev Sci Instrum* 64:1868–1873.
43. Condat L (2013) A direct algorithm for 1-D total variation denoising. *IEEE Signal Process Lett* 20:1054–1057.
44. Vanderlinden W, et al. (2012) Mesoscale DNA structural changes on binding and photoreaction with $Ru[(TAP)_2PHEHAT]^{2+}$. *J Am Chem Soc* 134(24):10214–10221.
45. Blanchet CE, et al. (2015) Versatile sample environments and automation for biological solution X-ray scattering experiments at the P12 beamline (PETRA III, DESY). *J Appl Cryst* 48(Pt 2):431–443.
46. Konarev PV, Volkov VV, Sokolova AV, Koch MHJ, Svergun DI (2003) PRIMUS: A Windows PC-based system for small-angle scattering data analysis. *J Appl Cryst* 36: 1277–1282.
47. Rivetti C, Guthold M, Bustamante C (1996) Scanning force microscopy of DNA deposited onto mica: Equilibration versus kinetic trapping studied by statistical polymer chain analysis. *J Mol Biol* 264(5):919–932.
48. Wen D, Foley SF, Hronowski XL, Gu S, Meier W (2013) Discovery and investigation of O-xylosylation in engineered proteins containing a $(GGGGS)_n$ linker. *Anal Chem* 85(9): 4805–4812.
49. Spahr C, et al. (2013) Recombinant human lecithin-cholesterol acyltransferase Fc fusion: Analysis of N- and O-linked glycans and identification and elimination of a xylose-based O-linked tetrasaccharide core in the linker region. *Protein Sci* 22(12): 1739–1753.
50. Spencer D, et al. (2013) O-xylosylation in a recombinant protein is directed at a common motif on glycine-serine linkers. *J Pharm Sci* 102(11):3920–3924.
51. Spahr C, Shi SD-H, Lu HS (2014) O-glycosylation of glycine-serine linkers in recombinant Fc-fusion proteins: Attachment of glycosaminoglycans and other intermediates with phosphorylation at the xylose sugar subunit. *MAbs* 6(4):904–914.

# Supporting Information

Müller et al. 10.1073/pnas.1516214113

## SI Results

**SAXS Results.** To characterize the conformation of dimeric A1-CK constructs in solution, we performed SAXS measurements, both in the presence and absence of divalent ions. SAXS is a powerful technique to probe the structural ensembles and conformational transitions of macromolecules in solution, under a wide range of buffer conditions (36–38). The Kratky representation [$q^2 \cdot I(q)$ vs. $q$] is frequently used to represent scattering data (intensity $I$, scattering vector $q$; for details, see SAXS data acquisition and analysis) of flexible or partially folded macromolecular ensembles (39). A well-defined peak in the Kratky plot is typical of well-folded globular proteins; in contrast, an increase of the $q^2$-weighted intensity at high $q$ is characteristic of unfolded or partially folded structures. The SAXS data indicate a conformational transition of the ensemble of dimeric VWF constructs upon the change from near-physiological buffer conditions (including 1 mM $Mg^{2+}$ and 1 mM $Ca^{2+}$) to buffer containing 10 mM EDTA (Fig. S9*E*). In the presence of divalent ions, the SAXS profile in Kratky representation exhibits a plateau shape (with two small peaks), implying an ensemble of mostly folded conformations. However, a population adopting a more flexible conformation may still be present. In the absence of divalent ions, the Kratky plot changes shape, exhibiting a nonparabolic diverging shape for higher $q$ values, indicative of the dimeric constructs adopting a more flexible ensemble. The radius of gyration determined from the SAXS data changes from 22.5 to 20.5 nm upon addition of EDTA. Moreover, the maximal intramolecular dimension $D_{max}$ of the dimeric constructs is reduced when divalent ions are absent: we found a $D_{max}$ of 70 nm for dimeric constructs in near-physiological buffer and a $D_{max}$ of 54 nm for constructs in EDTA buffer. The shape of the $P(r)$ function (a histogram of pairwise distances in the molecule) calculated from SAXS data of dimers under near-physiological conditions resembles the shape typical of rather extended rod-like molecules (Fig. S9*F*). In contrast, a shortening and steeper decay of the $P(r)$ occurs when divalent ions are absent, indicating a more globular ensemble of conformations of A1-CK dimers. Both in the absence and presence of divalent ions, the $P(r)$ functions exhibit a peak at a distance of 10 nm, corresponding to the approximate diameter of a partially or fully formed stem. Overall, the SAXS data are fully consistent with the findings from AFM imaging: under near-physiological buffer conditions, VWF dimers adopt elongated, rod-like conformations, while still maintaining some amount of flexibility. Removal of divalent ions by EDTA induces a conformational change of the ensemble, characterized by a larger degree of flexibility and as a result more globular conformations.

**Simple Model for C-Terminal Stem Formation in VWF Dimers.** The AFM imaging data indicate that the stem formed by interactions of the C domains in the VWF dimer has variable length (Fig. 4 and Fig. S9*D*). In the absence of divalent ions (Fig. S9*D*) or for the D4-deletion mutant (Fig. 4*C*), the stem length exhibits an approximately exponential distribution. Here, we present a simple, minimalistic model that can rationalize these observations. In our model, we make several assumptions: first, we assume that the C domains of both constituent monomers, which are covalently linked at their CK domains, form the stem similar to a zipper, i.e., that they "zip up" hierarchically from the C terminus. In particular, this means that we assume that C domain number $k$ (numbering from the C terminus) can only interact with C domain number $k$ on the opposite monomer and that this interaction is only possible if C domains $k-1$ are already interacting. In principle, other interactions between C domains could be possible as well, for example, intramonomeric interactions or interactions between monomers that do not correspond to the hierarchical zipper geometry. However, because we only observe such interactions very infrequently in the AFM images, we assume the probability of interactions that do not follow the strict zipper geometry to be negligible in our model. Second, we make the assumption that each pair of C domains in the zipper has an equal and constant interaction free energy if it is in contact and that each pair of C domains contributes equally to the length of the stem. These latter assumptions, too, could be refined, e.g., by allowing different interaction energies or different lengths for each pair of domains or by introducing cooperativity between domains. However, our aim was to build a simple and minimal model that can account for the data, but not for all possibilities.

Given the assumption that domain pairs zip up with a constant interaction free energy $\Delta G$, the probability of $n$ pairs of domains to interact (with $n = 0, 1, \ldots, 6$) is proportional to $\exp(-n \cdot \Delta G / k_B T)$ and the relative (normalized) fraction of dimers with $n$ interacting C domains is as follows:

$$f(n) = \frac{e^{-n \cdot \Delta G / k_B T}}{\sum_{k=0}^{k=6} e^{-k \cdot \Delta G / k_B T}}. \quad \textbf{[S1]}$$

We fitted Eq. **S1** with the interaction free energy $\Delta G$ as the only free parameter to the binned normalized stem length data (number of bins equal to 7, within a range from 0 to 1), assuming standard Poisson errors for the bins. We found that our simple model provides a good fit to the data (Fig. S11); the best fit for the D4-deletion construct yielded $\Delta G = 0.49\ k_B T \cong 0.29$ kcal/mol ($\chi^2_{red} = 1.3$), and for the EDTA condition we found $\Delta G = 0.56\ k_B T \cong 0.33$ kcal/mol ($\chi^2_{red} = 1.5$).

The fact that our simple hierarchical zipper model can account for the normalized stem length data in the absence of divalent ions and for the D4-deletion construct suggests that the C-domain interactions are close to thermodynamic equilibrium and do not feature a high degree of cooperativity, at least under our imaging conditions. The fact that the fitted interaction free energies are very similar for the full-length construct in the presence of EDTA and for the D4-deletion construct in the presence of divalent ions ($\Delta G = 0.56\ k_B T$ vs. $\Delta G = 0.49\ k_B T$) suggests that D4-domain interactions are strongly suppressed in the absence of divalent ions and that, in contrast, divalent ions do not play an important role for C-domain interactions.

The fact that our simple model suggests relatively weak C-domain interactions is fully consistent with the fact that we do not observe peaks that would correspond to the dissociation of pairwise interacting C domains in the single-molecule force measurements (Fig. 1*C*). The opening of one pair of interacting C domains lengthens the dimer by ~10 nm in the direction of the applied force (Fig. 1*B*, taking into account that there are six pairs of interactions). This length change implies that a force of 2 pN—below the detection limit of AFM force measurements—would bias the equilibrium of interaction between opposite C domains by 2 pN·10 nm = 20 pN·nm $\approx 5\ k_B T$, implying that in less than 1% of the cases at least one pair of C domains remains bound in thermodynamic equilibrium.

## SI Materials and Methods

**Single-Molecule Force Measurements.** VWF constructs, bearing a Twin-Strep-tag II (WSHPQFEKGGGSGGGSGGGSWSHPQFEK) and a ybbR-tag (DSLEFIASKLA), were covalently attached to CoA functionalized glass slides. For functionalization, slides were

silanized with (3-aminopropyl)-dimethyl-ethoxysilane (APDMES) (40), and then coated with 25 mM of a 5-kDa *N*-hydroxy-succinimide (NHS)-PEG-maleimide linker, and finally treated with 25 mM CoA. Functionalized slides were incubated overnight and at 4 °C with 1 mg·mL$^{-1}$ VWF constructs in OPTIPRO-SFM medium supplemented with Sfp-transferase and $MgCl_2$ (25). After incubation with proteins, slides were carefully rinsed with buffer. Before measurements with EDTA, immobilized proteins were incubated for 8 h with EDTA buffer.

AFM cantilevers with a silicon tip (BL-AC40TS-C2; Olympus) were silanized with APDMES and then coated with 25 mM of the 5-kDa NHS-PEG-maleimide linker. Maleimide chemistry allowed for covalent attachment of a Strep-Tactin construct bearing a single cysteine residue (Strep-Tactin-Cys). To this end, Strep-Tactin-Cys was initially reduced in the presence of tris(2-carboxyethyl)phosphine (TCEP) beads and then separated from TCEP beads by filtering. After incubation of cantilevers with the NHS-PEG-maleimide linker, cantilevers were incubated with 10 μM reduced Strep-Tactin-Cys.

Single-molecule force measurements were performed using custom-built instruments (41), driven each by an MFP-3D AFM controller (Asylum Research). Spring constants of the cantilevers were determined individually using the thermal-noise method (42). Force–extension traces were recorded in closed-loop mode at six different pulling speeds ranging from 200 to 6,400 nm·s$^{-1}$. To probe different VWF molecules, the *xy* stage was moved by 100 nm after each trace.

**Analysis of Force–Extension Traces.** For analysis, force–extension traces were subjected to total variation denoising (43). In the case of dimeric VWF constructs, only traces with two A2 unfolding peaks were evaluated. Overlays of force–extension traces were generated by offsetting undenoised characteristic traces in direction of the extension axis. The offsets, which were chosen to align curves with respect to the stretch before the rupture peak, were within ∼20 nm. Heat maps of overlays were generated based on a bin size of 2 pN × 2 nm.

**AFM Imaging.** VWF constructs carrying an N-terminal Twin-Strep-tag were purified via a HiTrap StrepTrap (GE Healthcare) using the AEKTA Explorer chromatography system (GE Healthcare) and eluted with buffer containing 50 mM Tris, 150 mM NaCl, and 2.5 mM d-Desthiobiotin (pH 8.0). Afterward, purified constructs were buffer exchanged to the measurement buffer. We observed O-glycosylation of the $(GGGS)_3$ linker region of the Twin-Strep-tag (Fig. S12), to a markedly higher extent for the full-length constructs than for the truncated constructs, such as A1-CK. We verified that the conformation of tagged constructs was unaffected, by comparison with dimers lacking peptide tags, which exhibited a very similar degree of compactness as both full-length and truncated constructs. Force–extension traces of dimers were unaffected by abovementioned glycosylation, as verified by pulling heterodimers with a single Strep-tag, lacking the $(GGGS)_3$ linker (Fig. S4).

Dimers lacking peptide tags were purified by centrifuge filtration using Amicon Ultra-15 MWCO 100 kDa (Merck Chemicals). Shown in Fig. 4*A* are dimers lacking peptide tags. DelD4 dimers shown in Fig. S10 were selected from a sample purified by centrifuge filtration only, and very likely correspond to ybbR-tagged homodimers, present as byproduct in the heterodimer sample. Multimeric samples were purified by centrifuge filtration using Amicon Ultra-15 MWCO 100 kDa and buffer exchanged to near-physiological buffer.

For substrate preparation, we used a method similar to the one reported by Vanderlinden et al. (44). Freshly cleaved mica sheets (grade I; SPI Supplies) were incubated with 20 μL of a poly-L-lysine solution [$M_n$, 500–2,000; 0.01% (wt/vol); Sigma-Aldrich; in ultrapure water] for 30 s. Subsequently, they were rinsed with 25 mL of ultrapure water and dried in a stream of nitrogen. Twenty microliters of buffer solution containing ∼5 μg·mL$^{-1}$ of either dimeric or multimeric VWF constructs were deposited on the functionalized mica substrates and incubated for 30 s. Afterward, the substrates were rinsed with 20 mL of ultrapure water and dried in a stream of nitrogen.

AFM images of 1 μm$^2$ and 1,024 × 1,024 pixels were recorded in tapping mode in air using an MFP-3D AFM (Asylum Research) and silicon tips with resonance frequencies of ∼300 kHz and a nominal spring constant of 26 N·m$^{-1}$ (AC160TS; Olympus).

**Processing and Analysis of AFM Images.** Raw image data were processed and analyzed using SPIP software (version 6.3.6; Image Metrology). Image processing included plane correction (third-order polynomial plane fitting and flattening according to the histogram alignment routine) and Gaussian filtering. Dimers were individually traced along their contour by following local maxima in height, and different characteristic lengths were extracted from the resulting height profiles. To quantify the compactness of a dimer, we determined its stem length, i.e., the distance from the CK domain to the position where the two constituent monomers separate from each other. We further measured the distance between the CK domain and the beginning of higher N-terminal domains for the two monomers and used the mean of these distances to normalize the stem length.

**Sample Preparation for SAXS Measurements.** For SAXS measurements, dimeric A1-CK constructs carrying an N-terminal Twin-Strep-tag were purified via a HiTrap StrepTrap using the AEKTA Explorer chromatography system and eluted with buffer containing 50 mM Tris, 150 mM NaCl, and 2.5 mM d-Desthiobiotin (pH 8.0). Eluates were buffer exchanged to near-physiological buffer or to buffer containing EDTA. Purified constructs were concentrated to the desired concentrations by centrifuge filtration using Amicon Ultra-15 MWCO 100 kDa. Before each SAXS measurement, samples were filtered again using a centrifuge filter with a pore size of 0.22 μm (Sigma-Aldrich). Concentrations of each sample were determined in a spectrophotometer (Thermo Scientific) assuming standard protein extinction coefficients at a wavelength of 280 nm.

**SAXS Data Acquisition and Analysis.** SAXS data were collected at the BM29 beamline (European Synchrotron Radiation Facility, Grenoble, France) and at the P12 beamline [Deutsches Elektronen-Synchrotron, Hamburg, Germany (45)]. SAXS data shown here were collected at the P12 beamline at an X-ray wavelength $\lambda$ of 1.24 Å and a sample-to-detector distance of 3 m, resulting in a $q$ range of 0.03–4.82 nm$^{-1}$ [$q = 4\pi \sin(\theta)/\lambda$, where $2\theta$ is the total scattering angle]. Data were acquired with an exposure time of 45 ms and 20 repeats per sample. Repeat exposures of the same sample showed no signs of radiation damage and were averaged. Matching buffer samples were measured using identical procedures, and buffer profiles were subtracted for background correction. Protein concentrations varied from 0.4 to 1.2 mg·mL$^{-1}$. Measurements for different protein concentrations showed good reproducibility after scaling by forward scattering intensity, indicating the absence of aggregation or interparticle interference. Data shown in Fig. S9*E* correspond to the highest measured concentrations. We obtained radii of gyration $R_g$ by Guinier analysis of the lowest $q$ data with the limit $q \cdot R_g < 1.3$. We used the program PRIMUS to compute the pair distance distribution function $P(r)$ (46) (Fig. S9*F*). This approach also provides an estimate for the maximum dimension of the macromolecule, $D_{max}$.

**Plasmid Construction.** VWF-cDNA was cut out from the plasmid pMT2-VWF (ATCC 67122; LGC Standards) by EcoRI (Life Technologies) and inserted into the EcoRI site of the plasmid pBKSJH- (a modified pBluescript KS, which has an EcoRI site flanked on both sides by NotI sites; Agilent). The resulting plasmid was digested with NotI (Life Technologies) and the insert

was ligated into the plasmids pIRESneo2 (Takara Bio Europe) (pIRESneo2-VWF) and pIREShygroTO2 (pIREShygroTO2-VWF). The latter plasmid (pIREShygroTO2) was constructed by initially cutting out the neomycin resistance of pIRESneo2 by SmaI (Life Technologies) and XbaI (Life Technologies), and by blunting the digest with T4-Polymerase (Life Technologies). From the plasmid pcDNA3.1/Hygro(−) (Life Technologies), the hygromycin B resistance was cut out by Eco72I (Life Technologies) and blunt-end ligated into the digested and blunted pIRESneo2. Finally, a silent mutation was introduced to destroy the EcoRI site of the hygromycin B resistance. Plasmids pIRESneo2-VWF and pIREShygroTO2-VWF were used for mutagenesis with the QuikChange Multi Site-Directed Mutagenesis Kit (Agilent) to delete the VWF-Pro amino acid sequence 26–763 (pIRESneo2-delPro-VWF and pIREShygroTO2-delPro-VWF). pIRESneo2-delPro-VWF and pIREShygroTO2-delPro-VWF were used to insert a 6×His-tag after amino acid 2813 by mutagenesis (pIRESneo2-delPro-VWF-His and pIREShygroTO2-delPro-VWF-His). Similarly, pIRESneo2-delPro-VWF-His was used to insert the yBBR-tag 5′ of amino acid 764 (pIRESneo2-delPro-yBBR-VWF-His) and pIREShygroTO2-delPro-VWF-His to insert the Twin-Strep-tag 5′ of amino acid 764 (pIREShygroTO2-delPro-Twin-Strep-VWF-His). pIRESneo2-delPro-yBBR-VWF-His was further used to introduce the C2771R mutation by mutagenesis and insert the Twin-Strep-tag 5′ of the His-tag using the QuikChange Multi Site-Directed Mutagenesis Kit (pIRESneo2-delPro-yBBR-VWF-C2771R-Twin-Strep-His). pIRESneo2-delPro-yBBR-VWF-His and pIREShygroTO2-delPro-Twin-Strep-VWF-His were used to insert mutations N1493C and C1670S by mutagenesis using the QuikChange Multi Site-Directed Mutagenesis Kit (pIRESneo2-delPro-yBBR-VWF-N1493C/C1670S-His and pIREShygroTO2-delPro-Twin-Strep-VWF-N1493C/C1670S-His) (16). pIRESneo2-delPro-yBBR-VWF-His and pIREShygroTO2-delPro-Twin-Strep-VWF-His were used for mutagenesis to delete amino acids 1873–2255 (D4-N-TIL4) (pIRESneo2-delPro-yBBR-VWF-delD4-His and pIREShygroTO2 delPro-Twin-Strep-VWF-delD4-His). pIRESneo2-delPro-yBBR-VWF-His and pIREShygroTO2-delPro-Twin-Strep-VWF-His were used for mutagenesis to delete amino acids 1672–1874 (pIRESneo2-delPro-yBBR-VWF-delA3-His and pIREShygroTO2 delPro-Twin-Strep-VWF-delA3-His). pIRESneo2-delPro-yBBR-VWF-His was used for PCR amplification of amino acids 1–25 and the yBBR-tag and cloned in the NheI and EcoRI site of pIRESneo2 (pIRESneo2-VWF-sig-peptide-yBBR). pIREShgroTO2-delPro-Twin-Strep-VWF-His was used for PCR amplification of amino acids 1–25 and the Twin-Strep-tag and cloned in the NheI and EcoRI site of pIREShygroTO2 (pIREShygrTO2-VWF-sig-peptide-Twin-Strep). In pIRESneo2-delPro-yBBR-VWF-His, an EcoRI site 5′ of the amino acid 1238 was inserted by mutagenesis. The resulting plasmid was digested by EcoRI, and the fragment encoding amino acids 1238–2813+His was ligated into pIRESneo2-VWF-sig-peptide-yBBR (pIRESneo2-VWF-sig-peptide-yBBR-VWF-A1-CTCK-His). The product of ligation into pIREShygroTO2-VWF-sig-peptide-Twin-Strep was designated pIREShygroTO2-VWF-sig-peptide-Twin-Strep-VWF-A1-CTCK-His. In pIRESneo2 delPro-yBBR-VWF-His, an EcoRI-site 5′ of the amino acid 1463 was inserted by mutagenesis. The resulting plasmid was digested by EcoRI, and the fragment encoding amino acids 1463–2813+His was ligated into pIRESneo2-VWF-sig-peptide-yBBR (pIRESneo2-VWF-sig-peptide-yBBR-VWF-A2-CTCK-His). The product of ligation into pIREShygroTO2-VWF-sig-peptide-Twin-Strep was designated pIREShygroTO2-VWF-sig-peptide-Twin-Strep-VWF-A2-CTCK-His. For encoding monomers with a single N-terminal Strep-tag, pIRESneo2-delPro-VWF-His was used to insert the Strep-tag 5′ of amino acid 764 by mutagenesis (pIRESneo2-delPro-Strep-tag-VWF-His). pIRESneo2-delPro-Strep-tag-VWF-His was further used to introduce the C2771R mutation by mutagenesis using the QuikChange Multi Site-Directed Mutagenesis Kit (pIRESneo2-delPro-Strep-tag-VWF-C2771R-His).

**Transfection and Expression.** HEK 293 cells (Deutsche Sammlung von Mikroorganismen und Zellkulturen, Braunschweig, Germany) were transfected in DMEM (Life Technologies) containing 10% (vol/vol) FBS (Life Technologies) with 4 μg of plasmid (for co-transfection, 2 μg of both plasmids) and 15 μL of Lipofectamine 2000 (Life Technologies). Twenty-four hours after transfection, cells were transferred into selection medium with 500 $\mu g \cdot mL^{-1}$ G418 (Invivogen). For cotransfected cells, the selection medium additionally contained 250 $\mu g \cdot mL^{-1}$ Hygromycin B (Invivogen). After 2–3 wk, the resulting polyclonal cell culture was seeded for expression. After 72 h of growing, the medium was changed against OPTIPRO-SFM (Life Technologies) for secretion of VWF. The culture supernatant was collected after 72 h and concentrated using Amicon Ultra-15 MWCO 100 kDa.

**Preparation of Strep-Tactin with a Single Cysteine.** Two Strep-Tactin (ST) constructs were designed: a wild-type construct and one harboring an N-terminal 6×His-tag as well as a unique cysteine (Cys) residue. Both ST variants were PCR amplified from synthetic templates (Centic) and cloned into pET vectors. Expression was achieved in 1-L and 500-mL SB cultures of transformed *Escherichia coli* BL21(DE3)-CodonPlus, respectively. The harvested cell pellets were treated separately in the beginning and dissolved in 4 mL per 1 g cell mass B-PER (Life Technologies). After addition of Lysozyme and DNase (Roche), cells were fully lysed by sonification. Insoluble cell debris as well as inclusion bodies were sedimented by centrifugation at 20,000 × *g* for 30 min. After discarding the supernatant, the inclusion body-containing pellet was again resuspended in 4 mL per 1 g washing buffer [30 mM Tris·HCl, pH 7.5, 150 mM NaCl, and 0.1% (vol/vol) Triton X-100]. Centrifugation and washing of the inclusion bodies were repeated four times, until the supernatant appeared fairly cleared. The inclusion bodies containing the Cys-modified ST were then dissolved in 6 mL of solubilization buffer (20 mM Tris·HCl, pH 7.5, 6 M guanidinium HCl), the ones containing unmodified ST in 12 mL. The solubilized protein fractions were again subjected to centrifugation for 30 min at 20,000 × *g*, and the supernatant with the unfolded ST constructs was collected. After determining the protein concentration in the solubilized fractions by measuring the absorbance at 280 nm, the entire amount of unmodified ST was used and mixed with the volume equivalent of a $10^{th}$ in mass of the latter with 6×His-Cys-ST. To accomplish refolding, the mixture was slowly and dropwise added to a stirred reservoir of 500 mM 1× PBS and 10 mM β-mercaptoethanol. The mixture was stirred overnight at 4 °C to maximize refolding of the mixed ST. Next, the 500-mL protein sample was filtered through a cellulose filter to remove precipitate and then loaded onto a 5-mL HisTrap FF column (GE Healthcare) for Ni–immobilized metal ion affinity chromatography purification. Elution of the reassembled 1× Cys-ST tetramer was achieved by a linear gradient from 10 to 300 mM imidazole (in 1× PBS, 10 mM β-mercaptoethanol). The intended 1:3 stoichiometry (1× 6×His-Cys-ST, 3× unmodified ST) was observed. Samples were pooled after elution from the affinity column and dialyzed against 1× PBS. As free reducing agent in the storage buffer would later on interfere with Mal-PEG immobilization of the 1× Cys-ST, bead-immobilized TCEP was added to the protein inside the dialysis tubing. ST was long-term stored at 4 °C in presence of TCEP beads. Typically, yields of 15 mg of purified protein per 1.5 L (500 mL for expression of His-tagged, Cys-ST, which is the yield affecting constituent) culture could be obtained.


**Fig. S1.** Single-molecule force measurements on VWF dimers with mutations N1493C and C1670S, which induce a disulfide bridge stabilizing the A2 domain. (*A*) Schematic representation of the pulling configuration. (*B* and *C*) Denoised force–extension traces (type I with the characteristic high-force peak and type II without) lacking the characteristic A2 unfolding peaks.

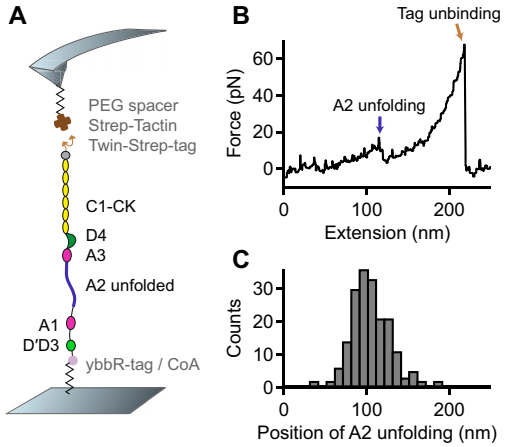


**Fig. S2.** Single-molecule force measurements on VWF monomers. (*A*) Schematic representation of the pulling configuration. A ybbR-tag at the N terminus and a Twin-Strep-tag at the C terminus enabled specific pulling via a Strep-Tactin functionalized cantilever. (*B*) Denoised force–extension trace showing a single A2 unfolding peak and lacking the high-force peak characteristic for the opening of firmly closed dimers. (*C*) Unimodal distribution of the position of A2 unfolding.

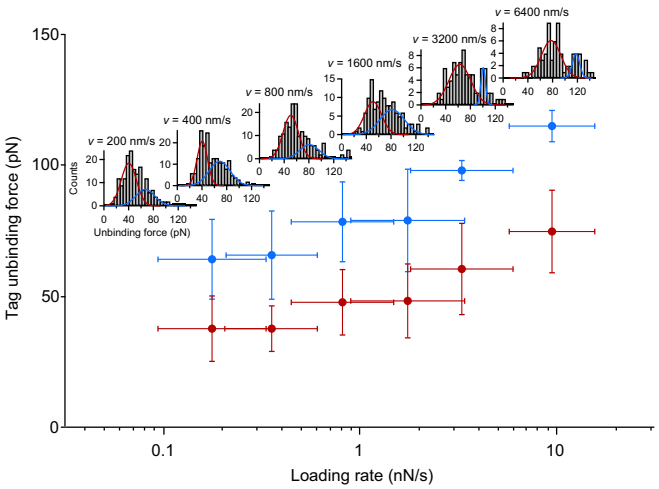


**Fig. S3.** Tag unbinding forces as a function of the applied loading rate. Tag unbinding represents the dissociation of the Twin-Strep-tag from tetravalent Strep-Tactin. Mean forces were obtained by fitting a bimodal Gaussian function to the distribution of unbinding forces for each pulling speed. Loading rates were obtained by fitting a line to force–extension traces before the last peak. Mean values of loading rates were obtained by fitting a Gaussian to the loading-rate distributions for each pulling speed. Error bars are 1 SD. Force–loading-rate dependency and bimodality of the individual force distributions are in line with previous investigations of the specific Strep-tag/Strep-Tactin interaction (27).

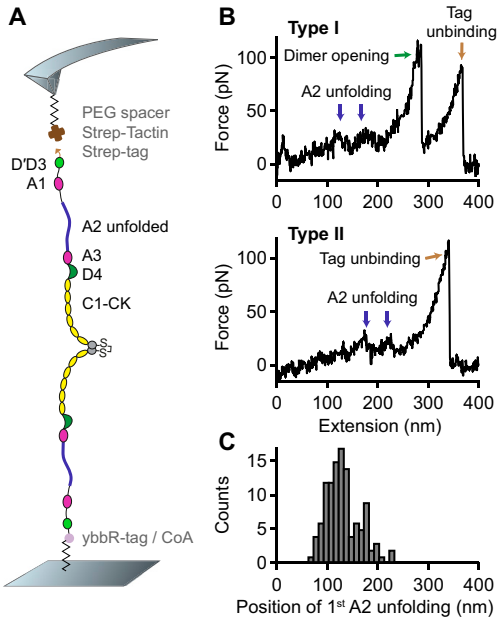


**Fig. S4.** Single-molecule force measurements on VWF heterodimers carrying a single Strep-tag instead of a Twin-Strep-tag. (*A*) Schematic representation of the pulling configuration. (*B*) Denoised force–extension traces. Traces of type I and II were still observed. (*C*) Bimodal distribution of the position of the first A2 unfolding event.

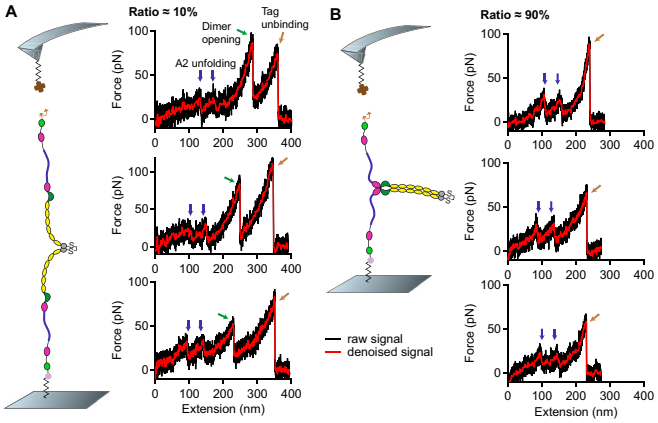


**Fig. S5.** Temporal order of events corresponding to dimer opening and tag unbinding. (*A*) Three representative force–extension traces of type I showing the characteristic high-force peak (green arrow), which corresponds to the dissociation of a strong intermonomer interaction in VWF dimers. After dissociation of the strong intermonomer interaction, the entire dimer is loaded with force and stretched. Finally, the construct detaches from the cantilever (brown arrow) as the Twin-Strep-tag dissociates from Strep-Tactin. (*B*) Three representative force–extension traces of type I exhibiting the peak of tag unbinding at an early stage of elongation. Positions of A2 unfolding events (blue arrows) are similar to the ones seen in the traces in *A*, strongly indicating that these traces likewise originate from pulling firmly closed dimers. However, as tag unbinding occurs too early, the strong intermonomer interaction is not dissociated and dimers remain only semistretched until tag unbinding.

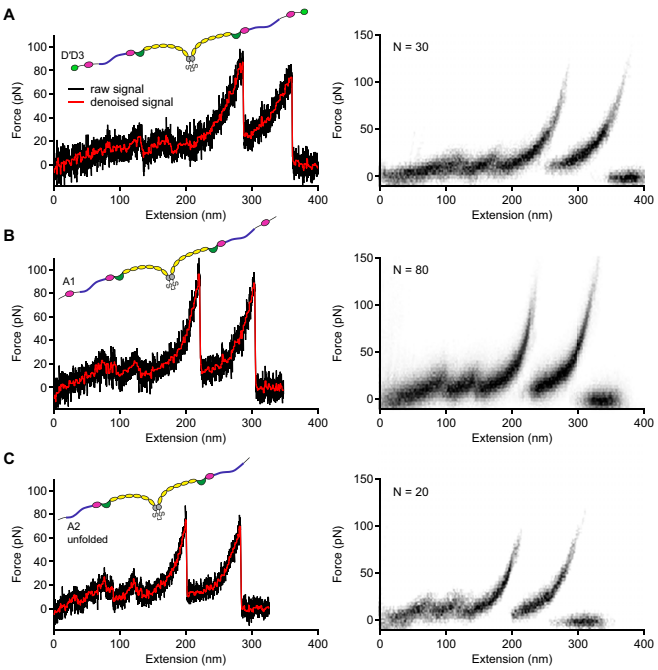


**Fig. S6.** Force–extension traces of type I for full-length and truncated dimers. (*A*–*C*) Individual traces (*Left*) and overlays of multiple traces (*Right*) for full-length dimers (*A*) and truncated dimers A1-CK (*B*) and A2-CK (*C*). The overlays are based on the raw signal of the underlying traces.

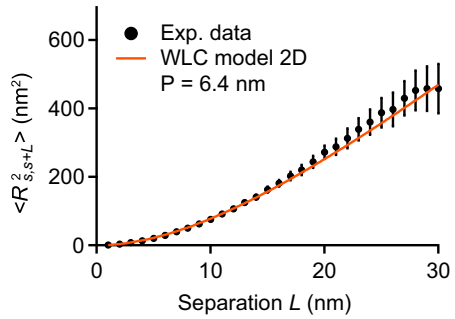


**Fig. S7.** Estimation of the persistence length of VWF's C-terminal region from AFM imaging. Shown is the mean value of the mean-squared distance $\langle R^2_{s,s+L}\rangle$ as a function of the separation $L$ along the contour of VWF monomers ($N = 10$), which was parameterized by the coordinate $s$. The experimental data were fitted using the following expression for 2D equilibrated polymer chains (47): $\langle R^2_{s,s+L}\rangle = 4P \cdot (L + 2P(e^{-L/2P} - 1))$. The fitting parameter $P$ denotes the bending persistence length in the context of the WLC model. The value of 6.4 nm (reduced $\chi^2_{red} = 0.76$) obtained for $P$ is close to the size of individual C domains (20). Fitting a different model that assumes kinetic trapping on adsorption yielded a clearly nonsensical value of $P = 3.5$ μm ($\chi^2_{red} = 6.85$), backing up the assumption of full equilibration. It should be noted that minor deviations from full equilibrium would imply that the obtained value slightly underestimates the persistence length. Errors bars represent the SD of the mean values.

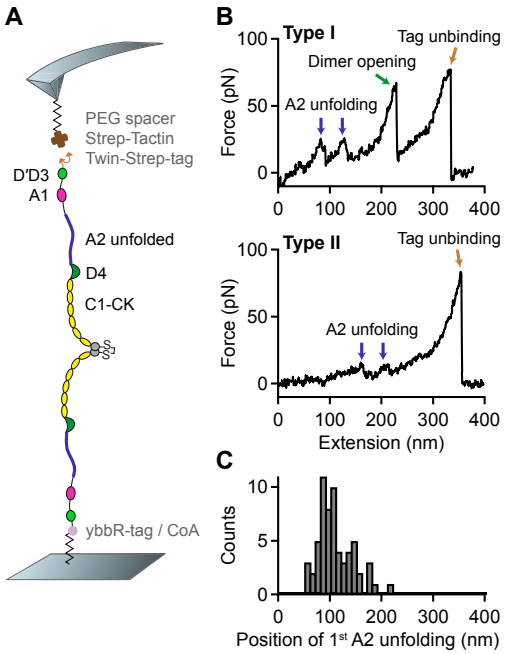


**Fig. S8.** Single-molecule force measurements on VWF dimers lacking the A3 domain. (*A*) Schematic representation of the pulling configuration. (*B*) Denoised force–extension traces. Traces were essentially unaffected by deletion of A3, in particular the characteristic high-force peak. (*C*) Bimodal distribution of the position of the first A2 unfolding event for all traces.

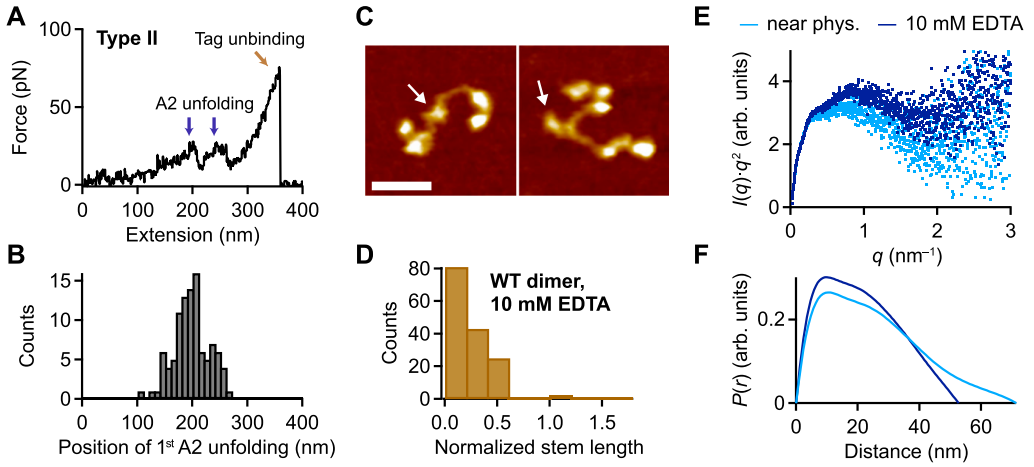


**Fig. S9.** Flexibility of VWF dimers induced by addition of EDTA. (*A*) Denoised force–extension traces of EDTA-treated dimers showing A2 unfolding peaks only at high extension values (type II). The characteristic high-force peak, which was observed for dimers under near-physiological conditions, was never observed. (*B*) Unimodal distribution of the position of the first A2 unfolding event. (*C*) Representative AFM images of individual VWF dimers adsorbed from EDTA buffer at pH 7.4. Arrows mark the positions of the CK domains. (Scale bar, 30 nm; range of color scale, 2.4 nm.) (*D*) Distribution of the normalized stem length of dimers adsorbed from EDTA buffer, showing a single peak decaying from zero stem length. (*E*) SAXS profiles in Kratky representation [$q^2 \cdot I(q)$ vs. $q$] for dimeric A1-CK constructs at pH 7.4 in the presence of divalent ions (light blue) and upon addition of EDTA (dark blue). (*F*) Distance distribution functions $P(r)$ of dimeric A1-CK constructs computed from experimental SAXS data represented in the same colors as in *E*. The $P(r)$ functions are normalized to give equal areas.

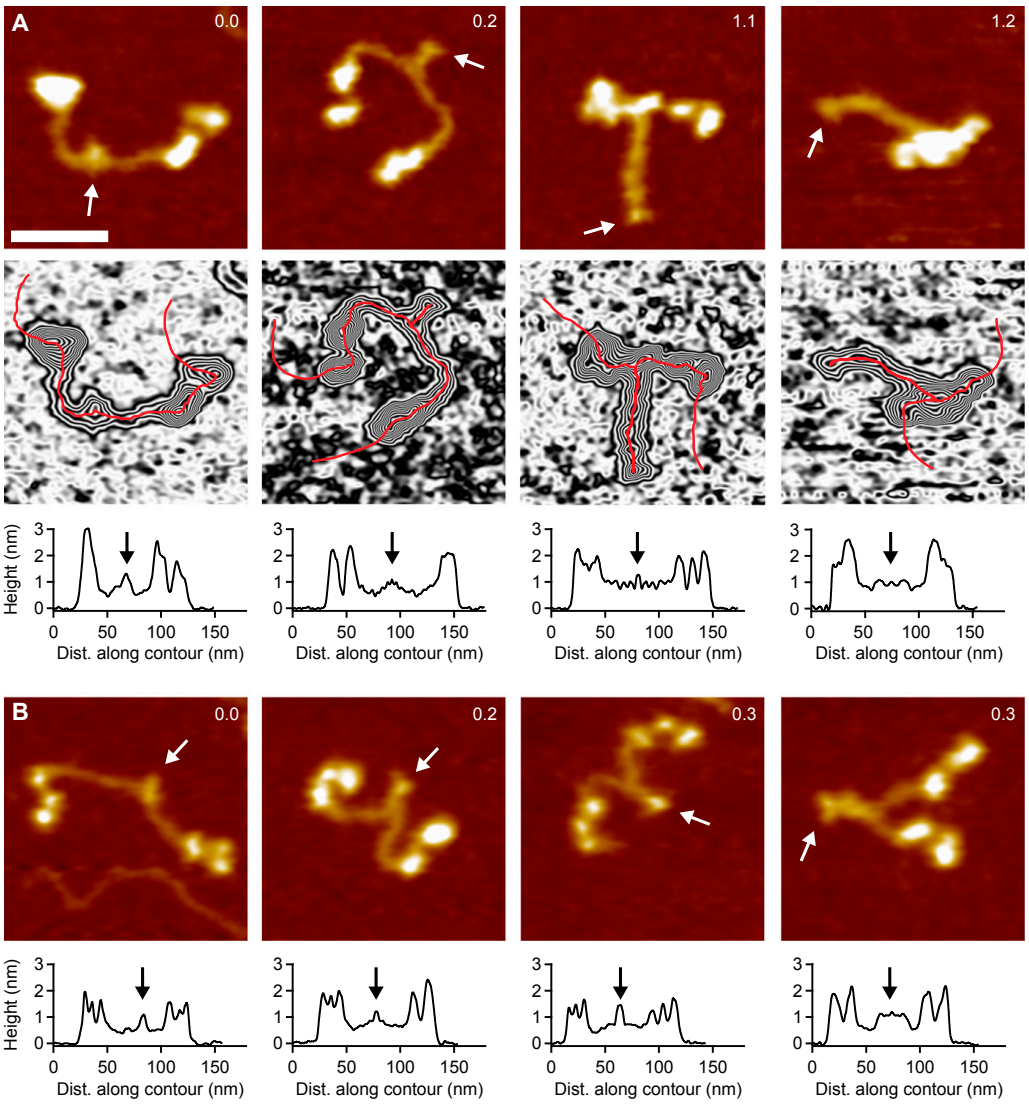


**Fig. S10.** Analysis of static lengths in dimeric VWF constructs. Characteristic lengths were determined from height profiles of individual dimers, obtained by tracing each dimer in AFM images individually along its contour, following local maxima in height. Arrows indicate the position of the CK domains, which were identified with the last C-terminal local maximum in height. The beginning of the higher N-terminal domains was defined as the position where the first large increase in height N-terminal of the CK domains reached its half-maximum value. (Scale bar, 30 nm; range of color scale, 2.4 nm.) (*A*) Analysis of wild-type dimers. (*B*) Analysis of dimers lacking the D4 domain.

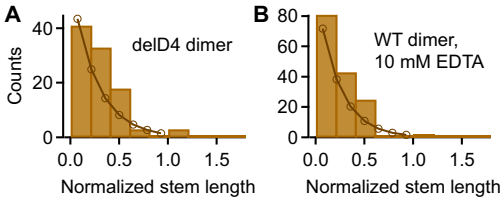


**Fig. S11.** Distributions of the normalized stem length of dimers lacking the D4 domain (*A*) and wild-type (WT) dimers adsorbed from EDTA buffer (*B*). Both distributions show a single peak decaying from zero stem length. To estimate the interaction free energy $\Delta G$ between opposite C domains, a simple model for C-terminal stem formation was fitted to both distributions. The fit yielded an interaction free energy $\Delta G = 0.49\ k_B T$ for delD4 dimers and $\Delta G = 0.56\ k_B T$ for WT dimers adsorbed from EDTA buffer (see *SI Results*).

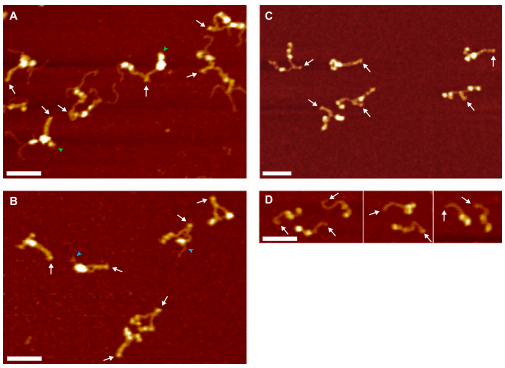


**Fig. S12.** O-Glycosylation of GGGS linker repeats in Twin-Strep-tagged VWF (48–51). (*A*) Representative AFM image of VWF dimers purified via a Strep-Tactin column. Most constituent monomers exhibited tentacle-like polymer chains protruding from their N termini. Such tentacles were only observed in dimers carrying a Twin-Strep-tag and never observed as isolated ones on the surface. As a result of purification, at least one of the two constituent monomers of a dimer carried an N-terminal Twin-Strep-tag and hence exhibited tentacles. Green arrowheads mark N termini free of tentacles, very likely corresponding to ybbR-tagged monomers. White arrows indicate the position of the CK domain. (Scale bar, 50 nm; range of color scale, 2.4 nm.) (*B*) Representative AFM image of truncated A1-CK dimers purified via a Strep-Tactin column. A1-CK dimers were—similarly to other truncated constructs—mostly free of tentacles. Blue arrowheads mark occasional N-terminal tentacles. The conformation of A1-CK constructs was very similar to the conformation of full-length constructs and constructs lacking tags. In particular, the observed ratios of compact and flexible dimers were very similar for all these constructs. Importantly, force measurements on truncated heterodimers (Fig. S6) yielded very similar ratios of firmly closed and open dimers as measurements on full-length constructs. White arrows indicate the position of the CK domains. Scale bar and range of color scale are as in *A*. (*C*) Representative AFM image of VWF homodimers carrying single N-terminal Strep-tags without GGGS linker repeats. Tentacle-like polymer chains were not observed. Importantly, force measurements on heterodimers with a single N-terminal Strep-tag yielded very similar ratios of firmly closed and open dimers as measurements on Twin-Strep-tagged heterodimers (Fig. S4). Scale bar and range of color scale are as in *A*. (*D*) Representative AFM image of VWF monomers carrying a single N-terminal Strep-tag without GGGS linker repeats. Tentacle-like polymer chains were not observed. Scale bar and range of color scale are as in *A*.

## A.2 Publication 2: Exponential Size Distribution of von Willebrand Factor

# Exponential Size Distribution of von Willebrand Factor

by

Svenja Lippok, Tobias Obser, Jochen P. Müller, Valentin K. Stierle, Martin Benoit, Ulrich Budde, Reinhard Schneppenheim, and Joachim O. Rädler

published in

Biophysical Journal, Vol. 105, No. 5, 1208–1216, 2013

1208 Biophysical Journal Volume 105 September 2013 1208–1216

# Exponential Size Distribution of von Willebrand Factor

Svenja Lippok,[†] Tobias Obser,[‡] Jochen P. Müller,[§] Valentin K. Stierle,[†] Martin Benoit,[§] Ulrich Budde,[¶] Reinhard Schneppenheim,[‡] and Joachim O. Rädler[†*]

[†]Faculty of Physics and Center for NanoScience, Ludwig Maximilian University, Munich, Germany; [‡]Department of Pediatric Hematology and Oncology, University Medical Center, Hamburg-Eppendorf, Hamburg, Germany; [§]Chair for Applied Physics, Ludwig Maximilian University, Munich, Germany; and [¶]Coagulation Lab, AescuLabor Hamburg, Hamburg, Germany

ABSTRACT Von Willebrand Factor (VWF) is a multimeric protein crucial for hemostasis. Under shear flow, it acts as a mechanosensor responding with a size-dependent globule-stretch transition to increasing shear rates. Here, we quantify for the first time, to our knowledge, the size distribution of recombinant VWF and VWF-eGFP using a multilateral approach that involves quantitative gel analysis, fluorescence correlation spectroscopy, and total internal reflection fluorescence microscopy. We find an exponentially decaying size distribution of multimers for recombinant VWF as well as for VWF derived from blood samples in accordance with the notion of a step-growth polymerization process during VWF biosynthesis. The distribution is solely described by the extent of polymerization, which was found to be reduced in the case of the pathologically relevant mutant VWF-IIC. The VWF-specific protease ADAMTS13 systematically shifts the VWF size distribution toward smaller sizes. This dynamic evolution is monitored using fluorescence correlation spectroscopy and compared to a computer simulation of a random cleavage process relating ADAMTS13 concentration to the degree of VWF breakdown. Quantitative assessment of VWF size distribution in terms of an exponential might prove to be useful both as a valuable biophysical characterization and as a possible disease indicator for clinical applications.

## INTRODUCTION

The large plasma glycoprotein von Willebrand Factor (VWF) is essential for the initiation of blood coagulation as it promotes adhesion of platelets to the injured vessel wall as well as platelet aggregation (1,2). It is present in human blood and the secretory granules of endothelial cells and platelets. Plasma VWF plays a crucial role in early hemostasis as it binds rapidly and tightly to collagen whenever blood is exposed to injured tissues (3). Remarkably, VWF is a multimer that consists of several identical subunits and its function in primary hemostasis strictly correlates with its multimer size. Even though much research is being done on its size-dependent functionality, only little is known about the exact size distribution and its origin. Quantitative deficiency of plasma VWF causes von Willebrand disease (VWD) type 1, the most common congenital bleeding disorder (1). Although VWD is often caused by a lack of long multimers, an aberrantly increased activity of VWF due to larger than normal multimers is assumed to be a pathogenic factor in thrombotic thrombocytopenic purpura (2,4). The size-dependent functionality relates to the shear flow-sensitive structure of VWF, which responds to shear by expansion to an elongated form, thereby exposing binding sites for collagen and the platelet receptor GPIb (5). This process highly depends on the extent of multimerization of VWF because smaller multimers are more resistant to shear forces than larger ones and subsequently binding sites for their ligands are not as readily exposed (6,7). Consequently, the size of the multimeric VWF is a critical factor for VWF's functionality and the question arises, which size distribution is produced by VWF biosynthesis and how it is controlled in homeostasis. In polymer science, the problem of polymer size distribution has been addressed by the seminal work of Paul Flory in 1936, in which he calculated the exact size distribution of polymers based on the model of step-growth polymerization reaction (8). He showed that a theoretical prediction of a multimer size distribution is possible if the mechanism and the kinetics of the synthesis reaction are known. Vice versa, the size distribution provides clues with respect to the polymerization mechanism.

VWF is expressed as a proprotein (Fig. 1 *A*), which is translocated into the endoplasmatic reticulum, where it dimerizes via intermonomer disulfide bonds in the C-terminal domain (Fig. 1 *B*). The dimers with a molecular mass of 500 kDa represent the repeating unit of the VWF multimer. They are transported from the endoplasmatic reticulum (pH $\approx$ 7.4) to the Golgi (pH $\approx$ 6.2). This is the place where multimerization occurs by formation of linear multimers via interchain disulfide bonds at the N-terminal resulting in multimeric VWF with molecular masses of up to $>$ 40.000 kDa (Fig. 1 *C*) (9–11). In this process, VWF propeptide acts as an oxidoreductase to promote VWF multimerization (12–14). The propeptide is then cleaved for separate secretion (15,16). After multimerization, VWF is either secreted constitutively to the plasma or stored in Weibel-Palade bodies and released upon certain stimuli (e.g., thrombin, plasmin, fibrin) without further multimerization taking place in the plasma (17). For a postsecretion size regulation, circulating VWF undergoes cleavage by

*Submitted April 3, 2013, and accepted for publication July 24, 2013.*

*Correspondence: raedler@lmu.de

Editor: Ashok Deniz.



0006-3495/13/09/1208/9 $2.00

http://dx.doi.org/10.1016/j.bpj.2013.07.037

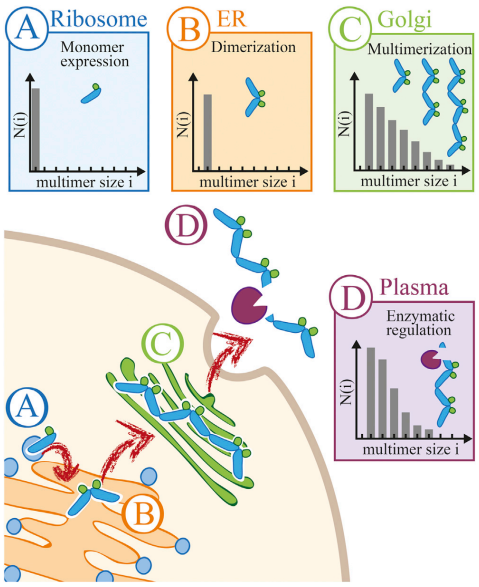


FIGURE 1 Schematic representation of plasma VWF size regulation. (*A*) VWF is synthesized by endothelial cells and megakaryocytes and originates from a 360 kDa monomer. (*B*) Monomeric VWF is transported to the endoplasmic reticulum where it is dimerized through intermonomer disulfide bonds. (*C*) Multimerization takes place in the Golgi apparatus, where the dimers form multimers with sizes ranging from 500 to 40.000 kDa, which are then secreted to the blood plasma. (*D*) Size control in plasma is provided by the protease ADAMTS13. No further multimerization occurs after secretion to the plasma.

the specific metalloprotease ADAMTS13, a disintegrin and metalloproteinase with a thrombospondin type 1 motif, member 13 (Fig. 1 *D*) (18). As known from bleeding disorders, defects in VWF multimer synthesis or size regulation have fundamental implications in hemostasis and exhibit defined patterns in VWF gel electrophoresis. Yet, the size distribution of VWF and its molecular causation has not been quantitatively studied so far.

Here, we investigate the size distribution of VWF using fluorescence correlation spectroscopy (FCS), quantitative gel analysis, and total internal reflection fluorescence microscopy (TIRFM). TIRFM allows for direct imaging of recombinant VWF-eGFP multimers including the assessment of VWF size by intensity analysis. Gel analysis is widely accepted in VWF diagnostics for screening patient samples for diseases. FCS measures the hydrodynamic size of fluorescently labeled species in solution. In contrast to gel analysis and TIRFM, FCS allows for measurements of fluorescent VWF-eGFP in blood plasma and is therefore well suited for VWF analysis in its native environment. We compare the size distribution of recombinant VWF and VWF-eGFP and its disease-related mutant VWF 2A (IIC), which is characterized by an increased concentration of dimers (19,20). We show that after secretion from VWF producing cells, VWF has an exponential size distribution in both healthy and pathologic form. The physiological and pathological distributions are distinct in the extent of polymerization characterizing the distribution. We also show that proteolytic cleavage by ADAMTS13 leads to non-exponential distributions that shift with time allowing for in situ monitoring of VWF cleavage under blood plasma conditions.

## MATERIALS AND METHODS

### Production of recombinant VWF

The recombinant fusion protein rVWF-eGFP was expressed and purified separately in its monomer, dimer, and multimer form as described in detail in the following:

#### *Cloning of a VWF-enhanced green fluorescent protein (EGFP) Plasmid*

From the plasmid pIRESneo2-vWF (Takara Bio Europe/Clontech, Saint-Germain-en-Laye, France) the stop codon was eliminated and an *Eco*RI restriction site was introduced. The EGFP sequence was cut out from the plasmid pEGFP-N2 (Takara Bio Europe/Clontech) by *Eco*RI and NotI and inserted into plasmid pIRESneo2 by using its *Eco*RI/NotI restriction sites (pIRESneo2-EGFP). Subsequently, VWF-cDNA from plasmid pIRESneo2-VWF lacking the stop codon was cut out by *Eco*RI and cloned into pIRESneo2-EGFP (pIRESneo2-VWF-EGFP).

pIRESneo2-VWF-EGFP was then used to produce three mutant constructs:

1) pIRESneo2-vWF-delPro-EGFP with the retained signal peptide sequence and the first three codons of the VWF propeptide but lacking the rest of the propeptide corresponding to codons 26–763 (delT26-R763). Expression of this construct will result in VWF monomers that assemble into carboxy-terminal dimers but not into larger multimers.
2) pIRESneo2-vWF-delPro/C2771R-EGFP, which was produced by in vitro-mutagenesis of construct 1), by exchanging codon 2771 for cysteine against the naturally occurring mutation to arginine (p.C2771R). Expression of this construct results in VWF monomers only, because p.C2771R causes a severe dimerization defect (R. Schneppenheim, unpublished) in addition to the multimerization defect of the VWF-delPro construct 1.
3) PIRESneo2-vWF-C1099Y-EGFP, which was produced by in vitro-mutagenesis of wild-type pIRESneo2-VWF-EGFP, by exchanging codon 1099 for cysteine against the naturally occurring mutation to tyrosine (p.C1099Y). Expression of this mutant results in near normal quantitative expression of mutant VWF, however, lacking large and medium sized VWF multimers as in the phenotype IIC of VWD type 2A.

#### *Generation of stable cell lines constitutively secreting VWF*

Transfection of 293 cells was carried out as described previously (21). 48 h after transfection cells were trypsinized and grown until confluence in Dulbecco's modified Eagle's medium buffer containing 10% fetal bovine serum and G418 at 500 $\mu$g/ml for selection. After further propagation of an aliquot of the stable cell line until 70–80% confluence, cell culture medium was changed to OPTIPRO-SFM medium for serum-free expression. Cell culture medium was harvested after 72 h and concentrated by Amicon Ultrafree (MWCO 100000 DA) if necessary.

### Blood samples

The patient samples were sent to our laboratory for the evaluation of VWF multimers and subtyping of the already known VWD. Informed consent was obtained from all subjects.

### Quantitative gel analysis

VWF multimer analysis was carried out in sodium dodecyl sulfate agarose gels combined with immunoblotting and luminescence visualization. The luminescent blot was stored on electronic media using photo imaging (FluorChem8000; Alpha Innotech, San Leandro, CA) (22). VWF multimers were separated via gel electrophoresis and visualized by detecting their luminescent signal. Electrophoretic bands were visualized by means of luminescent immunoblotting. Thereby, intensities were obtained by labeling the proteins with horseradish peroxidase-conjugated antibodies that cleave a chemiluminescent agent producing luminescence that is proportional to the amount of protein (23).

The multimer patterns of rVWF and rVWF-eGFP are taken from different gels, which were recorded on different days. Therefore, the run times vary from sample to sample. As the run times are not used for data analysis this does not have any influence on the analyzed data.

### FCS

FCS detects the dynamics of fluorescently labeled molecules diffusing in and out of a confocal volume (24–28) and can be applied to multicomponent systems with different fluorescent species (29). It can be used for measurements in crowded media like blood plasma, thus enabling the study of molecules in their native environment (30). This ensures that the investigated molecules keep their natural properties, because these often change in bulk fluids acting as solvents and thereby reducing effects such as aggregation. FCS data analysis is described in detail in the Supporting Material.

For FCS measurements, an Axiovert 200 microscope with a ConfoCor 2 unit (Carl Zeiss, Jena, Germany) equipped with a 40× (NA = 1.2) water immersion apochromat objective (Carl Zeiss) was used. An argon laser (488 nm) was used for illumination. Samples were measured in eight-well LabTek I chamber slides (Nunc, Rochester, NY). All measurements were performed in 5 mM Tris-HCl, pH 8.0 with 1.5 M urea at a temperature of 37°C controlled by an ibidi heating stage (ibidi GmbH, Martinsried, Germany). At this urea concentration, VWF can be conceived as a semi-flexible polymer as urea stretches it without affecting its basic structure. These conditions are widely used for VWF analysis if measurements with the stretched polymer have to be performed without shear flow (4,31). eGFP functionality was proved to be functional under this buffer condition in agreement with Alkaabi et al. (32). Measurements were performed for 10 × 60 s (eGFP, monomer and dimer) and 20 × 6 min (rVWF; rVWF-IIC). To ensure optimal fluctuation detection for multicomponent analysis, we chose long measurement times to obtain sufficient statistics while keeping concentrations low (20 nM for all samples). Correlation was performed using ConfoCor 2 software. For FCS data analysis, a Labview routine was implemented.

### TIRFM

TIRFM is a suitable technique for imaging fluorescent molecules on a transparent substrate with single molecule resolution (33,34). The technique uses the evanescent field of a totally internal reflected laser beam exciting only fluorophores above the substrate surface within typically 100 nm. This provides a high signal/noise ratio of the collected fluorescence and is therefore well suited for direct imaging of fluorescent molecules.

For TIRFM measurements, rVWF was immobilized on epoxy silane-coated glass slides and imaged using the TIRFM setup presented in (35). For excitation in the total internal reflection mode, a 473 nm laser (iBeam smart, TOPTICA, Gräfelfing, Germany) was used at a power of 0.4 mW. The corresponding filter set consisted of a Chroma z 470/10, a Chroma z 470 RDC, and a Chroma HQ 525/50 (Chroma Technology GmbH, Olching, Germany). The emitted light signal was detected by a back-illuminated EMCCD camera (DU-860D, Andor, Belfast, Ireland). The EMCCD chip was operated at a temperature of −90°C and the electron multiplication gain was set to 300-fold. 3000 frames (21 × 21 $\mu m^2$) were taken per image sequence with a recording rate of 10 frames/s. All measurements were carried out in phosphate buffered saline. To minimize eGFP bleaching before the actual measurement, all adjustment procedures were carried out at low laser power (0.1 mW).

Data analysis was obtained with a step detection algorithm. As the routine cannot distinguish between on- and off-steps and fails in detecting steps that occur within a very short time slot, the obtained step number was corrected by eye for blinking and missed steps.

### Proteolysis of full-length rVWF by ADAMTS13

Cleavage of recombinant VWF-eGFP by ADAMTS13 was achieved as reported in Pruss et al. (36). Cleaved samples were stored at −80°C until multimer analysis was performed.

## RESULTS

### Quantitative gel analysis of rVWF

Gel analysis is the most frequently used technique for VWF multimer analysis (22,23,36). By quantitative analysis of the intensity profiles obtained by antibody staining in gels (Fig. 2, *A*,*B* and *C*,*D*, respectively) we yield the size distribution of VWF, which in a semilogarithmic plot shows good agreement with an exponential (Fig. 2, *E* and *F*). Hereby we assume that antibody staining is proportional to the number of dimers in the VWF multimer. The gels were evaluated using luminescent immunoblotting implying that the measured luminescent signal intensities in each band reflect the number of antibody labels (Fig. 2, *C* and *D*). The signal was normalized by the number of dimers $i$ corresponding to the size of the multimers in the respective band. These normalized intensities correspond to the molar distribution function and were plotted in a semilogarithmic diagram versus the multimer size given in number of dimers $i$ (Fig. 2, *E* and *F*). We took gel data from both wild-type rVWF and rVWF-IIC and their eGFP fusion analogs (Fig. 2 *A*) as well as from VWF of normal plasma VWF-NP and patient plasma VWF-IIC (Fig. 2 *B*). For rVWF, clearly an exponential decay is found. One possible mechanistic explanation for such an exponential decay is the Flory theory of linear condensation polymers (8) that describes a step-growth polymerization process taking place in an enclosed reactor by the intermolecular reaction of bifunctional compounds (for details, see the Supporting Material). It predicts an exponential size distribution for step-growth polymerization resulting in a molar fraction of $i$-mers containing $i$ subunits (8)

$$\frac{N_i}{N} = (1-p)p^{i-1}. \quad (1)$$

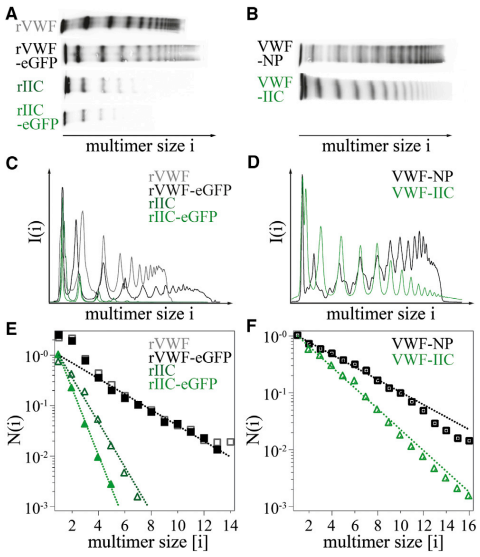


FIGURE 2 Quantitative gel analysis of recombinant and blood plasma VWF. (*A*) Multimer patterns of recombinant VWF distributions showing a ladder of multimers. (*B*) Multimer patterns of VWF distribution of normal plasma and of a patient with von Willebrand disease type IIC. (*C* and *D*) Densitogram intensity is plotted versus multimer size in terms of dimer number *i*. (*E*) Fits of normalized data show no significant difference in size distribution between rVWF (*gray squares*) and fluorescent rVWF-eGFP (*black squares*), stressing that the recombinant distribution with fused eGFP exhibits a normal multimerization behavior. Best fits to the gel data are obtained using an exponential function $N(i) = N_1 p^{i-1}$ with an extent of polymerization of $p = 0.70$ (*black dotted line*). For pathological rVWF-IIC (*green triangles*), a reduced extent of polymerization of $p = 0.36$ (*dark green dotted line*) for rVWF-IIC and $p = 0.22$ (*green dotted line*) for rVWF-IIC-eGFP is obtained. (*F*) Both plasma samples show likewise an exponential decay with a decreased $p = 0.66$ for pathological VWF-IIC (VWF-NP: $p = 0.78$). We observe a small, systematic deviation for large multimer sizes due to enzymatic cleavage in the plasma.

Here, $N_i$ and $N$ represent the number of *i*-mers and the total number of VWF molecules, respectively. $p$ indicates the extent of polymerization, i.e., the number of polymerized subunits to the total number of subunits, $N$. We assume that VWF multimerization complies with the step-growth polymerization model insofar as the formation of disulfide bonds can be assumed to be independent of size and the reaction volume is finite, which is a reasonable assumption considering the fact that multimerization occurs in the Golgi Apparatus only. Fitting the measured size distribution by the exponential function $N(i) = N_1 p^{i-1}$ yields an extent of polymerization of $p = 0.70 \pm 0.02$ for rVWF. $N_1$ is a constant fitting parameter that contains information about the number of dimers available for polymerization (for details, see the Supporting Material). $p$ describes the slope of the size distribution: high values of $p$ indicate a slowly decaying size distribution with long multimers being more abundant, whereas small values of $p$ indicate a steep decay with only a small amount of long multimers. The same exponential decay as for rVWF is found for rVWF-eGFP (*black squares*), showing that the shape of the distribution does not change significantly when fusing eGFP to VWF. The recombinant VWF-eGFP construct is therefore well suited for further studies employing fluorescence microscopy. The pathological rVWF-IIC appears only in a few bands of short sizes due to its lack of large multimers. Fitting yields an exponential, as for physiological VWF, yet with an extent of polymerization $p = 0.36 \pm 0.01$ for rVWF-IIC (*dark green*) and $p = 0.22 \pm 0.01$ for rVWF-IIC-eGFP (*green*).

Physiological VWF derived from blood samples also exhibits an exponential decrease (Fig. 2 *F*) with an extent of polymerization $p = 0.78 \pm 0.02$ for normal patients. However, the distribution function seems to exhibit a slight, but systematic deviation underrepresenting the larger fraction. This deviation can be attributed to ADAMTS13-induced cleavage that occurs in plasma and is depicted in the gels by the two satellite bands flanking the main bands that are known to be the products of proteolysis. Pathological VWF-IIC from plasma of patients suffering from von Willebrand disease type IIC shows an extent of polymerization $p = 0.66 \pm 0.01$.

## FCS single-component analysis of rVWF

FCS allows for size measurements of fluorescently labeled VWF in solution and is in principle capable to resolve multiple species with varying diffusion properties. We find that the measured FCS autocorrelation functions of recombinant VWF-eGFP are consistent with an exponential size distribution. First, we investigate recombinant VWF-eGFP (rVWF) monomer and dimer. A single-component analysis provides diffusion times (diffusion coefficients) of $\tau_D = 322\ \mu s$ ($D = 31.9\ \mu m^2/s$) for the monomer and $\tau_D = 447\ \mu s$ ($D = 19.5\ \mu m^2/s$) for the dimer (Fig. 3 *A*). Fig. 3 *A* also shows purified eGFP as a control. The eGFP diffusion time of $\tau_D = 90\ \mu s$ is in agreement with previous results (37). Because VWF is a rather elongated protein (11) a crude approximation of the VWF monomer and the VWF dimer as cylinders with the same diameter and twice the length for the dimer is reasonable. With these assumptions, the measured diffusion coefficients correspond to a cylinder 3 nm in diameter and 85.3 nm (*dimer*) and 42.7 nm (*monomer*) in length (for details, see the Supporting Material). This is in accordance with experiments performed by tapping mode atomic force microscopy (38) and electron microscopy measurements (11).

The single-component analysis can also be used as a first approximation of the full VWF distribution. Because it averages over all the species within the sample, it cannot

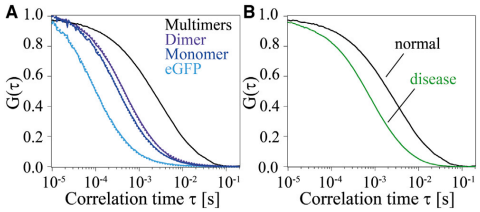


FIGURE 3 FCS measurements of recombinant VWF distributions and their building blocks. (*A*) Single-component fits of eGFP (*light blue*), rVWF monomer (*dark blue*), and rVWF dimer (*purple*) give correlation times $\tau_D$ of 90 $\mu$s, 322 $\mu$s, and 447 $\mu$s. Assuming a cylindrical shape for the dimer, the corresponding diffusion coefficient D = 19.5 $\mu m^2$/s characterizes a cylinder with length l = 85.3 nm and d = 3 nm. A clear shift toward longer diffusion times can be seen for the multimer distribution rVWF (*black*). (*B*) Single-component analysis was used as a first estimate of the autocorrelation function of physiological rVWF (*black*). A clear shift can be seen for pathological rVWF-IIC (*green*) that allows distinguishing between normal and abnormal conditions. Average diffusion times of $\tau_D$ = 2244 ± 515 $\mu$s (rVWF) and $\tau_D$ = 712 ± 22 $\mu$s (rVWF-IIC) are obtained.

reflect the different species within the VWF size distribution. Thus, single-component analysis is not able to provide the actual size distribution $N(i)$. However, it provides an average VWF size and is suited to rapidly pinpoint differences between the physiological distribution of rVWF and of the pathological distribution rVWF-IIC (Fig. 3 *B*) showing an average diffusion time of $\tau_D$ = 2244 ± 515 $\mu$s (*black line*) for physiological and $\tau_D$ = 712 ± 22 $\mu$s (*green line*) for pathological rVWF. For rVWF, the diffusion time is in good agreement with measurements performed by Torres et al. (39) who detected an average diffusion time of 2.0–3.5 ms for VWF-NP bound to fluorescently labeled antibodies. For rVWF-IIC, the lack of large multimers explains the shift to shorter diffusion times in our measurements. Although this single-component analysis does not contain quantitative information about the size distribution of VWF, it is clearly sufficient to distinguish between the physiological and the investigated pathological VWF distribution (Fig. 3 *B*).

### FCS multicomponent analysis of rVWF

To examine the nature of the VWF size distribution a multimer analysis was applied (Fig. 4) and found to be consistent with the exponential size distribution measured with quantitative gel analysis. The multimer analysis allows to compare the autocorrelation function expected for a given size distribution $N(i)$ with the experimental autocorrelation curve (see the Supporting Material, S1). Several distribution functions were tested for $N(i)$. Best results are achieved using an exponential function $N(i) = N_1 p^{i-1}$ in agreement with the data obtained with quantitative gel analysis. The base is found to be $p$ = 0.64 for physiological rVWF (Fig. 4 *A*) and $p$ = 0.18 for pathological rVWF-IIC (Fig. 4 *B*).

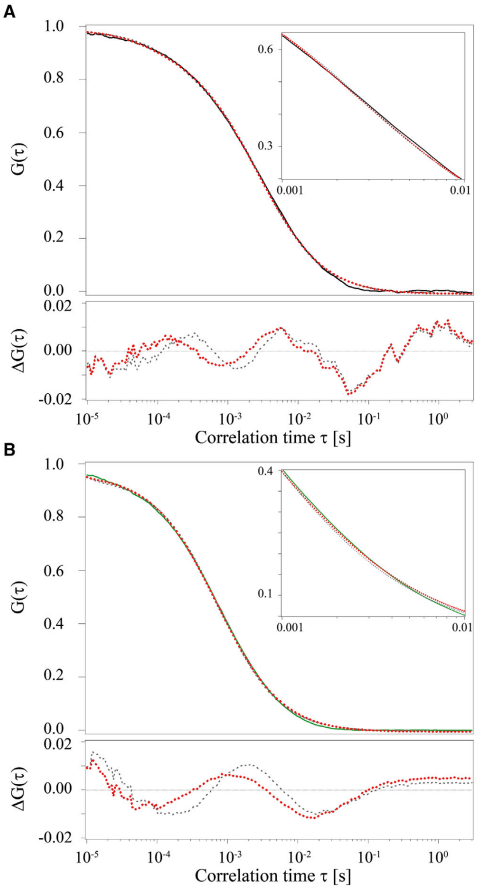


FIGURE 4 Multimer analysis of rVWF using FCS. (*A*) Multicomponent fit (*red dotted line*) of the autocorrelation function of physiological rVWF (*black line*) leads to a size distribution that decays with the base $p$ = 0.64. Furthermore, the single-component analysis (*gray dashed line*) fits the distribution well, yielding an average multimer size of $\bar{i}$ = 6.3 ± 1.4 dimers. (*B*) With the multicomponent fit (*red dotted line*) for the pathological distribution rVWF-IIC (*green line*), the base is determined to be $p$ = 0.18, indicating the lack of large VWF multimers. Single-component fit (*gray dashed line*) infers an average multimer size of $\bar{i}$ = 2.0 ± 0.1 dimers.

The best fit to the exponential distribution shows a small improvement over the initial single component analysis (Fig. 4). The fact that the multicomponent analysis is close to a single component fit is explained by the fact that the FCS autocorrelation function weights each molecule with its squared brightness (see the Supporting Material). For rVWF-eGFP the brightness scales with the number of dimers $i$, the resulting weighted size distribution

is $N'(i) = i^2\,N(i)$, which exhibits a sharp maximum at the average multimer size $\bar{i} = 4.7$. Due to the narrow weighted distribution function, the multicomponent fit appears to be close to the fit of a single species. The average multimer size is in good agreement with the average multimer size obtained with single-component analysis that yields $\bar{i} = 6.3 \pm 1.3$ for rVWF (for details see the Supporting Material S1). For the mutant rVWF-IIC with $p = 0.18$, an average multimer size of $\bar{i} = 1.5$ is calculated compared to $\bar{i} = 2.0 \pm 0.1$ measured with the single-component fit. However, it is important to note that the proper multicomponent analysis using the proposed exponential size distribution $N(i)$ describes the measured autocorrelation function the best within the experimental accuracy.

### Direct imaging of VWF with TIRFM

The data presented so far reveals an exponential size distribution of VWF. Using TIRFM, we confirmed these results by direct imaging. Under continuous excitation, the fluorescence signal of rVWF-eGFP was observed to decrease in discrete steps over time. As described in (40) and explained in detail in the Supporting Material S3, the number of bleaching steps can be taken as a measure for the number of eGFP-tagged VWF monomers. Counting bleaching steps therefore provides a means for analyzing the VWF size distribution. Measurements of an rVWF dimer sample proved that this analysis method is indeed suitable for our samples (see the Supporting Material S3).

For localizing the rVWF multimers, an average image of the first 100 frames was calculated (Fig. 5 *A*) and regions of interest were selected. Bleaching steps in the intensity-time traces of these regions were identified with the step detection algorithm described in (41) (Fig. 5, *B* and *C*). The relative frequency for detecting a certain number of steps was plotted versus the number of steps (Fig. 5 *D*) and each step number was assigned to a certain multimer size. As we count the multimer size in number of dimers $i$ but the bleaching steps scale with the number of monomers, two bleaching steps add up to an increase of one in the multimer size. Odd numbers of bleaching steps were round up to the next even number. The thereby obtained size distribution N($i$) was plotted versus the multimer size in number of dimers $i$. Fitting yields an exponentially decaying size distribution $N(i) = N_1 p^{i-1}$ with a base $p = 0.29$ (Fig. 5 *D*), convincingly confirming the findings from quantitative gel analysis and FCS.

### Effect of ADAMTS13 cleavage on VWF size distribution

The VWF size distribution is after secretion into the blood plasma dynamically controlled by the protease ADAMTS13 (Fig. 1 *D*) with defects in ADAMTS13 activity resulting in unusually large VWF that cause thrombotic thrombocytopenic purpura. We investigated this time-dependent evolution of the VWF size distribution with FCS and found systematic shifts to smaller multimer sizes that are no longer exponentially distributed. Various concentrations of ADAMTS13 were used to visualize different cleavage states. rVWF concentrated to 65% of normal plasma concentration (0.65 units/ml) was digested by 0.12, 0.25, and 1.00 units/ml ADAMTS13. As expected, the cleavage due to ADAMTS13 shifts the autocorrelation curves to higher particle numbers (lower amplitude) and shorter diffusion times (*steeper decay*). It is not possible to describe these autocorrelation curves with a multicomponent analysis with an exponentially decaying size distribution $N(i)$, indicating that the cleavage changes the shape of the distribution. Yet, using single-component analysis it is possible to extract average diffusion times of $\tau_D = 1045\ \mu s$, $813\ \mu s$, and $617\ \mu s$ (0.12, 0.25 and 1.00 units/ml ADAMTS13) (Fig. 6 *A*). We find an exponential dependence of the average multimer size in terms of dimer number $i$ on the

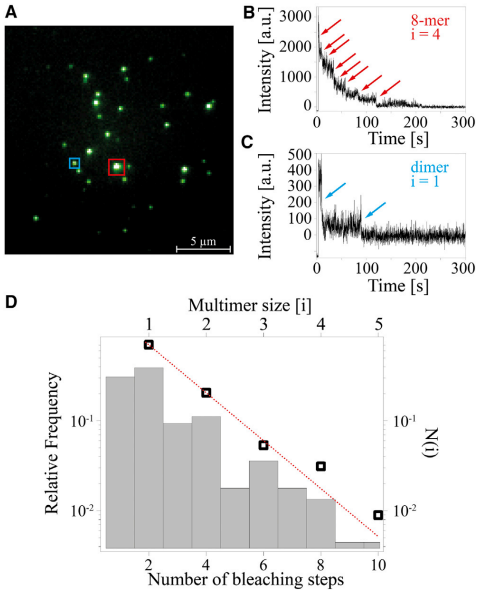


FIGURE 5 Direct imaging of rVWF using TIRFM. (*A*) TIRFM image of VWF multimers immobilized on a glass surface. The multimer size is determined by counting eGFP bleaching steps as each rVWF monomer is labeled with one eGFP. The intensity-time traces of the two highlighted molecules represent an 8-mer (*B*) and a dimer (*C*). The positions of the counted steps are indicated with arrows. (*D*) The relative frequency for detecting a certain number of steps in the intensity trace is shown as a bar chart. Size distribution analysis of $N(i)$ (*black squares*) yields, in good agreement with the results from quantitative gel analysis and FCS, an exponentially decaying size distribution $N(i) = N_1 p^{i-1}$ (*red dots*) with the base $p = 0.29$.

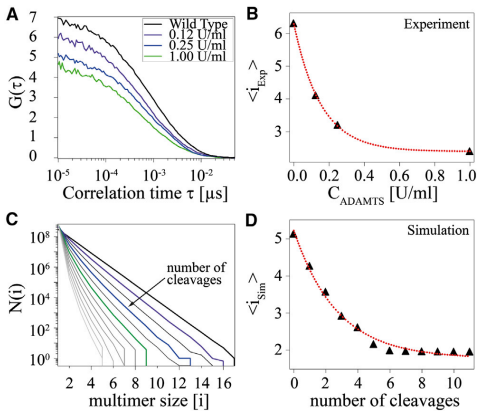


FIGURE 6 Multimer analysis after ADAMTS13-induced proteolytic cleavage. (*A*) Varying concentrations of ADAMTS13 are used to visualize different cleavage states. Correlation curves of rVWF distribution are shifted toward lower correlation times and higher particle concentrations (*lower* G(0)) with increasing protease concentration. (*B*) Single-component analysis indicates an exponential decay of the average multimer sizes with increasing ADAMTS13 concentration. (*C*) Simulation of a random cleavage process shows the changes in the size distribution due to ADAMTS13 cleavage. (*D*) Average multimer sizes decrease exponentially with an increasing number of cleavage steps per molecule. Comparing the decay constant in (*B*) and (*D*), ~0.1 units/ml ADAMTS13 and one cleavage step per molecule lead to a similar effect on the average multimer size.

ADAMTS13 concentration with $\bar{i} = 4.5$, 2.6, and 1.2, corresponding to 0.12, 0.25, and 1.00 units/ml concentration of ADAMTS13 (Fig. 6 *B*).

To get an estimate of the size distribution in the presence of ADAMTS13, the cleavage process was simulated based on a model that assumes random cleavage sites combined with equal cleavage probability for all multimer sizes (Fig. 6 *C*). Starting with the measured exponentially shaped multimer distribution, each iteration cuts each multimer once at a random site. For each iteration, the average multimer size of the generated size distribution is calculated and plotted against the number of cleavage steps (Fig. 6 *D*). Comparison of experiment and simulation (Fig. 6, *C* and *D*), shows that the average multimer size scales exponentially with the number of cleavages of each molecule, with ~0.1 units/ml ADAMTS13 and one cleavage step resulting in the same average multimer size. This means that a 0.1 units/ml ADAMTS13 concentration is necessary to cleave each molecule of a 0.65 units/ml VWF concentration once within 5 h.

## DISCUSSION

In this article, we found independent evidence that the size of recombinant VWF is exponentially distributed. First quantitative gel analysis of VWF based on antibody staining indicates an exponential size distribution, second a FCS multicomponent analysis of recombinant VWF-eGFP proves consistent with the proposed distribution function, and finally the frequency distribution obtained from direct single molecule fluorescence imaging yields an exponential dependence for the first five VWF-eGFP multimer sizes. An exponential size distribution as such is not unexpected and well known for both equilibrium polymers (42) and linear condensation polymers (8). An equilibrium polymer forms by reversible association of subunits with mutual binding constant affinity. Prominent examples for equilibrium polymers are actin, microtubulin, and other cytoskeleton filaments (43). Linear condensation polymers are formed by irreversible growth mechanisms. It is well established that VWF is a covalently linked multimer as the VWF multimerization occurs via formation of disulfide bonds. Furthermore, it is understood that the VWF multimerization takes place in the Golgi, where the propeptide of VWF itself acts as oxidoreductase, thereby facilitating disulfide bond formation that allows VWF to polymerize in this compartment (12–14). An exponential size distribution results if the reactivity of subunits is independent of the segment size and takes place in a finite compartment. In this case, the molar fraction of segments containing $i$ subunits is given by Eq. 1. The distribution is fully determined by a single parameter, the extent of polymerization, $p$. This extent of polymerization is limited both by the reaction rate of the VWF molecules to each other and by the reaction time, which is determined by the time the VWF remains in the Golgi. We find that the fraction of polymerized dimers is $p_{rVWF} = 0.70 \pm 0.02$ for rVWF and $p_{rVWF\text{-}IIC} = 0.22 \pm 0.01$ in case of the pathological form rVWF-IIC. It is noteworthy that for the disease mutant VWF-IIC, the exponentially decaying size distribution is maintained indicating that the mechanism of biosynthesis is the same. As aberrances in the size distribution of VWF-IIC are caused by mutations in the VWF propeptide that prevent multimerization in the Golgi (44), a decreased reaction rate can be assumed and explains the lower extent of polymerization.

The fact that the exponential VWF size distribution is in accordance with a step-growth reaction mechanism allows the quantification of a VWF distribution by a single parameter. Knowing the extent of polymerization p yields the entire range of multimers. An interesting finding is the fact that the extent of polymerization is in general fairly low with far less long multimers being formed than hitherto expected. For the physiological distribution rVWF, 30% of VWF dimers remain as non-polymeric species. Multimers consisting of five or more dimers account for only 24% of the total number of VWF molecules whereas multimers containing 10 or more dimers represent just 4%. Hence, the polymeric form of VWF that is supposed to be the one most relevant for VWF function is a minority species of VWF. Secondly, as characteristic for the base of an

exponential function, already small changes in p have a strong leverage on the multimer distribution and consequently a detrimental impact on the physiological state. A loss of 25% in the extent of polymerization reduces the number of 10mers by a factor of 100.

The size distribution of VWF is changed upon secretion to the blood plasma by ADAMTS13-induced cleavage. We used rVWF to mimic this cleavage process. Varied cleavage states represented by different concentrations of ADAMTS13 can be clearly distinguished from uncleaved rVWF. The exponentially shaped size distribution is not maintained during cleavage. Simulation of a random cleavage process allows us to relate the ADAMTS13 concentration to a certain number of cleavage steps. We show that cleavage with 0.1 units/ml ADAMTS13 concentration under partly denaturing condition in urea has the same effect on the average multimer size as cutting each VWF molecule once at a random site. In blood plasma, ADAMTS13-induced cleavage is assumed to require shear-induced stretching of VWF. We find that the size distribution of healthy patients exhibits almost the same exponential size dependence as recombinantly expressed VWF. Small deviations at larger size fractions could be indicative of extracellular ADAMTS13 activity in blood flow. Interestingly, the size distribution of patients exhibiting von Willebrand disease type IIC showed less deviation from the normal case as predicted from the recombinant expressed VWF-IIC. It must be assumed that the deficiency in the extent of polymerization is partly compensated, possibly by VWF expelled from Weibel-Palade bodies. Plasma VWF is essential for the initiation of blood coagulation but is immediately joined by VWF stored in the granules of endothelium cells (Weibel-Palade bodies) at the beginning of hemostasis so that long VWF multimers can be provided whenever needed.

From a measurement technique point of view, we showed that FCS is capable of following the evolution of VWF size distribution under blood plasma conditions. This opens up the possibility to use recombinant VWF-eGFP in combination with FCS as a diagnostic assay for ADAMTS13 activity in hematology. Moreover, FCS has the capability to use shear forces during measurement. Therefore, experiments with urea as a stretcher could become redundant and be replaced by measurements under shear flow in situ.

## CONCLUSION

In this work, we reported on the exponential size distribution of recombinant and physiological VWF multimers. We found evidence that the exponential distribution is the generic outcome of VWF biosynthesis as disease-related VWF mutant VWF-IIC also exhibits an exponential size distribution, albeit with a smaller extent of polymerization. In light of this finding, we hypothesize that the disease-related mutation type IIC affects the polymerization reaction. We show that FCS allows for monitoring the change in VWF-eGFP size distribution under blood plasma conditions over time. In particular, ADAMTS13 activity was measured and it was shown that the decreasing average VWF size is in agreement with the expected evolution of an exponential distribution under random cleavage. We believe that the extent of polymerization, describing the size distribution of VWF, provides a valuable indicator in VWF-related disease diagnostics and that FCS proves valuable as a quantitative tool to follow the evolution of VWF size distribution in vitro over time.

## SUPPORTING MATERIAL

Two figures, supporting analysis, and references (45,46) are available at http://www.biophysj.org/biophysj/supplemental/S0006-3495(13)00859-X.

We thank Hanna Engelke for fruitful discussions and reading the manuscript. Mathias Strackharn and Stephan Heucke are gratefully acknowledged for their support with the TIRFM setup.

This work was supported with seed funds from the Center for NanoScience and the priority network within the Deutsche Forschungsgemeinschaft SHENC (Shear Flow Regulation of Hemostasis - bridging the gap between Nanomechanics and Clinical presentation), DFG research unit FOR 1543. We thank all SHENC members, especially Maria A. Brehm. S.L. thanks the support by the Elite Network of Bavaria.

## REFERENCES

1. Sadler, J. E. 1998. Biochemistry and genetics of von Willebrand factor. *Annu. Rev. Biochem.* 67:395–424.
2. Ruggeri, Z. M. 2001. Structure of von Willebrand factor and its function in platelet adhesion and thrombus formation. *Best Pract. Res. Clin. Haematol.* 14:257–279.
3. Ruggeri, Z. M. 1997. von Willebrand factor. *J. Clin. Invest.* 99:559–564.
4. Furlan, M., R. Robles, and B. Lämmle. 1996. Partial purification and characterization of a protease from human plasma cleaving von Willebrand factor to fragments produced by in vivo proteolysis. *Blood.* 87:4223–4234.
5. Siedlecki, C. A., B. J. Lestini, …, R. E. Marchant. 1996. Shear-dependent changes in the three-dimensional structure of human von Willebrand factor. *Blood.* 88:2939–2950.
6. Schneider, S. W., S. Nuschele, …, M. F. Schneider. 2007. Shear-induced unfolding triggers adhesion of von Willebrand factor fibers. *Proc. Natl. Acad. Sci. USA.* 104:7899–7903.
7. Zhang, X., K. Halvorsen, …, T. A. Springer. 2009. Mechanoenzymatic cleavage of the ultralarge vascular protein von Willebrand factor. *Science.* 324:1330–1334.
8. Flory, P. J. 1936. Molecular size distribution in linear condensation polymers. *J. Am. Chem. Soc.* 58:1877–1885.
9. Wagner, D. D. 1990. Cell biology of von Willebrand factor. *Annu. Rev. Cell Biol.* 6:217–246.
10. Singh, I., H. Shankaran, …, S. Neelamegham. 2006. Solution structure of human von Willebrand factor studied using small angle neutron scattering. *J. Biol. Chem.* 281:38266–38275.
11. Springer, T. A. 2011. Biology and physics of von Willebrand factor concatamers. *J. Thromb. Haemost.* 9 (*Suppl 1*):130–143.
12. Wise, R. J., D. D. Pittman, …, S. H. Orkin. 1988. The propeptide of von Willebrand factor independently mediates the assembly of von Willebrand multimers. *Cell.* 52:229–236.

13. Purvis, A. R., and J. E. Sadler. 2004. A covalent oxidoreductase intermediate in propeptide-dependent von Willebrand factor multimerization. *J. Biol. Chem.* 279:49982–49988.
14. Dang, L. T., A. R. Purvis, …, J. E. Sadler. 2011. Phylogenetic and functional analysis of histidine residues essential for pH-dependent multimerization of von Willebrand factor. *J. Biol. Chem.* 286:25763–25769.
15. McCarroll, D. R., E. G. Levin, and R. R. Montgomery. 1985. Endothelial cell synthesis of von Willebrand antigen II, von Willebrand factor, and von Willebrand factor/von Willebrand antigen II complex. *J. Clin. Invest.* 75:1089–1095.
16. Fay, P. J., Y. Kawai, …, V. J. Marder. 1986. Propolypeptide of von Willebrand factor circulates in blood and is identical to von Willebrand antigen II. *Science.* 232:995–998.
17. de Wit, T. R., and J. A. van Mourik. 2001. Biosynthesis, processing and secretion of von Willebrand factor: biological implications. *Best Pract. Res. Clin. Haematol.* 14:241–255.
18. Tsai, H. M. 1996. Physiologic cleavage of von Willebrand factor by a plasma protease is dependent on its conformation and requires calcium ion. *Blood.* 87:4235–4244.
19. Gaucher, C., J. Diéval, and C. Mazurier. 1994. Characterization of von Willebrand factor gene defects in two unrelated patients with type IIC von Willebrand disease. *Blood.* 84:1024–1030.
20. Schneppenheim, R., K. B. Thomas, …, B. Zieger. 1995. Identification of a candidate missense mutation in a family with von Willebrand disease type IIC. *Hum. Genet.* 95:681–686.
21. Schneppenheim, R., J. J. Michiels, …, U. Budde. 2010. A cluster of mutations in the D3 domain of von Willebrand factor correlates with a distinct subgroup of von Willebrand disease: type 2A/IIE. *Blood.* 115:4894–4901.
22. Schneppenheim, R., H. Plendl, and U. Budde. 1988. Luminography—an alternative assay for detection of von Willebrand factor multimers. *Thromb. Haemost.* 60:133–136.
23. Budde, U., R. Schneppenheim, …, I. Peake. 2008. Detailed von Willebrand factor multimer analysis in patients with von Willebrand disease in the European study, molecular and clinical markers for the diagnosis and management of type 1 von Willebrand disease (MCMDM-1VWD). *J. Thromb. Haemost.* 6:762–771.
24. Magde, D., E. Elson, and W. W. Webb. 1972. Thermodynamic fluctuations in a reacting system-measurement by fluorescence correlation spectroscopy. *Phys. Rev. Lett.* 29:705–708.
25. Elson, E. L., and D. Magde. 1974. Fluorescence correlation spectroscopy. I. Conceptual basis and theory. *Biopolymers.* 13:1–27.
26. Magde, D., E. L. Elson, and W. W. Webb. 1974. Fluorescence correlation spectroscopy. II. An experimental realization. *Biopolymers.* 13:29–61.
27. Rigler, R., Ü. Mets, …, P. Kask. 1993. Fluorescence correlation spectroscopy with high count rate and low background: analysis of translational diffusion. *Eur. Biophys. J.* 22:169–175.
28. Petrov, E. P., and P. Schwille. 2008. State of the art and novel trends in fluorescence correlation spectroscopy. *In* Standardization and Quality Assurance in Fluorescence Measurements II. U. Resch-Grenger, editor. Springer, pp. 145–197.
29. Thompson, N. L. 1991. Fluorescence correlation spectroscopy. *In* Topics in Fluorescence Spectroscopy, Vol. 1. J. R. Lakowicz, editor. Plenum Press, New York, pp. 337–378.
30. Engelke, H., I. Dorn, and J. O. Rädler. 2009. Diffusion and molecular binding in crowded vesicle solutions measured by fluorescence correlation spectroscopy. *Soft Matter.* 5:4283–4289.
31. Zanardelli, S., A. C. K. Chion, …, D. A. Lane. 2009. A novel binding site for ADAMTS13 constitutively exposed on the surface of globular VWF. *Blood.* 114:2819–2828.
32. Alkaabi, K. M., A. Yafea, and S. S. Ashraf. 2005. Effect of pH on thermal- and chemical-induced denaturation of GFP. *Appl. Biochem. Biotechnol.* 126:149–156.
33. Axelrod, D. 1981. Cell-substrate contacts illuminated by total internal reflection fluorescence. *J. Cell Biol.* 89:141–145.
34. Kufer, S. K., M. Strackharn, …, H. E. Gaub. 2009. Optically monitoring the mechanical assembly of single molecules. *Nat. Nanotechnol.* 4:45–49.
35. Gumpp, H., S. W. Stahl, …, H. E. Gaub. 2009. Ultrastable combined atomic force and total internal fluorescence microscope. *Rev. Sci. Instrum.* 80:063704–063705.
36. Pruss, C. M., C. R. P. Notley, …, D. Lillicrap. 2008. ADAMTS13 cleavage efficiency is altered by mutagenic and, to a lesser extent, polymorphic sequence changes in the A1 and A2 domains of von Willebrand factor. *Br. J. Haematol.* 143:552–558.
37. Petrásek, Z., and P. Schwille. 2008. Precise measurement of diffusion coefficients using scanning fluorescence correlation spectroscopy. *Biophys. J.* 94:1437–1448.
38. Seyfried, B. K., G. Friedbacher, …, P. L. Turecek. 2010. Comparison of plasma-derived and recombinant von Willebrand factor by atomic force microscopy. *Thromb. Haemost.* 104:523–530.
39. Torres, R., J. R. Genzen, and M. J. Levene. 2012. Clinical measurement of von Willebrand factor by fluorescence correlation spectroscopy. *Clin. Chem.* 58:1010–1018.
40. Ulbrich, M. H., and E. Y. Isacoff. 2007. Subunit counting in membrane-bound proteins. *Nat. Methods.* 4:319–321.
41. Opfer, J., and K.-E. Gottschalk. 2012. Identifying discrete states of a biological system using a novel step detection algorithm. *PLoS ONE.* 7:e45896.
42. Hill, T. L. 1987. Linear aggregation theory in cell biology. Springer-Verlag, New York.
43. Howard, J. 2001. Mechanics of motor proteins and the cytoskeleton. Sinauer Associates, Sunderland, MA.
44. Sadler, J. E., U. Budde, …, A. B. Federici; Working Party on von Willebrand Disease Classification. 2006. Update on the pathophysiology and classification of von Willebrand disease: a report of the Subcommittee on von Willebrand Factor. *J. Thromb. Haemost.* 4:2103–2114.
45. Rouse, Jr., P. E. 1953. A theory of the linear viscoelastic properties of dilute solutions of coiling polymers. *J. Chem. Phys.* 21:1272–1280.
46. Inoué, S., O. Shimomura, …, P. T. Tran. 2002. Fluorescence polarization of green fluorescence protein. *Proc. Natl. Acad. Sci. USA.* 99:4272–4277.

## A.3 Publication 3: von Willebrand factor is dimerized by protein disulfide isomerase

# von Willebrand factor is dimerized by protein disulfide isomerase

by

Svenja Lippok, Katra Kolsek, Achim Löf, Dennis Eggert, Willem Vanderlinden, Jochen P. Müller, Gesa König, Tobias Obser, Karoline Röhrs, Sonja Schneppenheim, Ulrich Budde, Carsten Baldauf, Camilo Aponte-Santamaría, Frauke Gräter, Reinhard Schneppenheim, Joachim O. Rädler, and Maria A. Brehm

published in

Blood, Vol. 127, No. 9, 1183–1191, 2016

Regular Article

THROMBOSIS AND HEMOSTASIS

# von Willebrand factor is dimerized by protein disulfide isomerase

Svenja Lippok,[1] Katra Kolšek,[2] Achim Löf,[1] Dennis Eggert,[3,4] Willem Vanderlinden,[1,5] Jochen P. Müller,[1] Gesa König,[6] Tobias Obser,[6] Karoline Röhrs,[6] Sonja Schneppenheim,[7] Ulrich Budde,[7] Carsten Baldauf,[8] Camilo Aponte-Santamaría,[2] Frauke Gräter,[2] Reinhard Schneppenheim,[6] Joachim O. Rädler,[1] and Maria A. Brehm[6]

[1]Faculty of Physics and Center for NanoScience, Ludwig Maximilian University, Munich, Germany; [2]Molecular Biomechanics Group, Heidelberg Institute for Theoretical Studies, Heidelberg, Germany; [3]Max Planck Institute for the Structure and Dynamics of Matter, Hamburg, Germany; [4]Microscopy and Image Analysis Technology Platform, Heinrich-Pette-Institute, Leibniz Institute for Experimental Virology, Hamburg, Germany; [5]Department of Chemistry, Division of Molecular Imaging and Photonics, Katholieke Universiteit Leuven-University of Leuven, Leuven, Belgium; [6]Department of Pediatric Hematology and Oncology, University Medical Center Hamburg-Eppendorf, Hamburg, Germany; [7]Medilys Laborgesellschaft mbH, Hemostaseology, Asklepios Klinik Altona, Hamburg, Germany; and [8]Fritz-Haber-Institut der Max-Planck-Gesellschaft, Berlin, Germany

**Key Points**

- The protein disulfide isomerase is involved in VWF dimerization by initiating disulfide bond formation at cysteines 2771 and 2773.
- von Willebrand disease-associated mutations in the dimerization domain of von Willebrand factor disturb processing by the protein disulfide isomerase.

**Multimeric von Willebrand factor (VWF) is essential for primary hemostasis. The biosynthesis of VWF high-molecular-weight multimers requires spatial separation of each step because of varying pH value requirements. VWF is dimerized in the endoplasmic reticulum by formation of disulfide bonds between the C-terminal cysteine knot (CK) domains of 2 monomers. Here, we investigated the basic question of which protein catalyzes the dimerization. We examined the putative interaction of VWF and the protein disulfide isomerase PDIA1, which has previously been used to visualize endoplasmic reticulum localization of VWF. Excitingly, we were able to visualize the PDI–VWF dimer complex by high-resolution stochastic optical reconstruction microscopy and atomic force microscopy. We proved and quantified direct binding of PDIA1 to VWF, using microscale thermophoresis and fluorescence correlation spectroscopy (dissociation constants $K_D$ = 236 ± 66 nM and $K_D$ = 282 ± 123 nM by microscale thermophoresis and fluorescence correlation spectroscopy, respectively). The similar $K_D$ (258 ± 104 nM) measured for PDI interaction with the isolated CK domain and the atomic force microscopy images strongly indicate that PDIA1 binds exclusively to the CK domain, suggesting a key role of PDIA1 in VWF dimerization. On the basis of protein–protein docking and molecular dynamics simulations, combined with fluorescence microscopy studies of VWF CK-domain mutants, we suggest the following mechanism of VWF dimerization: PDI initiates VWF dimerization by forming the first 2 disulfide bonds Cys2771-2773′ and Cys2771′-2773. Subsequently, the third bond, Cys2811-2811′, is formed, presumably to protect the first 2 bonds from reduction, thereby rendering dimerization irreversible. This study deepens our understanding of the mechanism of VWF dimerization and the pathophysiological consequences of its inhibition. (*Blood*. 2016;127(9):1183-1191)**

## Introduction

von Willebrand factor (VWF) is a multimeric glycoprotein essential for platelet-dependent primary hemostasis. The shear-induced transition between a globular and a stretched conformation of VWF high-molecular-weight multimers (HMWMs) leads to exposure of binding sites for VWF partners, and thus the initiation of platelet adhesion and aggregation. Because smaller multimers experience lower shear forces than larger ones, VWF's shear stress-activated functions are dependent on multimer size.[1,2] Mutations within the VWF gene can lead to the inhibition of the VWF multimerization process, and thereby cause distinct forms of the bleeding disorder von Willebrand disease (VWD). To understand the pathomechanism behind these VWD variants, it is of paramount interest to unravel the details of VWF multimerization, which is established by the formation of intermolecular disulfide bonds.

The individual steps of VWF-HMWM biosynthesis rely on distinct pH conditions, which are realized by spatial separation of the involved processes to different cell organelles. The first multimerization step (dimerization) happens in the endoplasmic reticulum (ER) by disulfide bond formation between the C-terminal cysteine knot (CK) domains. The recently solved crystal structure revealed that 8 of the 11 cysteine residues within the CK domain form intrachain disulfide bonds, whereas 3 (namely, Cys2771, Cys2773, and Cys2811) are used to form the interchain connections for dimerization by formation of the 3 disulfide bonds (Cys2771-2773′, Cys2771′-2773, and Cys2811-2811′),[3] as suggested by Katsumi et al.[4] Dimerization is strongly disturbed in patients with CK domain mutations.[5]

The second multimerization step, the formation of N-terminal disulfide bonds between the D′-D3 assemblies of VWF dimers, occurs

Submitted April 22, 2015; accepted December 8, 2015. Prepublished online as *Blood* First Edition paper, December 15, 2015; DOI 10.1182/blood-2015-04-641902.

The online version of this article contains a data supplement.

The publication costs of this article were defrayed in part by page charge payment. Therefore, and solely to indicate this fact, this article is hereby marked "advertisement" in accordance with 18 USC section 1734.

in the trans-Golgi network and is facilitated by the VWF propeptide that consists of 2 D assemblies that both harbor a CGLC protein disulfide isomerase consensus sequence, which is also present in the D3 assembly. Enabled by the lower pH of the Golgi apparatus, this intrinsic oxidoreductase function is activated by protonation of histidine residues adjacent to these CGLC sequences.[6] Mutations within these sequences inhibit multimerization but do not affect dimerization. Therefore, dimerization does not appear to be performed by an intrinsic oxidoreductase activity within VWF.

Because dimerization occurs within the ER at neutral pH, it requires an ER-localized member of the thiol-disulfide oxidoreductase family. The protein disulfide isomerase PDI is one of the few members of this protein family that is known to catalyze disulfide bond formation and reduction, as well as isomerization. It has previously been described that VWF colocalizes with PDI to prove VWF ER localization.[7] Here we investigated whether PDIA1 might be the protein that dimerizes VWF.

## Materials and methods

### Immunofluorescence

Immunofluorescence was performed with transfected HEK293 or nontransfected human umbilical vein endothelial cells (HUVECs), as previously described by Brehm et al.[8] Antibodies used were rabbit anti-VWF (DAKO; 1:1000), mouse anti-PDI (abcam, 1:500, PDIA1 specific), goat anti-rabbit AF488 (Invitrogen, 1:5000), and goat anti-mouse AF546 (Invitrogen, 1:5000). Images were captured at room temperature (RT) with a confocal microscope (TCS SP5; Leica, Wetzlar, Germany) or the fluorescence microscope BZ9000 (Keyence). For settings, please refer to the respective figure legends.

### Coimmunoprecipitation

Coimmunoprecipitation was performed as described.[9] For details, please refer to the supplemental Methods, available on the *Blood* Web site.

### Stochastic optical reconstruction microscopy

Imaging was performed in Ibidi treat 8-well μ-slides (Ibidi), using an imaging buffer containing 100 mM β-mercaptoethylamine in phosphate-buffered saline to facilitate sufficient blinking of the fluorophores.[10] Stochastic optical reconstruction microscopy (STORM) data sets were acquired on a Nikon N-STORM microscope equipped with an Apo TIRF 100× oil immersion objective with a numerical aperture of 1.49 (Nikon GmbH, Düsseldorf, Germany), a back-illuminated electron-multiplying charge-coupled device (EMCCD) camera (iXon+ DU-897; Andor Technology Plc., Belfast, Northern Ireland), and a quadband filter composed of a quadline beamsplitter (zt405/488/561/640rpc TIRF; Chroma Technology Corporation, Bellows Falls, VT) and a quadline emission filter (brightline HC 446, 523, 600, 677; Semrock Inc., Rochester, NY) with an inclined illumination scheme[11] to achieve a good signal-to-noise ratio. For excitation of Alexa Fluor 647, a 647-nm continuous-wave fiber laser (2RU-VFL-P-300-647; MPB Communications Inc., Montréal, Canada), and for Alexa Fluor 488 the 488-nm line of an argon gas laser (35-IMA-840-019; Melles Griot GmbH, Bensheim, Germany), was used. For multicolor imaging, the lasers were switched on and off alternately, controlled by an acousto-optic tunable filter. The integration time of the EMCCD camera was set to 16 ms per frame, with an EM gain of 300. Super-resolution images were reconstructed from a series of 12 500 images per channel, using the N-STORM analysis module v. 3.3.1.15801 of NIS Elements AR v. 4.20 (Laboratory imaging s.r.o., Prague, Czech Republic), with overlapping peak detection enabled.

### Atomic force microscopy

Atomic force microscopy (AFM) imaging was performed in tapping mode in air, using an MFP-3D AFM (Asylum Research, Santa Barbara, CA) and silicon tips (AC160TS-R3; Olympus, Japan), with resonance frequencies of approximately 300 kHz and a nominal spring constant of 26 N/m. Images of 1 $\mu m^2$ were recorded with a resolution of 1024 × 1024 pixels and analyzed using SPIP software (Image Metrology, Denmark). Substrate preparation was performed as described.[12] Protein samples containing purified, recombinant VWF dimers (50 nM), recombinant human PDIA1 (100 nM) (Genway Biotech Inc., San Diego, CA), or a mixture of both proteins were incubated at pH 7.4 for 45 min at RT in buffer (20 mM HEPES, 150 mM NaCl, 20 mM EDTA) and quickly diluted 10-fold before sample deposition on the functionalized mica substrates. For details on AFM, protein expression, purification, and VWF:Ag ELISA, please refer to supplemental Material.

### Sample preparation for binding studies

Human PDIA1 (Genway Biotech. Inc, San Diego, CA) was labeled with Alexa Fluor 647 carboxylic acid, succinimidyl ester (Life Technologies GmbH, Darmstadt, Germany). Measurements were conducted in 5 mM Tris buffer containing 500 mM NaCl and 2.5 mM $CaCl_2$ at 21°C. A fixed concentration of labeled PDI (microscale thermophoresis [MST], 25 nM; fluorescence correlation spectroscopy [FCS], 3 nM) was titrated against varying concentrations of recombinant wild-type (wt) VWF, p.Cys2771Arg, and the isolated CK domain. Samples were incubated for 30 min at RT before measurement.

### MST

For MST experiments, a Monolith NT.115 system (NanoTemper Technologies, Munich, Germany) was used. Fifteen percent infrared laser and 20% light-emitting diode power were applied for generating local temperature gradients and illumination, respectively. Laser on and off times were set at 60 and 10 s, respectively. Cold fluorescence was averaged over a time period of 5 s before the temperature jump, and the warm fluorescence signal was averaged over 30 s, starting 5 s after the temperature jump. About 5-μL sample volumes were filled into standard treated capillaries (NanoTemper Technologies) for measurements. For the theoretical background and MST data analysis,[13,14] please refer to supplemental Material.

### FCS

FCS experiments were performed on an Axiovert 200 microscope with a ConfoCor2 unit (Carl Zeiss, Jena, Germany) equipped with a 40× (NA = 1.2) water immersion apochromat objective (Carl Zeiss, Jena). For sample illuminations, a 633 HeNe laser was used. Samples were measured in 8-well LabTekI chamber slides (Nunc, Rochester, NY) 3 times for 10 × 180 s. For details on FCS data analysis and theoretical background, refer to supplemental Material.

### PDI inhibitor studies

HUVECs in 8-well chamber slides (Ibidi) were incubated with 80 nM phorbol 12-myristate 13-acetate (PMA) for 25 min at 37°C/5% $CO_2$ to induce VWF release from Weibel Palade bodies (WPBs).[15] Cells were washed 5-fold with phosphate-buffered saline, and either medium or medium containing 2 μM 16F16 (Sigma-Aldrich, Taufkirchen, Germany) or 100 nM phenylarsine oxide (PAO, Merck Chemicals, Darmstadt, Germany) was added. After indicated times, VWF was detected by immunofluorescence. To visualize all WPBs within the cells, merged Z-stack images were recorded using the quick-full-focus function of the BZ9000 Keyence fluorescence microscope. In parallel, the same experiment was performed with HUVECs in 6-well plates, and after 4 and 8 h, cell lysates were prepared and investigated by standard Western Blot techniques (for details, refer to the supplemental Material).

### Protein–protein docking

Protein–protein docking was employed to study interactions between the VWF CK dimer and the catalytic region of PDI (the A domain). Structures of the CK dimer, in its reduced form, were extracted from molecular dynamics (MD) simulations (for details, see supplemental Material). CK dimer conformations, sampled during the MD simulations, were clustered based on their root mean square deviation (clustering cutoff of 0.15 nm), and 5 representative structures were selected. Five structures of the oxidized PDI A domain were picked from the nuclear magnetic resonance spectroscopy ensemble of conformations (Protein

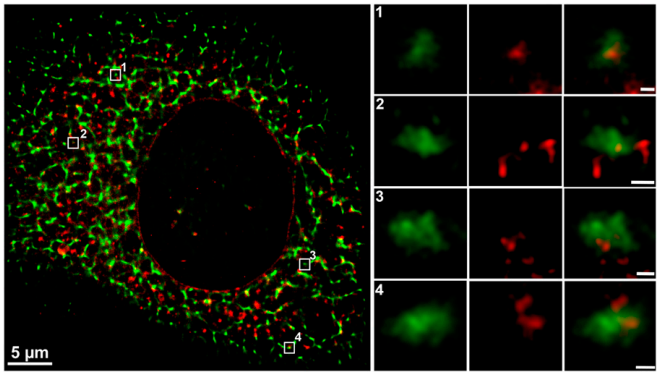


**Figure 1. Interaction of PDI and VWF shown by 2-color STORM super-resolution microscopy.** Endogenous VWF and PDI in HUVECs were detected by indirect immunofluorescence employing rabbit anti-VWF plus goat anti-rabbit Alexa Fluor 488 (shown in green) and mouse anti-PDI plus goat anti-mouse Alexa Fluor 647 (shown in red), respectively. Colocalization is shown in yellow. Locations of magnified ROIs in the cell (left) are indicated by white squares and numbers. STORM data sets were acquired on a Nikon N-STORM microscope with an Apo TIRF 100× oil immersion objective (NA 1.49), a back-illuminated EMCCD camera, and a quadband filter composed of a quadline beam splitter and a quadline emission filter. For excitation of Alexa Fluor 647 and 488, a 647-nm continuous wave fiber laser, and the 488-nm line of an argon gas laser were used. For multicolor imaging, the lasers were switched on and off alternately, controlled by an acousto-optic tunable filter. The integration time of the EMCCD camera was set to 16 ms per frame, with an EM gain of 300. Super-resolution images were reconstructed from a series of 12 500 images per channel, using the N-STORM analysis module v. 3.3.1.15801 of NIS Elements AR v. 4.20 with overlapping peak detection enabled. Scale bar in the left cell image represents 5 μm; in magnified images, 100 nm.

Data Bank ID: 1MEK[16]) by following the identical clustering approach as for CK, but with a cutoff of 0.1 nm. To account for protein-backbone and side chain flexibility, each of the CK dimer structures was docked to each of the PDI A domain structures, resulting in 25 different docking runs. To analyze effects of the p.Cys2771Arg mutation, the same procedure was repeated using a p.Cys2771Arg-containing CK dimer. To investigate the role of the CK C-termini, additional structural models were generated by considering a truncated CK dimer, both in its wt and its mutated form, with the last 5 C-terminal

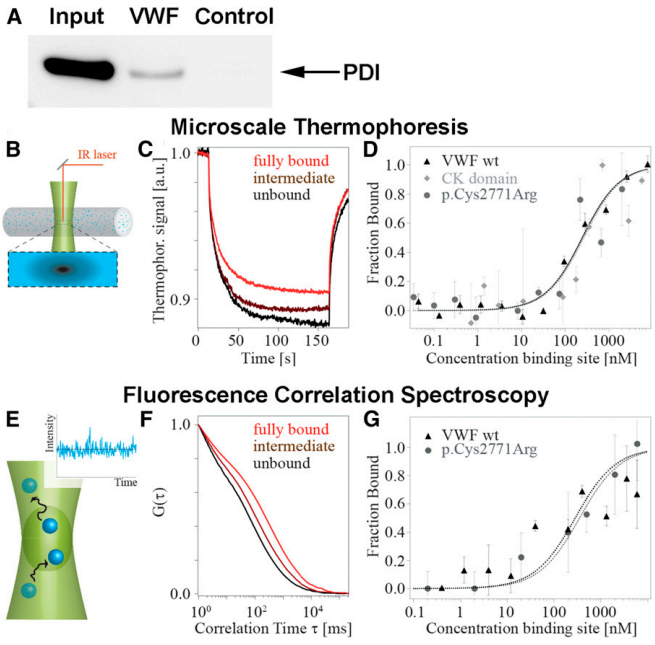


**Figure 2. PDI binds VWF.** (A) Coimmunoprecipitation of endogenous PDI and VWF from HUVEC lysates. Immunoprecipitation was performed using either rabbit anti-VWF antibody or control rabbit IgG bound to protein G-agarose. Coimmunoprecipitating proteins were separated by sodium dodecyl sulfate gel electrophoresis, and PDI was detected using mouse anti-PDI. Lanes: input, cell lysate of untreated HUVECs; VWF, immunoprecipitate from HUVEC lysate employing anti-VWF antibody; control, immunoprecipitate from HUVEC lysate employing rabbit control IgG. (B-D) MST analyzes the movement of molecules in a temperature gradient (B). (C) Binding of PDI to VWF was detected as a decrease in thermophoretic depletion. (D) PDI binds to wtVWF (black triangles), the isolated CK domain (gray squares), and p.Cys2771Arg (gray circles) with a very similar affinity ($K_D$ = 240 ± 100 nM). (E-G) FCS detects the diffusive dynamics of molecules (E). (F) Binding results in prolonged diffusion times visualized by a shift of the autocorrelation curve G(τ). (G) In agreement with the MST measurements, we detect similar affinities for wtVWF (black triangles) and mutant p.Cys2771Arg (gray circles) ($K_D$ = 300 ± 100 nM).

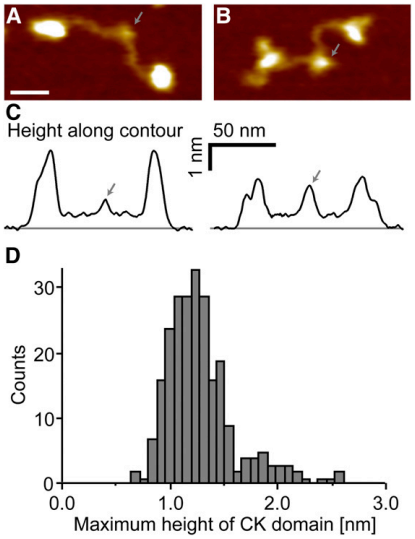


**Figure 3. Direct visualization of PDI bound to the VWF CK domain by AFM imaging.** AFM images (A-B) and respective height traces (C) of individual VWF dimers co-adsorbed with PDI. PDI-free VWF dimers (A) and PDI-complexed VWF dimers (B) show a clear difference in the apparent height of the CK domain (indicated by arrows). Heights were analyzed by tracing each dimer individually along its contour (for more details, please refer to supplemental Figures 3 and 4). Scale bar represents 20 nm; range of color scale is 2.2 nm. (D) The distribution of the maximum apparent height of n = 246 traced CK domains reveals 2 distinct peaks at approximately 1.2 and 1.9 nm, corresponding to PDI-free and PDI-complexed VWF, respectively.

amino acids of each monomer deleted. Docking calculations were carried out with PatchDock,[17] a rigid-body docking algorithm, which predicts structures of 2 proteins in complex based on their shape complementarity. Amino acids potentially participating in the binding were specified in the parameter file: the catalytic residue Cys36 of PDI and all the existing cysteines involved in interchain disulfide bonds of CK. All obtained conformations were further refined with FireDock, using suggested parameters for the full refinement.[18]

## Results

### Physiological relevance of PDI–VWF interaction

Colocalization of VWF and PDI in the ER has been observed previously,[7,19] but this putative interaction and its physiological relevance have not been described. Because the ER is the site of VWF dimerization, we hypothesized that PDI might be the protein that catalyzes the formation of the necessary interdimer disulfide bonds. This reaction would require interaction of PDI with 2 VWF monomers. To visualize these complexes, we performed high-resolution STORM of immunofluorescently labeled endogenous PDIA1 and VWF in HUVEC. We found PDI bound centrally within VWF clusters with a size of ~200 nm; the expected size of VWF dimers[20] (Figure 1; regions of interest 1-4; for antibody specificity, refer to supplemental Figure 1). The average localization precision of the STORM images is about 14 and 13 nm for Alexa Fluor 488 and 647, respectively (supplemental Figure 2). Coimmunoprecipitation of endogenous PDI and VWF from HUVEC lysates provides additional evidence for PDIA1–VWF interaction (Figure 2A). These findings support the hypothesis that PDI is involved in VWF dimerization.

### VWF and PDI are protein-binding partners

Because colocalization and coimmunoprecipitation per se do not prove direct interaction of 2 proteins, we performed extensive binding studies employing MST and FCS. These 2 methods detect complex formation by the change in movement of molecules in a temperature gradient (MST) or while diffusing through a confocal volume (FCS) after addition of a protein-binding partner. We measured binding of recombinant wtVWF to recombinant fluorescently labeled PDIA1 (Figure 2B-G) and demonstrated a direct interaction. To quantify this interaction, the dissociation constants were determined. The values measured by MST and FCS ($K_D$ = 236 ± 66 nM and $K_D$ = 282 ± 123 nM, respectively) indicate specific binding of intermediate strength, which would be expected for reversible protein interaction.

### PDI binds VWF exclusively within its CK domain

VWF is rich in cysteine residues that lock the tertiary structure of the VWF A1, A3, and C domains by formation of intramolecular disulfide bonds. In the C-terminal CK domain, cysteines do not only form stabilizing intramolecular disulfide bonds but also link VWF monomers through intermolecular disulfide bonds.[3] To clarify PDI's role in VWF processing, we further performed MST of PDIA1 and the isolated CK domain (Figure 2D). PDI binding to the CK domain exhibits a dissociation constant ($K_D$ of 258 ± 104 nM) similar to the $K_D$ of PDI binding to full-length VWF. These data indicate that PDI is not generally involved in VWF folding (which would require binding to all VWF domains); they rather point to exclusive binding of PDI to the CK domain of VWF. To confirm this hypothesis, we imaged adsorbed VWF dimers with PDIA1 in AFM tapping mode (Figure 3). As expected by the $K_D$ value for VWF–PDI binding, PDI was not bound to all VWF dimers (supplemental Figure 3). To distinguish VWF dimers without (Figure 3A) and with (Figure 3B) PDI bound to the CK domain, we quantified the apparent height of the CK domain by tracing each dimer individually along its contour (Figure 3C and supplemental Figure 3). A distribution of the maximum height yielded 2 distinct peaks (Figure 3D). The first peak, at 1.2 nm, coincides with the only peak for PDI-free VWF (supplemental Figure 4A), and the second peak, at 1.9 nm, matches the height expected for a complex of the CK domain and PDI (free mean apparent height of PDI is 0.6 nm; supplemental Figure 4B). Importantly, we did not observe binding of PDI to any VWF domain other than CK.

### PDI activity is required for VWF dimerization

To provide more evidence that it is exclusively the activity of PDI that is required for VWF dimerization, we investigated the effects of PDI inhibition on VWF processing. We stimulated HUVECs (Figure 4A) with PMA to deplete the cells of VWF stored in WPBs (Figure 4B), as previously described.[15] Then we observed the recovery of WPB formation in the absence and presence of the PDI inhibitors 16F16[21] and PAO.[22] As described previously,[23] the first small WPB-like structures were observed after 4 h (Figure 4C), and full recovery of cigar-shaped WPBs was reached after 8 h in the absence of PDI inhibitors (Figure 4F). In contrast, WPB formation was completely abolished in cells treated with 16F16 (Figure 4D,G) and strongly reduced in the PAO-treated cells (Figure 4E,H), indicating that VWF dimerization was inhibited, leading to loss of VWF multimers, and thus WPBs. The incomplete inhibition by PAO can most likely be explained by the concentration

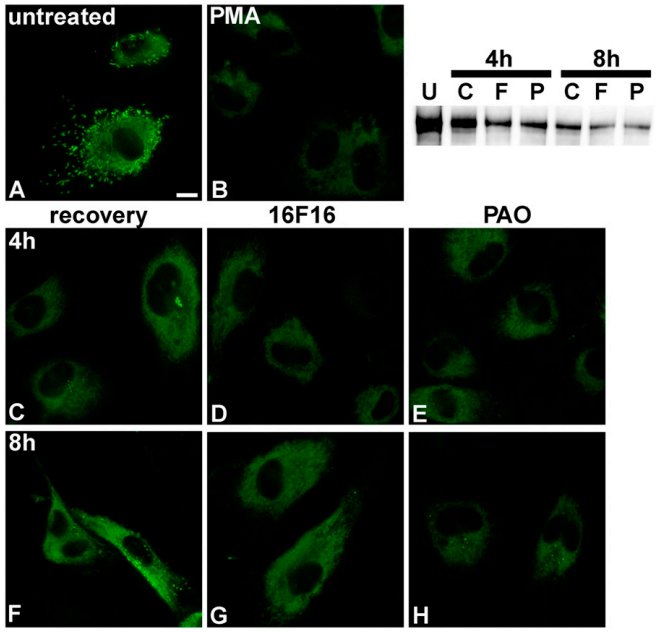


**Figure 4. Influence of PDI inhibitors on VWF processing.** HUVECs (A) were incubated with 80 nM PMA for 25 min at 37°C/5% $CO_2$ to induce VWF release from WPBs (B). Cells were washed 5-fold with phosphate-buffered saline, and either medium (C,F) or medium containing 2 μM 16F16 (D,G) or 100 nM PAO (E,H) was added. After 4 h (C-E) and 8 h (F-H), VWF was detected by immunofluorescence. Images that combine all planes of the cells were imaged, using the quick-full-focus function of the BZ9000 fluorescence microscope (Keyence) equipped with a CFI Plan Apo λ 60× H oil objective (Nikon). Representative images of 1 of 5 independent experiments are shown. Scale bar represents 10 μm. The western blot shows VWF dimers in HUVEC lysates before PMA treatment (U) and after 4 and 8 hours of recovery without PDI inhibitors (C) or in the presence of 16F16 (F) or PAO (P).

below the 50% inhibition/inhibitory concentration value (12 μM)[24] we had to use because the cells did not survive concentrations of PAO higher than 500 nM. Immunofluorescence after 2 h of recovery (Figure 4B) shows residual VWF within the cells, which most likely consists of monomers and N-terminal dimers. Western blot analysis of these HUVEC lysates showed that the VWF dimer content in the inhibitor-treated cells (Figure 4, lanes F and P) is significantly lower than in the cells that were allowed to recover from PMA treatment

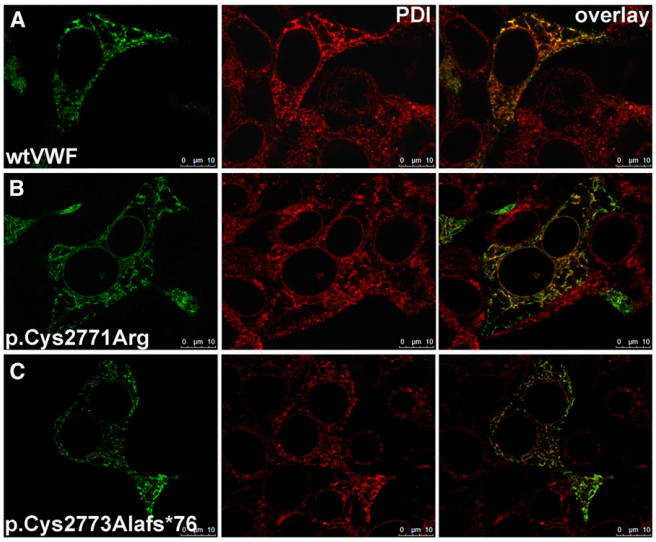


**Figure 5. Colocalization of VWF and PDI.** wtVWF (A) or VWF mutants p.Cys2771Arg (B) and p.Cys2773Alafs*76 (C) were transiently expressed in HEK293 cells. Forty-eight hours after transfection, cells were fixed and VWF proteins and PDI were detected by indirect immunofluorescence employing rabbit anti-VWF and mouse anti-PDI antibodies; secondary antibodies were goat anti-rabbitAF488 and goat anti-mouseAF546. Images were recorded with a confocal microscope (TCS SP5, Leica), using an HC PL APO CS2 63.0 × 1.40 oil ultraviolet objective and the following settings: image size of 512 × 512 pixels, laser power of the 543 and 488 lasers was set to 9% and 20%, respectively. Colocalization appears yellow in the overlay images; for colocalization analysis, please refer to supplemental Table 1. Scale bars represent 10 μm.

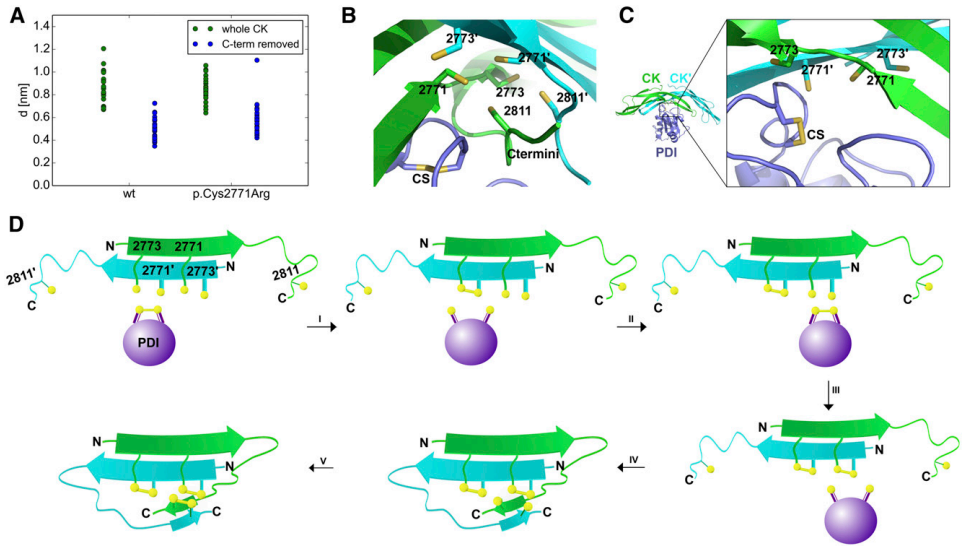


**Figure 6. Implications of the VWF CK-PDI A-domain complex from protein–protein docking.** (A) Minimum distance, *d*, between the PDI A domain catalytic site and the CK dimer cysteines involved in dimerization (sulfur–sulfur distances are shown). PDI was docked to either the wt or the hypothetical p.Cys2771Arg CK dimer. The complete dimer (green) or a truncated CK dimer (blue), lacking the C termini, was considered in each case (n = 25 for each set). (B) Typical conformation of the catalytic A domain of PDI (magenta) in complex with the wtCK dimer (monomers: green and cyan), recovered from docking. The cysteine side chains of CK and the catalytic site of PDI (CS) are shown in stick representation. CK termini prevent the CS from accessing the CK cysteines. (C) Structure of the typical docking conformation of PDI–wtCK complex (same colors and representations as in B) when the CK C-terminal amino acids were removed to mimic opening of C-termini. The PDI CS approaches the indicated CK cysteines. (D) Proposed mechanism of CK dimerization mediated by PDI.

without inhibitors (lane C) or untreated cells (lane U), indicating inhibition of the formation of new dimers after PMA treatment by PDI inhibitors. Because 16F16 is specific for PDIA1 and PDIA3,[21] these data reduce possible protein candidates for catalysis of VWF dimerization to these 2 isoforms.

### Effect of CK domain mutations on PDI–VWF interaction

In patients with VWD type 2A/IID carrying the heterozygous mutation p.Cys2771Arg, the formation of odd-numbered multimers resulting from N-terminal disulfide bonding to wt multimers was observed.[8,25] Homozygous expression yields N-terminally connected dimers only, showing a complete inhibition of the C-terminal dimerization. To investigate the mechanism of this inhibitory effect on dimerization, we performed colocalization and binding studies with the recombinant mutant. PDIA1 showed equal colocalization with mutant p.Cys2771Arg (Figure 5B; for quantification, see supplemental Table 1) compared with wtVWF (Figure 5A). The dissociation constants of p.Cys2771Arg binding to PDI, determined by both MST and FCS, exhibited values comparable to those of wtVWF–PDI binding ($K_D = 235 \pm 92$ nM [MST] and $K_D = 350 \pm 75$ nM [FCS]; Figure 2).

We further investigated colocalization of PDI and the VWF frameshift mutant p.Cys2773Alafs*76. This mutant, previously identified in patients with VWD, exhibits a single base pair deletion (8566delC) that leads to an altered amino acid sequence C-terminally of residue 2772.[26] PDI shows normal colocalization with mutant p.Cys2773Alafs*76 (Figure 5C; for quantification, see supplemental Table 1) compared with wtVWF. These data indicate that an initial association between PDI and VWF occurs N-terminally of residue 2772 before the formation of disulfide bonds.

### Mechanism of VWF dimerization by PDI

To predict potential binding modes of PDI to VWF and elucidate the order of disulfide bond formation, we first performed protein–protein docking of the catalytic A domain of PDI to the wtVWF CK domain dimer. For all the resulting conformations of the complex, the minimal distance between the catalytic site in the PDI A-domain and cysteines 2771, 2773, and 2811 of the CK dimer was between 0.6 and 1.2 nm (Figure 6A), which is too large to induce disulfide bond formation. Thus, these conformations do not correspond to any relevant catalytic state. This is a result of the presence of the CK C-termini, which obscured the accessibility of the PDI catalytic motif to cysteines Cys2771 and Cys2773 over the entire course of the simulations (Figure 6B). Although the bond linking the 2 C-termini (Cys2811-Cys2811′), was removed in the simulations, the separation between these cysteines was only observed to partially increase in the simulations (supplemental Figure 5A). We thus speculate that the conformational rearrangement of the C-termini, which gives accessibility to the catalytic cysteines Cys2771 and Cys2773, occurs on timescales beyond our simulations. Nevertheless, the lack of this bond increased the flexibility of the C-termini (supplemental Figure 5B). This result emphasizes the role of this bond stabilizing the C-termini in a conformation obstructing the catalytic cysteines. The docking procedure was repeated, this time after removal of the CK C-termini, mimicking open flexible C-termini in the absence of bond Cys2811-2811′. Now, the PDI catalytic motif was found closer to the CK cysteines 2771 and 2773, at distances between 0.35 and 0.7 nm (Figure 6C). These predicted structures of the complex likely represent realistic catalytic conformations (Figure 6C). Similar results were obtained when docking was performed with the mutant p.Cys2771Arg CK dimer: the

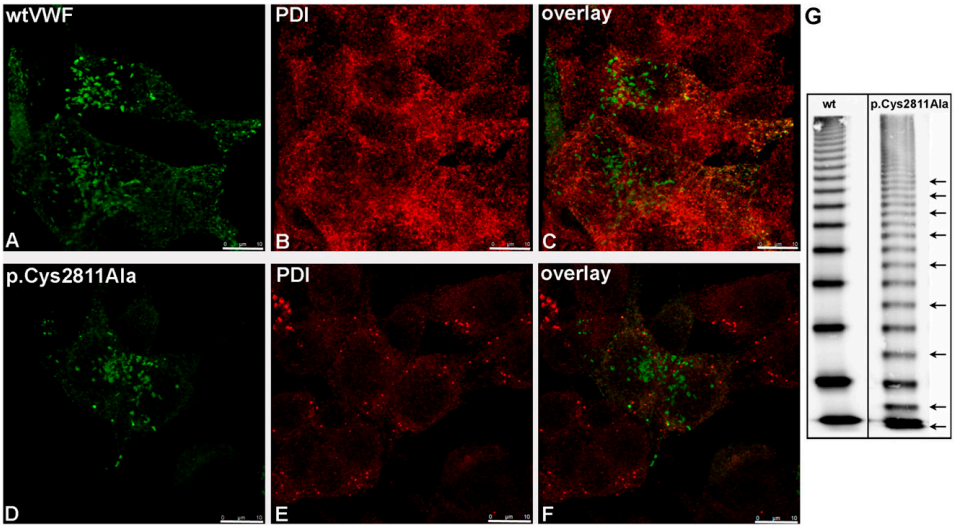


**Figure 7. Intracellular localization and multimer pattern of mutant p.Cys2811Ala.** wtVWF (A) and VWF mutant p.Cys2811Ala (D) were transiently expressed in HEK293 cells. Forty-eight hours after transfection, cells were fixed and VWF proteins (A,D) and PDI (B,E) were detected by indirect immunofluorescence employing rabbit anti-VWF and mouse anti-PDI antibodies, respectively. Z-stacks were recorded with a confocal microscope using an HC PL APO CS2 63.0 × 1.40 oil ultraviolet objective and the following settings: image size of 512 × 512 pixels, laser power of the 543 and 488 lasers was set to 9% and 20%, respectively. Overlays are shown in (C) and (F). Three-dimensional reconstruction was performed using the LAS software (Leica). Scale bars represent 10 μm. For movies of the rotating complete 3-dimensional reconstruction, please refer to supplemental Videos 1 and 2. (G) Multimer analysis of recombinant wtVWF and mutant p.Cys2811Ala was performed by sodium dodecyl sulfate–agarose gel electrophoresis and immunoblotting onto a nitrocellulose membrane with luminescent visualization. The figure is composed of one gel. The black line indicates deleted lanes with mutants not relevant for this study. Additional bands in mutant p.Cys2811Ala resulting from odd-numbered multimers are indicated by black arrows. For resolution of the monomer and dimer band, please refer to supplemental Figure 6.

PDI catalytic site approached the remaining Cys2773 only upon removal of the CK C-termini. The distances are comparable to those observed in calculations with the wtCK dimer (Figure 6A), suggesting binding in a catalytically inactive state. Taken together, our docking results suggest that PDI initiates VWF dimerization by catalyzing the formation of the Cys2771-2773′ and Cys2771′-2773 disulfide bonds. This reaction must occur before closing of the Cys2811-2811′ disulfide bond. The Cys2811-2811′ link thus most likely stabilizes the termini in a conformation shielding the other 2 disulfide bonds and renders them inaccessible to the enzyme and the environment. The stabilizing role of this link is supported by the observation of higher structural diversion and fluctuations of the reduced C-terminal β-hairpin even within the microsecond timescale of our simulations (supplemental Figure 5B).

#### Importance of disulfide bond Cys2811-2811′

The existence of bond Cys2811-2811′ in VWF dimers has been described by Zhou et al.,[3] but no patients with VWD carrying a Cys2811 mutation have been identified. Therefore, no clinical evidence is available to explain the importance of disulfide bond Cys2811-2811′. To confirm our hypothesis that this bond is necessary to stabilize dimerization, we cloned mutant p.Cys2811Ala and recombinantly expressed it in HEK293 cells. The intracellular localization of this mutant (Figure 7B; supplemental Video 2) was comparable to that of wtVWF (Figure 7A; supplemental Video 1), but multimer analysis revealed residual monomers, odd-numbered multimers (Figures 7G; supplemental Figure 6), and a mild loss of HMWMs (Figure 7G). These data support the hypothesis that bond Cys2811-2811′ is critical to protect bonds Cys2771-2773′ and Cys2771′-2773 from reduction.

## Discussion

Employing different high-resolution methods, we found independent evidence that PDIA1 directly binds to VWF with a strong affinity. Moreover, we identified the CK domain as the only PDIA1 binding domain within VWF. To show that VWF is dimerized by PDIA1 without the compensatory effect of other thiol isomerases, we could not use siRNA because PDIA1 protein levels can only be reduced to 20%, leading to overall reduction of VWF levels without an obvious effect on dimerization[27-29] (supplemental Figures 8 and 9). Nonetheless, we were able to rule out effects of PDIA2 because HUVECs do not express this PDI isoform (supplemental Figure 10). By employing the PDIA1- and PDIA3-specific inhibitor 16F16,[21] we were able to reduce the candidates to these 2 PDI isoforms. It has previously been reported that PDIA3 exhibits increased binding to misfolded VWF mutants with N-terminal mutations.[30] These data indicate that PDIA3 is able to bind to N-terminal regions of VWF, which speaks against an involvement of PDIA3 in dimerization, but for a role in protein repair of VWF mutants. Thus, our data provide strong evidence that VWF dimerization is performed mainly or even exclusively by PDIA1.

The combined data of our docking and MD simulations, as well as the colocalization studies of VWD-associated VWF mutants, suggest the following mechanism of VWF dimerization (Figure 6D): An initial, probably electrostatic, association between PDI and VWF occurs

N-terminally of residue 2772. The protein–protein docking calculations showed that the catalytic site of PDI can only interact with Cys2771 and Cys2773 as long as the C-termini are not obstructing them; a condition that is met when the disulfide bond Cys2811-Cys2811′ is not yet formed. Hence, the latter bond has to be formed last. The docking results further showed no preference of PDI for either Cys2771 or Cys2773 in wtCK, suggesting PDI does not distinguish between these 2 cysteines. Therefore, oxidized PDI initially establishes a disulfide bond between its catalytic residue Cys36 and either Cys2771 or Cys2773 in one VWF monomer. Then PDI catalyzes the formation of the first disulfide bond, which can either be Cys2771-2773′ or Cys2771′-2773 (step i, Figure 6D). In the next step, a new oxidized PDI molecule binds (II) and catalyzes (III) the formation of the second disulfide bond. The CK dimer is now stabilized by the 2 formed disulfide bonds, and the CK C-termini assemble into a β-sheet conformation (IV), which brings Cys2811 and Cys2811′ in proximity, enhancing their propensity to form the last disulfide bond Cys2811-2811′ (V). Our simulation data suggest that formation of the latter bond is not necessarily catalyzed by PDI. It could also be a spontaneous process or be catalyzed by a different enzyme or even a small molecule (eg, glutathione). We hypothesize that this far C-terminal disulfide bond acts as a protective cover, rendering oxidation of Cys2771 and Cys2773 by PDI (and thereby VWF dimerization) irreversible by sterically occluding these 2 essential disulfides. Indeed, we found odd-numbered multimers and residual monomers in the supernatant of cells expressing mutant p.Cys2811Ala, indicating partial reopening of VWF dimers by reduction of the first 2 bonds (Figure 7G; supplemental Figure 6). The normal intracellular localization and mild loss of HMWMs of this mutant suggest that mutation of Cys2811 would lead to no or only very mild bleeding symptoms. Together with the low incident of CK domain mutations and an effect only expected for homozygous expression, these data might explain why this mutation has never been identified in individuals with bleeding symptoms.

Our data can further explain the pathomechanism of VWD subtypes induced by CK domain mutations: For mutant p.Cys2771Arg, we found normal binding to PDI and complete abolishment of C-terminal dimerization.[5,8] Although MD simulations suggest small distances between the 2 Cys2773 residues within a hypothetical p.Cys2771Arg dimer (supplemental Figure 7), this bond cannot be formed as proven by multimer analysis.[5,8] Probably, conformational changes prevent the formation of an alternative Cys2773-2773′ bond, causing the dimerization defect in p.Cys2771Arg. This hypothesis is supported by our previous observation that conformational changes in the Cys2771Arg monomer lead to an extended conformation that impedes the formation of an alternative Cys2773-Cys2773′ bond.[8]

For mutant p.Cys2773Arg, it has previously been described that this mutation leads to odd-numbered multimers in heterozygous patients.[31] However, homozygous expression reduces only formation of HMWMs, showing merely a partial dimerization defect. The intracellular localization and colocalization with PDI were found to be normal.[31] Therefore, PDI seems to be able to at least use Cys2771 to form residual dimers by the formation of an alternative Cys2771-2771′ bond.

Summarizing, our data showed, for the first time to our knowledge, direct interaction of VWF and PDIA1. We suggest a mechanism for VWF dimerization and found indication that the pathomechanism of CK domain mutation-derived VWD phenotypes can be explained by inhibition of PDI-catalyzed disulfide bond formation. Further, we used high-resolution methods such as STORM, MST, FCS, and AFM that proved to be valuable tools to investigate protein–protein interactions. These methods are not yet commonly used in medical sciences or diagnostics but could become increasingly important in these fields because they allow the investigation of protein–protein interaction with higher resolution, sensitivity, and specificity than currently preferred methods.

## Acknowledgments

We thank the Nikon Center of Excellence for Integrative Microscopy at the Heinrich-Pette-Institute for providing the Nikon N-STORM microscope and the University Medical Center Hamburg-Eppendorf (UKE) Microscopy Imaging Facility for technical support and providing the Leica SP5 microscope. We thank Sarah Vollmers for technical assistance and Florian Langer for helpful discussions. W.V. thanks Research Foundation-Flanders (FWO) for a postdoctoral fellowship and a travel grant for a long stay abroad. This study was supported by research funding from the German Research Foundation to the Research Group FOR1543: "Shear flow regulation of hemostasis - bridging the gap between nanomechanics and clinical presentation" (J.O.R., S.L., R.S., M.A.B., T.O., G.K., C.B., C.A.-S., F.G., J.P.M.).

## Authorship

Contribution: S.L. performed MST and FCS experiments and wrote the manuscript. S.L. and J.O.R. analyzed the MST and FCS data. D.E. performed and analyzed STORM experiments. A.L., W.V., and J.P.M. performed and analyzed atomic force microscopy experiments. G.K. performed immunofluorescence, and K.R. performed the inhibitor experiments. T.O. cloned VWF mutants. R.S. designed VWF mutants and critically reviewed the manuscript. K.K. performed the docking calculations and MD simulations. K.K., C.B., C.A.-S., and F.G. designed and analyzed the docking and MD experiments. K.K., C.B., C.A.-S., and F.G. wrote the manuscript. S.S. and U.B. performed multimer analysis. M.A.B. designed this study, performed localization studies, and wrote and edited the manuscript.

Conflict-of-interest disclosure: The authors declare no competing financial interests.

Correspondence: Maria A. Brehm, Department of Pediatric Hematology and Oncology, University Medical Center Hamburg-Eppendorf, Martinistrasse 52, 20246 Hamburg, Germany; e-mail: m.brehm@uke.de.

## References

1. Wagner DD. Cell biology of von Willebrand factor. *Annu Rev Cell Biol.* 1990;6:217-246.
2. Alexander-Katz A, Schneider MF, Schneider SW, Wixforth A, Netz RR. Shear-flow-induced unfolding of polymeric globules. *Phys Rev Lett.* 2006;97(13):138101.
3. Zhou Y-F, Springer TA. Highly reinforced structure of a C-terminal dimerization domain in von Willebrand factor. *Blood.* 2014:123:1785-1793.
4. Katsumi A, Tuley EA, Bodó I, Sadler JE. Localization of disulfide bonds in the cystine knot domain of human von Willebrand factor. *J Biol Chem.* 2000;275(33):25585-25594.
5. Schneppenheim R, Brassard J, Krey S, et al. Defective dimerization of von Willebrand factor subunits due to a Cys->Arg mutation in type IID von Willebrand disease. *Proc Natl Acad Sci USA.* 1996;93(8):3581-3586.
6. Dang LT, Purvis AR, Huang RH, Westfield LA, Sadler JE. Phylogenetic and functional analysis of histidine residues essential for pH-dependent multimerization of von Willebrand factor. *J Biol Chem.* 2011;286(29): 25763-25769.
7. Michaux G, Hewlett LJ, Messenger SL, et al. Analysis of intracellular storage and regulated secretion of 3 von Willebrand disease-causing

variants of von Willebrand factor. *Blood.* 2003; 102(7):2452-2458.

8. Brehm MA, Huck V, Aponte-Santamaría C, et al. von Willebrand disease type 2A phenotypes IIC, IID and IIE: A day in the life of shear-stressed mutant von Willebrand factor. *Thromb Haemost.* 2014;112(1):96-108.
9. Meyer R, Nalaskowski MM, Ehm P, et al. Nucleocytoplasmic shuttling of human inositol phosphate multikinase is influenced by CK2 phosphorylation. *Biol Chem.* 2012;393(3): 149-160.
10. van de Linde S, Löschberger A, Klein T, et al. Direct stochastic optical reconstruction microscopy with standard fluorescent probes. *Nat Protoc.* 2011;6(7):991-1009.
11. Tokunaga M, Imamoto N, Sakata-Sogawa K. Highly inclined thin illumination enables clear single-molecule imaging in cells. *Nat Methods.* 2008;5(2):159-161.
12. Vanderlinden W, Lipfert J, Demeulemeester J, Debyser Z, De Feyter S. Structure, mechanics, and binding mode heterogeneity of LEDGF/p75-DNA nucleoprotein complexes revealed by scanning force microscopy. *Nanoscale.* 2014; 6(9):4611-4619.
13. Lippok S, Seidel SAI, Duhr S, et al. Direct detection of antibody concentration and affinity in human serum using microscale thermophoresis. *Anal Chem.* 2012;84(8): 3523-3530.
14. Wienken CJ, Baaske P, Rothbauer U, Braun D, Duhr S. Protein-binding assays in biological liquids using microscale thermophoresis. *Nat Commun.* 2010;1:100.
15. Valentijn KM, van Driel LF, Mourik MJ, et al. Multigranular exocytosis of Weibel-Palade bodies in vascular endothelial cells. *Blood.* 2010;116(10): 1807-1816.
16. Kemmink J, Darby NJ, Dijkstra K, Nilges M, Creighton TE. Structure determination of the N-terminal thioredoxin-like domain of protein disulfide isomerase using multidimensional heteronuclear 13C/15N NMR spectroscopy. *Biochemistry.* 1996;35(24):7684-7691.
17. Schneidman-Duhovny D, Inbar Y, Nussinov R, Wolfson HJ. PatchDock and SymmDock: servers for rigid and symmetric docking. *Nucleic Acids Res.* 2005;33(Web Server issue):W363-W367.
18. Mashiach E, Schneidman-Duhovny D, Andrusier N, Nussinov R, Wolfson HJ. FireDock: a web server for fast interaction refinement in molecular docking. *Nucleic Acids Res.* 2008;36(Web Server issue):W229-W232.
19. Wang JW, Valentijn KM, de Boer HC, et al. Intracellular storage and regulated secretion of von Willebrand factor in quantitative von Willebrand disease. *J Biol Chem.* 2011;286(27): 24180-24188.
20. Zhou YF, Eng ET, Nishida N, Lu C, Walz T, Springer TA. A pH-regulated dimeric bouquet in the structure of von Willebrand factor. *EMBO J.* 2011;30(19):4098-4111.
21. Hoffstrom BG, Kaplan A, Letso R, et al. Inhibitors of protein disulfide isomerase suppress apoptosis induced by misfolded proteins. *Nat Chem Biol.* 2010;6(12):900-906.
22. Santos CX, Stolf BS, Takemoto PV, et al. Protein disulfide isomerase (PDI) associates with NADPH oxidase and is required for phagocytosis of Leishmania chagasi promastigotes by macrophages. *J Leukoc Biol.* 2009;86(4): 989-998.
23. Mourik MJ, Faas FG, Zimmermann H, Voorberg J, Koster AJ, Eikenboom J. Content delivery to newly forming Weibel-Palade bodies is facilitated by multiple connections with the Golgi apparatus. *Blood.* 2015;125(22):3509-3516.
24. Gallina A, Hanley TM, Mandel R, et al. Inhibitors of protein-disulfide isomerase prevent cleavage of disulfide bonds in receptor-bound glycoprotein 120 and prevent HIV-1 entry. *J Biol Chem.* 2002; 277(52):50579-50588.
25. Enayat MS, Guilliatt AM, Surdhar GK, et al. Aberrant dimerization of von Willebrand factor as the result of mutations in the carboxy-terminal region: identification of 3 mutations in members of 3 different families with type 2A (phenotype IID) von Willebrand disease. *Blood.* 2001;98(3): 674-680.
26. Schneppenheim R, Budde U, Obser T, et al. Expression and characterization of von Willebrand factor dimerization defects in different types of von Willebrand disease. *Blood.* 2001; 97(7):2059-2066.
27. Ou W, Silver J. Role of protein disulfide isomerase and other thiol-reactive proteins in HIV-1 envelope protein-mediated fusion. *Virology.* 2006;350(2): 406-417.
28. Sullivan DC, Huminiecki L, Moore JW, et al. EndoPDI, a novel protein-disulfide isomerase-like protein that is preferentially expressed in endothelial cells acts as a stress survival factor. *J Biol Chem.* 2003;278(47):47079-47088.
29. Xu S, Butkevich AN, Yamada R, et al. Discovery of an orally active small-molecule irreversible inhibitor of protein disulfide isomerase for ovarian cancer treatment. *Proc Natl Acad Sci USA.* 2012; 109(40):16348-16353.
30. Allen S, Goodeve AC, Peake IR, Daly ME. Endoplasmic reticulum retention and prolonged association of a von Willebrand's disease-causing von Willebrand factor variant with ERp57 and calnexin. *Biochem Biophys Res Commun.* 2001; 280(2):448-453.
31. Wang JW, Groeneveld DJ, Cosemans G, et al. Biogenesis of Weibel-Palade bodies in von Willebrand's disease variants with impaired von Willebrand factor intrachain or interchain disulfide bond formation. *Haematologica.* 2012;97(6): 859-866.

2016 127: 1183-1191
doi:10.1182/blood-2015-04-641902 originally published online December 15, 2015

# von Willebrand factor is dimerized by protein disulfide isomerase

Svenja Lippok, Katra Kolsek, Achim Löf, Dennis Eggert, Willem Vanderlinden, Jochen P. Müller, Gesa König, Tobias Obser, Karoline Röhrs, Sonja Schneppenheim, Ulrich Budde, Carsten Baldauf, Camilo Aponte-Santamaría, Frauke Gräter, Reinhard Schneppenheim, Joachim O. Rädler and Maria A. Brehm



Blood (print ISSN 0006-4971, online ISSN 1528-0020), is published weekly by the American Society of Hematology, 2021 L St, NW, Suite 900, Washington DC 20036.

## A.4 Publication 4: A fast recoiling silk-like elastomer facilitates nanosecond nematocyst discharge

# A fast recoiling silk-like elastomer facilitates nanosecond nematocyst discharge

by

Anna Beckmann, Senbo Xiao, Jochen P. Müller, Davide Mercadante, Timm Nüchter, Niels Kröger, Florian Langhojer, Wolfgang Petrich, Thomas W. Holstein, Martin Benoit, Frauke Gräter, and Suat Özbek

published in

BMC Biology, 2015, 13:3, doi: 10.1186/s12915-014-0113-1

BMC Biology

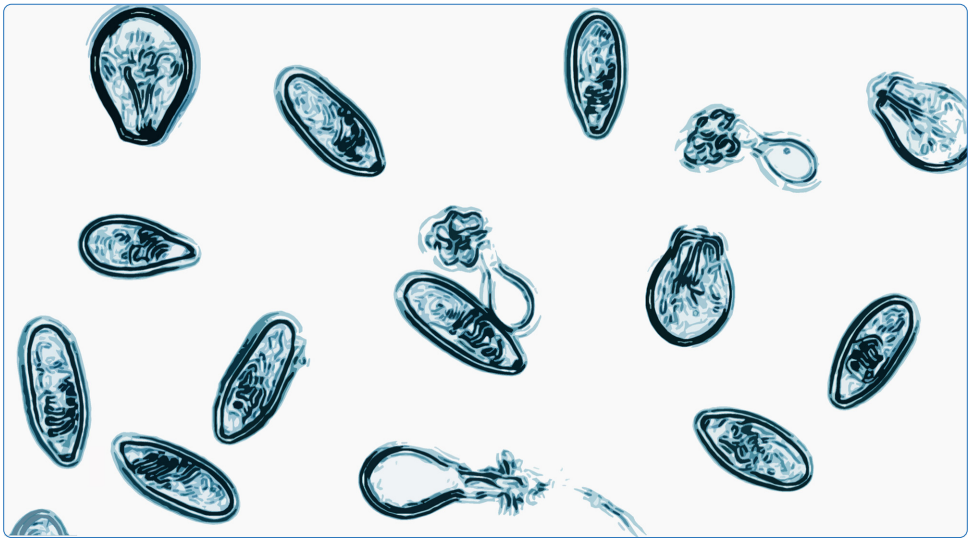

# A fast recoiling silk-like elastomer facilitates nanosecond nematocyst discharge

Beckmann *et al.*

BioMed Central

Beckmann *et al. BMC Biology* (2015) 13:3
DOI 10.1186/s12915-014-0113-1

Beckmann *et al. BMC Biology* (2015) 13:3
DOI 10.1186/s12915-014-0113-1

BMC Biology

RESEARCH ARTICLE Open Access

# A fast recoiling silk-like elastomer facilitates nanosecond nematocyst discharge

Anna Beckmann[1], Senbo Xiao[2], Jochen P Müller[5], Davide Mercadante[2], Timm Nüchter[1], Niels Kröger[3], Florian Langhojer[4], Wolfgang Petrich[3], Thomas W Holstein[1], Martin Benoit[5], Frauke Gräter[2] and Suat Özbek[1*]

**Abstract**

**Background:** The discharge of the Cnidarian stinging organelle, the nematocyst, is one of the fastest processes in biology and involves volume changes of the highly pressurised (150 bar) capsule of up to 50%. Hitherto, the molecular basis for the unusual biomechanical properties of nematocysts has been elusive, as their structure was mainly defined as a stress-resistant collagenous matrix.

**Results:** Here, we characterise Cnidoin, a novel elastic protein identified as a structural component of *Hydra* nematocysts. Cnidoin is expressed in nematocytes of all types and immunostainings revealed incorporation into capsule walls and tubules concomitant with minicollagens. Similar to spider silk proteins, to which it is related at sequence level, Cnidoin possesses high elasticity and fast coiling propensity as predicted by molecular dynamics simulations and quantified by force spectroscopy. Recombinant Cnidoin showed a high tendency for spontaneous aggregation to bundles of fibrillar structures.

**Conclusions:** Cnidoin represents the molecular factor involved in kinetic energy storage and release during the ultra-fast nematocyst discharge. Furthermore, it implies an early evolutionary origin of protein elastomers in basal metazoans.

**Keywords:** Hydra, Nematocyst, Elastomer, Molecular dynamics, Single molecule force spectroscopy

## Background

Elastic mechanisms in animals are highly diverse and involve either single rapid movements as in jumping froghoppers and many vertebrates [1] or rhythmic movements as in flying insects [2]. The molecular springs involved in elastic movements are as diverse but have in common unstructured domains that lose conformational entropy upon stretching, generating the restoring force, which finally drives the elastic movement. Although elastic mechanisms are well studied in arthropods, there are few data for lower metazoans and the evolutionary origin of elastic proteins.

Nematocytes or stinging cells of jellyfish and other cnidarians produce a unique toxic organelle consisting of a spherical capsule to which a long tubule is attached [3,4]. The tubule is tightly coiled inside the capsule matrix and expelled in a harpoon-like fashion during a nanosecond discharge process [5]. By the synthesis of poly-γ-glutamate at final maturation, nematocysts in hydrozoans are charged with an osmotic pressure of about 150 bars [6,7]. Prior to discharge, the capsule volume is increased by 30% due to osmotic swelling [5,8] and the explosive exocytosis releases the kinetic energy stored in the elastically stretched capsule wall with an extreme acceleration of 5,410,000 g [5]. After discharge, the size of the capsule is reduced to about 50% (Figure 1A) [8,9].

The nematocyst wall is built of a dense matrix consisting mainly of minicollagens, which represent a unique feature of cnidarians [10-12]. Minicollagens constitute a large protein family in *Hydra* and share a common domain organisation comprising a short central collagen triple helix flanked by variable polyproline stretches and cysteine-rich domains (CRDs) supposed to be involved in network formation [4,13,14]. While minicollagens can account for the high tensile strength required for the capsule wall to withstand a pressure of 150 bars [11],

* Correspondence: suat.oezbek@cos.uni-heidelberg.de
[1]Department of Molecular Evolution and Genomics, University of Heidelberg, Centre for Organismal Studies, Im Neuenheimer Feld 329, 69120 Heidelberg, Germany
Full list of author information is available at the end of the article

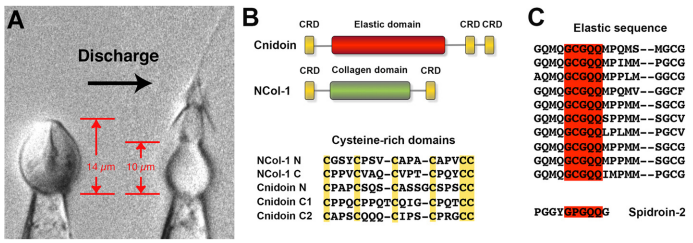


**Figure 1 Capsule recoil after nematocyst discharge and sequence elements in Cnidoin primary structure. (A)** capsule size change during discharge of a stenotele. **(B)** domain organisation of Cnidoin and Minicollagen-1 (NCol-1) and alignment of respective CRD domains. Conserved cysteines are highlighted. **(C)** alignment of the elastic domain of Cnidoin with a homologous sequence in Spidroin-2. Highlighted is the GxGQQ motif present in both sequences.

elastomeric proteins, which can store the energy for the extraordinarily fast kinetics of discharge, are unknown.

Recently, we have presented the proteome of *Hydra* nematocysts, which showed an extracellular matrix-like composition of the nematocyst supra-structure [14]. A novel component of the insoluble nematocyst shell was designated Cnidoin, a protein with a central glycine-glutamine-rich sequence flanked by minicollagen CRDs (Figure 1B). The highly repetitive central domain is homologous to the glycine-rich sequence of the spider silk protein Spidroin-2 [15]. A conserved motif in both proteins is GXGQQ, where X is cysteine in Cnidoin and proline in Spidroin-2 (Figure 1C). Cnidoin protein has been shown to be co-localised with minicollagens in the nematocyst wall, suggesting a mechanical function in nematocysts [14].

It is well accepted that disordered peptides such as Spidroins, the PEVK segment in titin, or resilin in the muscle of fly wings can serve as elastic elements in protein structures and materials [16-18]. Elongation of such an unstructured peptide is entropically unfavoured and involves rupturing of non-specific interactions of hydrophobic or electrostatic nature along the chain. Consequently, this process requires significant mechanical force, resulting in high elasticity. The elastic features of disordered peptides as defined by their amino acid sequence have been documented by both experimental atomic force microscopy (AFM) studies and molecular dynamics (MD) simulations, with remarkable agreement [16,19-21].

Here, we provide evidence for an elastomeric function of Cnidoin in nematocyst morphogenesis and discharge. As with minicollagens, Cnidoin is expressed exclusively in developing nematocytes in the body column of *Hydra*. We demonstrate a concomitant incorporation of Cnidoin and minicollagens into both the wall and tubule structures of all nematocyst types. Recombinantly expressed and purified Cnidoin protein has a high tendency for aggregation and forms amorphous sheets and fibres as described for spider silk proteins. MD simulations of the repetitive elastic sequence of Cnidoin suggest an elastic behaviour comparable to other elastomeric proteins, such as the silk disordered domain or resilin. The predicted molecular elasticity is in line with force spectroscopy measurements on single Cnidoin molecules. Our data provide an explanation for the unusual biomechanical properties of the Cnidarian nematocyst at the molecular level and give insights into the evolution of elastomeric proteins.

## Results

### Primary structure and domain organisation of Cnidoin

A full-length clone for Cnidoin was isolated from *Hydra magnipapillata* cDNA based on the predicted gene sequence annotated in our recent proteome analysis [14]. The primary structure comprises a signal peptide (1–21) and an unusually large putative propeptide (22–111) terminating at a basic Lys-Arg dipeptide sequence, which is conserved in diverse nematocyst proteins (see Additional file 1: Figure S1A). The predicted mature protein contains 403 amino acids and has a calculated molecular weight of 41.6 kDa. The central part of the protein comprises an extended sequence rich in glycine and glutamine residues whose repetitive motif QMQGCGQQXP (X is mostly methionine) shows high similarity to the elastic glycine-rich sequence of the major spider silk component from *Nephila clavipes*, Spidroin-2 [22] (Figure 1C). The amino acid composition of the elastic motif in Cnidoin is unusual in containing a high percentage of methionine and cysteine (see Additional file 1: Figure S1B). At both termini Cnidoin contains short CRDs homologous to those in canonical minicollagens as minicollagen-1 (NCol-1) [23], suggesting a possible linkage to the minicollagen network via intermolecular cysteine links (Figure 1B). The Cnidoin primary sequence does not contain N-glycosylation sites, but

several potential sites for O-glycosylation. Treatment of nematocyst preparations with N- and O-glycosidases, however, did not result in a molecular weight shift ruling out posttranslational modifications by sugars (data not shown).

### Cnidoin is expressed in developing nematocyst nests and co-localises with minicollagens

Whole mount *in situ* hybridisation (ISH) experiments were carried out to determine the expression pattern of the *Cnidoin* gene. As shown in Figure 2A the expression of *Cnidoin* is restricted to developing nests of nematocytes in the body column of *Hydra*. Tentacles, head and peduncle regions were free of signals. This pattern is highly reminiscent of other nematocyst-specific structural genes, such as minicollagens or NOWA [24,25]. As shown in Figure 2B, mostly late stages of developing capsules with a pronounced nematocyst vesicle showed a Cnidoin signal. In nests of early developmental stages the signal was not detectable probably due to lower expression rates (data not shown). When double ISH experiments using Cnidoin and NCol-1 probes were performed, the signals were mostly co-localised in developing nematocyte nests (Figure 2C).

To localise Cnidoin protein during capsule development, whole mount immunostainings were performed using a polyclonal Cnidoin antibody raised against the C-terminal CRD. Nematocytes in *Hydra* develop in nests of 8 to 32 cells that originate from interstitial stem cells (i-cells). Their morphogenesis involves the continuous secretion of proteins into a growing post-Golgi vesicle. Capsule maturation is marked by nematocyte separation into single cells that migrate to the tentacles to be incorporated into battery cells. Immunostainings using paraformaldehyde (PFA) fixation showed Cnidoin in developing nematocyst nests of all stages and capsule types in the body column of *Hydra* (Figure 2D-E). The staining pattern is again highly reminiscent of minicollagens that lose antigenicity during capsule maturation [24,25]. Co-staining using minicollagen-1 antibody revealed a co-localisation of the two proteins to a large extent in the developing capsule walls (Figure 2F, H). In contrast to PFA fixation, Lavdovsky fixated animals showed in addition tubule staining patterns in developing nests, which co-localised with the tubule-specific minicollagen-15 (Figure 2G, I). This observation might be due to an altered molecular arrangement of Cnidoin in the different capsule parts. The loss of Cnidoin staining

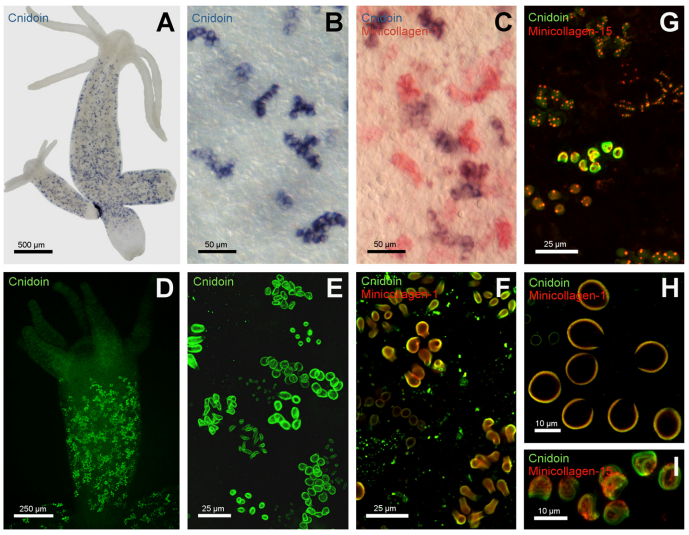


**Figure 2 Gene expression pattern and immunohistochemical localisation of Cnidoin. (A)** gene expression pattern as shown by *in situ* hybridisation. The signal is detected in nests of developing nematocytes in the body column. **(B)** close-up of nematocyte nests shown in A. **(C)** double *in situ* hybridisation of Minicollagen-1 (red) and Cnidoin (blue). **(D)** Antibody staining reveals nests of developing nematocytes in the body column of *Hydra*. **(E)** enlarged view of the immunostaining shown in D. **(F)** costaining of Minicollagen-1 and Cnidoin in PFA-fixed animals. Both signals localise to the capsule wall. **(G)** co-staining of Minicollagen-15 and Cnidoin in Lavdovsky-fixated animals. This fixation reveals the presence of both proteins in the tubule of developing nematocysts. **(H)** enlarged view of a nest with Cnidoin and Minicollagen-1 immunostaining. **(I)** magnification of a nest with a tubule-specific signal for Cnidoin and Minicollagen-15. PFA, paraformaldehyde.

in the tentacles indicates a tight incorporation of the protein into the collagenous wall and tubule structures as already suggested by the possession of CRDs.

### Recombinant Cnidoin is highly hydrophobic and spontaneously forms fibrous aggregates

In western blot analysis Cnidoin was detected as a single band of about 42 kDa in hydra lysates, isolated nematocyst capsules as well as in nematocyst ghosts (Figure 3A).

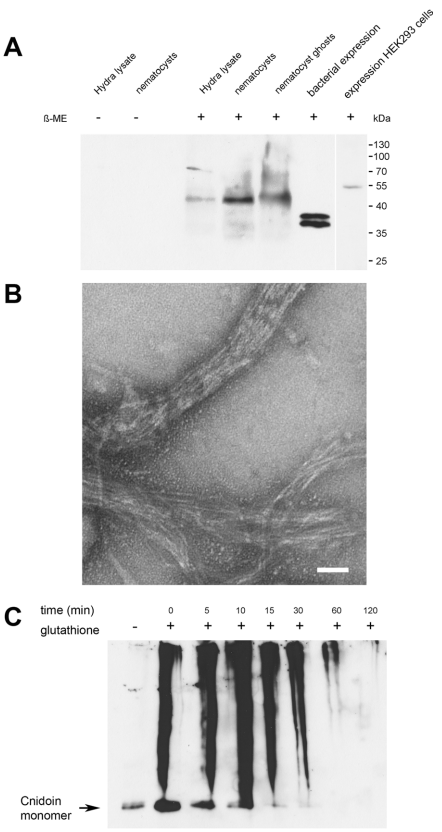


**Figure 3 Western blot detection and self-aggregation of Cnidoin.** **(A)** western blot analysis of Cnidoin in isolated nematocysts, the insoluble fraction of nematocysts (ghosts), whole hydra lysate, and after recombinant expression in bacteria and HEK293 cells. **(B)** transmission electron micrograph of recombinant Cnidoin forming bundles of fibres. Scale bar is 100 nm. **(C)** western blot analysis of recombinant Cnidoin induced to form disulphide-linked polymers by glutathione treatment.

This is slightly lower than the calculated molecular mass of 51.6 kDa including the putative propeptide, indicating that propeptide cleavage does occur during secretion into the nematocyst vesicle. When expressed recombinantly in HEK293 cells, full-length Cnidoin exhibited a molecular mass of about 53 kDa, which matches the calculated mass of Cnidoin including a C-terminal his-tag (53.1 kDa) (Figure 3A). We conclude that in HEK293 cells propeptide cleavage does not occur resulting in the observed molecular mass difference to the native protein, which accounts for the propeptide fragment. The western blot signal was exclusively detectable under reducing conditions suggesting an incorporation of Cnidoin into the disulphide-linked capsule wall polymer similar to NCol-1 and NOWA [13,26].

When full-length Cnidoin was expressed in bacteria the protein formed highly insoluble aggregates that were already detectable as large pellets after cell lysis. Purification of Cnidoin via histidine tag was, therefore, performed under denaturing conditions using 8 M urea, which led to transient solubilisation of the protein aggregates. Cnidoin was essentially insoluble in physiological aqueous buffers. The recombinantly expressed protein exhibited a lower apparent molecular mass of about 38 kDa and a prominent double band, probably indicative of altered migration behaviour by intramolecular disulphide bonding. Purified Cnidoin spontaneously formed macroscopic fibrillar structures in 8 M urea when cooled samples were gradually brought to room temperature [14]. This coacervation process is reminiscent of elastin-derived peptides where spontaneous self-assembly of monomers is induced by temperature increase depending on protein and salt concentration [27]. The driving force for coacervation, which precedes microfibrillar deposition and cross-linking in elastin, are hydrophobic domain interactions in an aqueous environment. Analysis of Cnidoin fibres by transmission electron microscopy revealed bundles of linear fibres in the nanometre range reflecting the common filamentous nature of elastomeric proteins (Figure 3B). Due to the presence of terminal minicollagen CRD domains we hypothesised that Cnidoin polymerisation was dependent on disulphide coupling. This was demonstrated by glutathione treatment of recombinant Cnidoin samples, which showed gradual formation of high molecular weight oligomers in non-reducing SDS-PAGE (Figure 3C). A similar behaviour is observed for recombinant NCol-1 samples [13], suggesting a possible copolymer formation of both proteins. Our hypothesis was further strengthened by incubating recombinant NCol-1 with increasing amounts of Cnidoin in the presence of glutathione, which resulted in a dose-dependent increase of disulphide-linked polymer formation (see Additional file 2: Figure S2).

### Cnidoin shares elastomeric functions with other disordered proteins

The sequence composition of Cnidoin (see Additional file 1: Figure S1B) with a high glycine and proline content of 24% and 10%, respectively, shows typical features of disordered proteins. Intrinsically unstructured proteins have been classified previously as sequences with low overall hydrophobicity and high net charge as compared to structured proteins [28,29]. These two properties are believed to prevent the formation of a solvent-inaccessible protein hydrophobic core typically formed by proteins with a well-defined structure. However, with a high mean hydrophobicity of 0.48 and a low mean net charge of 0.007, Cnidoin falls into the region known to be covered by natively folded proteins. Nevertheless, the high glycine and proline content impedes the formation of a native structure, as predicted by DisEMBL (see Additional file 3: Figure S3A) [30]. While the high hydrophobicity in this case does not result in protein core formation, it gives rise to the observed high propensity for self-aggregation (compare Figure 3B). Again, Spidroin-2 follows similar tendencies with a (slightly lower) mean hydrophobicity of 0.39, a mean net charge of 0.0002 and a proline content of 8% to 15%.

We investigated the degree of ordering additionally by using mid-infrared spectroscopy following the considerations of Byler and Susi [31], who showed that disordered proteins such as casein exhibit a low number of spectral components in the so-called Amide I band of the mid-infrared spectrum. Furthermore, both the existence and the above-average width of a peak around 1,645 $cm^{-1}$ (that is, around a wavelength of 6.08 μm) were considered as an indication of a low degree of ordering. The number of spectral components of casein together with the corresponding numbers for other standard proteins investigated is shown in Additional file 3: Figure S3B [31]. The optimum number of components in Cnidoin tended to be low in relation to standard proteins known to be highly ordered [31] and comparable to that of casein. Moreover, Cnidoin does exhibit a broad peak around 1,645 $cm^{-1}$ (see Additional file 3: Figure S3C). In this sense, our spectroscopic data and its analysis support the hypothesis of the disordered nature of Cnidoin.

To further experimentally confirm the sequence-based prediction of high disorder in Cnidoin, we performed AFM single molecule force spectroscopy using a Cnidoin construct with a C-terminal type I dockerin tag and an N-terminal ybbR tag (Figure 4A). While the ybbR tag allowed for attaching the construct covalently to a coenzyme A surface, the dockerin tag enabled specific non-covalent binding of the construct to a type I cohesin functionalised cantilever tip (see Additional file 4: Figure S4). By retracting the tip from the surface, Cnidoin molecules were stretched via the C-terminal dockerin tag while force-distance traces were recorded. As previously shown in AFM experiments, forced dissociation of the type I cohesin-dockerin interaction preferentially goes

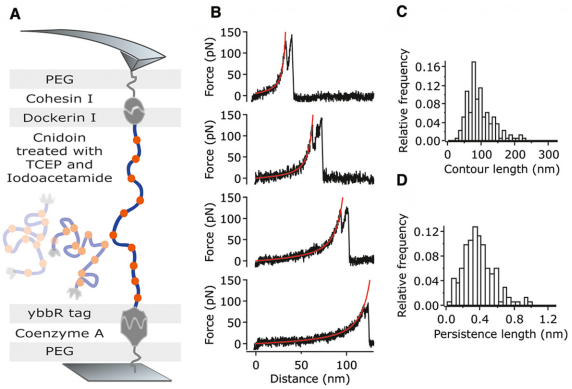


**Figure 4 AFM force spectroscopy on recombinant Cnidoin monomers. (A)** Schematic diagram of the AFM force spectroscopy experiment on single Cnidoin molecules, containing several cysteins with thiol groups (orange dots). For breaking disulphide bonds and preventing their reformation, Cnidoin was treated with TCEP and iodoacetamide. **(B)** Typical force-distance traces of Cnidoin displaying a final double peak, which is characteristic of the cohesin-dockerin rupture [1]. Force-distance traces show characteristic worm-like chain (WLC) behaviour and lack further pronounced features, corroborating the disordered nature of Cnidoin molecules. For quantification of contour and persistence length, a WLC model was fitted to the data (red line). **(C)** Histogram of the contour length distribution of stretched Cnidoin, yielding an average contour length of 94 nm and a standard deviation of 43 nm. **(D)** Histogram of the persistence length distribution of Cnidoin, yielding an average persistence length of 0.37 nm and a standard deviation of 0.23 nm. AFM, atomic force microscopy; TCEP, (tris(2-carboxyethyl)phosphine).

along with a characteristic double peak of 8 nm separation in contour length space [32]. This characteristic feature was used as a positive indicator for a specific stretching event (For evaluation of discarded curves see Additional file 5: Figure S5). Force-distance traces of Cnidoin molecules showed characteristic worm-like chain (WLC) behaviour without any further pronounced features (Figure 4B). The latter would indicate conformational rearrangements, as seen in stretching of structured proteins [33]. The lack of such features in force-distance traces of Cnidoin corroborates the disordered nature of the protein. Fitting a WLC model yields a distribution of both contour (Figure 4C) and persistence length (Figure 4D). Within a standard deviation of 43 nm, the average contour length of 94 nm is in good agreement with the estimated contour length of 110 nm (283 amino acids at an extension of 0.32 nm per amino acid plus an overall linker length of 20 nm including the polyethylene glycol (PEG) linker and the cellulose-binding module (CBM)-cohesin-dockerin anchor). The slight shift to smaller contour lengths may result from non-specific adsorption of Cnidoin molecules to the surface. Because of the harsh disulphide treatment, oppressing intermolecular bonds, only a minor fraction of curves yield contour lengths significantly larger than expected. Importantly, the featureless WLC characteristic of force-distance traces does not vary with the contour length, nor does the persistence length. The persistence length, which measures the apparent flexibility of a polymer against entropic force, yields an average of 0.37 ± 0.23 nm. This value matches the persistence length of 0.4 nm, which is frequently assumed for stretching unfolded proteins at similar force ranges in AFM experiments [33-35]. The standard deviation of the persistence length results predominantly from intrinsic uncertainty of the zero force in AFM experiments. In conclusion, the featureless and WLC like force-distance traces of Cnidoin measured by AFM confirm the high disorder of the protein's structure.

To complementary assess the elasticity of Cnidoin, we calculated the force-extension profile of two representative repeat units of Cnidoin using umbrella sampling [20]. To this end, Cnidoin peptide conformations were extensively sampled at varying end-to-end distances dZ (Figure 5A). Resulting average resisting forces against Cnidoin extension are shown in Figure 5B, with the resulting free energy shown in the inset. We observed a force plateau followed by a steep increase in force at larger extensions. The mean forces were fitted by the WLC model (solid line in Figure 5B), [36], which predicted persistence lengths of 0.89 ± 0.1 and 0.66 ± 0.06 nm for the Cnidoin repeat units shown in Figure 5B in red and black, respectively. Therefore, Cnidoin is found to be as elastic as silk disordered peptides, which have formerly been reported to have a persistence length of 0.74 nm in MD simulations in the force range probed here [20].

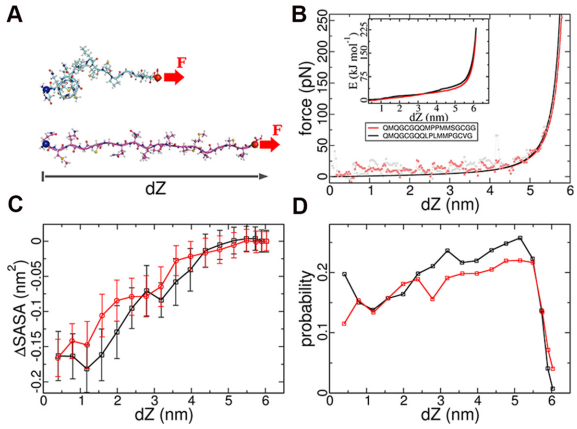


**Figure 5 Molecular elasticity of Cnidoin peptides from MD simulations. (A)** two representative (collapsed and extended) conformations of a Cnidoin peptide unit. To obtain force-extension curves, N-terminal C-alpha atoms (blue spheres) were fixed, while the C-termini (red spheres) were subjected to a force acted along the extension (red arrows). **(B)** mean forces calculated from umbrella sampling. The force profiles of two different Cnidoin repeat units (squares) were fitted with the worm-like chain model (solid lines). Resulting free energy profiles along the end-to-end distance are shown in the inset. **(C)** residue-averaged hydrophobic surface burial of two Cnidoin peptides measured by disappearance of solvent accessible surface area (ΔSASA). (**D**) PPII conformation content in the Cnidoin peptides along peptide extension. **(C)** and **(D)** use the same colour code as **(B)**. MD, molecular dynamics; PPII, polyproline II.

Hence, the MD simulations confirm the finding from AFM experiments of a featureless force-extension curve resembling a disordered protein such as silk. We note that for both silk [20,37] and Cnidoin investigated here, the persistence length from simulations is higher than in experiments, although the second simulated Cnidoin repeat unit lies within the experimental range (Figure 5B, red line).

As demonstrated in Figure 3, Cnidoin has a strong tendency for aggregation, which might be additionally enhanced by intermolecular disulphide links in the elastic domain. In order to assess Cnidoin in the biological environment of mature nematocysts, we resorted to MD simulations of single Cnidoin fragments and of a Cnidoin fragment embedded into a bundle of fragments, respectively. In agreement with the prediction of high disorder from sequence and the absence of forced unfolding events in AFM experiments (Figure 4B-D), Cnidoin peptide units did not form stable secondary structures in our simulations. The secondary structure of two Cnidoin peptides was monitored during 500-ns equilibrium MD simulations by DSSP: Dictionary of Secondary Structure for Proteins [38]. The peptides were found to form coils, bends and turns as well as a polyproline-II type structure (see below), all of which are typical backbone propensities of disordered peptides. The sequence motif *GCGQQ* was found to exist as a turn, and thus structurally related, but, due to the missing proline, not identical to the π-helix formed by the silk protein motif *GPGQQ* [39].

A mean force of 12.7 ± 0.7 pN was found to dominate at low extensions between 1.0 to 3.5 nm of single Cnidoin peptides. This mean resisting force results from both rupturing non-specific interactions along the chain and also entropic effects. We find the burial of hydrophobic side-chains from water to be one of the key driving factors that generate resisting forces against extension of Cnidoin. As shown in Figure 5C, the hydrophobic surface of Cnidoin buried during collapse is 0.17 ± 0.03 $nm^2$ per amino acid, as measured by the decrease in hydrophobic solvent accessible surface area (ΔSASA). This hydrophobic surface burial is similar in magnitude to the related silk peptides, and one of the highest among reported disordered proteins [20]. Together with the extraordinarily high mean hydrophobicity of these two types of disordered proteins, Cnidoin and silk have been apparently designed to self-assemble into larger aggregates driven by the hydrophobic effect. Polyproline II (PPII) conformation, an extended peptide conformation frequently observed in high proline-content peptides, was also monitored as a function of peptide extension [40]. As depicted in Figure 5D, the PPII content in the Cnidoin peptide increased with stretching as observed for other disordered proteins previously [20] and is another factor contributing to the resistance against extension and, thus, to the elasticity. We find the stretching of Cnidoin molecules within a bundle of Cnidoin proteins to give rise to higher force-extension curves (plateau at approximately 400 pN). Fitting yields an apparent persistence length of approximately 0.1 ± 0.003 nm, (see Additional file 6: Figure S6) which is lower than the one obtained for single Cnidoins (Figure 5B), reflecting a stronger coiling propensity. Thus, in the context of mature nematocysts, intermolecular interactions of similar nature as those discussed here for a single peptide can give rise to a further increase of the apparent elasticity of Cnidoin in bundles or networks.

The hypothesis that the shortening of Cnidoin peptides drives the extremely fast discharge of nematocysts has been confirmed by the observation that Cnidoin is equipped with the elasticity required to drive such a discharge. Fast collapse dynamics of Cnidoin would be required given the short sub-microsecond time scale of discharge [5]. To test the collapse dynamics, highly stretched conformations of the two repetitive Cnidoin peptide units were subjected to force-quench simulations to monitor collapse dynamics in comparison to other disordered peptides, namely two silk amorphous peptides and two domain linker peptides in the von Willebrand Factor (vWF). Both are also disordered peptides but with sequence compositions similar to folded proteins (see Additional file 7: Figure S7) [17,41]. The number of trajectories in which a fully stretched peptide has reached the collapsed state is shown in Figure 6, from which the lifetime of the extended state was calculated. The Cnidoin peptide was found to have a lifetime of 5.7 ns, which is longer than that of silk (3.7 ns) and shorter than that of the vWF linker (10.5 ns). Thus, Cnidoin has a moderate collapse dynamics between the highly elastic silk protein and the vWF linker, for which

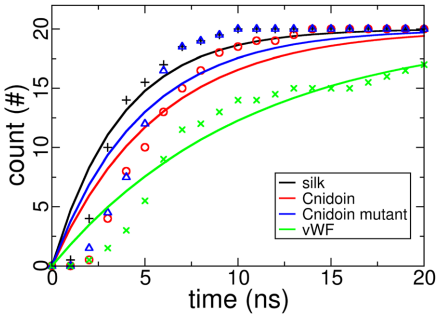


**Figure 6 Cumulative successful collapsing events of four disordered proteins.** Each data set contains 20 independent collapse simulations along with an exponential fit (solid line) to determine the lifetime of the extended state.

an elastomeric function is unknown. The lifetime of extended mutated Cnidoin peptides lacking methionines was found to be 4.7 ns, suggesting that the large methionine side chains do not favour fast collapse. The high content of methionine residues in Cnidoin thus is likely to have a function different from enhancing collapse.

## Discussion

Elastomeric proteins confer the biomechanical properties for fibres and matrices that undergo reversible and repetitive deformation [42]. They have evolved in a diverse range of animals and often fulfil highly specialised biological functions as in lung alveoli of higher vertebrates, wing joints of flying insects or in spider silk [43]. Although exhibiting a broad range of sequence variations, rubber-like elastomeric proteins share common properties in combining repetitive, highly disordered sequence elements with cross-linking motifs. In addition, most elastomeric proteins undergo spontaneous self-assembly to polymers by their hydrophobic nature [43].

Our combined experimental and computational study suggests that Cnidoin shares elastomeric functions with other disordered proteins. Having a similar persistence length with silk protein, the Cnidoin repetitive sequence features high flexibility among unstructured peptides. The extension of Cnidoin requires a noticeable mean force of around 12 pN for extensions between 10% and 70% of the contour length. We believe this high elasticity confers the high internal pressure of the nematocyst and agrees with the mechanical work upon collapsing Cnidoin with an apparent persistence length of 0.4 nm from 50% of its contour length to a fully collapsed state. This scenario brings the molecular measurements in line with the macroscopic mechanical observations, supporting the notion of a pressurised nematocyst that comprises a wall of assembled and highly extended elastomeric Cnidoin cross-linked by largely inextensible minicollagen and possibly disulphide bonds (Figure 7).

The biological function of the remarkably high methionine content of 17% in Cnidoin is intriguing. As the metabolic costs for methionine synthesis are the highest among all amino acids [44], rendering it a rare residue in proteins on average, and yet methionines do not favour fast peptide collapse nor feature outstanding hydrophobicity, they should contribute to the mechanics of nematocysts in a distinct way. The sulphur atom in methionine side-chains might be used as an additional cross-linking point, for example, via thioether bonds, in the peptide matrix of the nematocyst wall, which is subject to further investigations.

Apart from the extraordinary methionine and cysteine content, Cnidoin exhibits an overall amino acid composition, which on first sight is contradictory to its mechanical function. Most disordered proteins feature a lower

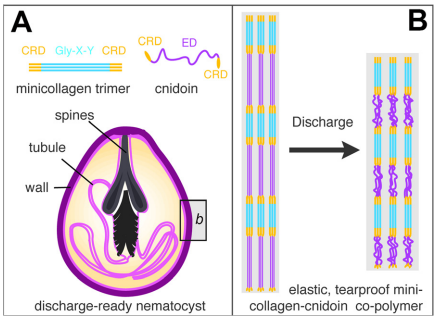


**Figure 7 Model of elastic nematocyst discharge. (A)** schematic representation of nematocyst architecture and minicollagen and Cnidoin components (capsule redrawn from [4]). **(B)** model of the elastic, tear-proof minicollagen-Cnidoin copolymer facilitating nematocyst discharge.

hydrophobicity and higher net charge than natively folded proteins, which is key to abstaining from forming a well-structured protein hydrophobic core. However, here and analogously for silk, the remarkably hydrophobic Cnidoin impedes core formation by a high glycine and proline content and yet drives self-assembly into a robust protein wall withstanding high pressure without leaking.

Interestingly, the high proline content of Cnidoin falls into the region covered by silk spidroin type-2 proteins and is known to be the primary reason for the high extensibility and elasticity of silk fibers [45,46], suggesting that prolines take over the same role in the nematocyst wall.

Cnidoin as a highly extensible and yet robust wall material provides the elasticity for a fast discharging nematocyst. Our computational analysis on single Cnidoins and Cnidoin bundles suggests that the disordered region can gain additional rubber-like elasticity through intermolecular interactions, which may additionally include covalent cross-links between cysteines and possibly methionines. Pressing questions are how numerous these cross-links are in the nematocyst wall, how they can cause a limited order in the network, how they possibly provide additional elasticity, similar to the tyrosine- or lysine-mediated cross-links in the elastomers resilin and elastin, and how they prevent leaking even under extreme pressures.

## Conclusions

Our data show for the first time how the extremely fast and powerful dynamics of nematocyst discharge in *Hydra* can be explained on the molecular level (Figure 7). The extraordinarily high speed of discharge is due to the

release of energy stored in the stretched configuration of the minicollagen-Cnidoin copolymer of the capsule wall that is under a very high initial osmotic pressure (Figure 7B). During discharge the capsule collapses and releases the energy (Figure 1A). The mode of copolymer formation as suggested by the possession of homologous CRDs in Cnidoin and minicollagens represents an attractive mechanism for biotechnological approaches as it offers unlimited fine-tuning of the ratio between elastic and stress-resistant components in forming polymers with different mechanical properties. Future research will show how the formation of such polymers might be feasible under controlled conditions.

## Methods

### Animals

*Hydra magnipapillata* was used for all experiments. Animals were cultured in Hydra medium at 18°C and fed two to three times a week with freshly hatched *Artemia salina* nauplii. Animals used for the experiments were starved for 24 hours. Intact nematocysts were isolated from whole Hydra tissue as described by Weber *et al*. [47]. Sucrose (10%) was added to the solutions in order to prevent an osmotically triggered discharge of the nematocysts.

### Isolation of Cnidoin cDNA and construction of expression vector

Preparation of whole RNA was performed using the RNeasy Mini Kit (Qiagen, Venlo, Netherlands) according to the manufacturer's instructions. The isolated RNA was transcribed by reverse transcriptase into cDNA. Using a pair of primers encompassing the predicted Cnidoin sequence (forward: ATGTCTCGATTACTACTTC, reverse: TTATCTCTTTTTACCAAAAGCTCC), a PCR was performed and the purified PCR product was ligated into the pGEM-T Vector (Promega, Madison, WI, USA) by TA cloning and the sequence was verified by automated sequencing.

Recombinant expression in *Escherchia coli* BL21 (DE3) cells was performed from a pET21b vector, which introduces a C-terminal polyhistidine tag. Cnidoin protein was exclusively found in inclusion bodies and purified under denaturing conditions (8 M urea) using Ni-NTA beads. For force spectroscopy experiments a Cnidoin fragment carrying an N-terminal ybbR-tag and a C-terminal dockerin-histidine-tag was generated by cloning the cDNA fragment coding for amino acid residues 150 to 419 including primer sequences coding for the respective tags into the pet21b vector.

### SDS PAGE and western blot

A polyclonal guinea pig antibody was raised against a peptide encompassing the sequence of the second C-terminal CRD domain (GCAPSCQQQCIPSCPRGCCGA) of Cnidoin (Eurogentec, Seraing, Liège, Belgium). Isolated nematocysts were solubilised by heating (95°C, 10 minutes) in sample buffer with or without 2-mercaptoethanol as indicated in the experiments. Hydra lysate was prepared by dissolving an animal in reducing or non-reducing sample buffer by heating and vortexing. Nematocyst ghosts, the insoluble fraction of nematocysts, were obtained by extended SDS washing of the isolated and discharged capsules. The ghosts were afterwards solubilised in sample buffer. The samples were separated by SDS-PAGE using 12% gels and transferred to nitrocellulose membranes by wet blotting. Blocking was performed for one hour with 5% milk powder in PBS 0.1% Tween20. After three 10-minute washes with 0.5% milk powder in PBS 0.1% Tween20, the membrane was incubated with the Cnidoin antibody (1:1000 in washing solution) for 1.5 hours, followed by three five-minute washing steps. The primary antibody was detected using an anti-guinea pig antibody coupled to horseradish peroxidase (1:1000 in washing solution) for one hour.

For the polymerisation assay, reduced glutathione was added to a final concentration of 1 mM to recombinantly expressed Cnidoin. The protein was incubated at 37°C. Samples were taken at indicated time points, mixed with non-reducing sample buffer and boiled for five minutes at 95°C. Afterwards the samples were kept on ice, until all time points were covered. The samples were separated by a gradient SDS-PAGE (4% to 20%), blotted on nitrocellulose, blocked with 5% BSA and detected by an anti-penta-his antibody.

The copolymerisation of recombinant Minicollagen-1 MBP (maltose binding protein) and Cnidoin was performed in the presence of 10 mM reduced glutathione. Minicollagen-1 MBP was purified by Ni-NTA from HEK293 cell culture supernatant as described [13,26]. Cnidoin was obtained by isolating recombinant protein from *E. coli*. As indicated in the experiment, various amounts of Cnidoin were added to the Minicollagen-1 containing sample in the presence of glutathione. The sample was mixed with non-reducing sample buffer and boiled immediately at 95°C. Separation and detection was performed as described above.

### Immunocytochemistry

*H. magnipapillata* were relaxed in 2% urethane in Hydra medium and then fixed in freshly prepared 4% PFA in hydra medium or Lavdovsky's fixative (50% ethanol, 10% formaldehyde, 4% acetic acid, 36% water) for thirty minutes or five hours, respectively. The fixative was removed by three 10-minute washing steps with PBS 0.1% Triton X100. The antibody was diluted 1:250 in PBS 1% BSA and incubated overnight at 4°C. For co-stainings with two antibodies, both antibodies (minicollagen-1

1:500, minicollagen-15 1:1000) were incubated simultaneously overnight at 4°C. To remove unbound antibodies three 10-minute wash steps with PBS 0.1% Triton X100 were performed. The incubation with the second antibodies was performed for two hours at room temperature. For detection of Cnidoin, a goat anti-guinea pig Alexa 568 coupled antibody was used, and for Minicollagen-1 and Minicollagen-15 a goat anti-rabbit Alexa 488 coupled antibody. The secondary antibodies were diluted 1:400 in PBS 1% BSA. To remove unbound antibodies, the animals were washed three times with PBS and then mounted on object slides with PBS 90% glycerol.

#### *In situ* hybridisation

The *in situ* probes were amplified from the Cnidoin-pGEM-T construct by PCR using the M13 forward and reverse primers. The purified PCR product was transcribed *in vitro* to DIG labelled RNA by Sp6 RNA polymerase (antisense probe), purified by precipitation with ammonium acetate and quality checked on a 1% agarose gel. As negative control, the sense probe was produced in the same way, using the T7 RNA polymerase. The *in situ* probes were diluted to approximately 5 ng/μl and then used in a 1:100 dilution for the experiment. Animals were relaxed with 2% urethane in Hydra medium and fixed overnight with freshly prepared 4% PFA in Hydra medium. The fixed animals were transferred to 100% ethanol and rehydrated in five minute steps using 75%, 50%, 25% ethanol in PBS, 0.1% Tween20 (PBT). After three five-minute washing steps with PBT the animals were incubated with 1× proteinase K in PBT for seven minutes. The reaction was stopped by adding 4 mg/ml glycine in PBT. Then, the animals were equilibrated twice in 0.1 M triethanolamine (TEA) for five minutes and incubated for five minutes each with 0.25% and 0.5% acetanhydride in TEA, followed by two washing steps with PBT. Then, a re-fixation with 4% PFA was performed for 20 minutes at room temperature, followed by five five-minute washing steps with PBT. The animals were incubated with hybridising solution (50% formamide, 5× SSC (0.75 M NaCl, 0.075 M sodium citrate in water, pH 7.0), 1× Denhardt's (0.02% polyvinyl pyrrolidone, 0.02% Ficoll, 0.021% BSA in water), 0.2 mg/ml yeast RNA, 0.1 mg/ml heparin, 0.1% Tween20, 0.1% Chaps, 10% $H_2O$) for 10 minutes and then pre-hybridised in hybridising solution for two hours at 55°C. The probes were diluted in hybridising solution and denatured by heating (75°C, 10 minutes). The animals were incubated with the probes for 2.5 days at 55°C. Unbound probes were removed by five-minute washing steps with 100%, 75%, 50%, 25% hybridising solution in 2× SSC (0.3 M NaCl, 0.03 M sodium citrate in water, pH 7.0) followed by two incubations for 30 minutes in 2× SSC, 0.1% Chaps. The animals were equilibrated in maleic acid buffer (MAB: 100 mM maleic acid, 150 mM NaCl in water, pH 7.5) 2× for 10 minutes and blocked in 1% blocking reagent (Roche, Indianapolis, IN, USA) in MAB for two hours at room temperature. For detection of the DIG labelled RNA probes, an anti-DIG antibody coupled to alkaline phosphatase was used at 1:4000 in blocking solution at 4°C overnight. Unbound antibody was washed out during eight 30- to 60-minute washing steps with MAB, followed by an overnight washing step. To detect the signal the animals were first equilibrated 2× for 10 minutes in NTMT (100 mM NaCl, 100 mM Tris pH 9.5, 50 mM $MgCl_2$, 0.1% Tween20) at room temperature and then incubated in NBT/BCIP (Roche, Indianapolis, IN, USA) 1:50 in NTMT in the dark at 37°C. When reaching the optimal signal to background ratio, the reaction was stopped by adding 100% ethanol. The animals were rehydrated by incubation for five minutes in 75%, 50% and 25% ethanol in 0.1× PBS. After a final rehydration step in PBS the animals were mounted on microscope slides in PBS 90% glycerol.

For double *in situ* hybridisation with Minicollagen-1 the animals were incubated simultaneously with DIG-labelled Cnidoin and fluorescein isothiocyanate (FITC)-labelled Minicollagen-1 probes. After incubation with the DIG antibody (1:2000) and MAB washing, the staining with NBT/BCIP was performed. The staining reaction was stopped with ethanol and after rehydration the animals were incubated with the FITC antibody (1:2000) overnight. After MAB washing, the minicollagen-signal was detected with the FastRed substrate (Roche). The reaction was stopped with 100 mM glycine, 0.1% Tween20, pH2.2. Samples were washed in PBS and mounted on microscope slides with PBS 90% glycerol.

#### Microscopy

Fluorescence images were captured with the Nikon A1R confocal laser-scanning microscope (Nikon, Tokyo, Japan), in part at the Nikon Imaging Center, Heidelberg, Germany. *In situ* images were captured with the Nikon Eclipse 80i (Nikon, Tokyo, Japan).

#### Transmission electron microscopy of recombinant Cnidoin

Supernatants of recombinant Cnidoin samples solubilised in 8 M urea were absorbed to freshly glow-discharged thin carbon films supported by thick perforated carbon layers and negatively stained with uranyl formiate following standard procedures [48].

#### AFM force spectroscopy on recombinant Cnidoin monomers

Purified Cnidoin samples were stored at −80°C and thawed on crushed ice. Following the manufacturer's protocol (Pierce, Rockford, Illinois, USA) samples were treated with

TCEP for breaking inter- and intramolecular disulphide bonds and additionally with iodoacetamide for preventing their reformation.

Cnidoin constructs, bearing a C-terminal type I dockerin tag (GDVNDDGKVNSTDAVALKRYVLRSGISINT DNADLNEDGRVNSTDLGILKRYILKEIDTLPYKN) and an N-terminal ybbR tag (DSLEFIASKLA), were covalently attached to a functionalised glass slide displaying a coenzyme A (CoA) surface (Figure 4A). For functionalisation, glass slides were silanised with 3-aminopropyldimethylethoxysilane (ABCR) [49], coated with 25 mM N-hydroxy-succinimide (NHS)-PEG-maleimide (M = 425.39 g/mol) and treated with 25 mM CoA. Functionalised glass slides were incubated with 1 mg/ml of treated proteins in the presence of Sfp-transferase and $MgCl_2$. After an incubation period of two hours, glass slides were carefully rinsed with Tris-buffered saline (25 mM Tris, 72 mM NaCl, pH 7.2), ensuring a permanent liquid environment for immobilised proteins and a loss of non-immobilised proteins. Silicon nitride AFM cantilevers bearing a silicon tip (BL-AC40TS-C2, Olympus, Center Valley, Pennsylvania, USA) were aminosilanised and coated with (NHS)-PEG-maleimide (M = 425.39 g/mol). Functionalised cantilevers were incubated with a 50 μM solution of CBM A2C-Cohesin (Addgene: pET28a-ybbR-HIS-CBM-CohI, 58709) [33] from *Clostridium thermocellum*, enabling specific binding to dockerin tagged proteins. All measurements were performed in Tris-buffered saline (25 mM Tris, 72 mM NaCl, pH 7.2) supplemented with 1 mM $CaCl_2$ and 10 mM dithiothreitol (DTT) and protease inhibitor mix (Roche).

Single molecule force spectroscopy was performed using custom-built instruments [50] each driven by an MFP-3D AFM controller. Spring constants of the cantilevers were determined individually using the thermal noise method within 20% deviation of the nominal value of 0.07 N/m. Force-distance traces were recorded in closed-loop mode at pulling speeds ranging from 200 nm/s to 6,400 nm/s. With each trace the *xy*-stage was moved by 150 nm to probe a new position on the surface. For studying Cnidoin stretching, only retract traces with a final double peak (Figure 4B) were considered. This feature is characteristic of the cohesin-dockerin rupture [32] and guarantees that Cnidoin was stretched specifically from its C-terminus. A WLC model was fitted from zero to the first of the double peaks.

#### Molecular dynamics simulations of Cnidoin's repetitive sequence units

Two repetitive sequence units, namely *QMQGCGQQM PPMMSGCGG* and *QMQGCGQQLPLMMPGCVG*, were selected for investigation with MD simulations. Both of the units contain the *GCGQQ* motif and also a high content of methionine, two major features of Cnidoin (Figure 1C, Additional file 1: Figure S1B). Initial extended structures of these two units were constructed using Pymol [51] and were parameterised at the all-atom level resolution using the OPLS-AA force field [52].

All simulations were carried out using the MD software package Gromacs 4.5.3 [53]. The two Cnidoin peptide units with extended initial structures were first solvated in boxes of TIP4P water molecules with an ion concentration ($Na^+$ and $Cl^-$) of 0.1 mol/liter [54]. A cut-off of 1.0 nm was used for non-bonded interactions, and the Particle-Mesh Ewald method was chosen to sample long-range electrostatic interactions [55]. Periodic boundary conditions were employed to remove artificial boundary effects. In order to use a time step of 0.2 fs, all covalent bonds were constrained using the LINCS algorithm [56]. All simulations were performed under a constant temperature of 300 K and a constant pressure of 1 bar, using Nose-Hoover temperature coupling and Parrinello-Rahman pressure coupling methods, with coupling time constants of 0.4 ps and 4 ps, respectively [57-59]. The simulation systems were first energy minimised by using the steepest descent method. Equilibration of the solvent molecules was carried out for 500 ps, with all heavy atoms in the peptide restrained by a force constant of 1000 $kJ \cdot mol^{-1} \cdot nm^{-2}$. The two Cnidoin units were then fully equilibrated for 500 ns individually. Energy and coordinates of the simulation systems were collected every 1,000 time steps. The same simulation parameters were used in the following simulations unless otherwise specified.

Umbrella sampling along the end-to-end distance of the two-peptide units was performed to probe their elasticity. Structures of the two units with shortest end-to-end distances in the above-mentioned 500 ns equilibration were chosen as starting points. Two new simulation systems comprising approximately 55,000 atoms, which were large enough to accommodate fully extended peptides, were set up. The peptides were extended by applying a pulling force as in force-probe MD simulations [60]. Peptide conformations covering Z-components of end-to-end distances between 0.4 and 7.0 nm were chosen as starting structures for the umbrella sampling runs, with distance intervals of 0.4 nm. A force constant of 500 $kJ \cdot mol^{-1} \cdot nm^{-2}$ was used for the umbrella potential. The sampling times were changed with peptide extensions, with longer simulation times of 150 ns for extensions shorter than 2.0 nm because of higher fluctuations, and shorter times of 50 ns for longer extensions. The potential of mean force was calculated by using the weighted histogram analysis method [61]. Representative structures obtained from sampling at different extensions are shown in Figure 5A.

The dynamics of Cnidoin peptide collapse were investigated in an additional set of MD simulations. In these

simulations, the two Cnidoin peptide units were first held by a constant pulling force of 415 pN at both termini for 20 ns to obtain a conformational ensemble with large end-to-end distances. We chose 10 of the stretched peptide conformations and initiated force-quench MD simulations in the absence of a pulling force to monitor peptide collapse. We defined structures with an end-to-end distance of 1.5 nm or smaller as the collapsed state, and measured the time each of the fully stretched peptides required to reach this state. For comparison, two disordered peptides from the sequence-related silk protein (Spidroin-1 and Spidroin-2) and, as a representative of a non-elastomeric protein, two disordered peptides from the vWF linker between domains A1 and A2, were chosen to perform the same collapse force-quench MD simulations (peptide sequences are shown in Additional file 7: Figure S7). Aiming at understanding the dynamical effects from the high percentage of methionine residues, for an additional set of simulations, all methionines in the Cnidoin peptides were mutated to alanines. The mutated Cnidoin peptides were then subjected to the same force-quench MD simulations.

#### Molecular dynamics simulations of a bundle of Cnidoin's repetitive sequence units

The repetitive sequence unit *QMQGCGQQLPLMMPG CVG* previously simulated in isolation was incubated with three other identical peptides spaced 2 nm along one of the Cartesian coordinates. Protein fragments were placed at the center of a cubic box with dimensions of 10 $nm^3$. Simulation parameters and force fields were adopted from the simulations described above, if not otherwise mentioned. After a first energy minimisation the system was equilibrated in two steps. Firstly, temperature was coupled in a canonical (NVT) ensemble using a Nose-Hoover thermostat and secondly, pressure was coupled in an isobaric (NPT) ensemble using a Parrinello-Rahman barostat [57-59]. NVT and NPT equilibration runs were performed for 500 ps each, during which solvent molecules were able to accommodate around the protein that was fixed in space through the application of a 1,000 $kJ \cdot mol^{-1} \cdot nm^{-2}$ force constant on each protein's Cα atom. During the temperature-coupling step a set of initial, Boltzmann-distributed, velocities was generated. After equilibration, a 50 ns production molecular dynamics run was performed at the equilibrium, at a constant temperature of 300 K and a pressure of 0.1 bar. During such a run, the four filaments collapsed into a bundle subsequently used for the pulling simulations.

For the pulling simulations of a Cnidoin fragment embedded into a bundle of Cnidoin segments, the filament with the highest number of intermolecular contacts inside the bundle was chosen for pulling. The C-terminus Cα was set as pulling group whereas on the N-terminus Cα a positional restraint was placed using a force constant of 1,000 $kJ \cdot mol^{-1} \cdot nm^{-2}$. The C-terminus Cα was pulled along the Z-component, as previously described, using an umbrella potential of 500 $kJ \cdot mol^{-1} \cdot nm^{-2}$. Ten independent, pulling simulations were carried out.

#### Fourier-transform mid-infrared spectroscopy

The degree of ordering was assessed on the basis of Fourier-transform mid-infrared spectroscopy of dried films of Cnidoin elastic domain. For recombinant expression of the Cnidoin elastic domain a DNA fragment coding for amino acids GGQM-AGCG was amplified by PCR and cloned four times as a tandem repeat into the pet21 vector (Novagen, Whitehouse Station, New Jersey, USA). Protein purification was performed under denaturing conditions via the C-terminal his-tag. For elution, buffer conditions were changed to PBS (136.9 mM NaCl; 2,7 mM KCl; 1.5 mM $KH_2PO_4$; 8 mM $Na_2PO_4$) including 10 mM DTT, 500 mM NaCl, 250 mM imidazole as well as protease inhibitor mix and the eluted protein was immediately used for the experiment. For comparison, nine further proteins (hemoglobin, bovine serum albumin, concanavalin, ribonuclease s, lysozyme, ferritin, cytochrome c, elastase, casein) were investigated in the same manner. Thus, nine different protein solutions at 1 mg/ml each were prepared in the elution buffer for Cnidoin elastic domain. Each solution was pipetted to 10 wells (50 μL per well) of a 96-well silicon sample carrier and left to dry. This procedure was repeated on three further sample carriers and each sample carrier was then investigated separately in order to check for consistency and reproducibility. Details of the technical setup for spectroscopy are described in [62]. After vector normalisation in the region from 1,600 $cm^{-1}$ to 1,715 $cm^{-1}$ and background subtraction, the median absorbance of each nine-fold replication on each sample carrier was calculated. In order to investigate the degree of ordering of the proteins we followed the implications of Byler and Susi [31] in that, both a low number of spectral components in the overall amide I band as well as the existence and strength of a peak around 1,645 $cm^{-1}$ are indicative for a low degree of ordering. The number of spectral components was estimated from fitting one Gaussian curve per spectral component and comparing the fit results on the basis of the Akaike Information Criterion [63]. Median spectra were fitted with up to 13 Gaussian curves and up to 10 random starting conditions for any fixed number of Gaussian curves. An example of a median spectrum of Cnidoin is shown in Additional file 3: Figure S3C together with a fit result for five Gaussian curves (that is, five spectral components). All fit results were analysed by means of the corrected Akaike Information Criterion (AICc). Weights for

the fit with i Gaussian curves were set to be $\frac{e^{-\frac{AICc_{min}-AICc_i}{2}}}{\sum_i e^{-\frac{AICc_{min}-AICc_i}{2}}}$ and the weighted arithmetic mean was calculated in order to yield the optimum number of Gaussians as well as its standard deviation.

For the investigation of peak positions and widths, those spectral components which contributed less than 1% to the total signal (area under the curve) were omitted from further analysis in order to avoid misleading conclusions. The peak around 1,645 $cm^{-1}$ in the case of Cnidoin had an average width of 17.3 $cm^{-1}$ and, mathematically, the difference from the widths of the other peaks is significant on the basis of a two-sided *t*-test.

However, despite the clear indications for the lower degree of ordering in Cnidoin, it has to be noted that many assumptions and simplifications enter into this analysis such that the results should be considered as supplementary information supporting the hypothesis of Cnidoin being a mainly unordered protein.

## Additional files

**Additional file 1: Figure S1.** Primary structure and amino acid composition of Cnidoin. (A) amino acid sequence and domain organization of Cnidoin. Signal peptide is in turquoise, propeptide in green, CRDs in yellow and the elastic domain in dark blue. Underlined is the second C-terminal CRD used as epitope for antibody generation. (B) amino acid composition of the elastic Cnidoin domain shows a high content in glycine, glutamine and methionine as well as cysteine and proline.

**Additional file 2: Figure S2.** Co-polymerisation of Minicollagen and Cnidoin. Polymer products of recombinant Minicollagen-1-MBP as detected by Western blot are more pronounced with increasing amounts of recombinant Cnidoin.

**Additional file 3: Figure S3.** (A) Disorder prediction of Cnidoin by DisEMBL. Disorder scores of loops and coils for each residue in Cnidoin are shown. Expected level of disorder is shown as orange dashed line. Repetitive sequence units in Cnidoin are highlighted by the light blue region. (B) Number of spectral components observed in the mid-infrared spectra of Cnidoin and other proteins. The red triangles represent the average number of components derived from multiple repetitions of the measurement procedure and the error bars indicate the standard deviation. Blue dots are the results obtained from Byler and Susi [31], from where it can be inferred that a low number of spectral components represents a low degree of ordering of the protein. (C) Example mid-infrared spectrum of Cnidoin together with a fit result for the case of five spectral components.

**Additional file 4: Figure S4.** Forces of cohesin-dockerin rupture events as a function of the corresponding loading rates. For double rupture events, the '2nd' denotes the final peak. In agreement with [32] forces are in the order of 100 pN and are highest for the second peak, followed by the first peak of double events, and are lowest for single rupture events.

**Additional file 5: Figure S5.** (A) Force-distance traces of Cnidoin displaying only a final single peak. Double as well as single peak traces show identical characteristic worm-like chain (WLC) behaviour and lack further pronounced features. For quantification of contour and persistence length, a WLC model was fitted to single peak traces (red line). (B) Histogram of the contour length distribution of Cnidoin based on single peak traces. The average contour length of 97 nm and its corresponding standard deviation of 38 nm are in excellent agreement with average contour length (94 nm) and standard deviation (43 nm) for double peak curves (Figure 4C). (C) Histogram of the persistence length distribution of Cnidoin based on single peak traces. The average persistence length of 0.42 nm and its corresponding standard deviation of 0.21 nm are in excellent agreement with average persistence length (0.37 nm) and standard deviation (0.23 nm) for double peak curves.

**Additional file 6: Figure S6.** Molecular elasticity of Cnidoin's repeat engaging intermolecular contacts. The figure shows force-extension profiles for Cnidoin's repetitive unit *QMQGCGQQLPLMMPGCVG* in the absence of other filaments in solution (red) and in the presence of four other identical fragments (black) as obtained from the average of 10 pulling simulations. The force-extension profiles have been fitted (solid lines) using a WLC model [36]. The obtained persistence length is 0.72 ± 0.02 nm for the single filament in water and 0.1 ± 0.003 nm for the filament embedded into the bundle. The snapshots at the top of the curves report the stretching of the pulled filament (orange) with respect to the bundle. The N-terminal position-restrained Cα is represented as a black sphere whereas the C-terminal pulled Cα is red. Filaments are represented as strings and atomic particles and bonds are shown using a balls and sticks representation and coloured by atom type.

**Additional file 7: Figure S7.** Disordered peptide sequences studied beside Cnidoin peptide units. Each of the sequences used in this study has 18 residues as those in Cnidoin peptides. Mutation points in Cnidoin peptides from methionine to alanine are highlighted in red in the figure.

**Competing interests**
The authors declare that they have no competing interests. In addition to his affiliation with the Kirchhoff-Institute for Physics, WP is also an employee of Roche Diagnostics GmbH, Mannheim, Germany.

**Authors' contributions**
SÖ, FG, MB, WP, and TH designed the experiments. AB, SX, DM, NK, FL, JM and TN performed experiments. SÖ, FG, MB, WP and TH wrote the manuscript. All authors read and approved the final manuscript.

**Acknowledgements**
We thank Jutta Tennigkeit for excellent technical assistance in preparation of recombinant Cnidoin and Wolfgang Ott for providing the CBM-Cohesin fusion proteins and helpful discussions concerning the dockerin tag. This work was supported by the DFG (Oe 416/4-1, HO 1046 1048/4-1/4-2), SFB 488 TP12, FOR 1543, the Klaus Tschira Foundation, and 1047 the Heidelberg Excellence Cluster Cellular Networks. We acknowledge financial support by Ruprecht-Karls-Universität Heidelberg within the funding programme Open Access Publishing. The funders had no role in study design, data collection and analysis, decision to publish or
preparation of the manuscript.

**Author details**
[1]Department of Molecular Evolution and Genomics, University of Heidelberg, Centre for Organismal Studies, Im Neuenheimer Feld 329, 69120 Heidelberg, Germany. [2]Heidelberg Institute for Theoretical Studies, Schloss-Wolfsbrunnenweg 35, 69118 Heidelberg, Germany. [3]Kirchhoff Institute for Physics, Heidelberg University, Im Neuenheimer Feld 227, 69210 Heidelberg, Germany. [4]Dioptic GmbH, Bergstraße 92A, D-69469 Weinheim, Germany. [5]Applied Physics and Center for NanoScience, Ludwig Maximilian University, Amalienstr. 54, 80799 München, Germany.

Received: 5 December 2014 Accepted: 24 December 2014
Published online: 16 January 2015

**References**

1. Roberts TJ, Azizi E. Flexible mechanisms: the diverse roles of biological springs in vertebrate movement. J Exp Biol. 2011;214:353–61.
2. Patek SN, Dudek DM, Rosario MV. From bouncy legs to poisoned arrows: elastic movements in invertebrates. J Exp Biol. 2011;214:1973–80.
3. Ozbek S, Balasubramanian PG, Holstein TW. Cnidocyst structure and the biomechanics of discharge. Toxicon. 2009;54:1038–45.
4. David CN, Ozbek S, Adamczyk P, Meier S, Pauly B, Chapman J, et al. Evolution of complex structures: minicollagens shape the cnidarian nematocyst. Trends Genet. 2008;24:431–8.
5. Nuchter T, Benoit M, Engel U, Ozbek S, Holstein TW. Nanosecond-scale kinetics of nematocyst discharge. Curr Biol. 2006;16:R316–8.

6. Weber J. Poly(gamma-glutamic acid)s are the major constituents of nematocysts in Hydra (Hydrozoa, Cnidaria). J Biol Chem. 1990;265:9664–9.
7. Szczepanek S, Cikala M, David CN. Poly-gamma-glutamate synthesis during formation of nematocyst capsules in Hydra. J Cell Sci. 2002;115:745–51.
8. Holstein T, Tardent P. An ultrahigh-speed analysis of exocytosis: nematocyst discharge. Science. 1984;223:830–3.
9. Tardent P, Holstein T. Morphology and morphodynamics of the stenotele nematocyst of Hydra attenuata Pall. (Hydrozoa, Cnidaria). Cell Tissue Res. 1982;224:269–90.
10. Kurz EM, Holstein TW, Petri BM, Engel J, David CN. Mini-collagens in hydra nematocytes. J Cell Biol. 1991;115:1159–69.
11. Holstein TW, Benoit GM, Herder GV, Wanner G, David CN, Gaub HE. Fibrous mini-collagens in hydra nematocysts. Science. 1994;265:402–4.
12. Engel U, Pertz O, Fauser C, Engel J, David CN, Holstein TW. A switch in disulfide linkage during minicollagen assembly in Hydra nematocysts. EMBO J. 2001;20:3063–73.
13. Özbek S, Pertz O, Schwager M, Lustig A, Holstein T, Engel J. Structure/function relationships in the minicollagen of Hydra nematocysts. J Biol Chem. 2002;277:49200–4.
14. Balasubramanian PG, Beckmann A, Warnken U, Schnoelzer M, Schueler A, Bornberg-Bauer E, et al. The Proteome of the hydra nematocyst. J Biol Chem. 2012;287:9672–81.
15. Vollrath F. Spiders' webs. Curr Biol. 2005;15:R364–5.
16. Linke WA, Kulke M, Li H, Fujita-Becker S, Neagoe C, Manstein DJ, et al. PEVK domain of titin: an entropic spring with actin-binding properties. J Struct Biol. 2002;137:194–205.
17. Dong Z, Lewis RV, Middaugh CR. Molecular mechanism of spider silk elasticity. Arch Biochem Biophys. 1991;284:53–7.
18. Qin G, Hu X, Cebe P, Kaplan DL. Mechanism of resilin elasticity. Nat Commun. 2012;3:1003.
19. Lv S, Dudek DM, Cao Y, Balamurali MM, Gosline J, Li HB. Designed biomaterials to mimic the mechanical properties of muscles. Nature. 2010;465:69–73.
20. Cheng S, Cetinkaya M, Grater F. How sequence determines elasticity of disordered proteins. Biophys J. 2010;99:3863–9.
21. Rico F, Gonzalez L, Casuso I, Puig-Vidal M, Scheuring S. High-speed force spectroscopy unfolds titin at the velocity of molecular dynamics simulations. Science. 2013;342:741–3.
22. Hinman MB, Lewis RV. Isolation of a clone encoding a second dragline silk fibroin. Nephila clavipes dragline silk is a two-protein fiber. J Biol Chem. 1992;267:19320–4.
23. Pokidysheva E, Milbradt AG, Meier S, Renner C, Haussinger D, Bachinger HP, et al. The structure of the Cys-rich terminal domain of Hydra minicollagen, which is involved in disulfide networks of the nematocyst wall. J Biol Chem. 2004;279:30395–401.
24. Engel U, Ozbek S, Engel R, Petri B, Lottspeich F, Holstein TW. NOWA, a novel protein with minicollagen Cys-rich domains involved in nematocyst formation in Hydra. J Cell Sci. 2002;115:3923–34.
25. Adamczyk P, Meier S, Gross T, Hobmayer B, Grzesiek S, Bachinger HP, et al. Minicollagen-15, a novel minicollagen isolated from Hydra, forms tubule structures in nematocysts. J Mol Biol. 2008;376:1008–20.
26. Ozbek S, Pokidysheva E, Schwager M, Schulthess T, Tariq N, Barth D, et al. The glycoprotein NOWA and minicollagens are part of a disulfide-linked polymer that forms the cnidarian nematocyst wall. J Biol Chem. 2004;279:52016–23.
27. Maeda I, Fukumoto Y, Nose T, Shimohigashi Y, Nezu T, Terada Y, et al. Structural requirements essential for elastin coacervation: favorable spatial arrangements of valine ridges on the three-dimensional structure of elastin-derived polypeptide (VPGVG)n. J Pept Sci. 2011;17:735–43.
28. Uversky VN, Gillespie JR, Fink AL. Why are "natively unfolded" proteins unstructured under physiologic conditions? Proteins. 2000;41:415–27.
29. Uversky VN. Natively unfolded proteins: a point where biology waits for physics. Protein Sci. 2002;11:739–56.
30. Linding R, Jensen LJ, Diella F, Bork P, Gibson TJ, Russell RB. Protein disorder prediction: implications for structural proteomics. Structure. 2003;11:1453–9.
31. Byler DM, Susi H. Examination of the secondary structure of proteins by deconvolved FTIR spectra. Biopolymers. 1986;25:469–87.
32. Stahl SW, Nash MA, Fried DB, Slutzki M, Barak Y, Bayer EA, et al. Single-molecule dissection of the high-affinity cohesin-dockerin complex. Proc Natl Acad Sci U S A. 2012;109:20431–6.
33. Otten M, Ott W, Jobst MA, Milles LF, Verdorfer T, Pippig DA, et al. From genes to protein mechanics on a chip. Nat Methods. 2014;11:1127–30.
34. Rief M, Gautel M, Oesterhelt F, Fernandez JM, Gaub HE. Reversible unfolding of individual titin immunoglobulin domains by AFM. Science. 1997;276:1109–12.
35. Rief M, Gautel M, Schemmel A, Gaub HE. The mechanical stability of immunoglobulin and fibronectin III domains in the muscle protein titin measured by atomic force microscopy. Biophys J. 1998;75:3008–14.
36. Bustamante C, Marko JF, Siggia ED, Smith S. Entropic elasticity of lambda-phage DNA. Science. 1994;265:1599–600.
37. Zhang WK, Xu QB, Zou S, Li HB, Xu WQ, Zhang X, et al. Single-molecule force spectroscopy on Bombyx mori silk fibroin by atomic force microscopy. Langmuir. 2000;16:4305–8.
38. Kabsch W, Sander C. Dictionary of protein secondary structure: pattern recognition of hydrogen-bonded and geometrical features. Biopolymers. 1983;22:2577–637.
39. Becker N, Oroudjev E, Mutz S, Cleveland JP, Hansma PK, Hayashi CY, et al. Molecular nanosprings in spider capture-silk threads. Nat Mater. 2003;2:278–83.
40. Mansiaux Y, Joseph AP, Gelly JC, de Brevern AG. Assignment of PolyProline II conformation and analysis of sequence–structure relationship. PLoS One. 2011;6:e18401.
41. Verweij CL, Diergaarde PJ, Hart M, Pannekoek H. Full-length von Willebrand factor (vWF) cDNA encodes a highly repetitive protein considerably larger than the mature vWF subunit. EMBO J. 1986;5:1839–47.
42. Tatham AS, Shewry PR. Elastomeric proteins: biological roles, structures and mechanisms. Trends Biochem Sci. 2000;25:567–71.
43. Rauscher S, Pomes R. Structural disorder and protein elasticity. Adv Exp Med Biol. 2012;725:159–83.
44. Phillips R, Kondev J, Theriot J. Physical biology of the cell. New York: Garland Science, Taylor & Francis Group; 2008.
45. Savage KN, Gosline JM. The role of proline in the elastic mechanism of hydrated spider silks. J Exp Biol. 2008;211:1948–57.
46. Liu Y, Sponner A, Porter D, Vollrath F. Proline and processing of spider silks. Biomacromolecules. 2008;9:116–21.
47. Weber J. Nematocysts (stinging capsules of Cnidaria) as Donnan-potential-dominated osmotic systems. Eur J Biochem. 1989;184:465–76.
48. Engel J. Electron microscopy of extracellular matrix components. Methods Enzymol. 1994;245:469–88.
49. Zimmermann JL, Nicolaus T, Neuert G, Blank K. Thiol-based, site-specific and covalent immobilization of biomolecules for single-molecule experiments. Nat Protoc. 2010;5:975–85.
50. Gumpp H, Stahl SW, Strackharn M, Puchner EM, Gaub HE. Ultrastable combined atomic force and total internal reflection fluorescence microscope [corrected]. Rev Sci Instrum. 2009;80:063704.
51. Schrödinger L. The PyMOL Molecular Graphics System, Version 1.5.0.4. Schrödinger, LLC http://www.pymol.org.
52. Jorgensen WL, Tiradorives J. The opls potential functions for proteins - energy minimizations for crystals of cyclic-peptides and crambin. J Am Chem Soc. 1988;110:1657–66.
53. Hess B, Kutzner C, van der Spoel D, Lindahl E. GROMACS 4: Algorithms for highly efficient, load-balanced, and scalable molecular simulation. J Chem Theor Comput. 2008;4:435–47.
54. Jorgensen WL, Chandrasekhar J, Madura JD, Impey R, Klein ML. Comparison of simple potential functions for simulating liquid water. J Chem Phys. 1983;79:926–35.
55. Darden T, York D, Pedersen L. Particle Mesh Ewald - an N. Log(N) method for Ewald sums in large systems. J Chem Phys. 1993;98:10089–92.
56. Hess B, Bekker H, Berendsen HJ, Fraaije JG. LINCS: a linear constraint solver for molecular simulations. J Comput Chem. 1997;18:1463–72.
57. Nose S. A molecular dynamics method for simulations in the canonical ensemble (Reprinted from Molecular Physics, vol 52, pg 255, 1984). Mol Phys. 2002;100:191–8.
58. Hoover WG. Canonical dynamics: equilibrium phase-space distributions. Phys Rev A. 1985;31:1695–7.
59. Parrinello M, Rahman A. Polymorphic transitions in single crystals: a new molecular dynamics method. J Appl Phys. 1981;52:7182–90.
60. Grubmuller H, Heymann B, Tavan P. Ligand binding: molecular mechanics calculation of the streptavidin biotin rupture force. Science. 1996;271:997–9.
61. Kumar SR, John M, Bouzida D, Swendsen RH, Kollman PA. The weighted histogram analysis method for free-energy calculations on biomolecules. I. The method. J Comput Chem. 1992;13:1011–21.

62. Rohleder D, Kocherscheidt G, Gerber K, Kiefer W, Kohler W, Mocks J, et al. Comparison of mid-infrared and Raman spectroscopy in the quantitative analysis of serum. J Biomed Opt. 2005;10:031108.
63. Akaike H. A new look at the statistical model identification. IEEE Trans Automat Contr. 1974;19:716–23.

# B Submitted Manuscript

## B.1 Submitted Manuscript: pH-Dependent Interactions in Dimers Govern Mechanics and Structure of von Willebrand Factor

# pH-Dependent Interactions in Dimers Govern Mechanics and Structure of von Willebrand Factor

by

Jochen P. Müller*, Achim Löf*, Salomé Mielke, Tobias Obser, Linda K. Bruetzel, Willem Vanderlinden, Jan Lipfert, Reinhard Schneppenheim, and Martin Benoit

submitted to

Biophysical Journal

on April 9th 2016

*These authors contributed equally to this work.

# pH-Dependent Interactions in Dimers Govern Mechanics and Structure of von Willebrand Factor

*J. P. Müller* [*+], *A. Löf* [*], *S. Mielke, T. Obser, L. K. Bruetzel, W. Vanderlinden, J. Lipfert, R. Schneppenheim, and M. Benoit*

* J.P.M. and A.L. contributed equally to this work.

[+] Corresponding author

**Running title:** pH-Dependent Interactions in VWF Dimers

**ABSTRACT**

Von Willebrand factor (VWF) is a multimeric plasma glycoprotein that is activated for hemostasis by increased hydrodynamic forces at sites of vascular injury. Here, we employ AFM single-molecule force measurements, AFM imaging, and small-angle X-ray scattering (SAXS) to show that structure and mechanics of VWF are governed by multiple pH-dependent interactions with opposite trends within dimeric subunits. Particularly, the recently discovered strong intermonomer interaction, which induces a firmly closed conformation of dimers and crucially involves the D4 domain, was observed with highest frequency at pH 7.4, but was essentially absent at pH values below 6.8. However, below pH 6.8, the ratio of compact dimers increased with decreasing pH, in line with a previous TEM study. These findings indicated that compactness of dimers at pH values below 6.8 is promoted by other interactions possessing low mechanical resistance compared to the strong intermonomer interaction. By investigating deletion constructs, we found compactness under acidic conditions to be primarily mediated by the D4 domain, i.e., remarkably by the same domain that also mediates the strong intermonomer interaction. As our data suggest highest mechanical resistance of VWF at physiological pH, local deviations from physiological pH, e.g., at sites of vascular injury, may represent a mechanism to enhance VWF's hemostatic activity where needed.

**INTRODUCTION**

In order to prevent excessive blood loss at sites of vascular injury, damaged vessel walls need to be sealed rapidly and effectively by a hemostatic plug. A key player for the formation of a hemostatic plug is the multimeric plasma glycoprotein von Willebrand factor (VWF). Activated by increased forces at sites of vascular injury, VWF critically mediates hemostasis by binding to subendothelial collagen and by promoting platelet aggregation (1–3). VWF's central role in hemostasis is underlined by a variety of mutations in VWF that cause the common bleeding disorder von Willebrand disease (4).

The complex biosynthesis of linear VWF multimers (concatamers) in vascular endothelial cells and megakaryocytes involves extensive posttranslational processing (4, 5), some steps of which crucially depend on pH-regulated conformational changes of the protein (6, 7). After expression as pre-pro-proteins – comprising a short signal peptide sequence and pro-peptide domains D1 and D2 in addition to the domains present in mature VWF (D'D3, A1, A2, A3, D4, C1-C6, CK; see **Fig. 1A**) – and subsequent cleavage of the signal peptide, monomers are dimerized in the endoplasmatic reticulum (ER, pH 7.4) in a tail-to-tail fashion via disulfide linkage between their CK domains (5, 8). Dimers are equipped with N- and O-linked glycans in the ER and the Golgi, respectively (5). At the lowered pH values of the Golgi and trans-Golgi (pH 6.2), dimers were shown to preferentially adopt a compact conformation, as monomers zip up from the CK domains up to the A2 domains to form so-called dimeric bouquets (7). However, A2 and A3 are not crucial for bouquet formation (7). Such compact dimeric bouquets are thought to favor the

formation of closely packed helical tubules built up from dimers in the trans-Golgi and Weibel-Palade bodies (6, 9). Latter are secretory granules of endothelial cells possessing a pH of approximately 5.4 (10), close to VWF's pI (11). Tubule formation crucially depends on pH-regulated association of the pro-peptide domains D1-D2 (5, 6) and goes hand in hand with orderly linear multimerization of dimers (6, 7). Templated by the tubule architecture, linkage of dimers occurs in a head-to-head fashion via formation of disulfide bonds between D'D3 domains (5, 7), resulting in concatamers built up from dimers as smallest repeating subunits, which after proteolytic cleavage of the pro-peptide possess a mass of ~ 500 kDa. It was speculated that histidine residues in VWF's C-terminal segment D4-CK mediate pH-dependent bouquet formation (7). Indeed, several of VWF's domains harbor a comparably large number of histidines (**Fig. 1A**). The highest density of histidines is found in VWF's D4 domain, which is an assembly of distinct sub-modules (D4N, D4, C8-4, and TIL4) (12).

Upon secretion into the vasculature, VWF encounters a pH of 7.4 and adopts an overall more flexible conformation (1). However, we recently showed that a strong intermonomer interaction is present in roughly half of VWF's dimeric subunits under near-physiological conditions (13). In brief, AFM single-molecule force measurements on VWF dimers revealed two types of characteristic force–extension traces. While traces of type II only exhibited peaks corresponding to the well-characterized unfolding of the A2 domains (~ 10-20 pN) (14–17), type I traces revealed an additional peak at high force (> 50 pN), which was identified with the dissociation of a strong intermonomer interaction, providing additional length of approximately 80 nm to the elongation of dimers. Our data further revealed that this interaction critically involves the D4 domain and divalent ions. Importantly, elongational forces on VWF in the bloodstream result from the interplay of an elongational flow component and VWF's extraordinary length (14, 18), which may exceed 15 µm in the plasma (2). Force sensing, i.e. conversion of flow into a physiological signal, is crucial for VWF's hemostatic function, as VWF's activation for collagen binding and binding to the platelet glycoprotein Ib (GPIb) was shown to be force-induced (2, 3). Increased forces acting on VWF are encountered where elongational flow components are elevated, as for instance at sites of vascular injury, but also in stenosed vessels, where VWF can provoke thrombosis (1). Importantly, by reducing the effective force-sensing length of concatamers, the strong intermonomer interaction in VWF's dimeric subunits can be assumed to increase critical rates of elongational flow to activate VWF for hemostasis (13).

While the pH crucially affects VWF's conformation, it has not been clarified to what extent it influences VWF's mechanics. It has been proposed that pH variations may play a pivotal role for VWF's activation by affecting critical rates of elongational flow (19). Certainly, the pH in healthy blood vessels is precisely buffered to maintain a pH of 7.4, and small deviations of 0.1 already represent pathophysiological conditions. However, as suggested by several studies (20–24), the pH may locally vary at sites of injury and inflammation. Furthermore, to shed light on the nature of the molecular mechanisms

underlying VWF's structure and mechanics, in particular of the strong intermonomer interaction, a comprehensive investigation of the influence of the pH is of general interest.

Here, we present data from AFM single-molecule force measurements, AFM imaging, and small-angle X-ray scattering (SAXS), showing that the ratio of dimers exhibiting the strong intermonomer interaction strongly depends on the pH, reaching a maximum at pH 7.4. Dimers were in the focus of our investigations, as they build up higher order concatamers without significantly changing their individual structure (13). Our data further reveal that compactness of dimers under acidic conditions is accomplished by another intermonomer interaction that has however a lower mechanical resistance. Overall, we combine force and imaging data to dissect and locate pH-dependent interactions within VWF's dimeric subunits and to characterize their mechanical resistance, which crucially affects force sensing by VWF and thereby VWF's activation for hemostasis.

## MATERIALS AND METHODS

### *Genetic engineering of recombinant proteins*

Heterodimeric VWF constructs were expressed in HEK 293 cells (DSMZ, Braunschweig, Germany), after initial co-transfection of cells with two different plasmids, encoding VWF sequence and N-terminal ybbR- or N-terminal Twin-Strep-tag, respectively (13). Constructs used for AFM imaging experiments possessed a Strep-tag instead of the Twin-Strep-tag. VWF monomers were expressed in HEK 293 cells, after transfection of cells with a single type of plasmid, encoding VWF sequence and both N-terminal ybbR-tag and C-terminal Twin-Strep-tag. Plasmid construction was carried out as previously described in detail (13). Transfection of cells occurred in DMEM (Life Technologies) containing 10% FBS (Life Technologies), 4 μg plasmid (for co-transfection 2 μg of both plasmids), and 15 μL Lipofectamine 2000 (Life Technologies). 24 h after transfection, cells were transferred into selection medium, which contained 500 μg/mL G418 (Invivogen, Toulouse, France). In the case of co-transfected cells, the selection medium additionally contained 250 μg/mL Hygromycin B (Invivogen). After 2 to 3 weeks, the polyclonal cell culture was seeded for expression. After 72 h of cell growing, the medium was exchanged against OPTIPRO-SFM for secretion of recombinant VWF. The culture supernatant was collected after 72 h and subsequently concentrated using Amicon Ultra-15 MWCO 100 kDa.

Strep-Tactin with a single Cysteine, which was used for pulling Twin-Strep-tagged VWF specifically, was prepared as described in (13, 26).

### *Buffers*

For experiments under varied pH conditions, buffer solutions containing 150 mM NaCl and 20 mM of one of the following buffering agents were used: Na-acetate (pH 5.4), BisTris (pH 6.2, 6.6, and 6.8),

Hepes (pH 7.1 and pH 7.4) or Tris (pH 8.0 and 8.6). The pH was adjusted using HCl and NaOH, respectively. Buffers used for measurements in the presence of divalent ions additionally contained 1 mM $CaCl_2$ and 1 mM $MgCl_2$. Buffers used for measurements in the presence of free Imidazole further contained 200 mM Imidazole in addition to $CaCl_2$ and $MgCl_2$. Prior to measurements in the absence of divalent ions, proteins were incubated with 10 mM EDTA for 8 h and afterwards buffer exchanged to the measurement buffer. For SAXS measurements in the presence of EDTA, buffers contained 10 mM EDTA.

*Single-molecule force measurements*

For single-molecule force measurements, samples and cantilevers were prepared as previously reported (13). In brief, VWF constructs, carrying a ybbR-tag (DSLEFIASKLA) and a Twin-Strep-tag (WSHPQFEKGGGSGGGSGGGSWSHPQFEK), were covalently attached to a glass surface functionalized with Coenzyme A (CoA). For preparation of CoA functionalized surfaces, glass slides were initially silanized with (3-aminopropyl)-dimethyl-ethoxysilane (APDMES) (25). Afterwards, a 5 kDa N-Hydroxy-Succinimide (NHS)-PEG-Maleimide linker (PEG linker, 25 mM) was conjugated to amine groups on the glass surface. The maleimide chemistry of the PEG linker allowed for subsequently coupling CoA (25 mM) to the PEGylated glass surfaces. Effective coupling was achieved in buffer containing 50 mM sodium phosphate, 50 mM NaCl, 10 mM EDTA, pH 7.2. Finally, CoA functionalized slides were incubated with VWF constructs (1 mg/mL) in OPTIPRO-SFM medium (Life Technologies, Darmstadt, Germany), in presence of Sfp-transferase and $MgCl_2$. Incubation occurred overnight at 4°C. After incubation, slides were carefully rinsed with buffer, ensuring a permanent liquid environment for immobilized proteins and a loss of non-immobilized proteins.

Similarly to surfaces, AFM cantilevers with a silicon tip (BL-AC40TS-C2, Olympus, Japan) were silanized with APDMES and incubated with the 5 kDa PEG linker (25 mM). Afterwards, Strep-Tactin bearing a single Cysteine residue (Strep-Tactin-Cys) was covalently attached to maleimide groups at the cantilever surface (13, 26). Before incubating cantilevers with Strep-Tactin-Cys, the latter was reduced in the presence of tris(2-carboxyethyl)phosphine (TCEP) beads and then separated from them by filtering. Cantilevers were incubated with reduced Strep-Tactin-Cys (10 mM) for 3 hours. Prior to experiments, cantilevers were relocated into the respective buffer that was used in the experiment.

Single-molecule force measurements were carried out as described (13), using custom built instruments (27), controlled each by an MFP-3D controller (Asylum Research, Santa Barbara, CA). Cantilever spring constants were determined using the thermal noise method (28). The cantilever was brought into contact with the sample surface and retracted at 6 different pulling speeds ranging from 0.2 to 6.4 μm/s. The sample was displaced in *x*–*y* direction after each force–extension trace to probe different molecules.

Force–extension traces were subjected to total variation denoising (TVD), and then further analyzed (29). In order to separate specific pulling events from unspecific ones, we used A2 unfolding peaks as a positive fingerprint (13). To estimate the ratio of type I and type II traces for pH values of 6.8 and above, bimodal distributions of the position of the first A2 unfolding peak were fitted with a double Gaussian function. More precisely, five free parameters were fitted, involving peak amplitudes and positions for both peaks individually and a single value for the width of either peak, accounting for experimental uncertainties that are virtually the same for type I and type II traces. To generate characteristic overlays of force–extension traces, undenoised force–extension traces were used. Traces were offset (offsets within 20 nm) along the extension axis, to achieve alignment with respect to the stretch prior to the rupture peak.

*AFM imaging*

Heterobifunctional dimeric VWF constructs [either full-length dimers or dimers with a deletion of the D4 domain (aa 1873-2255)], carrying both N-terminal Strep-tags and ybbR-tags, were purified using a HiTrap StrepTrap column (GE Healthcare Europe, Freiburg, Germany). Eluates were buffer exchanged to the respective measurement buffer and concentrated by centrifuge filtration using Amicon Ultra-15 MWCO 100 kDa (Merck Chemicals, Schwalbach, Germany).

Substrate preparation was as previously described (13). In brief, freshly cleaved mica sheets (grade I, SPI Supplies, West Chester, PA) were incubated with 20 μL of a poly-L-lysine (PLL) solution (MW 500-2000; 0.01% w/v; Sigma-Aldrich; in ultrapure water) for 30 s. Afterwards, they were thoroughly rinsed with 25 mL of ultrapure water and dried in a stream of nitrogen. 20 μL of buffer solution containing approximately 5 μg/mL of VWF constructs were deposited on the functionalized mica substrates and incubated for 30 s. Finally, the substrates were rinsed with 20 mL of ultrapure water and dried in a stream of nitrogen.

AFM images of 1 μm x 1 μm and 1024 x 1024 pixels were recorded in tapping mode in air, using an MFP-3D AFM (Asylum Research) and cantilevers with silicon tips (AC160TS, Olympus). These cantilevers have a nominal spring constant of 26 N/m and a resonance frequency of approximately 300 kHz. Raw image data were processed and analyzed using SPIP software (v6.4.4; Image Metrology, Denmark). Image processing involved plane correction (third order polynomial plane-fitting and flattening according to the histogram alignment routine) and Gaussian filtering.

Dimer conformations were analyzed by tracing dimers individually along their contour, following local maxima in height, employing poly-line profiling. In order to quantify the compactness of a dimer, we measured its stem length, i.e. the distance along the contour between the CK domain and the position at which the two constituent monomers separate from each other. We additionally determined the distance from the CK domain to the beginning of higher N-terminal domains for the two constituent monomers and used the mean of these distances to normalize the stem length.

For the sigmoidal fit shown in Fig. 3C, the following function was used:
$y = y_{max} / \{1 + \exp[(x_{half} - x) / rate]\}$.

*SAXS data acquisition and analysis*

For SAXS measurements, samples of A1-CK dimers, carrying an N-terminal Twin-Strep-tag, were prepared as described previously (13). Measurements were performed at beamline P12 (Deutsches Elektronen Synchrotron Hamburg, Germany) (Fig. 3D) (30), as described in (13), and at beamline X12SA (cSAXS) at the Swiss Light Source (Fig. S5). Measurements at beamline X12SA employed an X-ray energy of 12.4 keV and a sample-to-detector distance of 7 m, resulting in a $q$-range of $\sim (0.04 - 1.5)$ $nm^{-1}$ (with $q = 4 \cdot \pi \sin(\theta) / \lambda$, where $2\theta$ is the total scattering angle and $\lambda$ the X-ray wavelength). Sample solutions were added to 1-mm diameter quartz capillaries and kept at room temperature. Data were acquired with an exposure time of 1 s each at 10 positions along the length of the capillary. For all samples, the 10 profiles showed no signs of radiation damage. Matching profiles were averaged. Corresponding buffer samples were measured using identical procedures, and buffer profiles were subtracted for background correction.

**RESULTS**

*Force response of dimeric VWF under varied pH conditions*

For single-molecule force measurements, we used heterobifunctional VWF constructs (13), composed of two A1-CK monomers with different N-terminal tags (**Fig. 1B**). Dimeric A1-CK constructs were preferred over full-length constructs, as they resulted in significantly increased yields of specific pulling events. Higher yields may be a result of better accessible tags when located at the native linker N-terminal of A1 compared to being located directly at the N terminus of D'D3. A ybbR-tag at the N terminus of one of the A1-CK monomers enabled covalent attachment to a Coenzyme A functionalized glass surface (31), a Twin-Strep-tag at the N terminus of the other A1-CK monomer allowed for specific pulling via a Strep-Tactin functionalized AFM cantilever (32). We used polyethylene glycol (PEG) spacers both at glass surface and cantilever to minimize unspecific protein–surface interactions.

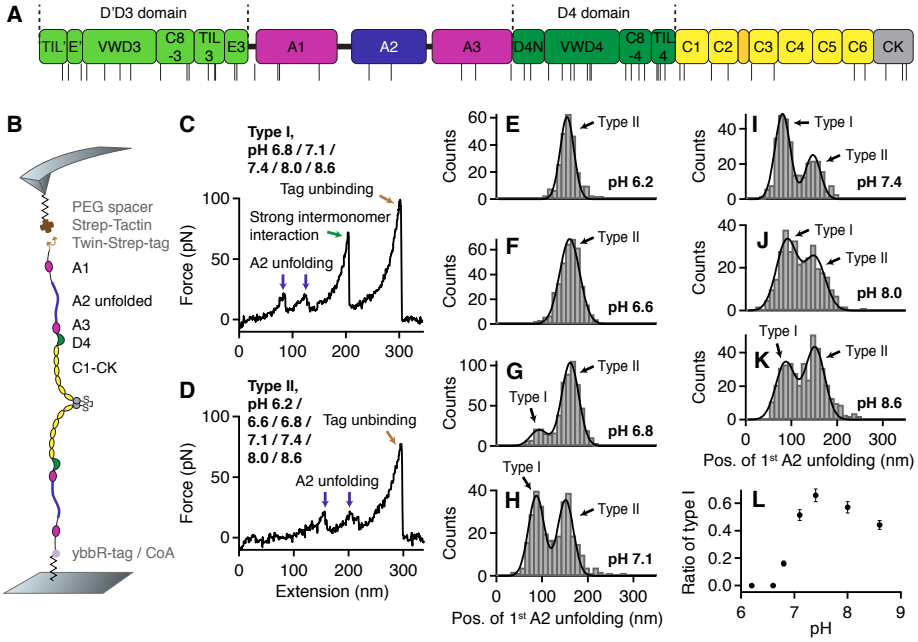


**Figure 1.** Single-molecule force measurements on dimeric VWF A1-CK constructs under varied pH conditions. (A) Domain organization of mature VWF (residues 764-2813), as described in (1, 12). Positions of histidine residues are indicated by black lines beneath. (B) Schematic of pulling dimeric A1-CK constructs (not drawn to scale). (C-D) Denoised force–extension traces of type I and type II, characterized by A2 unfolding peaks (blue arrows) at low (type I) and at high extension values (type II), respectively. While type II traces were observed throughout the probed pH range, type I traces, showing the force response of dimers that were initially firmly closed via the strong intermonomer interaction (13), were essentially only obtained at pH values of 6.8 and above. At all pH values at which type I traces were observed, dissociation of the strong intermonomer interaction (green arrow) yielded unvaried characteristic length increments. The final peak (brown arrow) corresponds to tag unbinding, i.e. to the dissociation of the specific Twin-Strep-tag/Strep-Tactin interaction and rupture of the probed molecule from the AFM tip (13, 33). (E-F) Unimodal distributions of the position of the first A2 unfolding peak, obtained for pH 6.2 (E) and 6.6 (F). The distributions are well described by fits of Gaussian functions (solid lines). (G-K) Bimodal distributions of the position of the first A2 unfolding peak, obtained for pH values of 6.8 (G), 7.1 (H), 7.4 (I), 8.0 (J), and 8.6 (K). To estimate the ratio of type I and type II traces, the

distributions were fitted with double Gaussian functions (solid lines). (L) Ratio of type I traces as a function of the pH. Error bars represent Poisson noise (1 SD).

Single-molecule force measurements were performed under different pH conditions, ranging from pH 6.2 to pH 8.6, while keeping ionic conditions fixed (150 mM NaCl, 1 mM $CaCl_2$, 1 mM $MgCl_2$). Force–extension traces corresponding to specific pulling events were identified using the appearance of two A2 unfolding peaks as a positive fingerprint (13). For all probed pH values, traces corresponding to specific pulling events did not exhibit any further characteristic peaks except those of A2 unfolding and – in traces of type I – the high-force peak corresponding to the dissociation of the strong intermonomer interaction in initially firmly closed dimers. Traces of type I exhibited A2 unfolding peaks at low extension values, traces of type II at high extension values (first A2 unfolding peak at roughly 80 and 150 nm, respectively) (13).

While traces of type I were only observed at pH values of 6.8 and above (**Fig. 1C**), traces of type II were observed for all examined pH values (**Fig. 1D**). In other words, at a pH of 6.2 and 6.6 only type II traces were observed (**Fig. S1** in the Supporting Material), whereas at pH values of 6.8 and above both type I and type II traces were obtained (**Fig. S2**), yet with markedly varied ratios. Accordingly, quantifying the position of the first A2 unfolding peak in force–extension traces yielded unimodal distributions for pH 6.2 and 6.6 (**Fig. 1E and 1F**), and characteristic bimodal distributions for pH values of 6.8 and above (**Fig. 1G-K**). These distributions revealed that the mean values of the positions of first A2 unfolding were, both for type I and type II traces, conserved throughout the probed pH range within a standard deviation of 5 nm, giving evidence that no domains were significantly destabilized by acidic pH, e.g. due to destabilized disulfide bonds. In line with this, force–extension traces of VWF monomers (D'D3-CK) at pH 6.2 were essentially identical to the ones obtained at pH 7.4 (**Fig. S3**). We estimated the ratios of type I and type II traces for pH 6.8 and above from double Gaussian fits to the distributions of the first A2 unfolding position. The ratio of type I traces as a function of the pH exhibited an abrupt increase at approximately pH 7.0 and a maximum value of (66 ± 5) % at pH 7.4 (**Fig. 1L**), closely matching the ratio previously observed for full-length dimers (13). Upon further alkalization, the ratio of type I traces slightly decreased, resulting in a value of (44 ± 3) % at pH 8.6. It should be noted that both at pH 8.0 and 8.6 the yield of specific pulling events, i.e. force–extension traces exhibiting two clear A2 unfolding peaks, was lower than at pH 7.4 and below. Overall, these data show that the formation of the strong intermonomer interaction in VWF's dimeric subunits strongly depends on the pH.

In order to test for reversibility of the underlying molecular mechanisms, we exchanged the buffer of immobilized proteins after measurements at pH 6.6 (histogram of first A2 unfolding position shown in **Fig. 1F** and **Fig. 2A**) to buffer solution adjusted to pH 7.4. Importantly, force–extension traces of type I were recovered, indicating that the pH-dependent mechanisms that critically affect the formation of firmly

closed dimers are largely reversible. However, the ratio of type I traces was lower [(35 ± 3) %] compared to experiments without prior incubation at acidic pH, as inferred from the bimodal distribution of the position of first A2 unfolding (**Fig. 2B**).

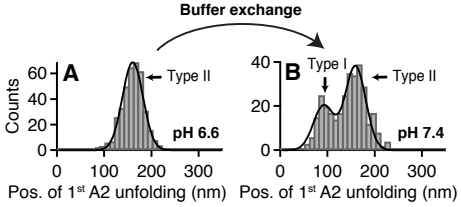


**Figure 2.** Reversibility of the pH-dependent mechanisms affecting the formation of the strong intermonomer interaction in VWF's dimeric subunits. (A) Unimodal distribution of the position of the first A2 unfolding peak in force–extension traces of A1-CK dimers measured at pH 6.6 (same histogram as shown in Fig. 1F), indicating that only type II traces were observed. (B) Histogram of the position of the first A2 unfolding peak, obtained after buffer exchanging immobilized proteins to buffer solution of pH 7.4 and with the same cantilever that was used at pH 6.6. Bimodality of the distribution indicates that a significant number of type I traces were observed, proving that the molecular mechanisms that critically affect the pH-dependent formation of the strong intermonomer interaction are largely reversible. Fitting a double Gaussian (solid line) yielded a ratio of (35 ± 3) % type I traces.

*Conformational ensemble of VWF dimers under varied pH conditions*

Complementarily to single-molecule force experiments, we employed AFM imaging to assess the conformations of dimeric VWF constructs adsorbed onto a poly-L-lysine coated mica substrate under different pH conditions (see ***Materials and Methods***, *Buffers*) (**Fig. 3A and 3B**). We quantified the ratio of compact dimers by analyzing the conformation of each dimer individually. More precisely, we analyzed the stem length for each dimer, i.e. the distance along the contour from the CK domain to the position at which the two constituent monomers separate from each other. We further measured the distance along the contour between the CK domain and the beginning of higher N-terminal domains for both monomers and used the mean of these distances to normalize the stem length. Dimers with a normalized stem length above 1, i.e. those possessing a fully formed C-terminal stem, were assigned as compact (13). It should be noted that at alkaline pH values, a non-negligible fraction of molecules – up to approximately 40 % at pH 8.6 – had to be discarded from analysis, as apparent self-aggregation repeatedly impeded unequivocal tracing, in line with observations from an earlier TEM study (7).

We determined the ratio of compact full-length dimers (D'D3-CK) as a function of the pH, both in the presence of divalent ions (**Fig. 3C**, blue circles), but also in the absence of divalent ions (**Fig. 3C**, red triangles), i.e., under conditions that obstruct the formation of the strong intermonomer interaction (13). In the absence of divalent ions, compactness decreased monotonically with increasing pH and was very well described by the fit of a simple sigmoidal function (dashed line) reaching its half-maximum at a pH of approximately 6.6. These findings suggest compactness to be mainly driven by a single mechanism in the absence of divalent ions. In the presence of divalent ions, for pH values of 6.8 and below, we obtained ratios of compact dimers essentially identical to the ones observed in the absence of divalent ions. Above a pH of 6.8, however, a second regime of compactness was observed. Intriguingly, the deviation to the data obtained in the absence of divalent ions was highest at a pH of 7.4. These findings are in line with the pH dependence of the strong intermonomer interaction observed in force measurements.

For further structural characterization, we performed SAXS measurements on A1-CK dimers at pH 6.2 and 7.4, both in the presence and absence of divalent ions. SAXS is a solution-based technique that does not require immobilization of samples onto a surface, making it a complementary tool to dissect conformational changes of dimeric VWF upon varying solution conditions in bulk (34, 35). We observed a conformational transition upon changing the pH from 6.2 (**Fig. 3D**, top, dark blue) to 7.4 (light blue) in the presence of divalent ions, as revealed by the SAXS profiles in Kratky representation. For both solution conditions, the Kratky plots exhibit a plateau shape with two slight peaks. However, at the lower pH value, the peaks are more pronounced and the intensity is lower at higher $q$ values, implying more compact and less flexible dimers at pH 6.2 than at pH 7.4. SAXS data were further acquired in the presence of EDTA, i.e., under conditions that obstruct the formation of the strong intermonomer interaction. At pH 7.4, we observed a transition to an ensemble of more flexible conformations (13), indicated by a more diverging shape at high $q$ values and less pronounced peaks in the Kratky plot (**Fig. 3D**, top, red). In contrast, at pH 6.2 no significant change was observed upon addition of EDTA (**Fig. S5**). These findings are further corroborated by comparison of the pair distance distribution functions $P(r)$ (histograms of pairwise distances in the molecule) (**Fig. 3D**, bottom). In the presence of divalent ions, the shape of the $P(r)$ function is indicative of a rather extended, rod-like molecule, even more pronounced for pH 6.2 than for pH 7.4. In contrast, upon addition of EDTA at pH 7.4, a shortening and steeper decay of $P(r)$ was observed, indicating a more flexible and thus more globular ensemble of dimer conformations. Overall, the SAXS data are fully in line with results from AFM imaging.

Furthermore, employing AFM imaging, we studied the compactness of dimers with a deletion of the D4 domain (delD4 dimers) in the presence of divalent ions (**Fig. 3C**, brown squares). Throughout the whole pH range, compact dimers were observed only occasionally (**Fig. 3B**), strongly suggesting the D4 domain to play a key role not only for the formation of the strong intermonomer interaction (13), but also for promoting compactness of dimers under acidic pH conditions.

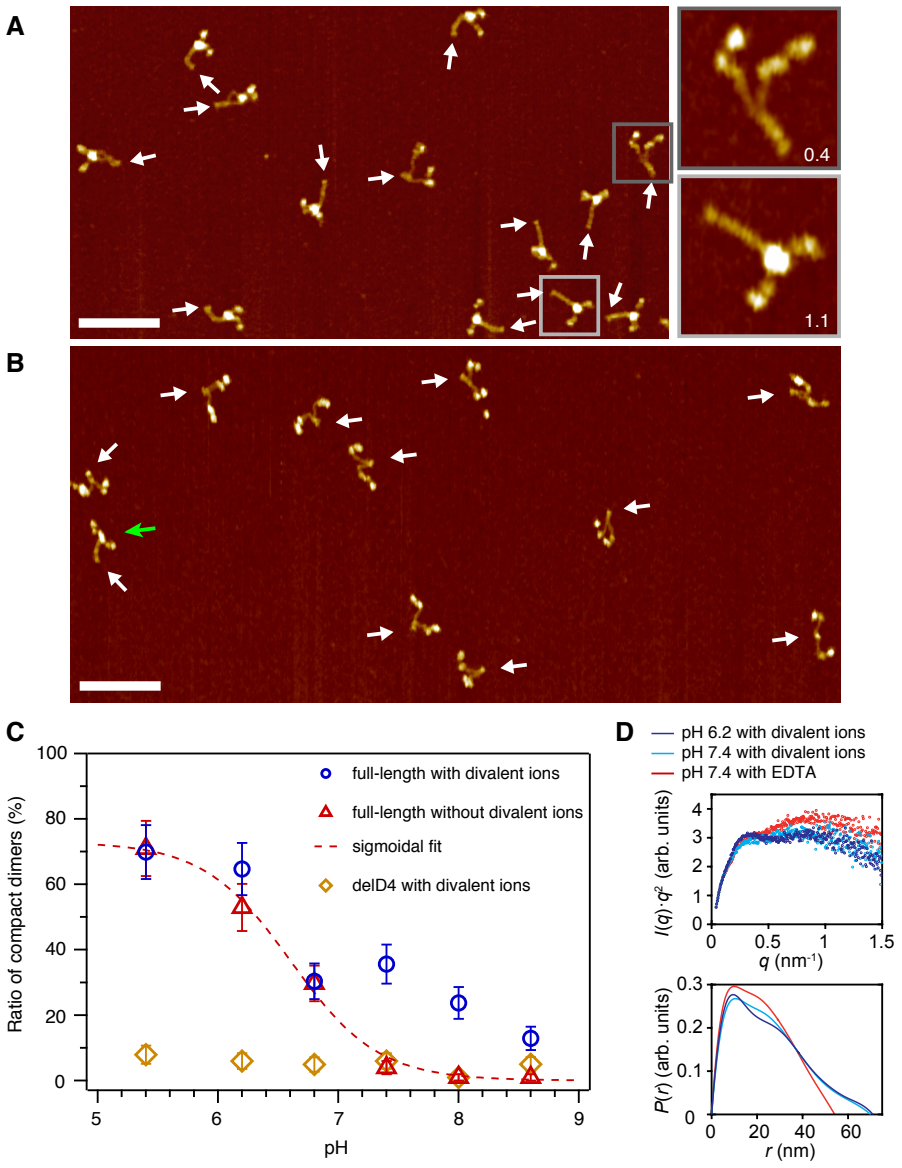


**Figure 3.** Conformation of dimeric VWF constructs under varied pH and ionic conditions. (A) Representative AFM image of full-length VWF dimers (D'D3-CK), adsorbed onto a

functionalized mica surface from buffer solution without divalent ions and adjusted to pH 6.2. Arrows mark positions of CK domains. A large fraction (> 50 %) of dimers exhibited a compact conformation with fully formed C-terminal stems. Insets exemplarily show a flexible dimer possessing a partially formed stem and a compact dimer with a fully formed stem, respectively. Numbers indicate values of the normalized stem length. Scale bar is 100 nm, range of color scale is 2.4 nm. (B) Representative AFM image of VWF dimers with a deletion of the D4 domain (delD4 dimers), adsorbed onto a functionalized mica substrate from buffer solution adjusted to pH 6.8 and containing divalent ions. White arrows mark positions of CK domains. Throughout the whole probed pH range, nearly all delD4 dimers exhibited a flexible conformation. The green arrow indicates an occasional compact dimer. Scale bar is 100 nm, range of color scale is 2.4 nm. (C) Ratio of compact VWF dimers as a function of pH. Only dimers with a normalized stem length above 1 were assigned as compact. Shown are data of full-length dimers in the presence (blue circles) and in the absence (red triangles) of divalent ions, and of delD4 dimers in the presence of divalent ions (brown squares). The dashed red line is a sigmoidal fit (half-maximum value at pH 6.6) to the data obtained for full-length dimers in the absence of divalent ions, i.e., under conditions that obstruct the formation of the strong intermonomer interaction mediated by the D4 domain (13). Error bars represent Poisson noise (1 SD). For each data point, $n \geq 100$ dimers were analyzed. (D) SAXS profiles in Kratky representation (top) and computed distance distribution functions $P(r)$ (bottom) for dimeric A1-CK constructs in the presence of divalent ions at pH 6.2 (dark blue) and pH 7.4 (light blue), and in the presence of 10 mM EDTA at pH 7.4 (red).

We further observed that the pH also affected the formation of C-terminal stems (7, 13). In order to investigate this effect without the influence of D4-mediated interactions, we analyzed distributions of the normalized stem length for the delD4 construct (**Fig. 4**), exhibiting virtually only values of the normalized stem length below 1, corresponding to flexible dimers. In general, higher average stem lengths were favored by low pH, even in the absence of D4-mediated mechanisms promoting compactness. In particular, also the functional shape of the stem length distributions changed considerably with the pH. While at alkaline pH values the distribution of the normalized stem length exhibited an approximately exponential shape, at lower pH values it revealed a maximum centered at roughly 0.4 that became more prominent with decreasing pH, suggesting that the pH-dependent stem formation is not mediated uniformly by all C-domains. This maximum centered at approximately 0.4 corresponds to dimers possessing roughly half-formed C-terminal stems, i.e. stems that are formed from CK domains up to a region comprising domains C5 to C3, which interestingly exhibit a comparably low density of histidine residues (**Fig. 1A**).

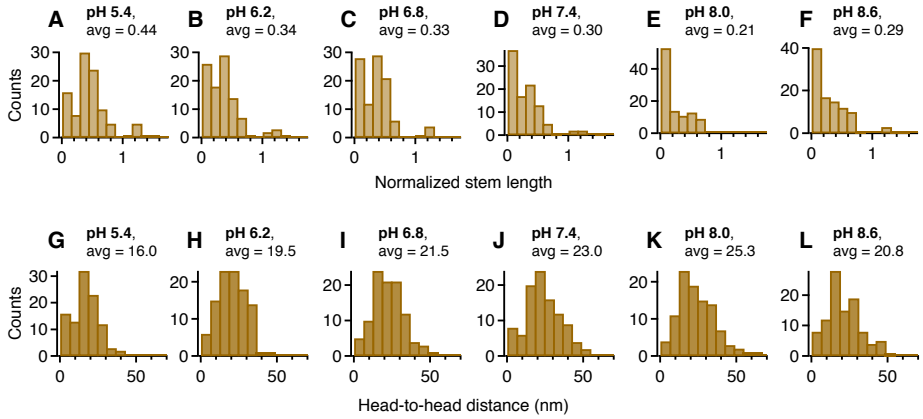


**Figure 4.** Impact of pH on C-terminal stem formation within dimeric VWF constructs with a deletion of the D4 domain. (A-F) Distributions of the normalized stem length of dimeric delD4 constructs and respective average values, obtained for pH 5.4 (A), 6.2 (B), 6.8 (C), 7.4 (D), 8.0 (E) and 8.6 (F), by tracing dimers in AFM images individually along their contour. It should be noted that at the alkaline pH values of 8.0 and especially 8.6, a non-negligible fraction of molecules had to be discarded from analysis due to apparent self-aggregation. (G-L) Distributions of the head-to-head distance of dimeric delD4 constructs, obtained for pH 5.4 (G), 6.2 (H), 6.8 (I), 7.4 (J), 8.0 (K) and 8.6 (L). Values of the head-to-head distance indicate the direct distance between the two positions within a dimer at which the stem regions adjoin to higher N-terminal domains. Consequently, distributions of the head-to-head distance provide a means for estimating effective concentrations of N-terminal domains. It should be noted that immobilization of VWF dimers onto the poly-L-lysine coated mica substrate might not proceed identically for varying pH conditions, as VWF's net charge changes with pH. Low pH conditions near VWF's pI may allow dimers to more effectively equilibrate than at higher pH values (11), at which the higher (negative) net charge of VWF molecules might lead to faster trapping on the surface. Consequently, the actual difference between average head-to-head distances for varying pH conditions might be slightly higher than observed.

*Obstruction of the strong intermonomer interaction by Imidazole*

The data presented above indicate that the strong intermonomer interaction is most favorable at pH 7.4, and only occurs in the presence of divalent ions. We aimed to gain further insight into the underlying molecular mechanism. To this end, we tested whether the role of divalent ions in the strong intermonomer interaction originates from an electrostatic effect or rather involves coordination chemistry,

possibly with the Histidine residues which are abundant in the D4 domain (**Fig. 1A**). We performed force experiments on A1-CK dimers at pH 7.4 in buffer solution supplemented with free Imidazole (200 mM) in addition to $MgCl_2$ and $CaCl_2$. In contrast to EDTA, which has only very low selectivity among the different divalent cations, Imidazole has virtually no affinity towards $Mg^{2+}$ and $Ca^{2+}$, but is capable of strong coordination bond formation with transition metal ions (36), which might be available during the biosynthesis of VWF. Strikingly, essentially only force–extension traces of type II were obtained (**Fig. 5A**), as inferred from a unimodal distribution of the position of the first A2 unfolding event (**Fig. 5B**). Obstruction of the strong intermonomer interaction by free Imidazole was further corroborated by AFM imaging on full-length dimers, adsorbed from the same buffer solution. In the presence of Imidazole, nearly all dimers exhibited a flexible conformation (**Fig. 5C-D**), which is in line with a scenario in which divalent (transition) metals are involved in the formation of the strong intermonomer interaction.

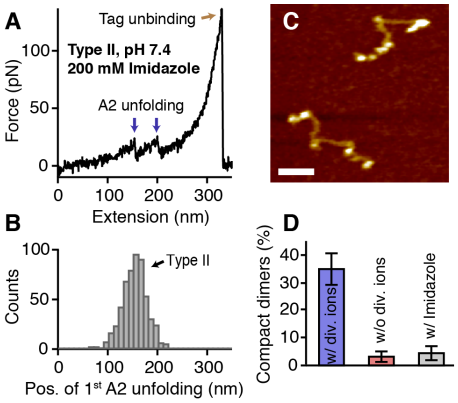


**Figure 5.** Obstruction of the strong intermonomer interaction by Imidazole. (A-B) Single-molecule force measurements on A1-CK dimers at pH 7.4 in the presence of divalent ions and 200 mM Imidazole. Force–extension traces of type II (A) were observed almost exclusively, as inferred from a unimodal distribution of the position of the first A2 unfolding peak (B). (C-D) AFM imaging of full-length VWF dimers adsorbed onto a functionalized mica surface from buffer solution adjusted to pH 7.4 and containing 200 mM Imidazole in addition to divalent ions. Nearly all dimers exhibited a flexible conformation (C). Scale bar is 30 nm, range of color scale is 2.4 nm. The ratio of compact dimers was close to zero (D, $n = 81$), similarly to the one obtained in the absence of divalent ions (see Fig. 3C). Further co-plotted is the markedly higher ratio observed for dimers adsorbed from buffer containing divalent ions, but no Imidazole (see Fig. 3C). Error bars represent Poisson noise (1 SD).

**DISCUSSION**

In this work, we performed AFM-based single-molecule force measurements, AFM imaging, and SAXS to characterize VWF's force response and conformational ensemble under different pH conditions. We initially found that the mechanical resistance of VWF's dimeric subunits strongly depends on the pH, as quantified by the ratio of type I force–extension traces, i.e. traces corresponding to the force response of dimers that were initially firmly closed via the strong intermonomer interaction (13). Interestingly, at low pH values of 6.2 and 6.6, virtually no dimers exhibited the strong intermonomer interaction. At first glance, this finding may appear contradictory to imaging data, which revealed that, almost throughout the whole examined pH range, low pH favors a compact conformation of dimers, thereby confirming a previous TEM study (7). In fact, combining the results from force and imaging experiments leads to the conclusion that compact dimers below pH 6.8 have a low mechanical resistance (**Fig. 6**, top), and accordingly, that the strong intermonomer interaction in VWF dimers is absent at these low pH values. In other words, compactness of dimers under acidic pH conditions is not accomplished by the strong intermonomer interaction, suggesting a second pH-dependent process to promote compactness under acidic pH conditions (7). Indeed, in the presence of divalent ions, the compactness of dimers as a function of pH revealed two regimes, strongly suggesting at least two pH-dependent mechanisms promoting compactness.

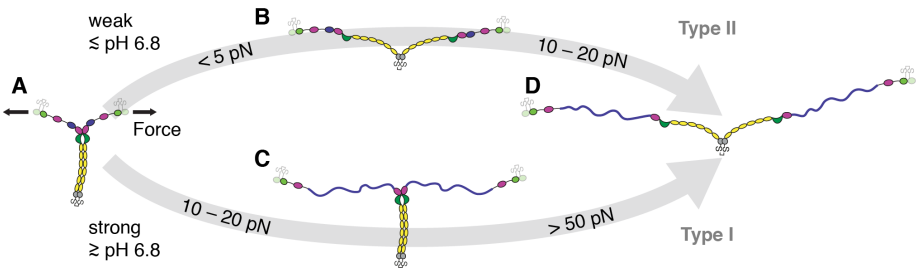


**Figure 6.** Strong and weak C-terminal rods in VWF's dimeric subunits. Schematically depicted are force-induced conformational changes (indicated forces correspond to loading rates probed in single-molecule force experiments) of VWF dimers that initially possess a fully formed C-terminal stem (C-terminal rod, A). At pH values below approximately 6.8, C-terminal rods are by trend weak and can dissociate at forces clearly below the detection limit of AFM force experiments, i.e. dissociation occurs very likely well below 5 pN (B). At forces of roughly 10 to 20 pN, VWF's A2 domains unfold and add a contour length of approximately 60-70 nm (lengths in schematic are drawn roughly to scale) each to the elongation of dimers (14–17) (D). At pH values above approximately 6.8 however, C-terminal rods are by trend firmly closed via the strong intermonomer

interaction. In this case, unfolding of the A2 domains at 10 to 20 pN is the first critical step of elongation (C). At forces above 50 pN the strong intermonomer interaction can dissociate and add approximately 80 nm to the elongation of dimers (D). Importantly, forces on VWF result from a positive feedback between elongational flow and length. For a VWF concatamer subjected to elongational flow under acidic pH conditions, forces of for instance 10 to 20 pN, as required for A2 unfolding, will be reached more readily, compared to near-physiological conditions, due to rapid initial opening of weak rods.

The mechanism that promotes compactness above pH 6.8 is the formation of the strong intermonomer interaction (**Fig. 6**, bottom), as inferred from two observations: first, the critical pH of 6.8, above which a second regime of compactness was observed, equals the critical pH of the strong intermonomer interaction observed in force experiments, and second, compactness above pH 6.8 can be abolished by taking out divalent ions from solution, in line with a loss of the strong intermonomer interaction observed in force experiments after treating samples with EDTA (13). In the absence of divalent ions, a monotonic decrease of the compactness of dimers with increasing pH was observed. The fact that this decrease was well described by the fit of a sigmoidal function suggests unidirectional pH-dependent interactions that do not rely on divalent ions. AFM imaging experiments on dimeric delD4 constructs revealed a crucial role of the D4 domain for promoting compactness at acidic pH, by keeping C-terminal stems (C1-CK) closed. This finding strongly suggests the existence of a second intermonomer interaction mediated by D4, which is mechanically less stable than the strong intermonomer interaction.

Importantly, C-terminal stem formation by itself, based on weak interactions between C domains (13), was also affected by the pH, as revealed by distributions of the normalized stem length obtained for delD4 dimers under varying pH conditions. While at alkaline pH values the distributions exhibited an approximately exponential shape, decreasing the pH led to the emergence of a maximum corresponding to dimers possessing roughly half-formed stems, suggesting that the pH dependence of the stem formation is not mediated uniformly by all C-domains. Going along with this observation, the average value of the normalized stem length increased by trend with decreasing pH, resulting in a decreased average distance between the two D4 domains within a dimer (**Fig. 4**). As a decreased distance between D4 domains in turn results in a higher effective concentration of these two putative binding partners, one could speculate that the pH dependence of the stem formation might be the only pH dependence underlying the increase of compactness of dimers with decreasing pH. A simple estimation, based on the observed distances between the D4 domains in a dimer (**Fig. 4G–L**) and the assumption that the effective concentration of D4 scales with the inverse cube of these distances, suggests that the pH-induced changes of the distance between the D4 domains of a dimer may well lead to an increase of their effective concentration by a factor of 4 over the probed pH range. However, the strong pH dependence of the ratios of compact dimers in the absence

of divalent ions (**Fig. 3C**, red), suggests that – assuming a constant affinity for the interaction between the two D4 domains – a change of the effective concentration by almost two orders of magnitude would be necessary to explain the observed increase of compactness with decreasing pH. Therefore, we assume that the mechanically weak intermonomer interaction mediated by D4 under acidic conditions possesses an intrinsic pH dependence. Remarkably, latter is opposed to the pH dependence of the strong intermonomer interaction mediated by the same domain. Both the pH dependence of the weak D4-mediated interaction and of the stem formation may play a pivotal role for orderly multimerization and packing of VWF in the trans-Golgi and WPB (7).

Undoubtedly, a key finding of this study is the pH dependence of the strong intermonomer interaction in VWF's dimeric subunits. Strikingly, decreasing the pH from 7.4 by less than one unit switches off the strong intermonomer interaction, thereby drastically decreasing the mechanical resistance of dimers. While at pH 6.6 the strong intermonomer interaction was virtually not observed, it could form again after buffer exchange to buffer solution adjusted to pH 7.4. This finding indicates that the molecular mechanisms that underlie the pH dependence of the strong intermonomer interaction are largely reversible. Importantly, the key domain D4 possesses a high density of histidine residues, whose Imidazole sidechains can be protonated, resulting in a change of their net charge, around a pH of approximately 6.5 [the $pK_a$-value of free histidines (37)]. This value is very close to the pH range over which the strong intermonomer interaction was abruptly switched off. A possible role of histidines was indeed indicated by measurements in the presence of free Imidazole, which revealed obstruction of the strong intermonomer interaction. Given that the strong intermonomer interaction crucially depends on divalent ions (13), we propose that coordination of metal ions by histidine residues may play a fundamental role for the formation of the strong intermonomer interaction. Indeed, it is well-known that coordination chemistry through Imidazole is impeded by protonation. It should be noted that full obstruction of the strong intermonomer interaction by removal of divalent ions was not achieved by a simple buffer exchange to buffer not containing divalent ions, but required addition of, e.g., EDTA (see ***Materials and Methods***, *Buffers*). This implies that also ion species not added to our buffer solutions, for instance ions of transition metals such as Zinc, could be involved in the formation of the strong intermonomer interaction. We further note that the effect of Imidazole should be taken into account when using it in protein purification procedures.

Histidine residues might also play a role for mediating the increase in compactness of dimers under acidic conditions, as suggested by the sigmoidal fit to the data obtained in the absence of divalent ions, which reached its half-maximum value at a pH of approximately 6.6, close to the $pK_a$-value of histidines. We believe that high-resolution structures, especially of the D4 domain and its constituent modules, will be of great value to elucidate pH dependencies within VWF.

In the vasculature, activation of VWF for hemostasis crucially depends on its ability to sense hydrodynamic forces (1, 2, 38), originating from an interplay of concatamer length and elongational flow components (14, 39, 40). Importantly, force sensing by VWF is tuned by the strong intermonomer interaction in its dimeric subunits, as it markedly shortens the effective length of a concatamer contributing to force sensing (13). For the pH values probed in our experiments, the fraction of firmly closed dimers reached a maximum at a pH of 7.4, indicating that VWF's mechanical resistance is maximized with respect to the physiological pH of 7.4 in the blood. Accordingly, critical rates of elongational flow needed to activate VWF for hemostasis, i.e., to initiate collagen binding and platelet aggregation, will be highest at physiological pH, assuming that the interaction of VWF with collagen and platelets as such remains unvaried by pH.

It is tempting to speculate on the role of this pH dependence, considering that locally the pH may be disturbed at sites of vascular injury. Indeed, it is widely accepted that local pH variations, especially acidification, occur in connection with injury and inflammation (20–24), although it remains unclear to what extent and on which timescales the blood pH might be affected. Clearly, our data suggest that deviations from physiological pH will lower critical rates of elongational flow to activate VWF for hemostasis. In particular, acidification is expected to very effectively reduce such critical elongational flow rates. Indeed, data obtained from flow experiments and published within the framework of a PhD thesis (Dr. Daniel Steppich, University of Augsburg, Germany) suggest that critical shear rates for elongation of VWF are lowered both upon acidification and alkalization (41). In principle, the relative impact of pH on critical elongational flow rates can be estimated based on the ratio of firmly closed dimers in VWF, observed at a given pH (13). For instance, at a pH of 6.6, where virtually no dimers exhibit the strong intermonomer interaction, the critical elongational flow may only be roughly half compared to the one at pH 7.4, as in the latter case VWF's effective force sensing length is expected to be decreased by approximately 30 %, assuming approximately half of VWF's dimeric subunits to be firmly closed via the strong intermonomer interaction. It should be noted that under acidic conditions, VWF's force sensing length will initially be lower than under physiological conditions, due to compact, yet mechanically relatively unstable dimers. However, as strongly suggested by our force data, most compact dimers below pH 6.8 will open up at comparably very low elongational flow rates and consequently increase VWF's effective force sensing length very rapidly, thereby triggering further elongation, due to the positive feedback between hydrodynamic force and length. In a nutshell, one could speculate that VWF's pH-dependent elongation behavior represents a smart mechanism to enhance VWF's hemostatic activity where needed.

In summary, structure and mechanics of VWF are governed primarily by two distinct intermonomer interactions within its dimeric subunits (**Fig. 6**). Remarkably, the two interactions exhibit opposed pH

dependencies, while at the same time they both appear to be mediated by modules of VWF's D4 domain. Strikingly, decreasing the pH by one unit from physiological pH yields a markedly increased degree of compactness of dimers, yet a considerably lowered mechanical stability. While high compactness at acidic pH can be assumed to be a prerequisite for orderly multimerization in the trans-Golgi and storage in Weibel-Palade bodies, low mechanical resistance at acidic pH may enhance VWF's hemostatic activity at sites of locally lowered pH encountered in the wake of injuries. Therefore, our data should provide further insights into VWF's activation for hemostasis.

**SUPPORTING MATERIAL**

Five supporting figures can be found in the Supporting Material.

**AUTHOR CONTRIBUTIONS**

JPM and AL designed experiments, acquired, analyzed and interpreted AFM force and imaging data, and wrote the manuscript. SM acquired and analyzed force data. TO designed and prepared constructs. LKB acquired and analyzed SAXS data. WV designed imaging experiments and interpreted data. JL designed SAXS experiments and analyzed data. RS and MB designed the overall research.

**ACKNOWLEDGMENTS**

We are very grateful to Prof. Dr. Hermann E. Gaub and Prof Dr. Erich Sackmann for helpful discussions. We further thank Prof. Dr. Matthias F. Schneider and Dr. Volker Huck for fruitful conversations. Gesa König is acknowledged for technical assistance in preparation of recombinant VWF. Moreover, we thank Dr. Diana A. Pippig for providing tetravalent Strep-Tactin with a single Cystein, Thomas Nicolaus for technical assistance in protein purification, and Lukas Milles for sharing a data processing and denoising algorithm. Furthermore, Dr. Cy. M. Jeffries and Dr. Marianne Liebi are acknowledged for support at the SAXS beamlines P12 and X12SA, respectively.

This study was supported by research funding from the German Research Foundation (DFG) to the Research Group FOR1543: "Shear flow regulation of hemostasis – bridging the gap between nanomechanics and clinical presentation" (SHENC). The authors thank the Nanosystems Initiative Munich (NIM) and the Center for Nanoscience (CeNS) for support. WV acknowledges the Research Foundation Flanders for a postdoctoral fellowship and a travel grant.

The authors declare that they have no conflict of interest.

**REFERENCES**


1. Springer, T.A. 2014. von Willebrand factor, Jedi knight of the bloodstream. Blood. 124: 1412–1425.
2. Schneider, S.W., S. Nuschele, A. Wixforth, C. Gorzelanny, A. Alexander-Katz, R.R. Netz, and M.F. Schneider. 2007. Shear-induced unfolding triggers adhesion of von Willebrand factor fibers. Proc Natl Acad Sci USA. 104: 7899–7903.
3. Ruggeri, Z.M., J.N. Orje, R. Habermann, A.B. Federici, and A.J. Reininger. 2006. Activation-independent platelet adhesion and aggregation under elevated shear stress. Blood. 108: 1903–1911.
4. Sadler, J.E. 1998. Biochemistry and genetics of von Willebrand factor. Annu Rev Biochem. 67: 395–424.
5. Wagner, D. 1990. Cell biology of von Willebrand factor. Annu Rev Cell Biol. 6: 217–246.
6. Huang, R.-H., Y. Wang, R. Roth, X. Yu, A.R. Purvis, J.E. Heuser, E.H. Egelman, and J.E. Sadler. 2008. Assembly of Weibel-Palade body-like tubules from N-terminal domains of von Willebrand factor. Proc Natl Acad Sci USA. 105: 482–487.
7. Zhou, Y.-F., E.T. Eng, N. Nishida, C. Lu, T. Walz, and T.A. Springer. 2011. A pH-regulated dimeric bouquet in the structure of von Willebrand factor. EMBO J. 30: 4098–4111.
8. Lippok, S., K. Kolsek, A. Löf, D. Eggert, W. Vanderlinden, J.P. Müller, G. König, T. Obser, K. Röhrs, S. Schneppenheim, U. Budde, C. Baldauf, C. Aponte-Santamaría, F. Gräter, R. Schneppenheim, J.O. Rädler, and M.A. Brehm. 2016. von Willebrand factor is dimerized by protein disulfide isomerase. Blood. 127: 1183–1191.
9. Springer, T.A. 2011. Biology and physics of von Willebrand factor concatamers. J Thromb Haemost. 9 Suppl 1: 130–143.
10. Erent, M., A. Meli, N. Moisoi, V. Babich, M.J. Hannah, P. Skehel, L. Knipe, G. Zupancic, D. Ogden, and T. Carter. 2007. Rate, extent and concentration dependence of histamine-evoked Weibel-Palade body exocytosis determined from individual fusion events in human endothelial cells. J. Physiol. 583: 195–212.
11. Fulcher, C.A., Z.M. Ruggeri, and T.S. Zimmerman. 1983. Isoelectric focusing of human von Willebrand factor in urea-agarose gels. Blood. 61: 304–310.
12. Zhou, Y.-F., E.T. Eng, J. Zhu, C. Lu, T. Walz, and T.A. Springer. 2012. Sequence and structure relationships within von Willebrand factor. Blood. 120: 449–458.
13. Müller, J.P., S. Mielke, A. Löf, T. Obser, C. Beer, L.K. Bruetzel, D.A. Pippig, W. Vanderlinden, J. Lipfert, R. Schneppenheim, and M. Benoit. 2016. Force sensing by the vascular protein von Willebrand factor is tuned by a strong intermonomer interaction. Proc Natl Acad Sci USA. 113: 1208–1213.
14. Zhang, X., K. Halvorsen, C.-Z. Zhang, W.P. Wong, and T.A. Springer. 2009. Mechanoenzymatic

cleavage of the ultralarge vascular protein von Willebrand factor. Science. 324: 1330–1334.

15. Ying, J., Y. Ling, L.A. Westfield, J.E. Sadler, and J.-Y. Shao. 2010. Unfolding the A2 domain of von Willebrand factor with the optical trap. Biophys J. 98: 1685–1693.
16. Jakobi, A.J., A. Mashaghi, S.J. Tans, and E.G. Huizinga. 2011. Calcium modulates force sensing by the von Willebrand factor A2 domain. Nat Commun. 2: 385.
17. Xu, A.J., and T.A. Springer. 2012. Calcium stabilizes the von Willebrand factor A2 domain by promoting refolding. Proc Natl Acad Sci USA. 109: 3742–3747.
18. Sing, C.E., and A. Alexander-Katz. 2010. Elongational flow induces the unfolding of von Willebrand factor at physiological flow rates. Biophys J. 98: L35–37.
19. Huck, V., M.F. Schneider, C. Gorzelanny, and S.W. Schneider. 2014. The various states of von Willebrand factor and their function in physiology and pathophysiology. Thromb Haemost. 3: 598–609.
20. Christou, H., N. Bailey, M.S. Kluger, S.A. Mitsialis, and S. Kourembanas. 2005. Extracellular acidosis induces heme oxygenase-1 expression in vascular smooth muscle cells. Am J Physiol Hear. Circ Physiol. 288: H2647–2652.
21. Babich, V., L. Knipe, L. Hewlett, A. Meli, J. Dempster, M.J. Hannah, and T. Carter. 2009. Differential effect of extracellular acidosis on the release and dispersal of soluble and membrane proteins secreted from the Weibel-Palade body. J Biol Chem. 284: 12459–12468.
22. Serrano, C. V, A. Fraticelli, R. Paniccia, A. Teti, B. Noble, S. Corda, T. Faraggiana, R.C. Ziegelstein, J.L. Zweier, and M.C. Capogrossi. 1996. pH dependence of neutrophil-endothelial cell adhesion and adhesion molecule expression. Am J Physiol. 271: C962–C970.
23. Ihrcke, N.S., W. Parker, K.J. Reissner, and J.L. Platt. 1998. Regulation of platelet heparanase during inflammation: role of pH and proteinases. J Cell Phys. 175: 255–267.
24. De Backer, D. 2003. Lactic acidosis. Minerva Anestesiol. 69: 281–284.
25. Zimmermann, J.L., T. Nicolaus, G. Neuert, and K. Blank. 2010. Thiol-based, site-specific and covalent immobilization of biomolecules for single-molecule experiments. Nat Protoc. 5: 975–985.
26. Baumann, F., M.S. Bauer, L.F. Milles, A. Alexandrovich, H.E. Gaub, and D.A. Pippig. 2016. Monovalent Strep-Tactin for strong and site-specific tethering in nanospectroscopy. Nat Nanotechnol. 11: 89–94.
27. Gumpp, H., S.W. Stahl, M. Strackharn, E.M. Puchner, and H.E. Gaub. 2009. Ultrastable combined atomic force and total internal reflection fluorescence microscope. Rev Sci Instrum. 80: 063704.
28. Hutter, J.L., and J. Bechhoefer. 1993. Calibration of atomic-force microscope tips. Rev Sci Instrum. 64: 1868–1873.
29. Condat, L. 2013. A direct algorithm for 1-D total variation denoising. IEEE Signal Proc Let. 20: 1054–1057.

30. Blanchet, C.E., A. Spilotros, F. Schwemmer, A. Melissa, A. Kikhney, C.M. Jeffries, D. Franke, D. Mark, F. Cipriani, S. Fiedler, M. Roessle, and D.I. Svergun. 2015. Versatile sample environments and automation for biological solution X-ray scattering experiments at the P12 beamline (PETRA III, DESY). J Appl Crystallogr. 48: 431–443.
31. Yin, J., P.D. Straight, S.M. McLoughlin, Z. Zhou, A.J. Lin, D.E. Golan, N.L. Kelleher, R. Kolter, and C.T. Walsh. 2005. Genetically encoded short peptide tag for versatile protein labeling by Sfp phosphopantetheinyl transferase. Proc Natl Acad Sci USA. 102: 15815–15820.
32. Schmidt, T.G.M., L. Batz, L. Bonet, U. Carl, G. Holzapfel, K. Kiem, K. Matulewicz, D. Niermeier, I. Schuchardt, and K. Stanar. 2013. Development of the Twin-Strep-tag® and its application for purification of recombinant proteins from cell culture supernatants. Protein Express Purif. 92: 54–61.
33. Kim, M., C.C. Wang, F. Benedetti, and P.E. Marszalek. 2012. A nanoscale force probe for gauging intermolecular interactions. Angew Chem Int Ed Engl. 51: 1903–1906.
34. Lipfert, J., and S. Doniach. 2007. Small-angle X-ray scattering from RNA, proteins, and protein complexes. Annu Rev Biophys Biomol Struct. 36: 307–327.
35. Mertens, H.D.T., and D.I. Svergun. 2010. Structural characterization of proteins and complexes using small-angle X-ray solution scattering. J Struct Biol. 172: 128–141.
36. Schmitt, L., M. Ludwig, H.E. Gaub, and R. Tampé. 2000. A metal-chelating microscopy tip as a new toolbox for single-molecule experiments by atomic force microscopy. Biophys J. 78: 3275–3285.
37. Srivastava, J., D.L. Barber, and M.P. Jacobson. 2007. Intracellular pH sensors: design principles and functional significance. Physiology. 22: 30–39.
38. Ruggeri, Z.M. 1997. von Willebrand factor. J Clin Invest. 99: 559–564.
39. Perkins, T.T., D.E. Smith, and S. Chu. 1997. Single polymer dynamics in an elongational flow. Science. 276: 2016–2021.
40. Smith, D.E., H.P. Babcock, and S. Chu. 1999. Single-polymer dynamics in steady shear flow. Science. 283: 1724–1727.
41. Steppich, D.M. 2009. The Physics of Von Willebrand Factor. PhD thesis, University of Augsburg, Germany. : 53–56, urn:nbn:de:bvb:384–opus–13637.

# pH-Dependent Interactions in Dimers Govern Mechanics and Structure of von Willebrand Factor

## SUPPORTING MATERIAL

*J. P. Müller* [*+], *A. Löf* [*], *S. Mielke, T. Obser, L. K. Bruetzel, W. Vanderlinden, J. Lipfert, R. Schneppenheim, and M. Benoit*

* J.P.M. and A.L. contributed equally to this work.

**SUPPORTING FIGURES**

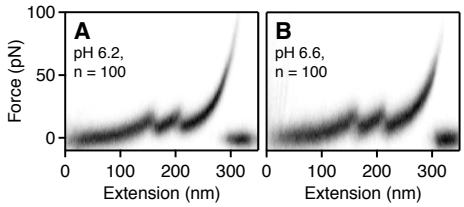


**Figure S1** Overlays of 100 force–extension traces of A1-CK dimers, measured at pH 6.2 (A) and pH 6.6 (B), respectively.

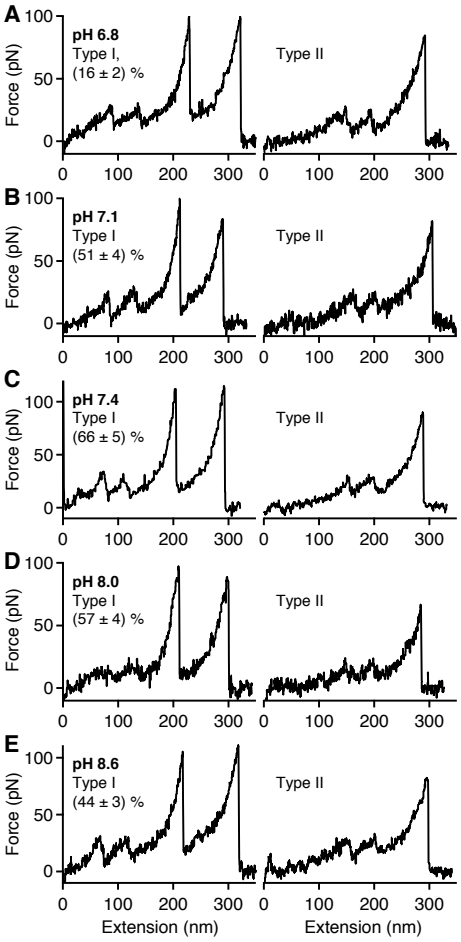


**Figure S2** Denoised force–extension traces of type I and II showing the force response of A1-CK dimers at pH 6.8 (A), 7.1 (B), 7.4 (C), 8.0 (D), and 8.6 (E). While the functional shape of type I and type II traces was conserved within the specified range of the pH, the frequency of both types of traces was significantly affected by pH (see Fig. 1L)

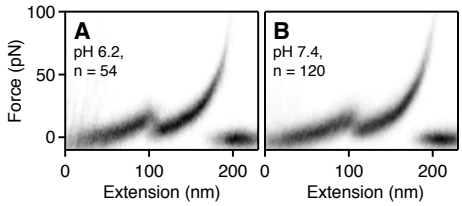


**Figure S3** Overlays of force–extension traces of VWF monomers (D'D3-CK), measured at pH 6.2 (n = 54) and at pH 7.4 (n = 120). Importantly, monomer traces were essentially unaffected by pH.

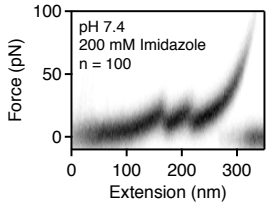


**Figure S4** Overlay of 100 force–extension traces of A1-CK dimers, measured in near-physiological buffer, supplemented with 200 mM Imidazole.

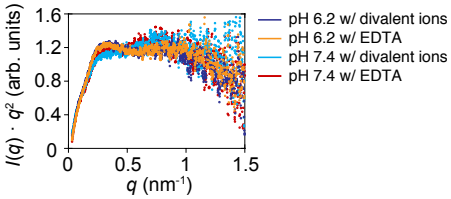


**Figure S5** SAXS profiles of A1-CK dimers, collected at the X12SA (cSAXS) beamline at the Swiss Light Source. Data were acquired at pH 6.2 and 7.4 in the presence of divalent ions (dark blue and light blue, respectively) and upon addition of EDTA (orange and red, respectively). Data are displayed in Kratky representation ($q^2 \cdot I(q)$ vs. $q$) and were scaled by a constant factor. The background level for these measurements was somewhat higher than for the profiles shown in Fig. 3D of the main manuscript – collected at the beamline P12 (Deutsches Elektronensynchrotron, Hamburg, Germany) – making reliable inversion to $P(r)$ difficult. Nonetheless, it is apparent that –

within experimental noise – the two profiles at pH 6.2 match very closely, whereas the profiles at pH 7.4 exhibit the same trends as the ones shown in Fig. 3D.

# Bibliography


1. Schneppenheim, R. & Budde, U. *von Willebrand-Syndrom und von Willebrand-Faktor - Aktuelle Aspekte der Diagnostik und Therapie* 3. Aufl. ISBN: 978-3837412482 (UNI-MED Verlag AG, Bremen, Germany, 2010).
2. Marieb, E. N. & Hoehn, K. *Human Anatomy & Physiology* 9th ed. ISBN: 978-0321802187 (Pearson Education, Upper Saddle River, NJ, 2012).
3. Schmidt, R. F. *et al. Physiologie des Menschen* 31. Aufl. ISBN: 978-3642016509 (Springer, Berlin/Heidelberg, Germany, 2010).
4. Truskey, G. A. *et al. Transport Phenomena in Biological Systems* 2nd ed. ISBN: 978-0136091943 (Pearson Education, Upper Saddle River, NJ, 2009).
5. Jackson, S. P. The growing complexity of platelet aggregation. *Blood* **109,** 5087–5095 (2006).
6. Schneider, S. W. *et al.* Shear-induced unfolding triggers adhesion of von Willebrand factor fibers. *Proc Natl Acad Sci USA* **104,** 7899–7903 (2007).
7. Ruggeri, Z. M. & Mendolicchio, G. L. Adhesion Mechanisms in Platelet Function. *Circ Res* **100,** 1673–1685 (2007).
8. Ruggeri, Z. M. *et al.* Activation-independent platelet adhesion and aggregation under elevated shear stress. *Blood* **108,** 1903–1911 (2006).
9. Sing, C. E. & Alexander-Katz, A. Elongational Flow Induces the Unfolding of von Willebrand Factor at Physiological Flow Rates. *Biophys J* **98,** L35–L37 (2010).
10. Springer, T. A. von Willebrand factor, Jedi knight of the bloodstream. *Blood* **124,** 1412–1425 (2014).
11. Smith, D. E. *et al.* Single-Polymer Dynamics in Steady Shear Flow. *Science* **283,** 1724–1727 (1999).
12. Zhang, X. *et al.* Mechanoenzymatic Cleavage of the Ultralarge Vascular Protein von Willebrand Factor. *Science* **324,** 1330–1334 (2009).
13. Springer, T. A. Biology and physics of von Willebrand factor concatamers. *J Thromb Haemost* **9 Suppl 1,** 130–143 (2011).

14. Nesbitt, W. S. *et al.* A shear gradient–dependent platelet aggregation mechanism drives thrombus formation. *Nat Med* **15,** 665–673 (2009).

15. Sadler, J. E. New concepts in von Willebrand disease. *Annu Rev Med* **56,** 173–191 (2005).

16. Methia, N. *et al.* Localized reduction of atherosclerosis in von Willebrand factor-deficient mice. *Blood* **98,** 1424–1428 (2001).

17. Theilmeier, G. *et al.* Endothelial von Willebrand factor recruits platelets to atherosclerosis-prone sites in response to hypercholesterolemia. *Blood* **99,** 4486–4493 (2002).

18. Sakai, H *et al.* Plasma Concentration of von Willebrand Factor in Acute Myocardial Infarction. *Thromb Haemost* **84,** 204–209 (2000).

19. Wagner, D. D. Cell biology of von Willebrand factor. *Annu Rev Cell Biol* **6,** 217–246 (1990).

20. Sadler, J. E. Biochemistry and genetics of von Willebrand factor. *Annu Rev Biochem* **67,** 395–424 (1998).

21. Brehm, M. A. *et al.* von Willebrand disease type 2A phenotypes IIC, IID and IIE: A day in the life of shear-stressed mutant von Willebrand factor. *Thromb Haemost* **112,** 1–13 (2014).

22. Schneppenheim, R *et al.* Defective dimerization of von Willebrand factor subunits due to a Cys -> Arg mutation in type IID von Willebrand disease. *Proc Natl Acad Sci USA* **93,** 3581–3586 (1996).

23. Purvis, A. R. *et al.* Two Cys residues essential for von Willebrand factor multimer assembly in the Golgi. *Proc Natl Acad Sci USA* **104,** 15647–15652 (2007).

24. Axelrod, D. Cell-Substrate Contacts Illuminated by Total Internal Reflection Fluorescence. *J Cell Biol* **89,** 141–145 (1981).

25. Binnig, G. *et al.* Atomic Force Microscope. *Phys Rev Lett* **56,** 930–933 (1986).

26. Vogel, V. Mechanotransduction Involving Multimodular Proteins: Converting Force into Biochemical Signals. *Annu Rev Biophys Biomol Struct* **35,** 459–488 (2006).

27. Puchner, E. M. *et al.* Mechanoenzymatics of titin kinase. *Proc Natl Acad Sci USA* **105,** 13385–13390 (2008).

28. Del Rio, A. *et al.* Stretching Single Talin Rod Molecules Activates Vinculin Binding. *Science* **323,** 638–641 (2009).

29. Puchner, E. M. & Gaub, H. E. Single-Molecule Mechanoenzymatics. *Annu Rev Biophys* **41,** 497–518 (2012).

30. Neuman, K. C. & Nagy, A. Single-molecule force spectroscopy: optical tweezers, magnetic tweezers and atomic force microscopy. *Nat Methods* **5,** 491–505 (2008).

31. Kim, J. *et al.* Force-induced on-rate switching and modulation by mutations in gain-of-function von Willebrand diseases. *Proc Natl Acad Sci USA* **112,** 4648–4653 (2015).

32. Zhang, Q. *et al.* Structural specializations of A2, a force-sensing domain in the ultralarge vascular protein von Willebrand factor. *Proc Natl Acad Sci USA* **106,** 9226–9231 (2009).

33. Alexander-Katz, A. *et al.* Shear-flow induced unfolding of polymeric globules. *Phys Rev Lett* **97,** 1–4 (2006).

34. Alberts, B *et al. Molecular Biology of the Cell,* 5th ed. ISBN: 978-0815341055 (Garland Publishing, Hamden, CT, 2007).

35. Nelson, D. L. & Cox, M. M. *Lehninger Principles of Biochemistry* 4th ed. ISBN: 978-0716743392 (W. H. Freeman, New York, NY, 2004).

36. Wilkinson, B. & Gilbert, H. F. Protein disulfide isomerase. *Biochim Biophys Acta* **1699,** 35–44 (2004).

37. Lippok, S. *et al.* von Willebrand factor is dimerized by protein disulfide isomerase. *Blood* **127,** 1183–1191 (2016).

38. Chen, K. *et al.* Immunoglobulin D enhances immune surveillance by activating antimicrobial, proinflammatory and B cell–stimulating programs in basophils. *Nat Immunol* **10,** 889–898 (2009).

39. Lukin, J. A. & Ho, C. The Structure–Function Relationship of Hemoglobin in Solution at Atomic Resolution. *Chem Rev* **104,** 1219–1230 (2004).

40. Shiltagh, N. *et al.* Solution structure of the major factor VIII binding region on von Willebrand factor. *Blood* **123,** 4143–4151 (2014).

41. Wenger, M. P. *et al.* Mechanical Properties of Collagen Fibrils. *Biophysical Journal* **93,** 1255–1263 (2007).

42. Seifert, C. & Gräter, F. Protein mechanics: How force regulates molecular function. *Biochim Biophys Acta* **1830,** 4762–4768 (2013).

43. Politou, A. S. *et al.* The Elastic I-band Region of Titin is Assembled in a "Modular" Fashion by Weakly Interacting Ig-like Domains. *J. Mol. Biol.* **255,** 604–616 (1996).

44. Mosesson, M. W. Fibrinogen and fibrin structure and functions. *J Thromb Haemost* **3,** 1894–1904 (2005).

45. Pankov, R. & Yamada, K. M. Fibronectin at a glance. *J Cell Sci* **115,** 3861–3863 (2002).

46. Emsley, J. *et al.* Crystal Structure of the von Willebrand Factor A1 Domain and Implications for the Binding of Platelet Glycoprotein Ib. *J Biol Chem* **273,** 10396–10401 (1998).

47. Huizinga, E. G. *et al.* Structures of Glycoprotein Ibα and Its Complex with von Willebrand Factor A1 Domain. *Science* **297,** 1176–1179 (2002).

48. Dumas, J. J. *et al.* Crystal Structure of the Wild-type von Willebrand Factor A1-Glycoprotein Ibα Complex Reveals Conformation Differences with a Complex Bearing von Willebrand Disease Mutations. *J Biol Chem* **279,** 23327–23334 (2004).

49. Blenner, M. A. *et al.* Structural Basis of Regulation of von Willebrand Factor Binding to Glycoprotein Ib. *J Biol Chem* **289,** 5565–5579 (2014).

50. Huizinga, E. G. *et al.* Crystal structure of the A3 domain of human von Willebrand factor: implications for collagen binding. *Structure* **5,** 1147–1156 (1997).

51. Bienkowska, J. *et al.* The von Willebrand Factor A3 Domain Does Not Contain a Metal Ion-dependent Adhesion Site Motif. *J Biol Chem* **272,** 25162–25167 (1997).

52. Brondijk, T. H. C. *et al.* Implications for collagen I chain registry from the structure of the collagen von Willebrand factor A3 domain complex. *Proc Natl Acad Sci USA* **109,** 5253–5258 (2012).

53. Baldauf, C. *et al.* Shear-induced unfolding activates von Willebrand factor A2 domain for proteolysis. *J Thromb Haemost* **7,** 2096–2105 (2009).

54. Huang, R.-H. *et al.* Assembly of Weibel-Palade body-like tubules from N-terminal domains of von Willebrand factor. *Proc Natl Acad Sci USA* **105,** 482–487 (2008).

55. Zhou, Y.-F. *et al.* A pH-regulated dimeric bouquet in the structure of von Willebrand factor. *EMBO J* **30,** 4098–4111 (2011).

56. Müller, J. P. *et al.* Force sensing by the vascular protein von Willebrand factor is tuned by a strong intermonomer interaction. *Proc Natl Acad Sci USA* **113,** 1208–1213 (2016).

57. Zhou, M. *et al.* A novel calcium-binding site of von Willebrand factor A2 domain regulates its cleavage by ADAMTS13. *Blood* **117,** 4623–4631 (2011).

58. Jakobi, A. J. *et al.* Calcium modulates force sensing by the von Willebrand factor A2 domain. *Nat Commun* **2,** 385 (2011).

59. Xu, A. J. & Springer, T. A. Calcium stabilizes the von Willebrand factor A2 domain by promoting refolding. *Proc Natl Acad Sci USA* **109,** 3742–3747 (2012).

60. Srivastava, J. *et al.* Intracellular pH Sensors: Design Principles and Functional Significance. *Physiology* **22,** 30–39 (2007).

61. Zhou, Y.-F. *et al.* Sequence and structure relationships within von Willebrand factor. *Blood* **120,** 449–458 (2012).

62. Soucie, J. M. *et al.* Occurrence of Hemophilia in the United States. *Am J Hematol* **59,** 288–294 (1998).

63. Girma, J. P. *et al.* Limited Proteolysis of Human von Willebrand Factor by Staphylococcus aureus V-8 Protease: Isolation and Partial Characterization of a Platelet-Binding Domain. *Biochemistry* **25,** 3156–3163 (1986).

64. Zhou, Y.-F. & Springer, T. A. Highly reinforced structure of a C-terminal dimerization domain in von Willebrand factor. *Blood* **123,** 1785–1793 (2014).

65. Lang, T. *et al.* Gel-forming mucins appeared early in metazoan evolution. *Proc Natl Acad Sci USA* **104,** 16209–16214 (2007).

66. Ambort, D. *et al.* Calcium and pH-dependent packing and release of the gel-forming MUC2 mucin. *Proc Natl Acad Sci USA* **109,** 5645–5650 (2012).

67. Sobel, M *et al.* Localization and Characterization of a Heparin Binding Domain Peptide of Human von Willebrand Factor. *J Biol Chem* **267,** 8857–8862 (1992).

68. Grässle, S. *et al.* von Willebrand Factor Directly Interacts With DNA From Neutrophil Extracellular Traps. *Arterioscler Thromb Vasc Biol* **34,** 1382–1389 (2014).

69. Erent, M *et al.* Rate, extent and concentration dependence of histamine-evoked Weibel-Palade body exocytosis determined from individual fusion events in human endothelial cells. *J Physiol* **583,** 195–212 (2007).

70. Fulcher, C. A. *et al.* Isoelectric focusing of human von Willebrand factor in urea-agarose gels. *Blood* **61,** 304–310 (1983).

71. Gijsen, F. J. H. *et al.* The influence of the non-Newtonian properties of blood on the flow in large arteries: steady flow in a carotid bifurcation model. *J Biomech* **32,** 601–608 (1999).

72. Müller, K. *et al.* Margination of micro- and nano-particles in blood flow and its effect on drug delivery. *Sci Rep* **4,** 4871 (2014).

73. Zhao, H. *et al.* Shear-induced particle migration and margination in a cellular suspension. *Phys Fluids* **24,** 011902 (2012).

74. Sherman, T. F. On Connecting Large Vessels to Small. The Meaning of Murray's Law. *J Gen Physiol* **78,** 431–453 (1981).

75. Wiedeman, M. P. Dimensions of Blood Vessels from Distributing Artery to Collecting Vein. *Circ Res* **12,** 375–378 (1963).

76. Ku, D. N. Blood flow in arteries. *Annu Rev Fluid Mech* **29,** 399–434 (1997).

77. Peterson, L. H. The Dynamics of Pulsatile Blood Flow. *Circ Res* **2,** 127–139 (1954).

78. Papaioannou, T. G. & Stefanadis, C. Vascular Wall Shear Stress: Basic Principles and Methods. *Hellenic J Cardiol* **46,** 9–15 (2005).

79. Shankaran, H & Neelamegham, S. Hydrodynamic Forces Applied on Intercellular Bonds, Soluble Molecules, and Cell-Surface Receptors. *Biophys J* **86,** 576–588 (2004).

80. Fowler, W. E. *et al.* Substructure of Human von Willebrand Factor. *J Clin Invest* **76,** 1491–1500 (1985).

81. Chen, H. *et al.* Blood-clotting-inspired reversible polymer-colloid composite assembly in flow. *Nat Commun* **4,** 1333 (2013).

82. Ulrichts, H. *et al.* Shielding of the A1 Domain by the D'D3 Domains of von Willebrand Factor Modulates Its Interaction with Platelet Glycoprotein Ib-IX-V. *J Biol Chem* **281,** 4699–4707 (2006).

83. Madabhushi, S. R. *et al.* Platelet GpIb$\alpha$ Binding to von Willebrand Factor Under Fluid Shear: Contributions of the D'D3-Domain, A1-Domain Flanking Peptide and O-Linked Glycans. *J Am Heart Assoc* **3,** 1–13 (2014).

84. Aponte-Santamaría, C. *et al.* Force-Sensitive Autoinhibition of the von Willebrand Factor Is Mediated by Interdomain Interactions. *Biophys J* **108,** 2312–2321 (2015).

85. Tsai, H.-M. *et al.* Shear Stress Enhances the Proteolysis of von Willebrand Factor in Normal Plasma. *Blood* **83,** 2171–2179 (1994).

86. Tsai, H. M. Physiologic cleavage of von Willebrand factor by a plasma protease is dependent on its conformation and requires calcium ion. *Blood* **87,** 4235–4244 (1996).

87. Zheng, X. L. ADAMTS13 and von Willebrand Factor in Thrombotic Thrombocytopenic Purpura. *Annu Rev Med* **66,** 211–225 (2015).

88. Ying, J. *et al.* Unfolding the A2 Domain of Von Willebrand Factor with the Optical Trap. *Biophys J* **98,** 1685–1693 (2010).

89. Xu, A. J. & Springer, T. A. Mechanisms by which von Willebrand Disease Mutations Destabilize the A2 Domain. *J Biol Chem* **288,** 6317–6324 (2013).

90. Dong, J.-f. *et al.* ADAMTS-13 rapidly cleaves newly secreted ultralarge von Willebrand factor multimers on the endothelial surface under flowing conditions. *Blood* **100,** 4033–4039 (2002).

91. Donadelli, R. *et al.* Size regulation of von Willebrand factor–mediated platelet thrombi by ADAMTS13 in flowing blood. *Blood* **107,** 1943–1950 (2006).

92. Alexander-Katz, A. Toward Novel Polymer-Based Materials Inspired in Blood Clotting. *Macromolecules* **47,** 1503–1513 (2014).

93. Savage, B. *et al.* Functional self-association of von Willebrand factor during platelet adhesion under flow. *Proc Natl Acad Sci USA* **99,** 425–430 (2002).

94. Ulrichts, H. *et al.* The von Willebrand factor self-association is modulated by a multiple domain interaction. *J Thromb Haemost* **3,** 552–561 (2005).

95. Huck, V. *et al.* The various states of von Willebrand factor and their function in physiology and pathophysiology. *Thromb Haemost* **3,** 598–609 (2014).

96. Christou, H *et al.* Extracellular acidosis induces heme oxygenase-1 expression in vascular smooth muscle cells. *Am J Physiol Heart Circ Physiol* **288,** H2647–H2652 (2005).

97. Babich, V. *et al.* Differential Effect of Extracellular Acidosis on the Release and Dispersal of Soluble and Membrane Proteins Secreted from the Weibel-Palade Body. *J Biol Chem* **284,** 12459–12468 (2009).

98. Serrano, C. V. *et al.* pH dependence of neutrophil-endothelial cell adhesion and adhesion molecule expression. *Am J Physiol* **271,** C962–C970 (1996).

99. Ihrcke, N. S. *et al.* Regulation of Platelet Heparanase During Inflammation: Role of pH and Proteinases. *J Cell Phys* **175,** 255–267 (1998).

100. De Backer, D. Lactic acidosis. *Minerva Anestesiol* **69,** 281–284 (2003).

101. Lippok, S. *et al.* Exponential Size Distribution of von Willebrand Factor. *Biophys J* **105,** 1208–1216 (2013).

102. Mielke, S. Dissecting the force response of Von Willebrand Factor at single-molecule level. *Master's thesis, LMU Munich, Prof. Dr. Hermann Gaub* (2015).

103. Löf, A. Conformational and Binding Studies on Single Von Willebrand Factor Dimers. *Master's thesis, LMU Munich, Prof. Dr. Hermann Gaub* (2015).

104. Beer, C. G. AFM Imaging Studies on Von Willebrand Factor. *Master's thesis, LMU Munich, Prof. Dr. Hermann Gaub* (2015).

105. Graham, F. L. *et al.* Characteristics of a Human Cell Line Transformed by DNA from Human Adenovirus Type 5. *J Gen Virol* **36,** 59–72 (1977).

106. Treder, N. Polymorphismus Phe/Tyr 2561 im Von-Willebrand-Faktor-Gen als Risikofaktor für Myokardinfarkt und koronare Herzkrankheit. *PhD thesis, University of Hamburg, Prof. Dr. Reinhard Schneppenheim,* urn:nbn:de:gbv:18–30270 (2006).

107. Cormack, B. P. *et al.* FACS-optimized mutants of the green fluorescent protein (GFP). *Gene* **173,** 33–38 (1996).

108. Kufer, S. K. *et al.* Single-Molecule Cut-and-Paste Surface Assembly. *Science* **319,** 594–596 (2008).

109. Moy, V. T. *et al.* Intermolecular Forces and Energies Between Ligands and Receptors. *Science* **266,** 257–259 (1994).

110. Schmitt, L *et al.* A Metal-Chelating Microscopy Tip as a New Toolbox for Single-Molecule Experiments by Atomic Force Microscopy. *Biophys J* **78,** 3275–3285 (2000).

111. Grandbois, M. *et al.* How Strong is a Covalent Bond? *Science* **283,** 1727–1730 (1999).

112. Suresh, S. Nanomedicine: Elastic clues in cancer detection. *Nat Nanotechnol* **2,** 748–749 (2007).

113. Cross, S. E. *et al.* Nanomechanical analysis of cells from cancer patients. *Nat Nanotechnol* **2,** 780–783 (2007).

114. Roduit, C. *et al.* Stiffness Tomography by Atomic Force Microscopy. *Biophys J* **97,** 674–677 (2009).

115. Hecht, F. M. *et al.* Imaging viscoelastic properties of live cells by AFM: power-law rheology on the nanoscale. *Soft Matter* **11,** 4584–4591 (2015).

116. Rief, M. *et al.* Single Molecule Force Spectroscopy on Polysaccharides by Atomic Force Microscopy. *Science* **275,** 1295–1297 (1997).

117. Rief, M. *et al.* Reversible Unfolding of Individual Titin Immunoglobulin Domains by AFM. *Science* **276,** 1109–1112 (1997).

118. Hutter, J. L. & Bechhoefer, J. Calibration of atomic-force microscope tips. *Rev Sci Instrum* **64,** 1868–1873 (1993).

119. Halvorsen, K. & Wong, W. P. Massively Parallel Single-Molecule Manipulation Using Centrifugal Force. *Biophys J* **98,** L53–L55 (2010).

120. Viani, M. B. *et al.* Small cantilevers for force spectroscopy of single molecules. *J Appl Phys* **86,** 2258 (1999).

121. Beckmann, A. *et al.* A fast recoiling silk-like elastomer facilitates nanosecond nematocyst discharge. *BMC Biol* **13:3.** doi:10.1186/s12915-014-0113-1 (2015).

122. Stahl, S. W. *et al.* Single-molecule dissection of the high-affinity cohesin–dockerin complex. *Proc Natl Acad Sci USA* **109,** 20431–20436 (2012).

123. Jaschke, M. & Butt, H.-J. Height calibration of optical lever atomic force microscopes by simple laser interferometry. *Rev Sci Instrum* **66,** 1258–1259 (1995).

124. Bustamante, C *et al.* Entropic Elasticity of lambda-Phage DNA. *Science* **265,** 1599–1600 (1994).

125. Marko, J. F. & Siggia, E. D. Stretching DNA. *Macromolecules* **28,** 8759–8770 (1995).

126. Odijk, T. Stiff Chains and Filaments under Tension. *Macromolecules* **28,** 7016–7018 (1995).

127. Smith, S. B. *et al.* Direct Mechanical Measurements of the Elasticity of Single DNA Molecules by Using Magnetic Beads. *Science* **258,** 1122–1126 (1992).

128. Verdier, P. H. Relaxation Behavior of the Freely Jointed Chain. *J Chem Phys* **52,** 5512–5517 (1970).

129. Perico, A. *et al.* Polymer Dynamics in Dilute Solutions. The Freely Rotating Chain. *Macromolecules* **17,** 2686–2689 (1984).

130. Schoeler, C. *et al.* Ultrastable cellulosome-adhesion complex tightens under load. *Nat Commun* **5,** 5635 (2014).

131. Jobst, M. A. *et al.* Resolving dual binding conformations of cellulosome cohesin-dockerin complexes using single-molecule force spectroscopy. *eLife* **4,** e10319 (2015).

132. Puchner, E. M. *et al.* Comparing Proteins by Their Unfolding Pattern. *Biophys J* **95,** 426–434 (2008).

133. Silverman, B. W. Density estimation for statistics and data analysis. *Monogr Statist Appl Probab* **37,** 1–22 (1986).

134. Bell, G. I. Models for the Specific Adhesion of Cells to Cells. *Science* **200,** 618–627 (1978).

135. Evans, E. & Ritchie, K. Dynamic Strength of Molecular Adhesion Bonds. *Biophys J* **72,** 1541–1555 (1997).

136. Merkel, R *et al.* Energy landscapes of receptor–ligand bonds explored with dynamic force spectroscopy. *Nature* **397,** 50–53 (1999).

137. Evans, E. & Ritchie, K. Strength of a Weak Bond Connecting Flexible Polymer Chains. *Biophys J* **76,** 2439–2447 (1999).

138. Evans, E. A. & Calderwood, D. A. Forces and Bond Dynamics in Cell Adhesion. *Science* **316,** 1148–1153 (2007).

139. Dudko, O. K. *et al.* Theory, analysis, and interpretation of single-molecule force spectroscopy experiments. *Proc Natl Acad Sci USA* **105,** 15755–15760 (2008).

140. Kim, J. *et al.* A mechanically stabilized receptor-ligand flex-bond important in the vasculature. *Nature* **466,** 992–995 (2010).

141. Zimmermann, J. L. *et al.* Thiol-based, site-specific and covalent immobilization of biomolecules for single-molecule experiments. *Nat Protoc* **5,** 975–985 (2010).

142. Yin, J. *et al.* Genetically encoded short peptide tag for versatile protein labeling by Sfp phosphopantetheinyl transferase. *Proc Natl Acad Sci USA* **102,** 15815–15820 (2005).

143. Gumpp, H *et al.* Ultrastable combined atomic force and total internal reflection fluorescence microscope. *Rev Sci Instrum* **80,** 063704 (2009).

144. Condat, L. A Direct Algorithm for 1D Total Variation Denoising. *IEEE Signal Proc Let* **20,** 1054–1057 (2013).

145. Milles, L. F. Single Molecule Studies on Cellulosomal Proteins in Simulation and Experiment. *Master's thesis, LMU Munich, Prof. Dr. Hermann Gaub* (2013).

146. Radmacher, M. *et al.* From Molecules to Cells: Imaging Soft Samples with the Atomic Force Microscope. *Science* **257,** 1900–1905 (1992).

147. Müller, D. J. *et al.* Imaging Purple Membranes in Aqueous Solutions at Sub-Nanometer Resolution by Atomic Force Microscopy. *Biophys J* **68,** 1681–1686 (1995).

148. Scheuring, S. *et al.* Single Proteins Observed by Atomic Force Microscopy. *Single Mol* **2,** 59–67 (2001).

149. Stahl, S. W. *et al.* Photothermal cantilever actuation for fast single-molecule force spectroscopy. *Rev Sci Instrum* **80,** 073702 (2009).

150. Bhushan, B. *Handbook of Nanotechnology* 2nd ed. ISBN: 978-3540298557 (Springer, Berlin/Heidelberg, Germany, 2007).

151. Wen, D. *et al.* Discovery and Investigation of O-Xylosylation in Engineered Proteins Containing a $(GGGGS)_n$ Linker. *Anal Chem* **85,** 4805–4812 (2013).

152. Spahr, C. *et al.* Recombinant human lecithin-cholesterol acyltransferase Fc fusion: Analysis of N- and O-linked glycans and identification and elimination of a xylose-based O-linked tetrasaccharide core in the linker region. *Prot Sci* **22,** 1739–1753 (2013).

153. Spencer, D. *et al.* O-xylosylation in a Recombinant Protein is Directed at a Common Motif on Glycine–Serine Linkers. *J Pharm Sci* **102,** 3920–3924 (2013).

154. Spahr, C. *et al.* O-Glycosylation of glycine-serine linkers in recombinant Fc-fusion proteins. *mAbs* **6,** 904–914 (2014).

155. Vanderlinden, W. *et al.* Mesoscale DNA Structural Changes on Binding and Photoreaction with $Ru[(TAP)_2PHEHAT]^{2+}$. *J Am Chem Soc* **134,** 10214–10221 (2012).

156. Stephens, D. J. & Allan, V. J. Light Microscopy Techniques for Live Cell Imaging. *Science* **300,** 82–86 (2003).

157. Ulbrich, M. H. & Isacoff, E. Y. Subunit counting in membrane-bound proteins. *Nat Methods* **4,** 319–321 (2007).

158. Hallworth, R. & Nichols, M. G. Prestin in HEK cells is an obligate tetramer. *J Neurophysiol* **107,** 5–11 (2012).

159. Hallworth, R. & Nichols, M. G. Single Molecule Imaging Approach to Membrane Protein Stoichiometry. *Microsc Microanal* **18,** 771–780 (2012).

160. Opfer, J. & Gottschalk, K.-E. Identifying Discrete States of a Biological System Using a Novel Step Detection Algorithm. *PLOS ONE* **7,** e45896 (2012).

161. Yin, J. *et al.* Site-specific protein labeling by Sfp phosphopantetheinyl transferase. *Nat Protoc* **1,** 280–285 (2006).

162. Schmidt, T. G. M. *et al.* Development of the Twin-Strep-tag® and its application for purification of recombinant proteins from cell culture supernatants. *Protein Express Purif* **92,** 54–61 (2013).

163. Kim, M. *et al.* A Nanoscale Force Probe for Gauging Intermolecular Interactions. *Angew Chem Int Ed Engl* **51,** 1903–1906 (2012).

164. Baumann, F. *et al.* Monovalent Strep-Tactin for strong and site-specific tethering in nanospectroscopy. *Nat Nanotechnol* **11,** 89–94 (2016).

165. Rivetti, C *et al.* Scanning Force Microscopy of DNA Deposited Onto Mica: Equilibration versus Kinetic Trapping Studied by Statistical Polymer Chain Analysis. *J Mol Biol* **264,** 919–932 (1996).

166. Ott, W. *et al.* Single-molecule force spectroscopy on polyproteins and receptor–ligand complexes: The current toolbox. *J Struct Biol.* doi:10.1016/j.jsb.2016.02.011. http://dx.doi.org/10.1016/j.jsb.2016.02.011 (2016).

167. Steppich, D. M. *et al.* Relaxation of ultralarge VWF bundles in a microfluidic–AFM hybrid reactor. *Biochem Biophys Res Com* **369,** 507–512 (2008).

168. Perkins, T. T. *et al.* Single Polymer Dynamics in an Elongational Flow. *Science* **276,** 2016–2021 (1997).

169. Steppich, D. M. The Physics of Von Willebrand Factor (VWF). *PhD thesis, University of Augsburg, Prof. Dr. Achim Wixforth,* 53–56, urn:nbn:de:bvb:384–opus–13637 (2009).

170. Lippok, S. *et al.* Shear-Induced Unfolding and Enzymatic Cleavage of Full-Length VWF Multimers. *Biophys J* **110,** 545–554 (2016).

171. Inoué, S. *et al.* Fluorescence polarization of green fluorescence protein. *Proc Natl Acad Sci USA* **99,** 4272–4277 (2002).

172. Alexander-Katz, A. & Netz, R. R. Surface-enhanced unfolding of collapsed polymers in shear flow. *EPL* **80,** 18001 (2007).

# List of Figures

# List of Tables

# Acknowledgments

I would like to sincerely thank all the people who helped me during my doctoral studies with support, advice, and motivation. Special thanks go to:

**Prof. Dr. Hermann Gaub** for the opportunity to perform the research for this thesis in his lab and for providing an incredible working environment. It has been a privilege to work in the Gaub lab and to benefit from the expertise of all lab members. I am particularly thankful for helpful discussions on VWF and invaluable advice regarding publications.
**Dr. Martin Benoit** for recruiting me for this very interesting research project, and for all his contributions of time, ideas, and funding to make this PhD work productive. I also want to express my thanks for giving me sufficient space for developing my own ideas and strategies, as well as for the possibility to participate in diverse international conferences, workshops, and seminars. The annual sailing trips will remain in very good memory, too.

**Achim Löf** for simply being the best colleague that one could wish for. It has truly been a pleasure working with him, and I am greatly indebted for many helpful discussions, very good advice, constant support, and great teamwork. Also, I look back on a lot of fun outside the lab, and I am glad for our great friendship. Achim, I wish you all the best and much success, both for your private life and future research on VWF – but never call it blood clotting!
**Christof Beer** and **Salomé Mielke** for their support, great teamwork, fruitful discussions and the nice time that we had together.
**Dr. Willem Vanderlinden** for sharing his surface functionalization protocol for imaging experiments, very helpful discussions both on quantitative image analysis and coordination chemistry, and for nice Champions League evenings with Belgian beer and German fries.
**Prof. Dr. Jan Lipfert** for helpful discussions on VWF, in particular on the formation of stems in dimers, and excellent advice for our manuscripts. I further want to thank him and **Linda Brützel** for SAXS measurements and the reliable and harmonic cooperation.
**Dr. Diana Pippig** for manifold support in the chemistry lab, advice regarding peptide tags for force measurements, and for providing tetravalent Strep-Tactin with a single Cystein.
**Wolfgang Ott** for advice concerning the use of type I Dockerin as a tag for Cnidoin.
**Lukas Milles** for sharing a very useful data processing and denoising algorithm.
**Magnus Bauer** for sloth tamer tools and constant support with them.

**Constantin Schöler** for helpful discussions on SMFS, support whenever I had problems with my computer, and for convincing me of the benefits of Mac OS. I always enjoyed our conversations in pubs with beer and gin tonic, and I am thankful for our friendship.
**Dr. Anna-Kristina Marel** for initial help with Adobe Illustrator, a great year together, and beautiful hiking tours with perfect weather guarantee.
**Katherine Erlich** for many efforts spent on proofreading, not only concerning this thesis, but also regarding manuscripts and other texts.
**Klara Malinowska** and **Sonja Westermayer** for a pleasant and productive time as CeNS Student Representatives.
**Dr. Mathias Strackharn** for support with the TIRF microscopy setup.
**Dr. Stefan Stahl** for introducing me to the custom-built AFM setups.
**Thomas Nicolaus** for help and advice in the chemistry lab, support with the purification of VWF, constant supply of aminosilanized glass slides, and for feel-good music.
**Angelika Kardinal** for help in the chemistry lab and support in gel electrophoresis.
**All LS Gaub members** for help and advice when needed, and steady cake-supply.

**Prof. Dr. Reinhard Schneppenheim** for supply of recombinant VWF, his interest in the work of our lab, and his enthusiasm for VWF and the research group SHENC.
**Dr. Maria Brehm** for the great cooperation, especially regarding the PDI manuscript.
**Tobias Obser** for genetic engineering of all the VWF constructs we could wish for.
**Gesa König** for technical assistance in preparation of recombinant VWF.
**Prof. Dr. Joachim Rädler** for the great collaboration on the size distribution project, very helpful discussions on VWF, and for being the second reviewer of this thesis.
**Dr. Svenja Lippok** and **Judith Mittag** for the uncomplicated cooperation.
**Prof. Dr. Frauke Gräter** for insightful discussions on interactions in VWF.
**Prof. Dr. Matthias Schneider** and **Dr. Volker Huck** for fruitful conversations.
**All SHENC members** for the multidisciplinary framework from which this thesis originated.

**Prof. Dr. Alfredo Alexander-Katz** for helpful discussions on the behavior of VWF in shear and elongational flow, and for a lot of skiing fun at the NIM Winterschool 2013.
**Prof. Dr. Erich Sackmann** for inspiring discussions on VWF and the role of the pH.

Finally, I would like to thank my parents and my sister Birgit for their constant interest in my work and their infinite support in everything I do. I feel blessed to always have my family to count on. Moreover, I am very grateful to Ana-María for continuously encouraging me to do my best, for standing me after difficult days, and for always being there for me. Last of all, I would like to express my sincere thanks to my friends for supporting me on my way and for always having an open ear for me.

Ich versichere, diese Arbeit selbstständig angefertigt und dazu nur die im Literaturverzeichnis angegebenen Quellen benutzt zu haben.

München, 20. Mai 2016